NASA CR-167964
PWA-5515-176

NASA

JT9D THERMAL BARRIER COATED VANES

by

Dr. K. G. Sheffler
Mr. R. A. Graziani
Mr. G. C. Sinko

UNITED TECHNOLOGIES CORPORATION
Pratt & Whitney Aircraft Group
Commercial Products Division

Prepared for

NATIONAL AERONAUTICS AND SPACE ADMINISTRATION

Lewis Research Center
Cleveland, Ohio 44135

Contract NAS3-20630

1.REPORT NO. CR-167964	2. GOVERNMENT ACCESSION NO.	3.RECIPIENT'S CATALOG NO.
4.TITLE AND SUBTITLE JT9D THERMAL BARRIER COATED VANES		5. REPORT DATE April 1982 6. PERFORMING ORG. CODE
7.AUTHOR(S) Dr. K. D. Sheffler, Mr. R. A. Graziani, and Mr. G. C. Sinko		8. PERFORMING ORG. REPT. NO. PWA-5515-176
9.PERFORMING ORG. NAME AND ADDRESS UNITED TECHNOLOGIES CORPORATION Pratt & Whitney Aircraft Group Commercial Products Division East Hartford, Connecticut 01608		10. WORK UNIT NO. 11. CONTRACT OR GRANT NO. NAS3-20630
12. SPONSORING AGENCY NAME AND ADDRESS NATIONAL AERONAUTICS AND SPACE ADMINISTRATION Lewis Research Center 21000 Brookpark Road, Cleveland, Ohio 44135		13. TYPE REPT./PERIOD COVERED CONTRACTOR REPORT 14. SPONSORING AGENCY CODE

15. SUPPLEMENTARY NOTES

16. ABSTRACT

The technology of plasma sprayed thermal barrier coatings applied to turbine vane platforms in modern high temperature commercial engines was advanced to the point of demonstrated feasibility for application to commercial aircraft engines. The three thermal barrier coatings refined under this program are zirconia stabilized with twenty-one percent magnesia (21% MSZ), six percent yttria (6% YSZ), and twenty percent yttria (20% YSZ). Improvement in thermal cyclic endurance by a factor of 40 times was demonstrated in rig tests. A cooling system evolved during the program which featured air impingement cooling for the vane platforms rather than film cooling. The impingement cooling system, in combination with the thermal barrier coatings, reduced platform cooling air requirements by 44% relative to the current film cooling system. Improved durability and reduced cooling air requirements were demonstrated in rig and engine endurance tests. Two engine tests were conducted, one of 1000 cycles and the other of 1500 cycles. All three coatings applied to vanes fabricated with the final cooling system configuration completed the final 1500 cycle engine endurance test. Results of this test clearly demonstrated the durability of the 6% YSZ coating which was in very good condition after the test. The 21% MSZ and 20% YSZ coatings had numerous occurrences of significant spalling in the test.

17. KEY WORDS (SUGGESTED BY AUTHOR(S))	18. DISTRIBUTION STATEMENT
Thermal barrier coating Turbine vane platform Impingement cooling Durability improvement	

19. SECURITY CLASS (THIS REPORT)	20. SECURITY CLASS (THIS PAGE)	21. NO. PGS	22. PRICE *
UNCLASSIFIED	UNCLASSIFIED		

* For sale by the National Technical Information Service, Springfield, VA 22161

FOREWORD

The refinement and demonstration effort described in this report was conducted by the Commercial Products Division of Pratt & Whitney Aircraft Group, United Technologies Corporation, under NASA contract NAS3-20630. Mr. John E. McAulay and Mr. Irving E. Sumner of the NASA Lewis Research Center were Project Manager and Project Engineer, respectively, for the contract.

This report was prepared by Mr. George C. Sinko, Mr. Raymond A. Graziani and Dr. Keith D. Sheffler under the direction of Mr. William O. Gaffin, Pratt & Whitney Aircraft Program Manager. This report has been assigned the Commercial Products Division, Pratt & Whitney Aircraft Group internal report number PWA-5515-176.

TABLE OF CONTENTS

LIST OF ILLUSTRATIONS

LIST OF ILLUSTRATIONS (Continued)

LIST OF ILLUSTRATIONS (Continued)

LIST OF ILLUSTRATIONS (Continued)

LIST OF ILLUSTRATIONS (Continued)

LIST OF ILLUSTRATIONS (Continued)

LIST OF ILLUSTRATIONS (Continued)

LIST OF TABLES

LIST OF TABLES (Continued)

1.0 SUMMARY

The technology of plasma sprayed thermal barrier coatings applied to turbine vane platforms in modern high temperature commercial engines was advanced to the point of demonstrated feasibility for application to commercial aircraft engines as part of the NASA sponsored Engine Component Improvement - Performance Improvement (ECI-PI) project. The durability of three different coating chemistries was improved dramatically by refinements in materials and spray processes. Improvement in thermal cyclic endurance by a factor of 40 times was demonstrated in rig tests, relative to state-of-the-art coatings at the beginning of the program.

An impingement cooling system which, in combination with the thermal barrier coatings, reduces platform cooling air requirements by 44% relative to the current film cooling system was designed and developed. The adequacy of the coating and cooling system combination was developed and demonstrated in two JT9D engine cycle endurance tests. The initial and final engine tests consisted of 1000 and 1500 thermal cycles, respectively.

The three thermal barrier coatings refined under this program are zirconia stabilized with twenty-one percent magnesia (21% MSZ), six percent yttria (6% YSZ), and twenty percent yttria (20% YSZ), respectively. This variation in stabilizer material and amount, combined with the plasma spray process techniques developed under the program, resulted in three different types of thermal strain relief in the coating microstructure. All three demonstrated acceptable durability in thermal cyclic rig tests, but with somewhat different response to variations in coating thickness and in the maximum cyclic temperature applied. All three coatings were included in the engine endurance tests to evaluate the effect of these differences in the actual engine environment.

The cooling system which evolved from the program features air impingement through small, spaced holes in newly designed plates on the back side of most of the vane platform area. The aft edge regions of the platforms are convectively cooled by the outflow of the impingement air through drilled holes in the vane casting.

All three coatings applied to vanes fabricated with the final cooling system configuration completed the final 1500 cycle engine endurance test. The 6% YSZ coating was generally in very good condition, but the 21% MSZ coating and the 20% YSZ coating had numerous occurrences of significant spalling in several different platform locations. The final engine endurance test evaluation of substrate temperature control was inconclusive relative to the initial engine test, with coatings sprayed without benefit of controlled substrate temperature. Both the initial and final endurance tests resulted in spalling of some of the coatings in the hottest regions of the vane platforms. It was expected that the relative performance of all the coatings in the final engine test would be improved based on the benefit of substrate temperature control demonstrated in burner rig tests on laboratory specimens. It should be noted, however, that the average PACER turbine inlet temperature of the final engine

endurance test exceeded the initial test by about 11°C (20°F). Also, the average PACER turbine inlet temperature in the final engine test exceeded considerably (by as much as 61°C (110°F)) the temperatures in the first engine test for some cycles. This more severe vane platform environment in the final test may have masked the potential benefit of substrate temperature control.

2.0 INTRODUCTION

National energy demand has outpaced domestic supply, creating an increased U.S. dependence on foreign oil. This increased dependence was dramatized by the OPEC oil embargo in the winter of 1973-74. In addition, the embargo triggered a rapid rise in the cost of fuel which, along with the potential of further increases, brought about a changing economic circumstance with regard to the use of energy. These events were felt in the air transport industry as well as other forms of transportation. As a result of these experiences, the government, with the support of the aviation industry, initiated programs aimed at both the supply (sources) and demand (consumption) aspects of the problem. The supply problem is being investigated by looking at increasing fuel availability from such sources as coal and oil shale. Efforts are currently underway to develop engine combustor and fuel systems that will accept fuels with broader specifications.

An approach to the demand aspect of the problem is to evolve new technology for commercial aircraft propulsion systems which will permit development of a more energy efficient turbofan, or the use of a different approach such as a turboprop. Although studies have indicated large reductions in fuel consumption usage are possible with advanced turbofan or turboprop engines (e.g., 15 to 40 percent), any significant fuel savings impact of these approaches is at least fifteen years away. In the near term, the only practical fuel savings approach is to improve the fuel efficiency of current engines. Examination of this approach has indicated that a five percent fuel reduction goal, starting in the 1980-82 time period, is feasible for current commercial engines. Inasmuch as commercial aircraft in the free world are using fuel at a rate in excess of 80 billion liters of fuel per year, even five percent represents significant fuel savings.

Accordingly, NASA is sponsoring the Aircraft Energy Efficient (ACEE) Program (based on a Congressional request), which is directed at reduced fuel consumption of commercial air transports. The Engine Component Improvement (ECI) Program is the element of the ACEE Program directed at reducing fuel consumption of current commercial aircraft engines. The Engine Component Improvement (ECI) Program consists of two parts: Engine Diagnostics and Performance Improvement. The Engine Diagnostics effort is to provide information to identify the sources and causes of engine deterioration. The Performance Improvement effort is directed at developing engine components having performance improvement and retention characteristics which can be incorporated into new production and existing engines.

The Pratt & Whitney Aircraft Performance Improvement effort was initiated with a feasibility analysis, which identified many potential engine performance improvement concepts. These concepts were then assessed for technical and economic merit. This assessment included a determination of airline acceptability (measured by the amount of time the concept would require to pay for itself, or "payback period"), the probability of introducing the concepts into production by the 1980 to 1982 time period, and their retrofit potential. Since a major portion of the present commercial aircraft fleet is powered by

the JT8D and JT9D engines, performance improvements were investigated for both engines. The study was conducted in cooperation with Boeing and Douglas aircraft companies, and American, United and Trans World Airlines, and is reported in Reference 1.

The concept of coating turbine vane platforms with ceramic to reduce the rate of heat transfer into the metal was selected for development and demonstration based on the Feasibility Analysis results. These results showed excellent airline acceptability for the concept applied to new and existing JT9D engines. The fuel saving potential was estimated at 980,000,000 liters (259,000,000 gallons) in these engines. Furthermore, it was projected that development of the concept for vane platforms might stimulate more ambitious programs to apply thermal barrier coatings to turbine vane and blade airfoils, with even more impressive fuel saving potential.

The vane platform development program consisted of an initial coating process refinement effort and initial cooling system design effort, culminating in a 1000 cycle engine endurance test. The results of this work were used to direct a second process refinement effort and a cooling system redesign effort, culminating in a final 1500 cycle engine endurance test.

The process refinement efforts explored three different coating chemistries, several variations in coating application techniques, pre-stressing the coatings, remelting of the ceramic surface, and coating thickness variations to improve the durability of the coatings. This effort is described in Section 5.1.

An impingement cooling system was evolved for the coated vane platforms to substantially reduce the cooling air requirements relative to the bill-of-material film cooling system. The reduction in cooling airflow results in reduced engine fuel consumption by improving the efficiency of the engine cycle and the turbine. The design evolution of the impingement cooling system is described in Section 5.2.

The final impingement cooled vane configuration and the process used to apply the three coating chemistries to these vanes are described in Section 3. The results of the final engine endurance test with these vanes are presented in Section 4.

3.0 FINAL VANE CONFIGURATION

Thermal barrier coated turbine vanes were prepared for the final engine endurance test by modifying bill-of-material semi-finished vane castings. Modifications included stripping the bill-of-material coating from the platforms, welding on impingement plates and cover plates, and plasma spraying a metallic layer and a thermal barrier layer on the platforms. The designs, materials and processes used in making these modifications are described below.

3.1 COATINGS

The bill-of-material oxidation coating was stripped from the platforms of the semi-finished vane castings by a chemical etching process. This step would not be necessary with production parts, since the platforms would be left uncoated. The impingement cooling plates and cover plates (described in Section 3.2) were welded to the vane casting before proceeding with the coating process.

A layer of metallic NiCoCrAlY bond coat, 0.008 to 0.013 cm (0.003 to 0.005 inch) thick, was applied to the vane platforms to provide oxidation protection for the vane metal.

The platforms of each vane were coated in ambient atmosphere with a nominal 0.025 cm (0.010 inch) thick layer of one of the three ceramic chemistries to be evaluated.

The ceramic coatings, as well as the metallic bond coating, were applied with a hand-held plasma spray gun. The vane platform metal temperature was maintained at 149°C (300°F) during the ceramic coating process by means of temperature regulated air flowing through the vane impingement cooling system.

The three ceramic chemistries evaluated by the program are:

- 21% magnesia stabilized zirconia (21% MSZ)
- 6% yttria stabilized zirconia (6% YSZ)
- 20% yttria stabilized zirconia (20% YSZ)

Each ceramic chemistry provides a different approach to thermal strain tolerance. Rig tests indicated that each of these ceramic chemistries respond differently to variations in maximum cyclic temperature, aging and coating thickness (see Section 5.1); consequently, all three were evaluated in the final engine endurance test.

3.2 COOLING SYSTEM

The prototype vane design substitutes an impingement cooling system for the bill-of-material film cooling system on the vane platforms while retaining the bill-of-material impingement/film cooling system for the vane airfoil, resulting in the general arrangement shown on Figure 1. The prototype vanes are fabricated from bill-of-material vane castings that had been finish machined in all areas except for drilling the platform film cooling holes. Sheet metal platform impingement plates and cover plates are welded to the castings. Weld material is also used to build up a parapet around the airfoil impingement

tube hole in the casting to isolate the platform cooling air from the airfoil cooling air. Holes are drilled from the downstream edge of each platform into the impingement cavity. The platform cooling air flows out through these holes, convectively cooling this area of the platforms.

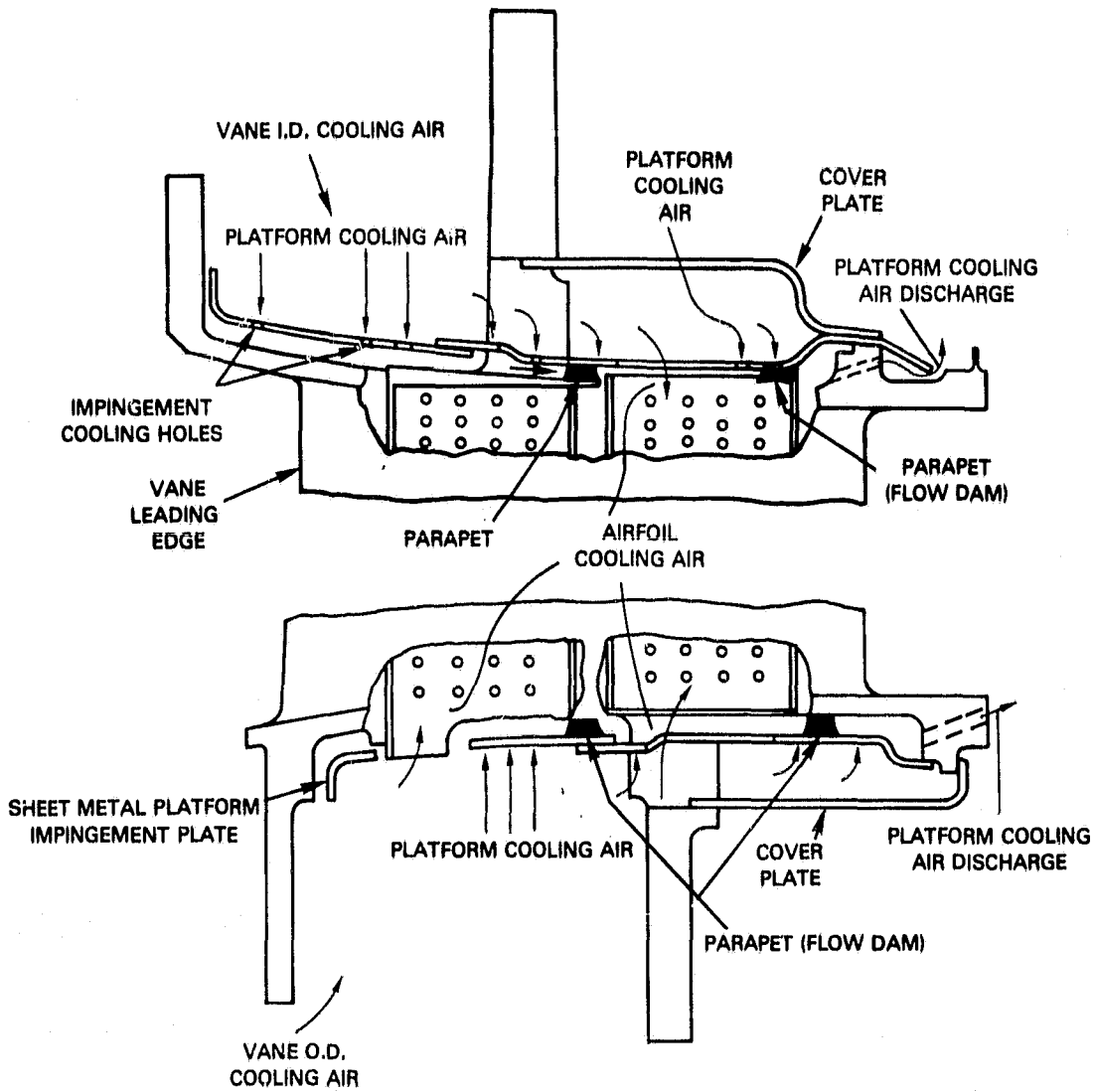

Figure 1 Cooling System Design. Impingement cooling is substituted for film cooling for the vane platforms.

The platform cooling system design point is based on an average gas temperature and a cooling air temperature corresponding approximately to the maximum operating conditions allowed in a deteriorated JT9D-59/70/7Q engine in service. The platform impingement and convective cooling holes were located and sized to maintain a uniform metal temperature with a heat load distribution shown on Figure 2. The impingement hole patterns shown in Figure 3 are designed to accommodate the varying heat loads on the platforms at maximum operating conditions. The impingement plate distance to hole diameter ratio is nominally 3.

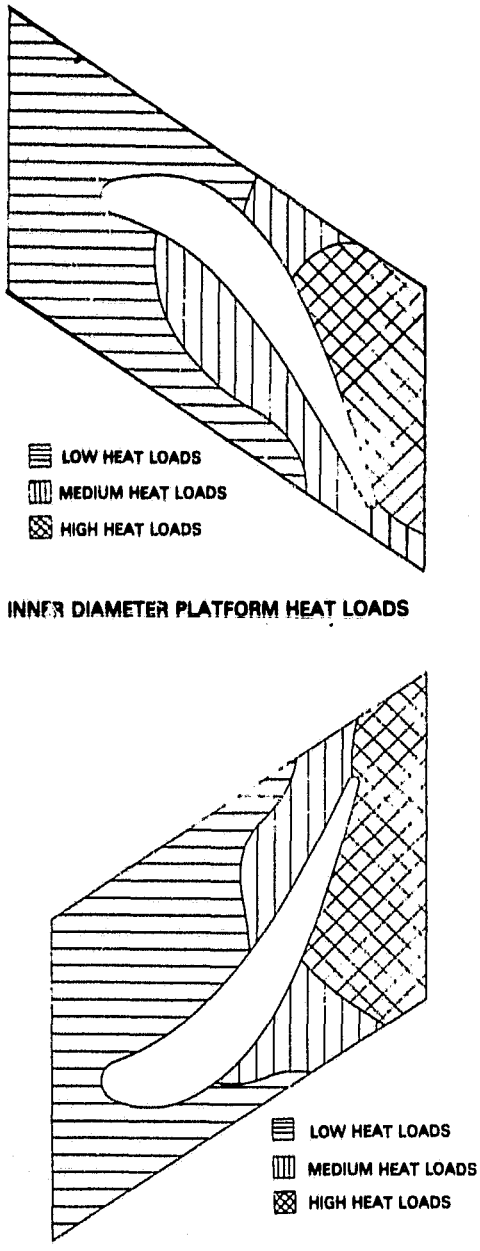

Figure 2 Inner and Outer Diameter Platform Heat Loads. The cooling system was designed to accommodate the heat loads shown.

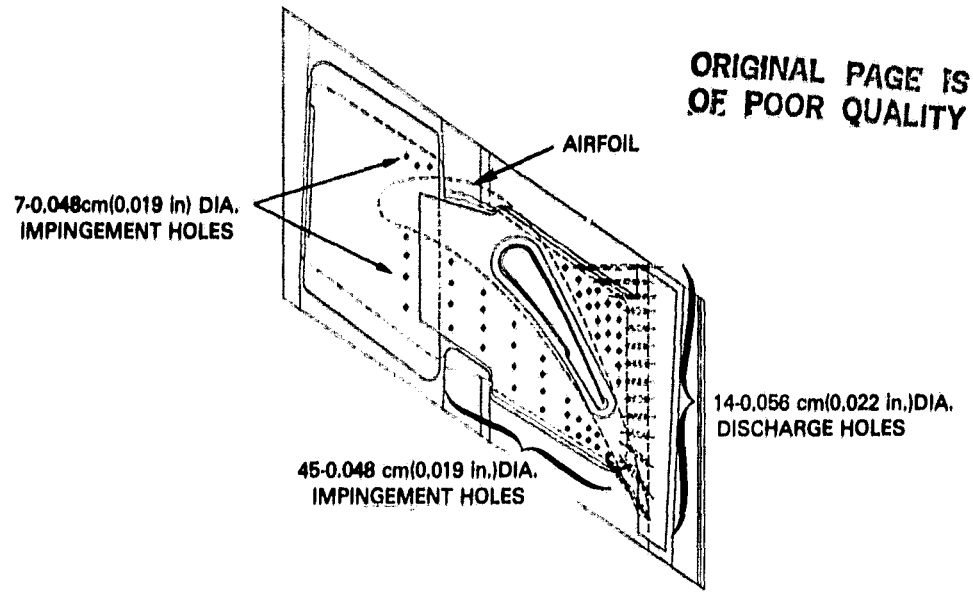

INNER DIAMETER VANE PLATFORM

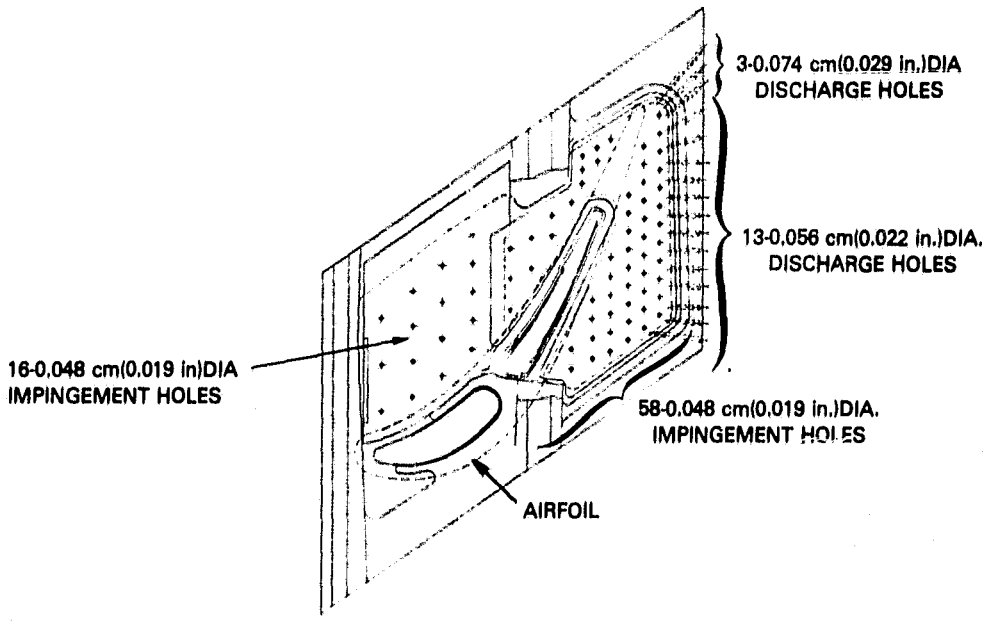

OUTER DIAMETER VANE PLATFORM

Figure 3 Platform Cooling Hole Patterns Inner and Outer Diameter Final Engine Test. Impingement hole pattern meets the cooling requirement at maximum operating conditions.

The prototype platform cooling system uses 44 percent less cooling airflow than the bill-of-material system, improving the engine performance. The cooling air that it does use reenters the gaspath downstream of the vane; this relocation and reduction of the cooling flow reduces momentum losses and further improves turbine efficiency. The net effect on engine fuel consumption was estimated to be 0.17% improvement at cruise conditions.

4.0 FINAL ENGINE TEST

Twenty-four vanes fabricated to the final design described in Section 3 were initially subjected to a short 32-hour hot time variable thrust level performance calibration test in a JT9D-7Q engine. All three thermal barrier coating chemistries were represented, with eight vanes carrying each coating. In addition, two vanes that were fabricated to the initial design and had completed two previous 1000 cycle engine tests, and two Bill-of-Material film cooled vanes were included in the final test for comparison. Following the performance test, one 20% YSZ vane and one 21% MSZ vane were removed because of airfoil distress not related to the platform design. The remaining vanes were then subjected to a 1500 cycle endurance test in the JT9D-7Q engine. The details of the engine test procedures are presented in Section 2.0 of Appendix A.

The coated vane platforms were visually and metallographically inspected after the endurance test and the results are presented in Section 4.1. Vane platform metal temperatures and cooling air pressures and temperatures were measured during the engine performance calibrations. These data were analyzed to determine the operating characteristics of the platform cooling system, and the results are presented in Section 4.2.

4.1 COATINGS

Visual inspection after the 32-hour performance calibration test showed the 6% YSZ and 21% MSZ coatings to be in excellent condition. Spalling of the 20% YSZ coating was noted on six outer diameter platforms and one inner diameter platform.

Post-endurance test visual and metallographic inspection of the vanes showed the 6% YSZ coating to be in very good condition, including the vane which had been exposed to 2000 prior endurance cycles. The 21% MSZ and the 20% YSZ coatings generally were in poor condition, an exception being the 21% MSZ coated vane, which saw 2000 prior cycles, that was in good condition. Post-endurance test conditions of each coating chemistry (Figure 4) varied somewhat depending on the vane's circumferential and radial (inner diameter vs. outer diameter) locations (see Figure 5) in the engine. This variability is partially attributable to the environment resulting from the temperature pattern produced by the combustor. Relative environment conditions estimated from vane airfoil distress are shown on Figures 4 and 5.

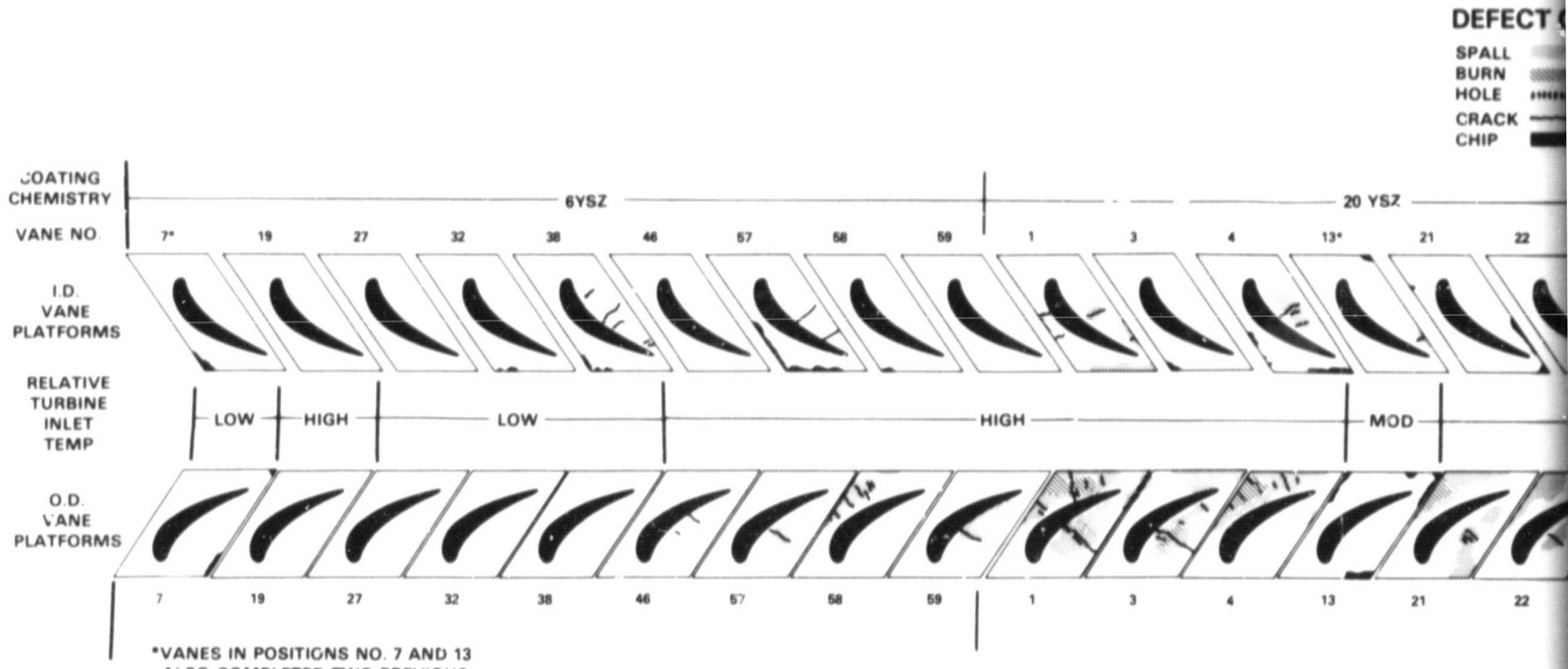

*VANES IN POSITIONS NO. 7 AND 13 ALSO COMPLETED TWO PREVIOUS 1000-CYCLE ENGINE TESTS.

FOLDOUT FRAME

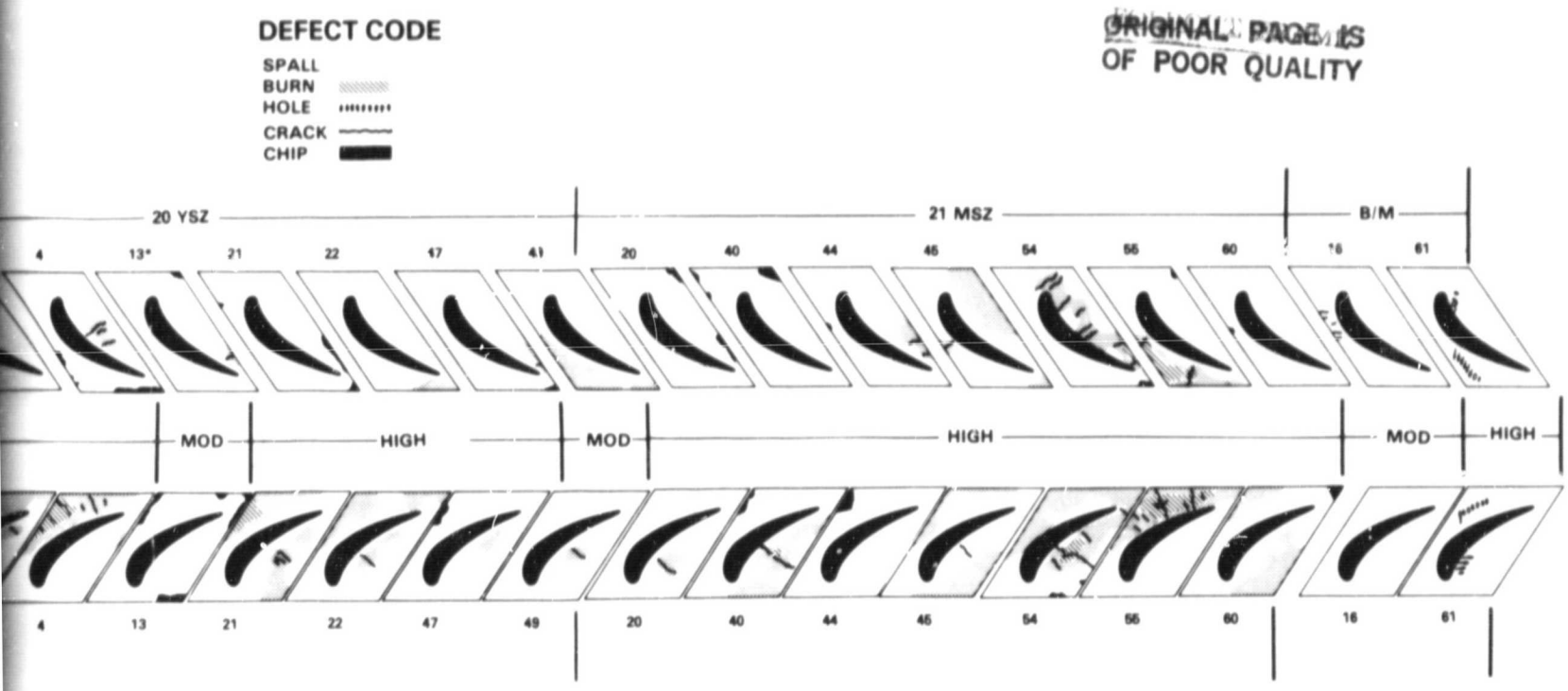

Figure 4 Post Endurance-Test Condition. Coating condition varied depending on circumferential and radial position.

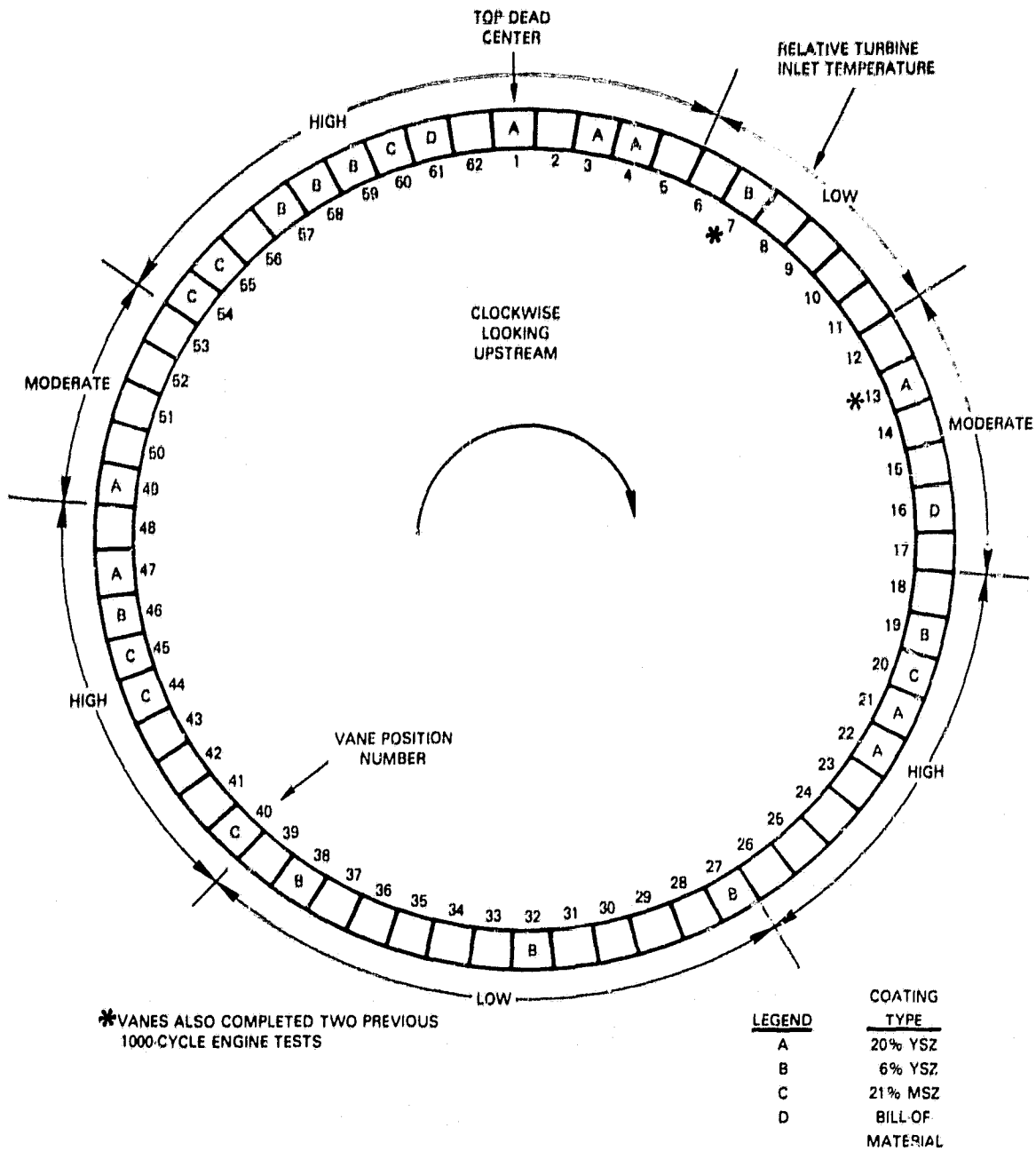

Figure 5 Circumferential Location of the Twenty-Six Test Vanes in the Final Engine Test

The distribution of spalling after the 1500 cycle endurance test for each coating system is summarized as follows:

System	Code Name	Number of Vanes	Number of Vanes Exhibiting Significant Spalling		Number of Vanes in Highest Temperature Environment
			O.D.	I.D.	
6% Y_2O_3-ZrO_2	6% YSZ	9	1	0	5
20% Y_2O_3-ZrO_2	20% YSZ	8	5	2	7
21% MgO-ZrO_2	21% MSZ	7	5	3	5

The favorable results of the 6% YSZ coating system is typified in the photograph shown in Figure 6. Representative spalled areas, which were numerous for the 20% YSZ and 21% MSZ systems, are shown in Figure 7.

Examination of the vanes revealed that they possessed considerable variation in coating thicknesses, as expected for manually sprayed components; typical examples are shown in Figures 8 through 10. (Pre-test thickness measurements were not obtained because of the lack of a suitable non-destructive measurement technique.) Microstructures observed on engine tested vanes are shown in Figures 11 through 13. The structures of the 21% MSZ and 20% YSZ coatings (Figures 11 and 12 respectively) show combinations of microcracking and porosity which were typical of those observed in the laboratory tested specimens. The structure of the 6% YSZ coatings on the turbine vanes also contained a combination of porosity and microcracking (Figure 13). As discussed in more detail in Section 5.1.5.2, this structure is different from that seen on laboratory test specimens using similar plasma process conditions. The laboratory specimens had a more dense ceramic structure with high levels of segmentation cracking. This difference is thought to be due to the different geometries between specimens and components; however the specific causes are not understood.

The excellent durability exhibited by the 6% YSZ coating relative to the other ceramic compositions verified the observations of the first engine test. In both tests, the 6% YSZ vane coatings contained porosity and microcracking rather than segmentation cracking as the strain tolerant microstructure. Since similar microstructures were present in the less durable 20% YSZ coatings, it is not readily apparent why there was such a substantial difference in ceramic spalling resistance between the two systems. No significant difference had been observed in the laboratory burner rig tests of these two YSZ compositions (Sections 5.1.4.1 and 5.1.5.2). In contrast, the higher temperature laboratory tests (Section 5.1.5.2) did reveal a debit in the durability of the 21% MSZ relative to the YSZ compositions; this was consistent with the results of both engine tests.

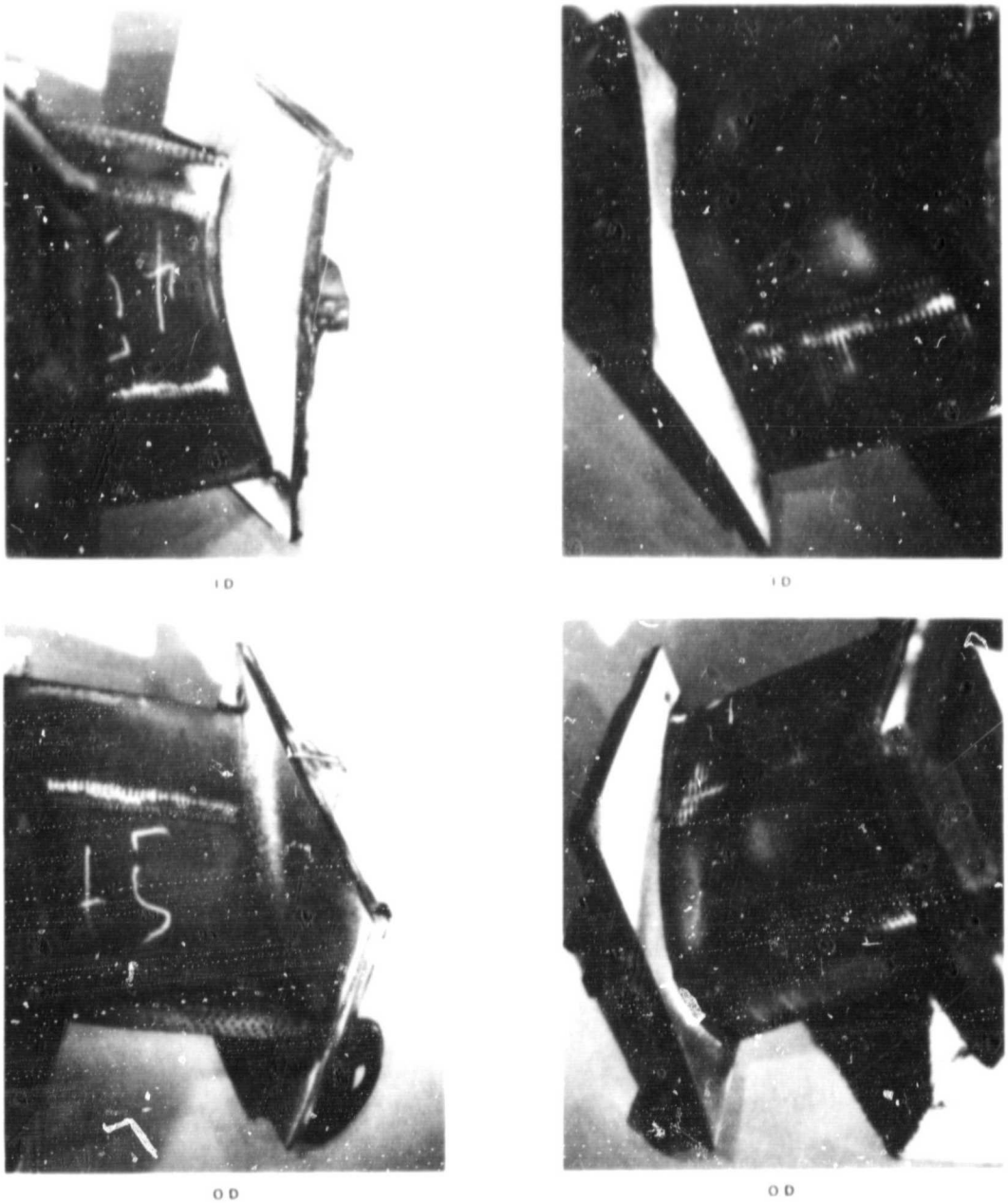

Figure 6 Post-test Condition of 6% YSZ Coating System. The favorable results shown in this photograph are typical of the 6% YSZ system. Vane position No. 46. (Numbers shown on vanes do not refer to wheel chart location on Figure 5.)

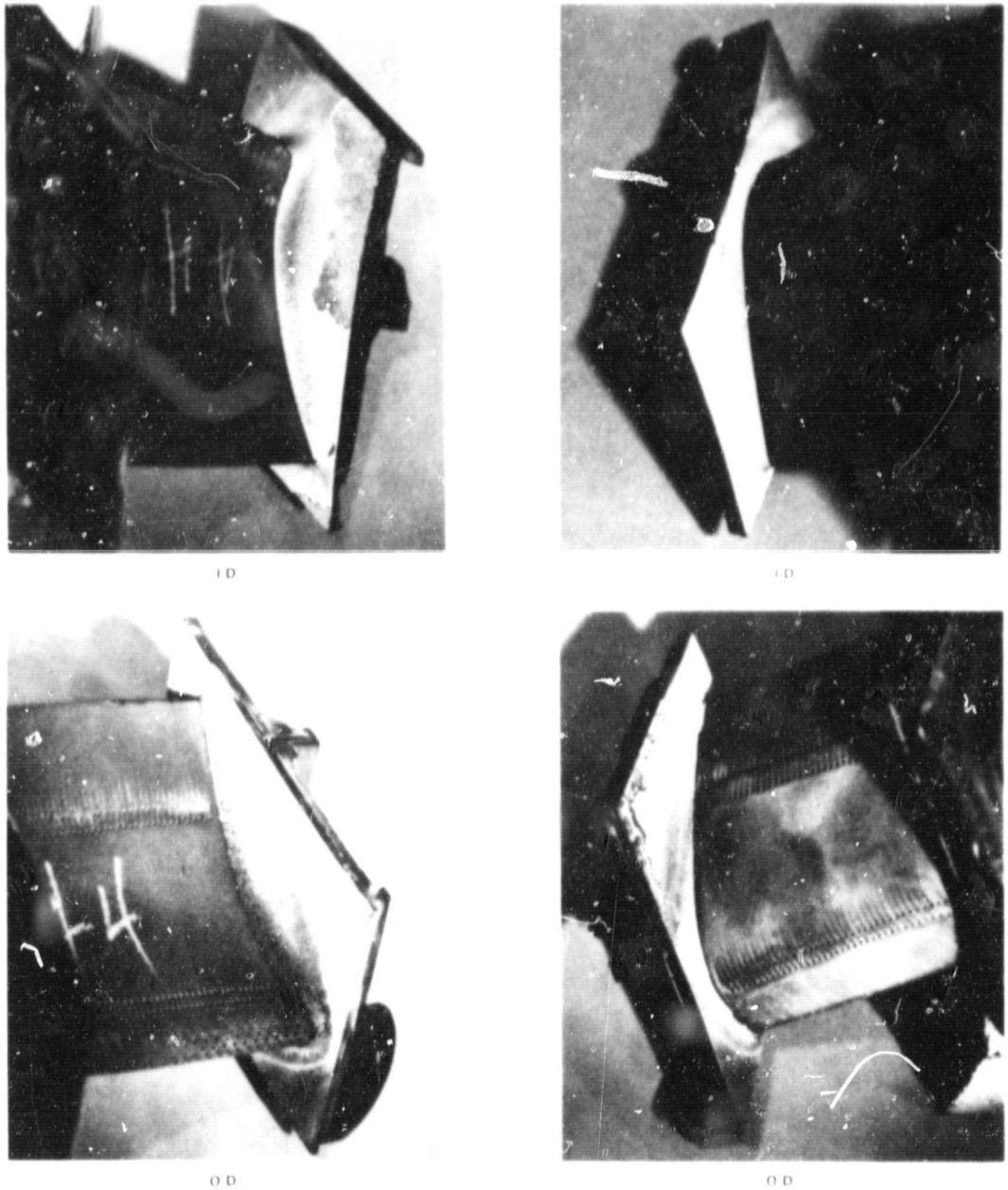

Figure 7 Post-test Condition of the 20% YSZ and 21% MSZ Coating Systems. The spallings shown in this photograph are representative of the condition of the 20% YSZ and 21% MSZ systems. Vane position No. 45. (Numbers shown on vanes do not refer to wheel chart location on Figure 5.)

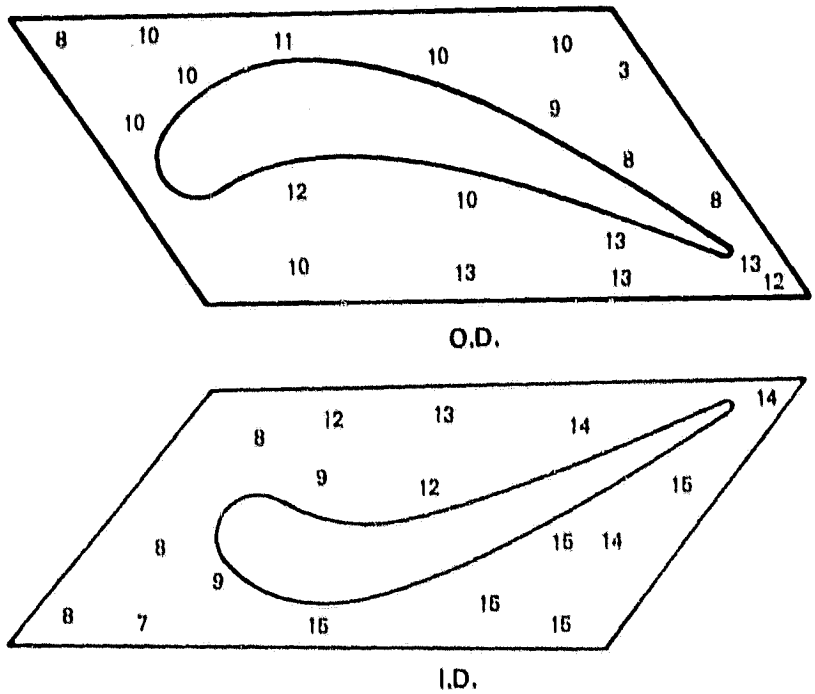

Figure 8 Schematic Representation of a Typical Ceramic Coating Thickness Distribution on Vane Platform Coated with 21% MSZ. Thicknesses were measured after engine testing and are shown in inches x 10^{-3}. (Vane No. 44)

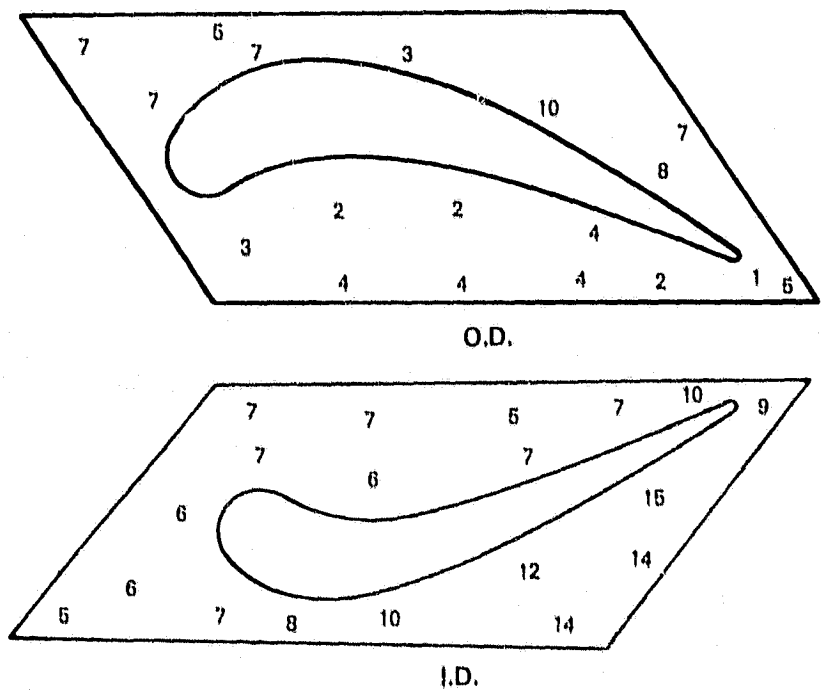

Figure 9 Schematic Representation of a Typical Ceramic Coating Thickness Distribution on Vane Platform Coated with 20% YSZ. Thicknesses were measured after engine testing and are shown in inches x 10^{-3}. (Vane No. 21)

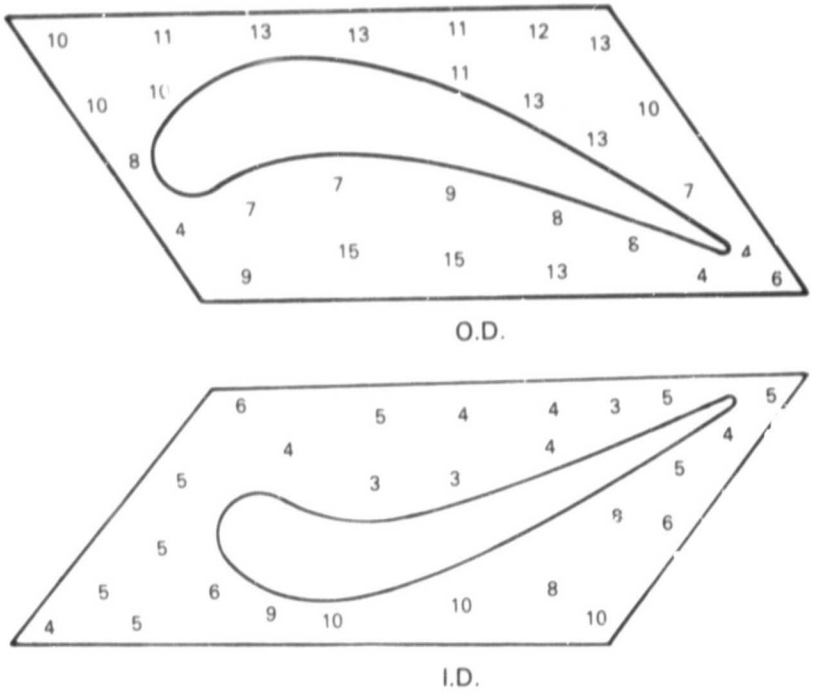

Figure 10 Schematic Representation of a Typical Ceramic Coating Thickness Distribution on Vane Platform Coated with 6% YSZ. Thicknesses were measured after engine testing and are shown in inches x 10^{-3}. (Vane No. 46)

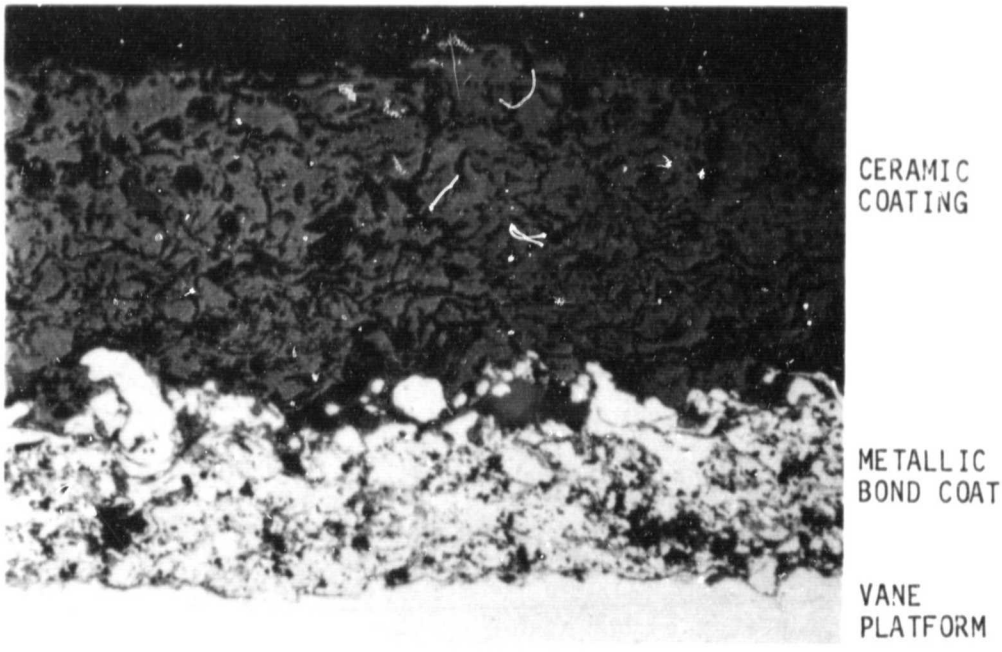

Figure 11 Representative Coating Microstructure Found in 21% MSZ Thermal Barrier Coated Vane No. 44. A high degree of random microcracking is present in the ceramic structure.

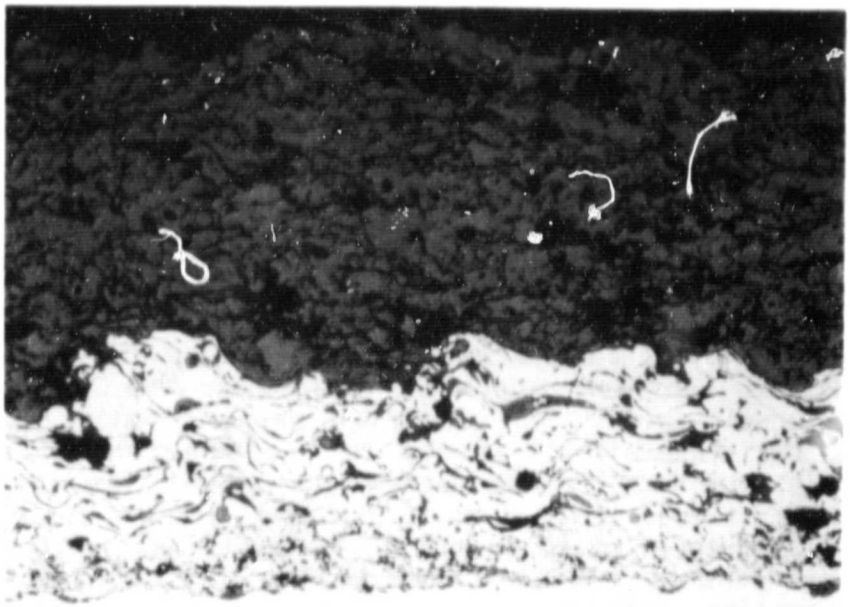

200X

Figure 12 Representative Coating Microstructure Found in 20% YSZ Thermal Barrier Coated Vane No. 47. The microstructure contains a random distribution of porosity and microcracking.

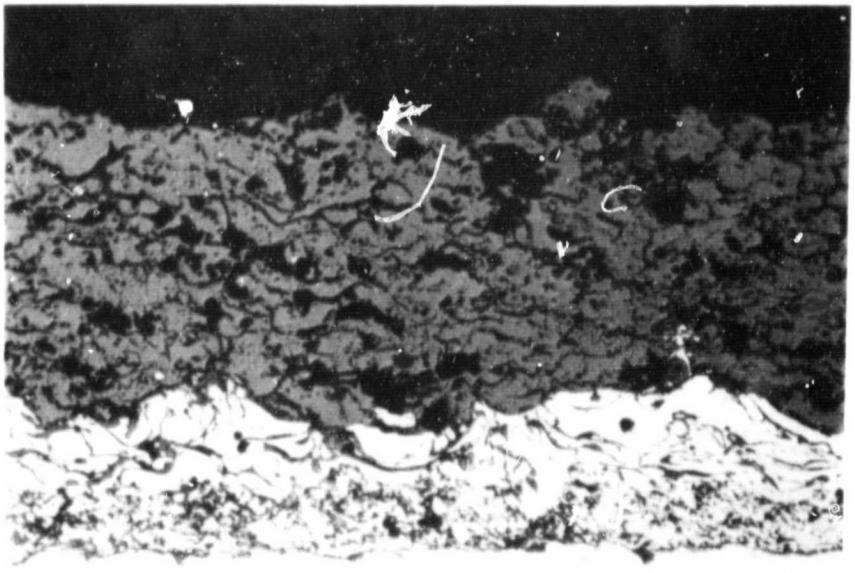

200X

Figure 13 Representative Coating Microstructure Found in 6% YSZ Thermal Barrier Coated Vane No. 27. The porous microcracked microstructure observed in the vane coatings differed from the segmented structure seen in 6% YSZ coatings on laboratory specimens.

4.2 COOLING SYSTEM

Evaluation of the vane instrumentation data taken during the performance calibration engine test shows that the prototype cooling system functioned as intended. Platform cooling air pressures were monitored in the performance calibration test via static pressure sensors located in the leading edge of the plenum of two selected OD platforms (see Appendix, Table A-V). These additional measured data were in agreement with design intent and helped confirm that the cooling flows to the vane and vane platform were as planned.

The cooling system, in combination with a nominal 0.025 cm (0.010 inch) thick ceramic thermal barrier coating, maintained the vane platform metal temperatures well within the material design limits specified for the bill-of-material vane with 44 percent less cooling airflow. The range of vane metal/ceramic interface temperatures measured with the engine operating at maximum takeoff thrust (244,651 N (55,000 lbf)) and the analytically predicted interface temperatures based on the engine platform gas temperature for this condition are shown in terms of the "cooling effectiveness factor" on Figure 14. The cooling effectiveness factor is defined as $(T_g-T_p)/(T_g-T_c)$, where T_g is the gas temperature over the platform at the platform metal temperature location, T_p is the vane platform temperature, and T_c is the vane cooling air temperature. The temperature range in the platform aft section appears reasonable and the agreement between measured and predicted values is acceptable considering the variability of the burner gas temperature profile and the predicted metal temperature gradients near the platform corners. While the circumferential gas temperature profile of the particular burner used in this engine test is not precisely known, a typical profile based on measured data from engine tests using similar burners varied as much as 399°C (750°F) about the average gas temperature.

The calculated metal temperature gradient in the vicinity of each trailing edge thermocouple, shown on Figure 14, implies the possibility of an 8°C (15°F) temperature error for a location error of only 0.025 cm (0.010 inch). The poor agreement in the leading edge region is attributable to the relative uncertainties in modeling conductive and convective heat transfer near the airfoil platform interface and is not considered unusual. A collective summary of measured platform cooling effectiveness, coating compositions, and environmental conditions is shown in Figure 15.

Assessment of the observed post endurance test condition of the coated vane platforms and the information shown in Figures 14 and 15 indicates that the impingement/thermal barrier coated cooling system functioned successfully. In all cases, measured cooling effectiveness was near or better than predicted and, for the 6% YSZ composition, the post test coating condition in the area of measurement was excellent. Furthermore, of all the instrumented vane coated platforms, only the 20% YSZ cooled vane platform (vane 22) exhibited spalling. The nearly identical cooling system effectiveness measured for this vane platform as compared with a 6% YSZ vane platform (vane 59) which experienced a similar environment indicates that the poorer performance of the 20% YSZ vane platform was due to the coating composition rather than the cooling design. Also substantiating the integrity of the cooling design is the relatively good agreement between the level of measured cooling effectiveness between the bill-of-material design and the impingement/thermal barrier coated design. This agreement in measured values indicates that the thermal barrier coated design gave comparable performance at reduced cooling flows as was intended.

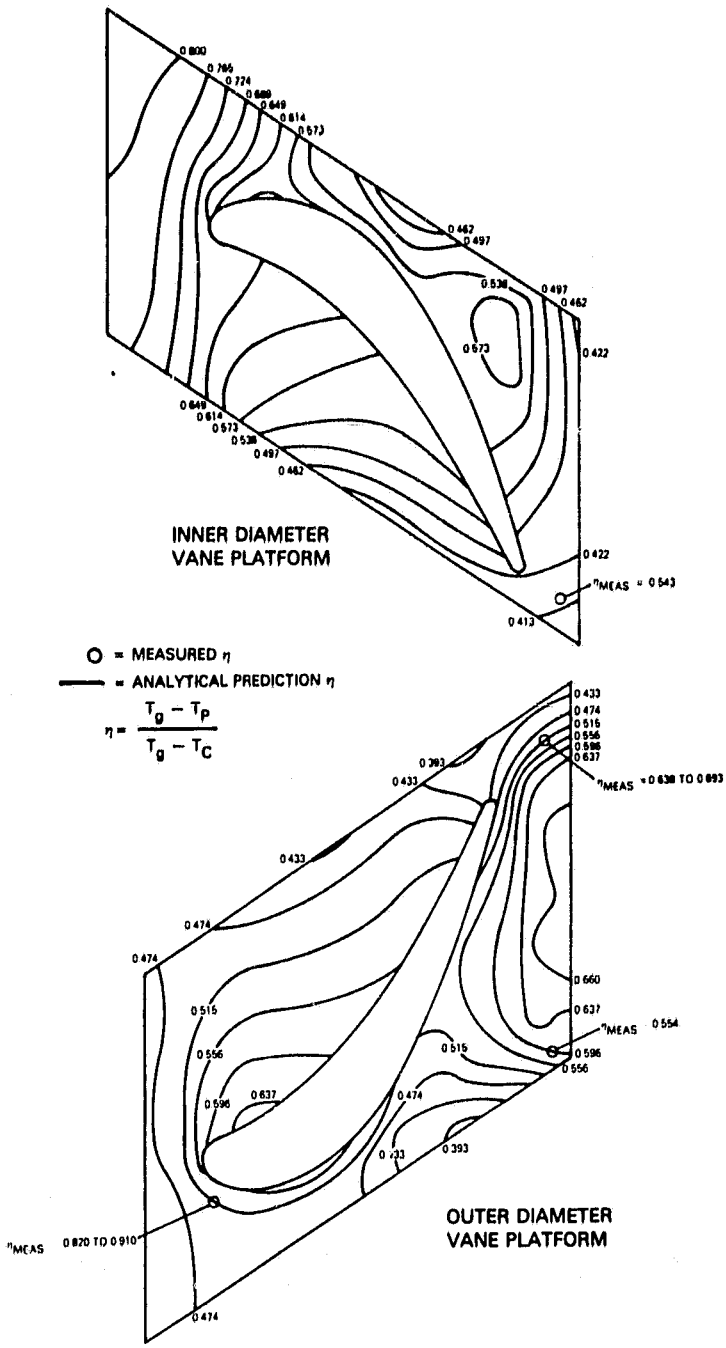

Figure 14 Cooling effectiveness ID and OD Platforms. Measured and predicted metal/ceramic interface temperatures are shown in terms of cooling effectiveness factor.

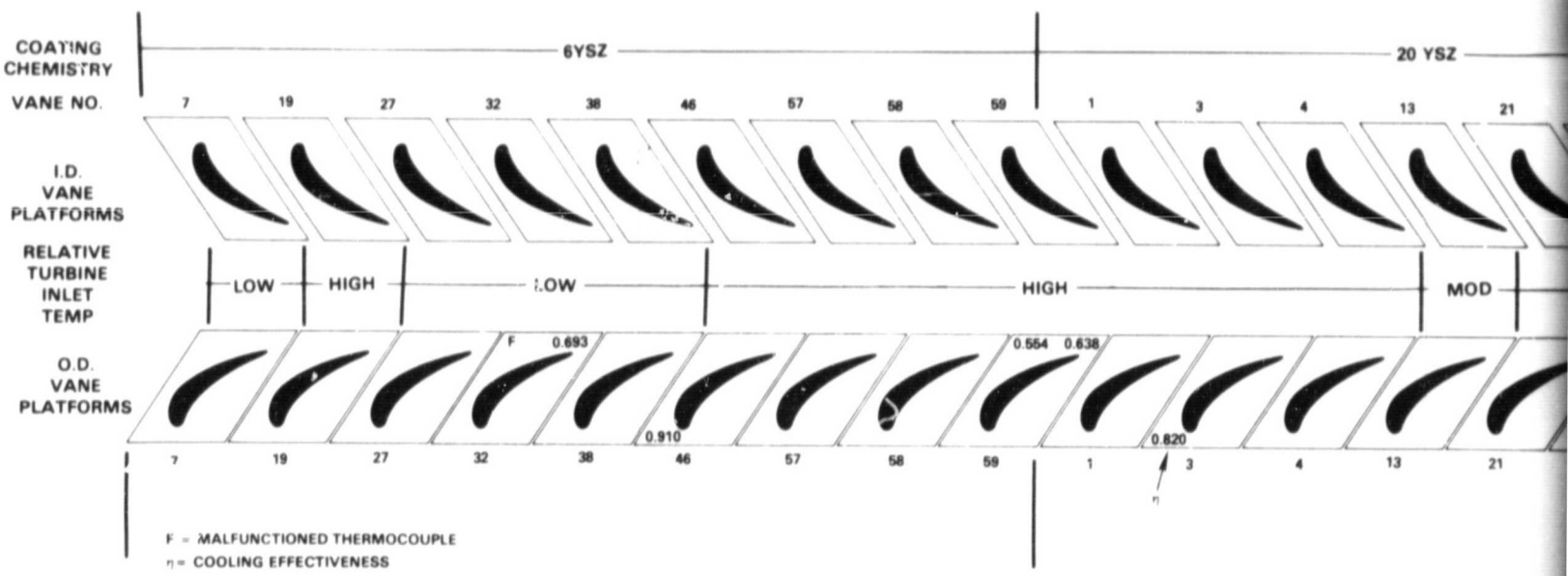

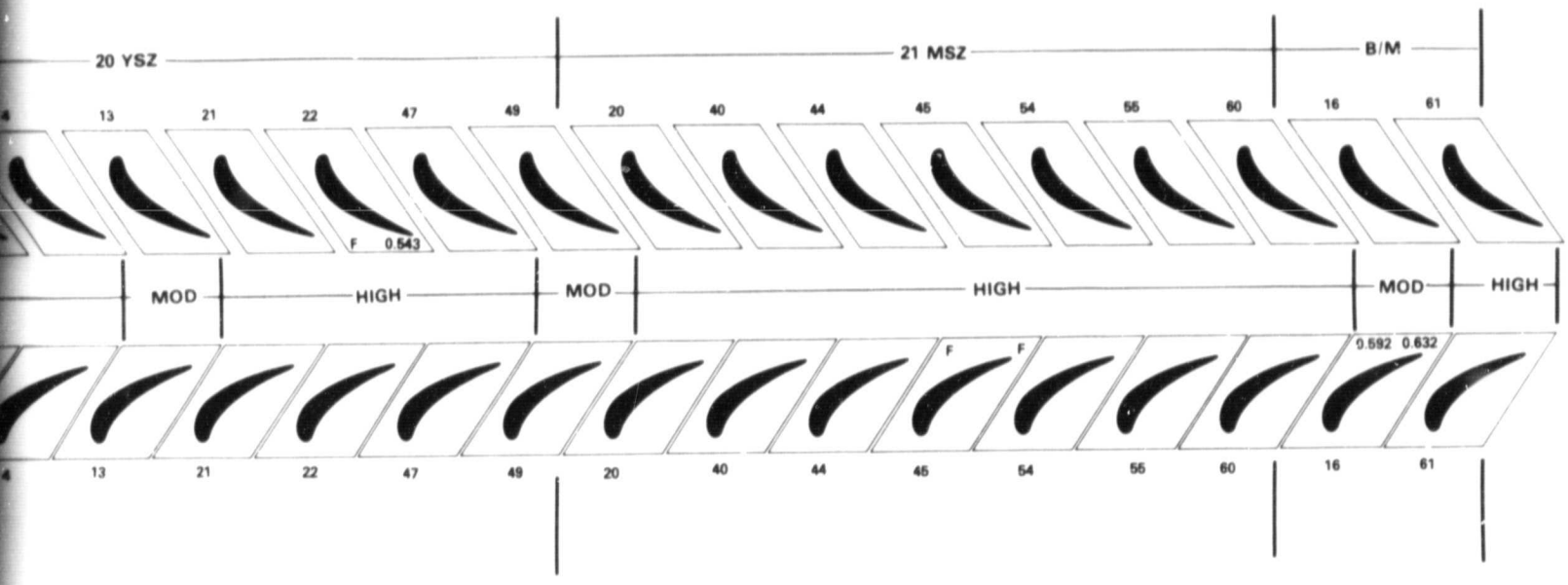

Figure 15 Cooling System Performance. Evaluation of measured cooling effectiveness with circumferential location, coating composition, and environment.

5.0 CONCEPT DEVELOPMENT

5.1 COATING SYSTEM DEVELOPMENT AND OPTIMIZATION

5.1.1 Introduction

The objective of this phase of the program was to increase the durability of thermal barrier coatings by optimization of ceramic composition and process methods. An initial series of experiments was conducted to select candidate compositions, to identify preferred coating application methods and process parameters, and to provide laboratory demonstration of coating durability enhancements (Sections 5.1.3 and 5.1.4). This initial study led to selection of three candidate coating/process systems for evaluation in the first engine test. Based on results of this engine evaluation, a second series of composition/process optimization experiments was conducted to further refine coating process methods and to provide additional laboratory evaluation of coating performance (Section 5.1.5). Results of these studies led to selection of three coating/ process modifications for evaluation and substantiation in the second engine test, the results of which are described in Section 4.0.

5.1.2 Background

The use of ceramic thermal barrier coatings on cooled turbine components offers the potential for substantial improvements in operating economy through reduction in fuel usage and maintenance requirements. Realization of these benefits is limited only by progress in achieving satisfactory coating durability, i.e., the ability of the ceramic to remain attached to the component and to provide continued thermal insulation through thousands of hours in the hostile engine environment.

The most significant problem in achieving useful lifetimes in thermal barrier coatings is spalling of the ceramic. This spalling is primarily caused by the strains which occur in the ceramic layer because of mismatch in coefficients of thermal expansion between the substrate and ceramic. In order to minimize the thermal expansion mismatch strain directly, it has been customary to specify ceramic surface materials which have relatively high coefficients of thermal expansion. In addition, it is desirable that the ceramic exhibit low thermal conductivity so that coatings of minimum thickness can be used without compromising the thermal barrier effect.

Zirconia base ceramic materials have an extremely attractive combination of low thermal conductivity and relatively high coefficient of expansion. For these reasons zirconia base ceramics have almost exclusively been used in thermal barrier coating systems. Zirconia is, however, subject to an allotropic phase transformation from the high temperature cubic to the low temperature monoclinic form. This causes large volume changes and high internal stresses which progressively destroy the structural integrity of the ceramic. In order to limit these phase transformations, other ceramics (magnesia, yttria, ceria, calcia, etc.) are generally added in an attempt to stabilize the high temperature zirconia phase across the range of temperature exposure.

Zirconia-based plasma sprayed thermal barrier coatings have been successfully used for over 20 years in combustor and afterburner gas-turbine applications to improve component durability. Unfortunately, the benefits of ceramic coatings have not been available for turbine blade and vane applications because of the more stringent environment of these components and the limited durability of state-of-the-art ceramic coatings in these applications. In early testing, for example, 0.25 mm (10 mils) thick plasma sprayed yttria-stabilized zirconia (YSZ) coatings applied to JT9D first stage turbine vane platforms began to fail by spalling in less than three hundred cycles of experimental engine endurance running.

In the mid 1970's, however, a series of successful engine tests of ceramic coated turbine blades at NASA's Lewis Research Center demonstrated that thermal barrier coating of turbine airfoils was feasible (Ref. 2). This result led to an expanded effort at industrial and Government laboratories to define the actual capabilities of then state-of-the-art thermal barriers, their deficiencies, and methods for improvement. Additional engine tests of coated turbine blades showed that still greater ceramic spall resistance was required (Ref. 3,4), and laboratory experiments uncovered susceptibilities to thermal barrier degradation from oxidation and hot corrosion effects (Ref. 3,5,6,7). Nevertheless, some of these studies indicated that considerable improvements in ceramic coating durability could be achieved (Ref. 4,8). In particular, it was found that a considerable increase in zirconia spall resistance was achieved when certain strain tolerant microstructures were built into the deposited ceramic layer through process variations (Ref. 4,9,13,14). One approach to increase coating durability is to increase the in-plane tensile compliance of the coating (i.e., the ability of the coating to absorb strain parallel to the plane of the coating), thus reducing the magnitude of the crack tip stress field developed by thermally induced tensile strains. In-plane coating tensile compliance is enhanced through control of ceramic microstructure. As shown in Figure 16a, the ideal ceramic coating microstructure consists of aligned ceramic columns, each of which is strongly bonded to the metallic substrate but is independent of adjacent columns. The in-plane compliance of this coating is essentially infinite, so that crack driving in-plane shear stresses developed by applied in-plane thermal displacements are essentially zero. Other microstructural features which enhance in-plane ceramic coating compliance include the more coarsely segmented structure shown in Figure 16b, preferentially or randomly oriented microcracking (Figure 16c), and porosity (Figure 16d).

While control of microstructure can substantially enhance in-plane tensile compliance, none of the microstructural features discussed above provides a significant increase of in-plane compressive compliance. To avoid development of high in-plane compressive stresses and stress gradients, which not only drive in-plane crack propagation but can cause triaxial tensile strains normal to the plane of the coating, a method was demonstrated in this program to control the residual stress state of the coating so that large or detrimental compressive ceramic strains are not developed during thermal cycling. This method, which involves the control of metal substrate temperature during coating application, is described in the following section together with processing experiments which were performed to optimize coating composition and microstructure.

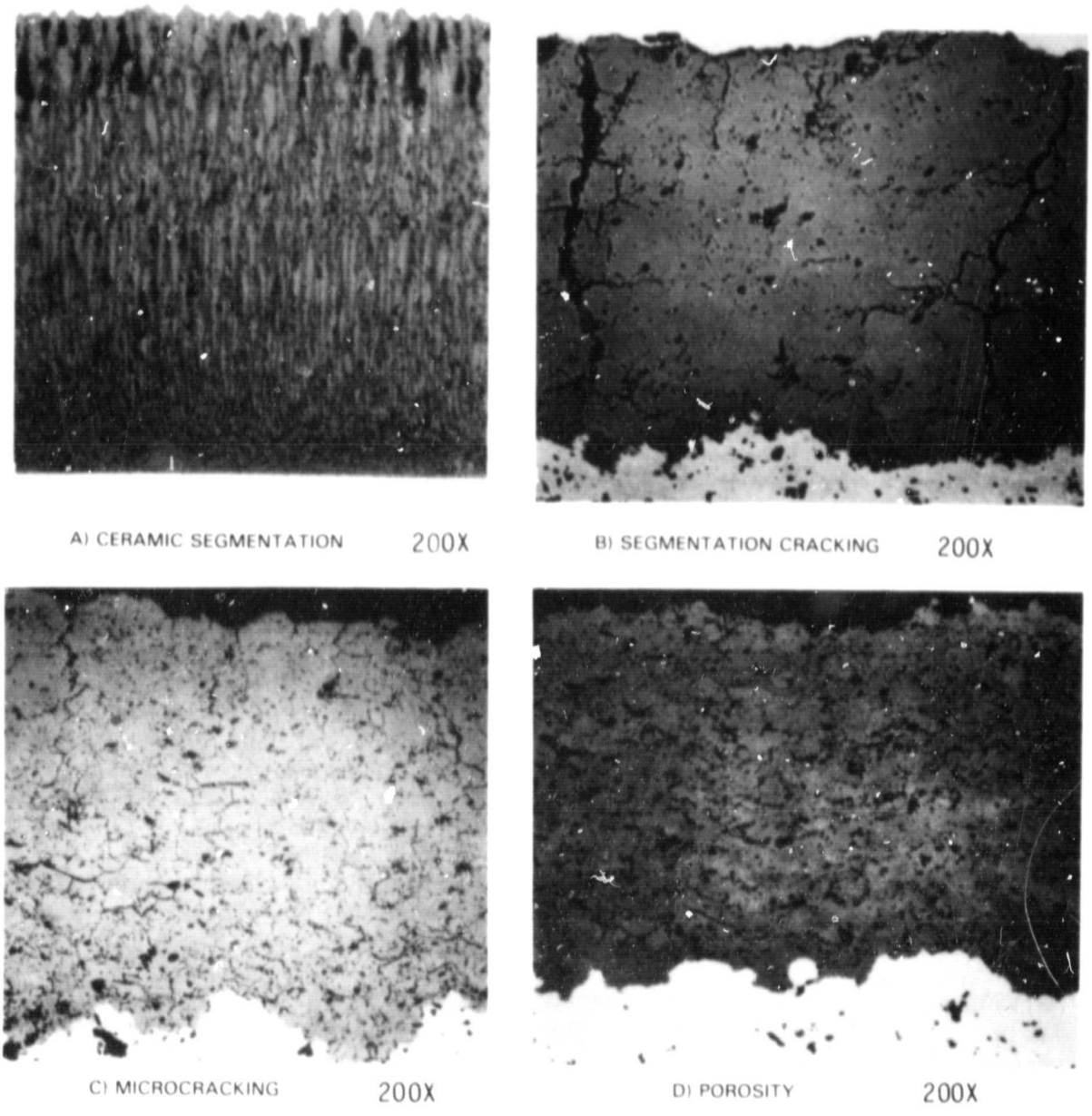

Figure 16 Idealized Ceramic Structures Illustrating Various Microstructural Features which can be Incorporated to Increase Ceramic Strain Tolerance. All structures shown are of 6% YSZ ceramic composition.

5.1.3 Initial Process Refinement

Three ceramic structural concepts for plasma sprayed coatings were selected for further evaluation as a part of the ECI-PI thermal barrier coated vane platform development program. The selected concepts included increased porosity, controlled microcracking, and segmented (columns perpendicular to the plane of the coating) ceramic structures in addition to other systems designed to explore the performance of various chemistries and processing approaches. A unique coating process previously developed at Pratt & Whitney Aircraft was also included in the program for evaluation. This process involves electron beam physical vapor deposition (EB-PVD) of the ceramic coating system and results in a fine segmented ceramic structure made up of small columns of ceramic with sufficient free space at the boundaries to accommodate thermal expansion mismatch strains. The concept involving plasma spray process temperature control to minimize harmful residual stresses also was selected for evaluation.

5.1.3.1 Plasma Spray Processing Parameter Study

The objective of this study was to determine the influence of plasma process parameters on the development of microstructural features such as those shown in Figure 16, which serve to increase the ability of the coating to absorb strain parallel to the plane of the coating. Plasma process parameters which were investigated included gun to specimen distance (varied from 2.5 to 19.1 cm (1 to 7.5 inches)) and powder feed rate (varied from 10 to 40 grams/minute). Two powder particle size ranges of the ceramic also were investigated. A total of 20 stainless steel rods, 10.2 cm (4 inches) long and 1.3 cm (0.5 inches) in diameter, were coated with the parameters varied as indicated in Table I. The substrate surface was prepared by using a coarse (60 grit) alumina grit blast. The metallic bond coating layer was NiCoCrAlY (Co-22, Cr-18, Al-13, Y-0.7, Ni-balance, in weight percent) applied to a thickness of 0.008 to 0.013 cm (0.003 to 0.005 inches). Two ceramic compositions were used, 20 w/o Y_2O_3 stabilized ZrO_2 (20% YSZ) and 21 w/o MgO stabilized ZrO_2 (21% MSZ), each having a nominal thickness of 0.025 cm (0.010 inches). All of the plasma spray coating systems evaluated in this study were applied by the Pratt & Whitney Aircraft Manufacturing Research and Development Group.

Metallographic evaluation of specimens coated using the parameters listed in Table I indicated that the inherent microstructures of the two ceramic chemistries were essentially unaffected by powder feed rate and gun distance, with the exception of those specimens sprayed from a 2.5 cm (1 inch) distance. Photomicrographs comparing 20% YSZ coatings prepared at feed rates of 10 and 30 grams per minute are shown in Figure 17 to illustrate the insensitivity of structure to feed rate. In the case of the 2.5 cm (1 inch) gun distance, both systems exhibited considerable densification through melting due to the extreme heat, resulting in cracking perpendicular as well as parallel to the plane of the coating (Figure 18). The MgO stabilized ZrO_2 system also exhibited considerable spalling when sprayed from a 2.5 cm (1 inch) distance. The microstructure shown in Figure 18 exhibits desirable segmentation perpendicular to the plane of the coating, such as that shown in Figure 16b.

However, the accompanying in-plane cracking considerably increases the tendency for ceramic spallation, as evidenced by behavior of the MgO stabilized ZrO_2 specimens sprayed form a 2.5 cm (1 inch) distance. This result indicates the very precise control of all parameters would be required during use of this approach to achieve the desired degree of perpendicular cracking while eliminating cracks parallel to the plane of the coating.

As noted in Table I, two particle size ranges of the 20% YSZ material were investigated, one of which had a range of -170 mesh to +10 microns. The other powder was considerably finer, with all particles in the -325 mesh range. Metallographic evaluation indicated that the coarser particle size powder produced a coating with a higher porosity level than the coating produced with the finer powder, which had an extremely dense structure (Figure 19). Increased porosity in coatings sprayed with coarse powder is probably related to a reduction in melting efficiency for large particles during transport in the plasma and consequent packing defects in the deposited ceramic*.

The inherent microstructures of the two ceramic chemistries used, 20% Y_2O_3 stabilized ZrO_2 and 21 w/o MgO stabilized ZrO_2, were found to be unaffected by the varying process parameters. The 20 w/o Y_2O_3 stabilized ZrO_2 system results in a single fully stabilized cubic phase. The 21 w/o MgO stabilized ZrO_2 has a partially stabilized cubic structure which may be cubic or tetragonal with a considerable fraction of monoclinic phase in addition to free MgO particles. Both monoclinic ZrO_2 and free MgO contribute to the high degree of microcracking present in the structure (Figure 20).

---

* Quantitative measurements of porosity level were not performed due to the tendency for high degrees of error with conventional measurement techniques. For example, water displacement techniques do not account for the presence of closed pores. With quantitative metallographic methods, the apparent porosity of a polished surface of a ceramic is extremely dependent upon the metallographic preparation techniques used; however, relative degrees of porosity can be determined on specimens prepared using consistent polishing techniques.

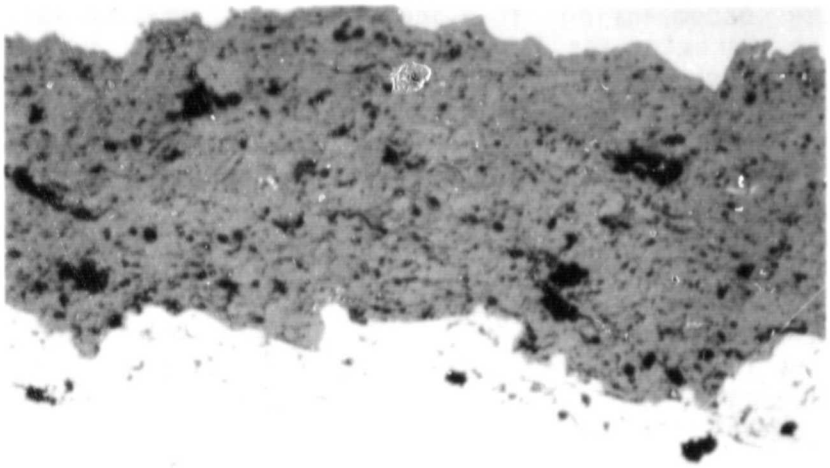

a) 10 GPM 200X

b) 30 GPM 200X

Figure 17 Microstructure of Coatings Produced with 10 gram/minute (top) and 30 gram/minute (bottom) Powder Feed Rate from Plasma Spray Process Parameter Study; 20 w/o Y_2O_3 Stabilized ZrO_2.

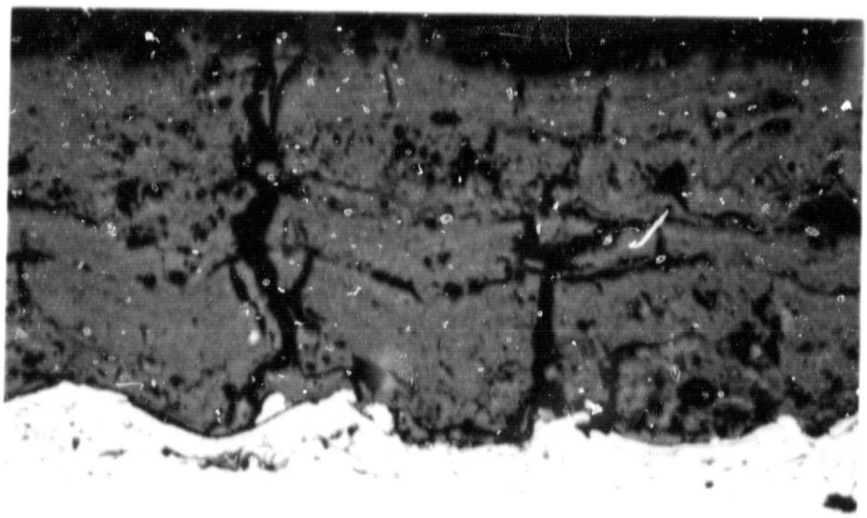

250X

Figure 18 Microstructure of 20 w/o Y_2O_3 Stabilized ZrO_2 Coating Produced Using a 2.5 cm (1 inch) Gun to Specimen Distance. Note resultant densification and segmentation cracking normal to the ceramic layer.

TABLE I

PLASMA SPRAY PROCESSING PARAMETERS

Arc Gas; Argon, Helium Mixture
Power Input; 50 Volts, 800 Amps

Ceramic Layer Composition	Sample Number	Gun Distance cm (in.)	Powder Feed Rate (g/min)	Comments
20% YSZ	1	7.6 (3)	10	
	2	7.6 (3)	20	
	3	7.6 (3)	30	
	4	7.6 (3)	40	
	5	2.5 (1)	35	Powder contamination; trial repeated (see sample No. 6)
	6	2.5 (1)	35	
	7	5.1 (2)	35	
	8	7.6 (3)	35	
	9	10.2 (4)	35	
	10	12.7 (5)	35	
	11	15.2 (6)	35	
	12	5.1 (2)	35	Fine particle size (-325 mesh)
	13	7.6 (3)	35	Fine particle size (-325 mesh)
21% MSZ	14	2.5 (1)	35	Almost total spallation of ceramic layer
	15	5.1 (2)	35	
	16	7.6 (3)	35	
	17	10.2 (4)	35	
	18	12.7 (5)	35	
	19	15.2 (6)	35	
	20	19.1 (7.5)	35	

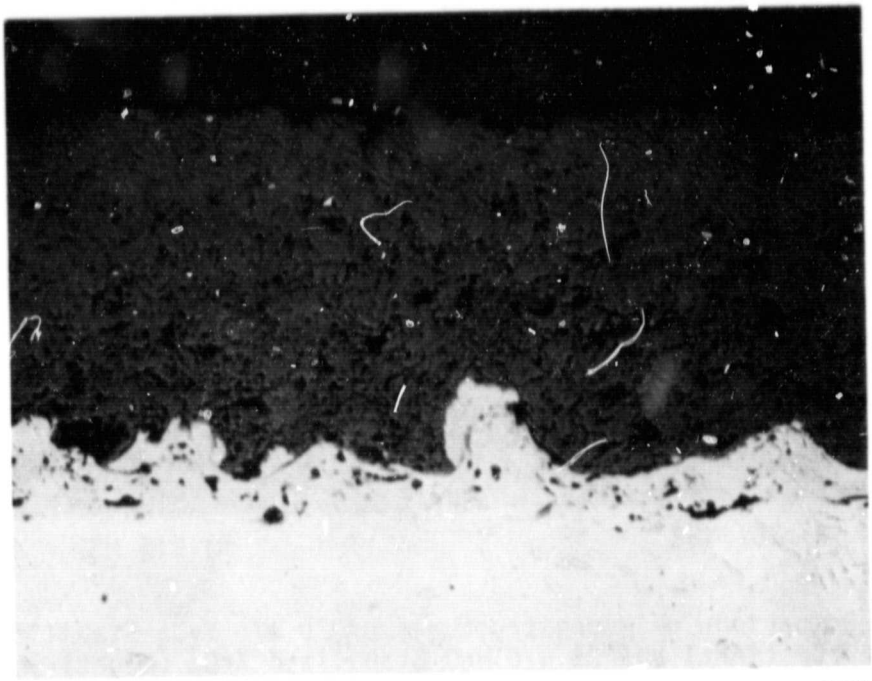

100% −325 MESH

200X

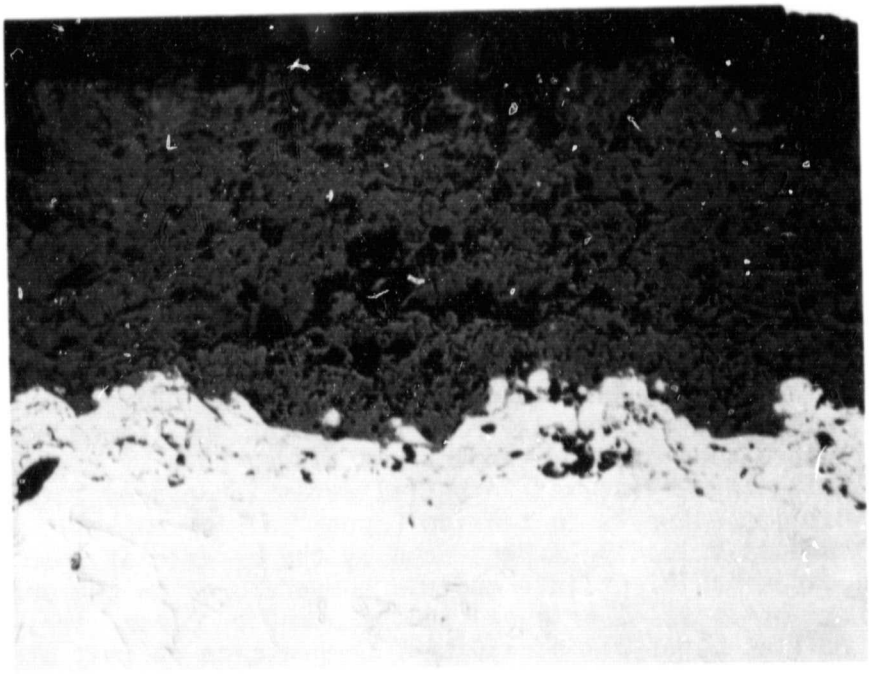

40% −325 MESH
40% − 120, +230 MESH

200X

Figure 19 Microstructures of 20 w/o Y_2O_3 Stabilized ZrO_2 Coatings Produced From Varying Powder Particle Sizes Showing Change in Porosity Level.

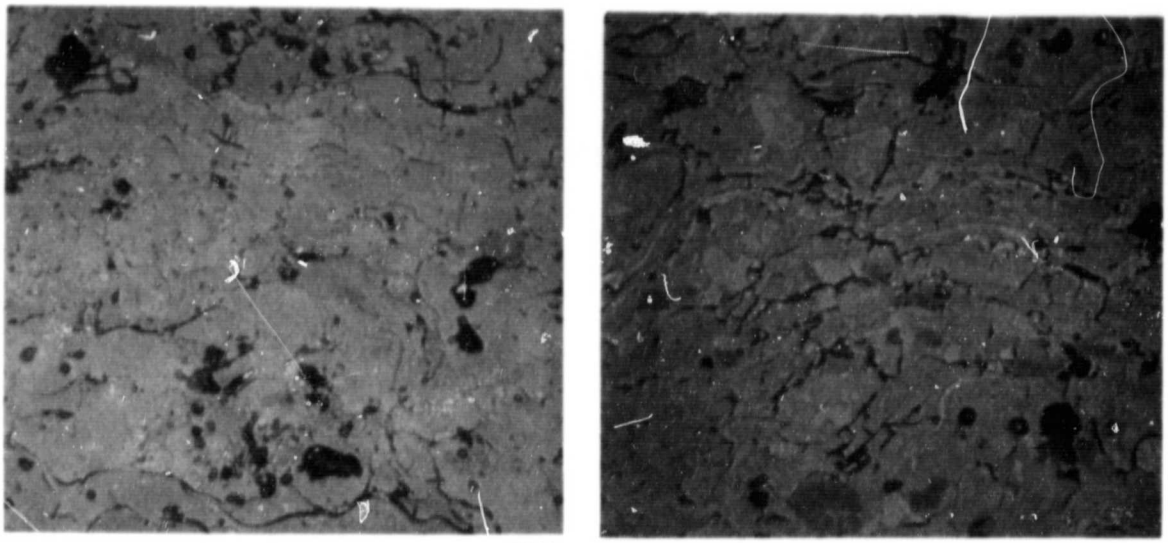

a) 20% YSZ 500X

b) 21% MSZ 500X

Figure 20 Comparison of Microstructures of 20 w/o Y_2O_3 Stabilized ZrO_2 (left) and 21 w/o MgO Stabilized ZrO_2 (Right) Showing Increased Level of Microcracking in the MgO Stabilized ZrO_2 System Due to Free MgO Particles.

5.1.3.2 Residual Stress Control

As mentioned in section 5.1.2, control of ceramic residual stress state is desirable to avoid loading of the ceramic in compression during thermal cycling. The approach developed in this program to control ceramic residual stress was to control the temperature of the substrate during coating deposition. Figure 21 illustrates the calculated variation of in-service ceramic strains with the substrate temperature during coating deposition. Shown in this figure are the algebraic magnitudes of ceramic and substrate strains in the plane of the coating at the coating base metal interface, calculated for various values of the temperature of the substrate at the time of coating application. At high substrate temperatures, differential contraction of the metal substrate on cooling from the process temperature places both the ceramic and the layer of base metal located adjacent to the interface in compression at room temperature (lower pair of curves). During subsequent heating in service, differential expansion places both ceramic and interfacial metallic elements in tension (upper pair of curves). As mentioned above, the compressive loading experienced by the ceramic at room temperature is considered undesirable. At intermediate temperatures on the order of 427°C (800°F), typical of those experienced in uncontrolled plasma spray ceramic application, smaller but still significant compressive ceramic strains are experienced at room temperature. With further reduction of substrate temperature, low temperature compressive ceramic strain becomes sufficiently small that coating durability improves substantially.

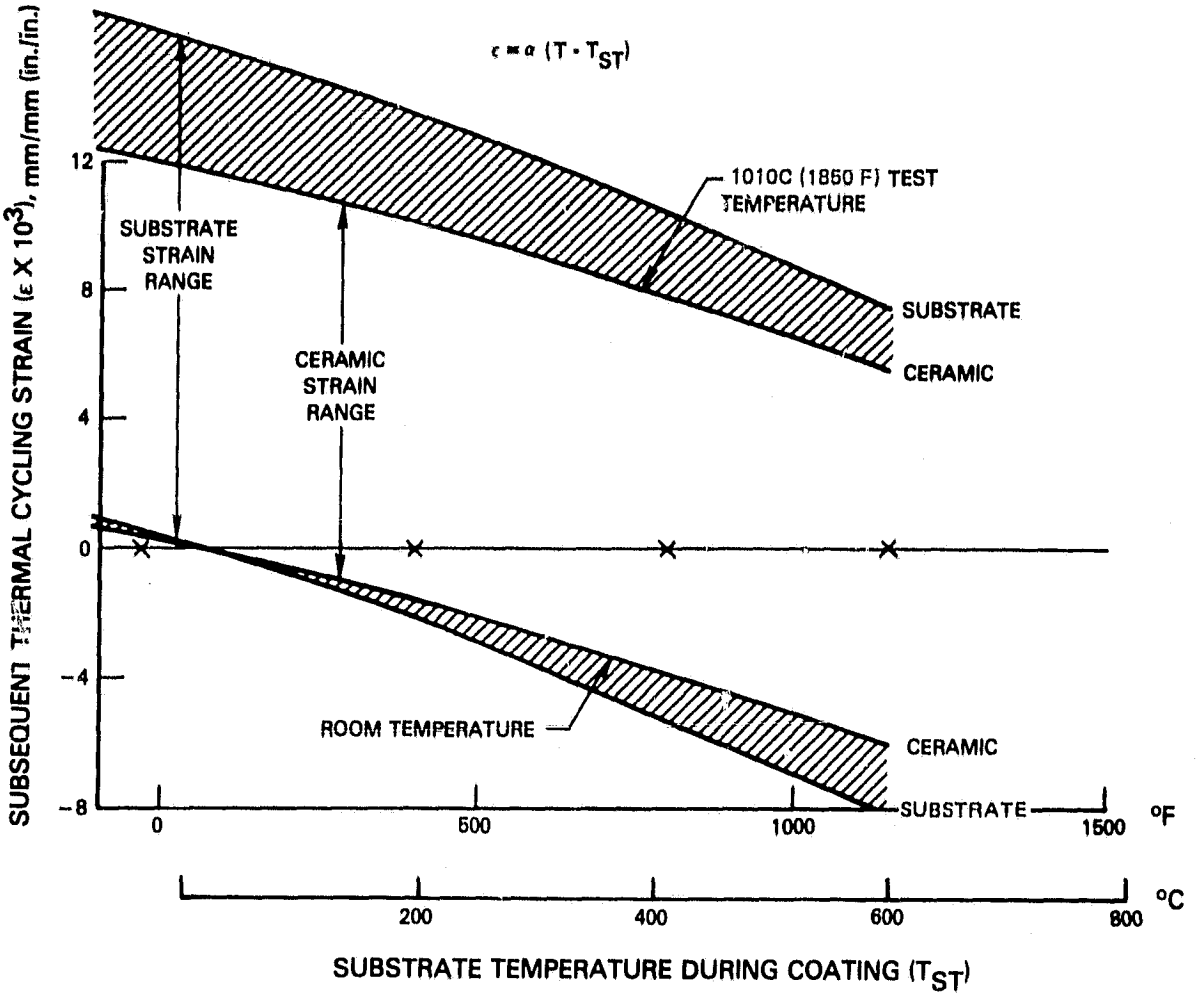

Figure 21 Variation of Interface Strain Range With Substrate Temperature During Coating.

To quantitatively investigate the influence of substrate temperature during coating deposition on subsequent coating performance, twelve specimens were coated with 20% YSZ for subsequent burner rig testing (described in section 5.1.4). Three specimens were coated at each of the following substrate temperatures: -37, 21, 316, and 649°C (-35, 70, 600 and 1200°F). The apparatus shown in Figures 22 and 23 was used to control substrate temperature during coating. As shown in Figure 22 the 1.3 x 10.2 cm long (1/2 inch diameter x 4 inch long) cylindrical burner rig test specimen is center drilled to 6mm (1/4 inch) to allow passage of cooling air during coating. Cooling air is injected into the rotating specimen tip from a stationary tube, passes through the specimen, and exits through ports drilled in the specimen holder. Specimen temperature during coating is measured by a thermocouple buried to one-half the specimen wall thickness at the specimen longitudinal mid-point. Output of the thermocouple is measured through a slip ring located on the drive shaft.

To maintain temperature at ambient and -37°C (-35°F), liquid nitrogen was passed through the specimen rather than air. A natural gas burner was used to heat the bars which were maintained at 649°C (1200°F). The temperature range which was maintained during the spray operation increased with increasing nominal temperature. For example, bars coated at -37°C (-35°F) were maintained to +8°C (15°F), while the 649°C (1200°F) temperature was maintained to +56°C (100°F). The bars which were coated a -37°C (-35°F) were coated in an argon atmosphere chamber to eliminate frost formation. All other bars were coated in an ambient air atmosphere.

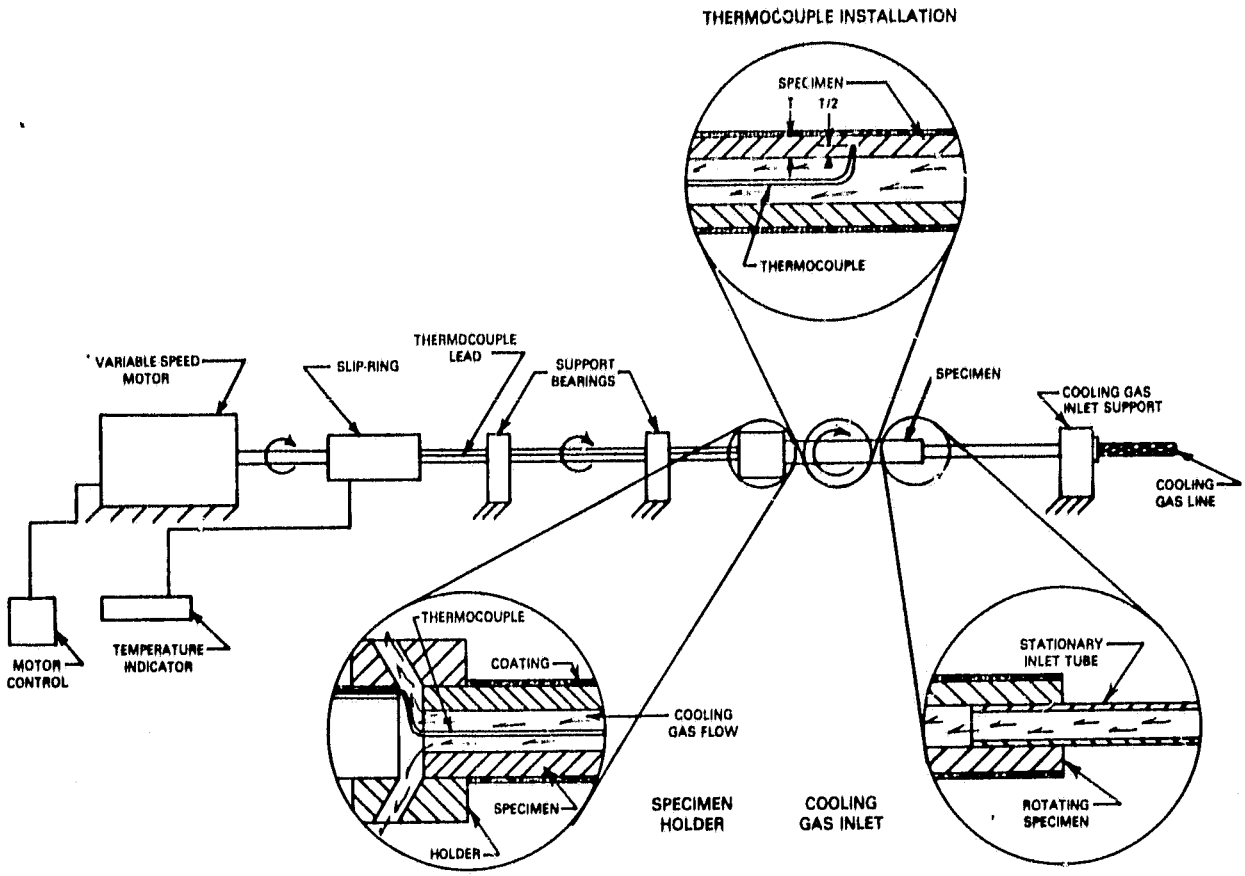

Figure 22 Schematic Diagram of Plasma Spray Substrate Temperature Control Rig.

5.1.3.3 Post Coating Thermal Treatment

The objective of this task was to evaluate the capability of post coating laser processing to produce segmentation such as that shown in Figure 16b. The technique involved an attempt to thermally shock the coating using a rapidly scanned laser beam. As shown in Table II, a series of trials were performed on ceramic coated specimens to investigate the effects of various laser scanning parameters such as beam size and shape, power input, and scanning speed on resultant coating structure. As indicated by the comments in Table II, the

laser process proved very difficult to control. Further, it was found that techniques developed on flat plate specimens did not translate to round bars, with an entirely new set of process conditions being needed to approach a segmented structure on burner rig test specimens. As described in section 5.1.4, burner rig testing of bars processed with post-coat laser scanning exhibited very poor performance due to inability to control the depth of ceramic melting and cracking. Post coat laser processing thus was judged unsuitable as a production method for enhancement of thermal barrier coating durability.

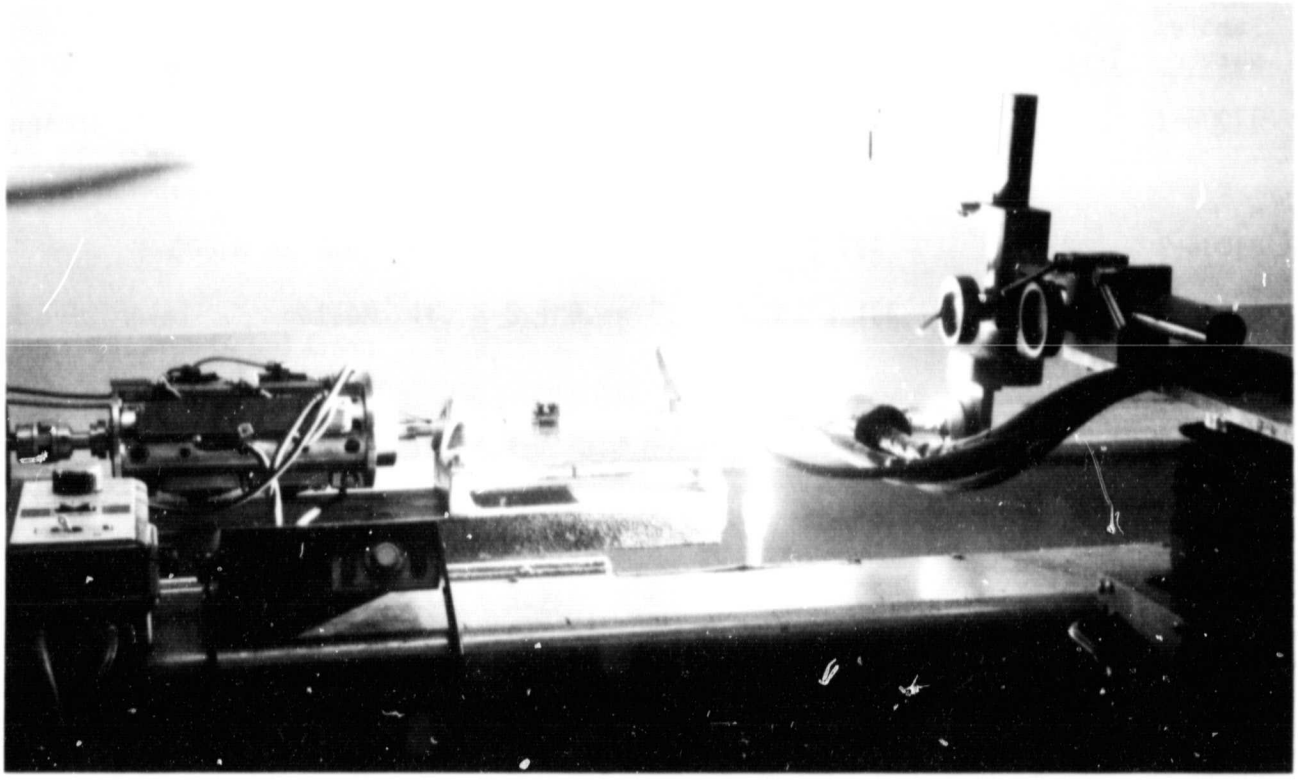

Figure 23 Plasma Spray Coating Rig Which Was Used for Substrate Temperature Control. The temperature of the specimen is shown in the form of a digital readout.

TABLE II

LASER SCANNING TRIALS

1. Samples - flat plates
2. Ceramic Coating - 0.025 cm (0.010 inches) 19 w/o Y_2O_3 stabilized ZrO_2
3. 12 tube CO_2 laser (wavelength = 10.6 microns), unstable resonator gives doughnut shaped beam.
4. First 10 trials run in argon atmosphere; all others run in air.

Sample Number	Power Input kW	Scanning Speed cm/min (in/min)	Beam Size cm (in)	Comments
81006-1	3	191 (75)	.5 x .8 (.2 x .3)	Melting & cracking thru ceramic layer with much evaporation
81006-2	2	191 (75)	.5 x .8 (.2 x .3)	Same as 81006-1
81006-3	2	381 (150)	.5 x .8 (.2 x .3)	Molten layer & cracking halfway thru ceramic layer
81006-4	2	762 (300)	.5 x .8 (.2 x .3)	Shallow surface melting; cracks nearly thru ceramic with local spalling
81006-5	2	508 (200)	.5 x .8 (.2 x .3)	Same as 81006-4
81006-6	1.5	762 (300)	.5 x .8 (.2 x .3)	Shallow surface melting with pieces of molten layer spalling
81006-7	1.2	762 (300)	.5 x .8 (.2 x .3)	Shallow surface melting with pieces of molten layer spalling
81006-8	1	762 (300)	.5 x .8 (.2 x .3)	Some cracking with only surface melting
81006-9	1	762 (300)	.5 x .8 (.2 x .3)	Some cracking with only surface melting
81006-10	1.5	762 (300)	.5 x .8 (.2 x .3)	Surface melting with cracks about halfway thru ceramic
81006-11	1.5	762 (300)	.5 x .8 (.2 x .3)	Surface melting with cracks about halfway thru ceramic

TABLE II (Cont'd)

LASER SCANNING TRIALS

Sample Number	Power Input kW	Scanning Speed cm/min (in/min)	Beam Size cm (in)	Comments
81006-12	1.5	762 (300)	.5 x .8 (.2 x .3)	Overlapped to scan large area; surface melting with cracks about halfway thru ceramic
81006-13	1.5	762 (300)	.5 x .8 (.2 x .3)	
81006-14	1.5	762 (300)	.5 x .8 (.2 x .3)	
81006-15	1.5	762 (300)	.5 x .8 (.2 x .3)	
81013-1	5.5	25 (10)	5 (2) wide	Some glazing and cracking of surface; not cross sectioned
81013-2	5.5	25 (10)	5 (2) wide	
81013-3	5.5	25 (10)	5 (2) wide	
81013-4	5.5	25 (10)	5 (2) wide	
81025-1	2	508 (200)	.5 x .8 (.2 x .3)	Cracks partially thru ceramic
81025-2	2	254 (100)	.5 x .8 (.2 x .3)	Cracks thru ceramic layer
81025-3	2	381 (150)	.5 x .8 (.2 x .3)	Cracks partially thru ceramic
81025-4	3	508 (200)	.5 x .8 (.2 x .3)	Cracks partially thru ceramic
81025-5	3	508 (200), 762 (300)	.5 x .8 (.2 x .3)	One pass over another; cracks partially thru ceramic
81025-6	3	762 (300)	.5 x .8 (.2 x .3)	Cracks partially thru ceramic
81025-7	3	762 (300)	.5 x .8 (.2 x .3)	Cracks 1/5 thru ceramic layer
81025-8	3	762 (300)	.5 x .8 (.2 x .3)	
81025-9	3	762 (300)	.5 x .8 (.2 x .3)	
81025-10	3	762 (300)	.5 x .8 (.2 x .3)	
81025-11	3	762 (300)	.5 x .8 (.2 x .3)	
81025-12	1.5	762 (300)	.5 x .8 (.2 x .3)	2 coincident passes; cracks with molten layer on surface spalling off

TABLE II (Cont'd)

LASER SCANNING TRIALS

Sample Number	Power Input kW	Scanning Speed cm/min (in/min)	Beam Size cm (in)	Comments
81025-13	1.5	762 (300)	.5 x .8 (.2 x .3)	3 coincident passes, with cracks and melting 1/4 thru coating
81025-14	1.5	762 (300)	.5 x .8 (.2 x .3)	3 coincident passes, similar to 81025-13
81025-15	1.5	508 (200)	.5 x .8 (.2 x .3)	2 coincident passes with cracks and melting 1/5 thru coating
81025-16	1.5	508 (200)	.5 x .8 (.2 x .3)	3 coincident passes, similar to 81025-15
81025-17	4	508 (200)	6.1 (2.4) wide	Very shallow layer of surface melting
81025-18	4	254 (100)	6.1 (2.4) wide	Cracks and melting 1/5 thru coating
81025-19	5	254 (100)	6.1 (2.4) wide	Cracks and melting 1/4 thru coating
81025-20	5	127 (50)	6.1 (2.4) wide	Cracks and melting 3/4 thru coating
81025-21	5	254 (100)	6.1 (2.4) wide	Cracks and melting 1/2 thru coating
81025-22	5	127 (50)	6.1 (2.4) wide	Cracks and melting thru nearly entire ceramic layer
81025-23	5	127 (50)	6.1 (2.4) wide	Water quenched; cracks thru nearly entire ceramic layer, no visible melting
81025-24	5	254 (100)	6.1 (2.4) wide	Water quenched; exhibited spalling

5.1.4 Laboratory Coating Performance Evaluation

Two types of laboratory tests were used to evaluate ceramic coating strain tolerance. The primary test method was cyclic burner rig testing, which simulates the engine thermal environment. Monotonic tensile and compressive tests also were conducted to determine the critical strain for coating spallation.

5.1.4.1 Burner Rig Thermal Cycle Testing

5.1.4.1.1 Test Procedure

As noted above, the primary laboratory test method used for evaluation of ceramic coating strain tolerance was burner rig testing. This test involves cyclic flame heating and forced air cooling of a coated cylindrical test specimen such as illustrated in Figure 24. A set of twelve specimens installed in a spindle ready for testing is shown in Figure 25. These bars are rotated at 1725 rpm in the exhaust gases of a jet fuel burner (Figure 26) to provide a uniform temperature for all specimens. The exhaust gases are the combustion products of Jet A fuel and air, with a velocity of Mach 0.3. Specimen temperature is monitored and controlled using an optical pyrometer and automatic feed-back controller. Emittance of the bars is periodically measured, and corrections are made to maintain the acquired set point temperature. During rig operation the fuel pressure is regulated automatically to maintain the designated temperature. To provide cyclic cooling, the burner is automatically moved away from the specimens for the cool portion of the cycle, during which a compressed air blast is applied to the specimens. Testing is interrupted approximately every 20 hours to allow for visual examination of the specimens. Failure is considered to have been achieved when spallation occurs over at least 50% of the "test" zone of the bar. The "test" zone includes an area which is approximately 2.5cm (1 inch) long at the center of the exposed portion of the bar, having a uniform temperature during testing. For the evaluations reported in this section, testing was conducted using a cycle of 1010°C (1850°F) for 4 minutes and forced air cool for 2 minutes. Tests reported in later sections involved higher exposure temperatures which are noted where appropriate.

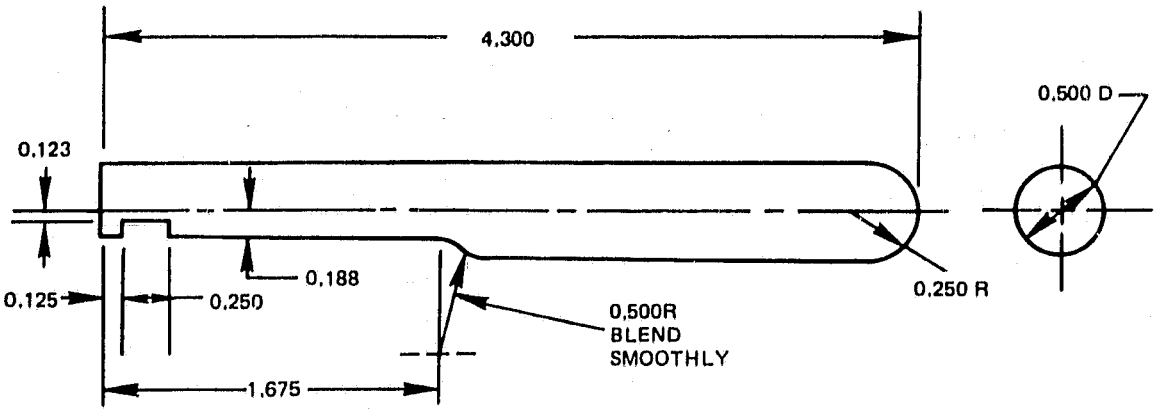

Figure 24 Diagram of Specimen Used For Burner Rig Testing. Dimensions are expressed in inches.

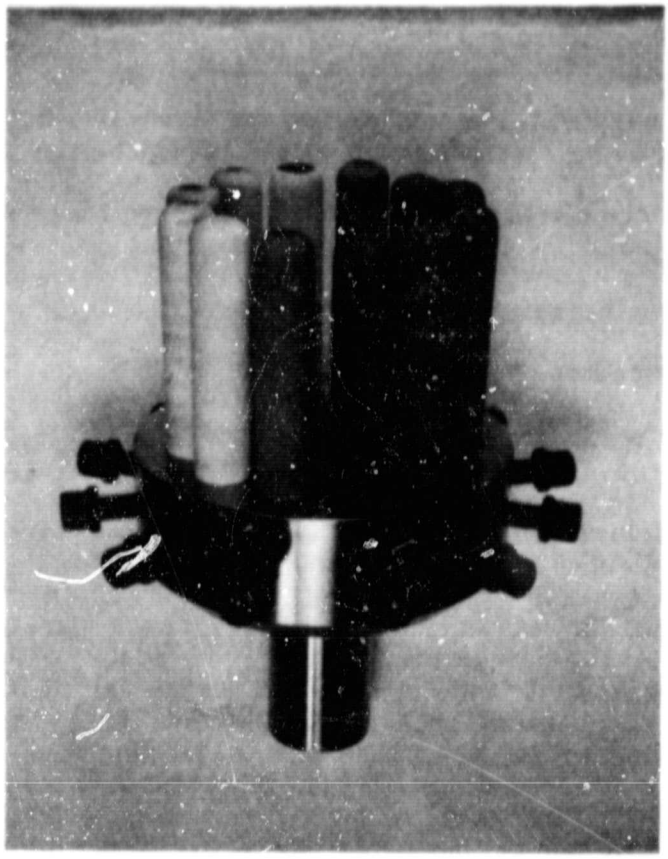

0.5X

Figure 25 Specimens in Fixture Ready For Burner Rig Testing. Coating color variations are due to slight losses of stoichiometry (oxygen depletion) from the heat treat operation.

5.1.4.1.2 Selection and Application of Coatings

Plasma sprayed coating systems tested in the initial set of burner rig tests (Table III) were selected to evaluate a wide range of ceramic compositions, process conditions, and strain tolerant structures. One EB-PVD applied coating system previously developed at Pratt & Whitney Aircraft was also tested. The ceramic layer of this system was a 0.25 mm (10 mil) thick Y_2O_3 stabilized ZrO_2. Four specimens of this system were included in the burner rig test.

All plasma sprayed ceramic compositions tested represented fully or partially stabilized zirconia, with various types and amounts of stabilizing additives as listed below:

Coating Description	Stabilizing Additive	Composition Evaluated (Weight Percent)
CSZ	CaO	5%
MSZ	MgO	21%
YSZ	Y_2O_3	6%, 12%, 20%

With one exception, fine (nominal -325 mesh) spray powders were used, with measured distribution showing fractions in the range of 70 to 100% of the powder in the -325 mesh range. The exception was a coarse 20% YSZ powder having approximately a 40% fraction on the -120 +230 mesh range, with the balance predominantly -325 mesh.

Ceramic coatings were plasma sprayed using a Plasmadyne SG100 gun. MAR M509 cobalt base alloy specimens were grit blasted with 60 grit Al_2O_3 to roughen the surface and were pre-coated with 0.076 to 0.127 mm (3 to 5 mils) of plasma sprayed NiCoCrAlY bond coat to provide oxidation protection and a better surface for ceramic adhesion. A thickness of 0.25 mm (0.010 inch) of ceramic was applied using an automated procedure with the bar being rotated at 600 rpm while the gun was traversed in front of it at a speed of 91.4 cm (36 inches)/minute. Baseline spray parameters were:

Voltage	50 volts
Current	800 amps
Gas	85% Ar/15% He
Powder feed rate	35 gm/minute
Gun-specimen distance	7.6 cm (3 inches)

All plasma sprayed coatings listed in Table III were coated with these conditions except for those noted as being sprayed at standoffs of 2.5 cm (1 inch) and 15.2 cm (6 inches). With the exception of the 21% MSZ and the laser scanned coatings, all specimens were heat treated at 1079°C (1975°F) for 4 hours in a hydrogen atmosphere prior to testing. This heat treatment resulted in a grayish coloring of the ceramic due to a slight loss in stoichiometry through oxygen depletion. However, stoichiometry was restored immediately upon exposure in the hot portion of the burner rig test cycle. Key process parameters together with significant process and composition variations studied in this portion of the program are summarized in Tables IV and V.

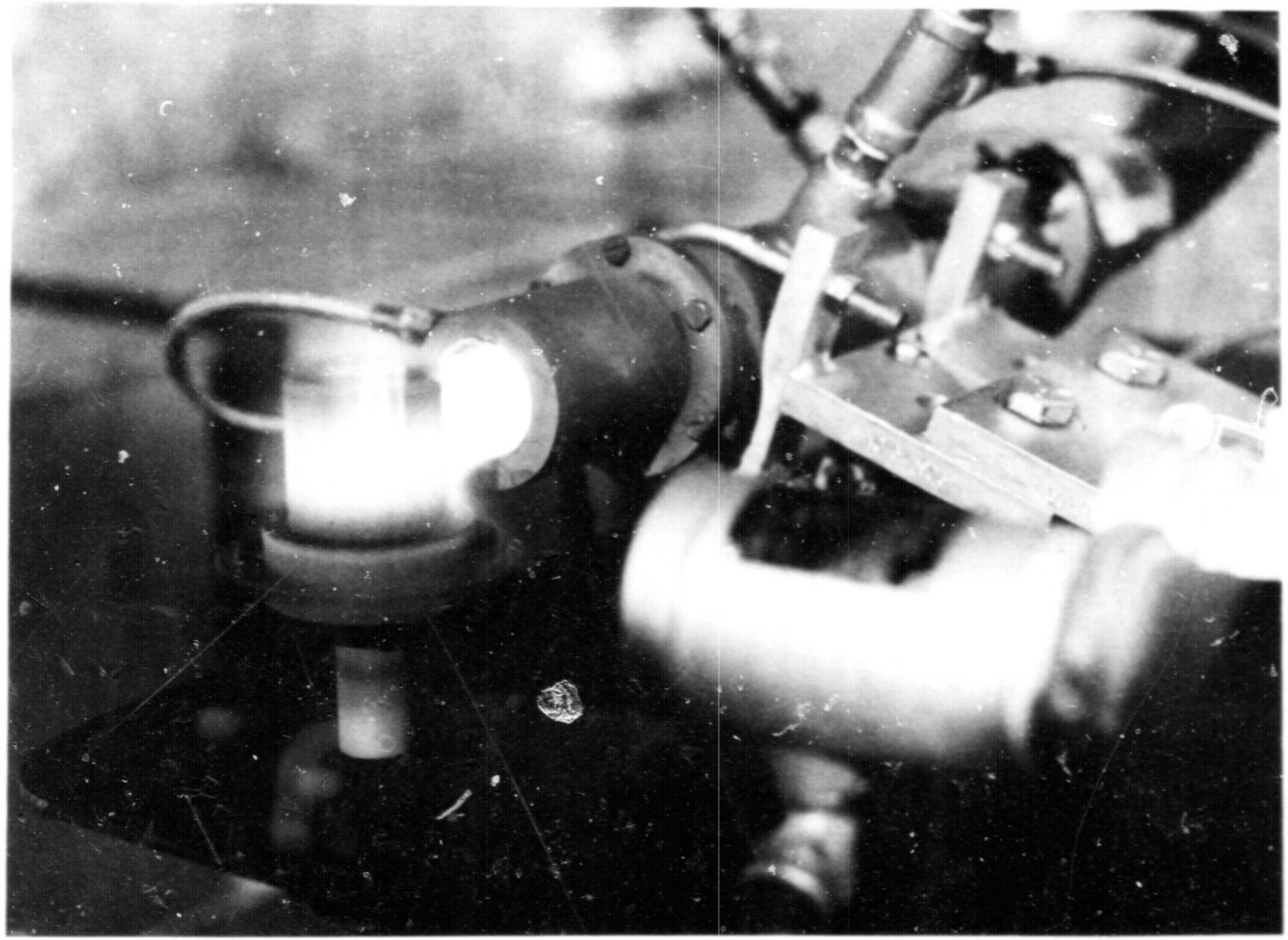

Figure 26 Burner Rig in Operation During the Hot Portion of the Cycle. The cycle used in initial screening tests was 1010°C (1850°F) for 4 minutes + forced air cool for 2 minutes.

TABLE III

BURNER RIG TEST RESULTS

Cycle: 1,010°C (1850°F)/4 min. + forced air cool/2 min.

System Designation	Ceramic Composition	Process Conditions[1]	Cycles to Failure	Average Cycles to Failure
A	20% YSZ	Coarse powder	5260 5580 7150	5997
B	20% YSZ	Baseline	170 180 280	210
C	20% YSZ	2.5 cm (1 inch) standoff	5240 5260 5970	5490
D	20% YSZ	7.6 cm (6 inch) standoff	1420 3450 4780	3217
E	12% YSZ	Baseline	280 580 710	523
F	6% YSZ	Baseline	1570 4410 5040	3673
G	21% MSZ	Baseline	4340 4540 6800	5227
H	5% CSZ	Baseline	740 1970 2970	1893
I	20% YSZ	Baseline + laser scanned	200 200 260	220
J	20% YSZ	648°C (1200°F) substrate temp.	0 180 200	127

TABLE III (Cont'd.)

System Description	Ceramic Composition	Process Conditions[1]	Cycles to Failure	Average Cycles to Failure
K	20% YSZ	315°C (600°F) substrate temp.	7380 9740 10660	9260
L	20% YSZ	Ambient substrate temperature	8160 9930 10130	9407
M	20% YSZ	-37°C (-35°F) substrate temp.	370 2930 7640[2]	3647
N	YSZ	EB-PVD applied	8720 9570 11670 11720	10420

[1]All process parameters baseline except as noted

[2]Exhibited first evidence of local spalling at 2110 cycles

TABLE IV

PLASMA SPRAY COATING PARAMETERS INVESTIGATED

Parameter	Range investigated	Baseline value
Chemistry	6-20 w/o YSZ[a] 21 w/o MSZ[b] 5 w/o CSZ[c]	20 w/o YSZ
Gun to specimen distance	2.5 - 15 cm	7.6 cm
Powder particle size	-325 mesh (fine) -120 mesh (coarse)	-325 mesh
Powder feed rate	10-40 gm/min	35 gm/min
Substrate temperature	Uncontrolled Controlled (-35° to 650°C)	Uncontrolled

[a]Yttria stabilized zirconia (Y_2O_3/ZrO_2).

[b]Magnesium oxide stabilized zirconia (MgO/ZrO_2).

[c]Calcium oxide stabilized zirconia (CaO/ZrO_2).

TABLE V

SIGNIFICANT THERMAL BARRIER COATING SYSTEMS SUBJECTED TO BURNER RIG TESTS

TBC systems	Change from baseline coating	Improved strain tolerance characteristics
20 w/o YSZ	Baseline	
20 w/o YSZ	Coarse powder	Porosity
21 w/o MSZ	Coating chemistry	Microcracking
20 w/o YSZ	2.5 cm gun to specimen distance, coarse powder	Segmentation
6 w/o YSZ	Coating chemistry	Segmentation
20 w/o YSZ	Surface laser scanned, coarse powder	Segmentation
20 w/o YSZ	EB/PVD coating	Segmentation
20 w/o YSZ	Controlled substrate temperature, coarse powder	Strain mismatch

5.1.4.1.3 Burner Rig Test Results

Burner rig test results, listed in Table III and shown in bar chart form in Figure 27, indicated that the refinements in the coating fabrication process had been very successful. Many specimens exhibited thermal cyclic lives 20 times greater than the baseline system B*, which is representative of previous state-of-the-art systems. These benefits were achieved through the incorporation of controlled porosity, microcracking, or segmented structures such as those illustrated in Figures 16b thru 16d. The most significant improvements were evident on specimens which were coated while controlling the substrate temperature. This was a significant advancement in thermal barrier coating technology and suggested that further improvement is possible through the combination of strain tolerant microstructures with controlled substrate temperature processing.

---

* See Table III for system designation.

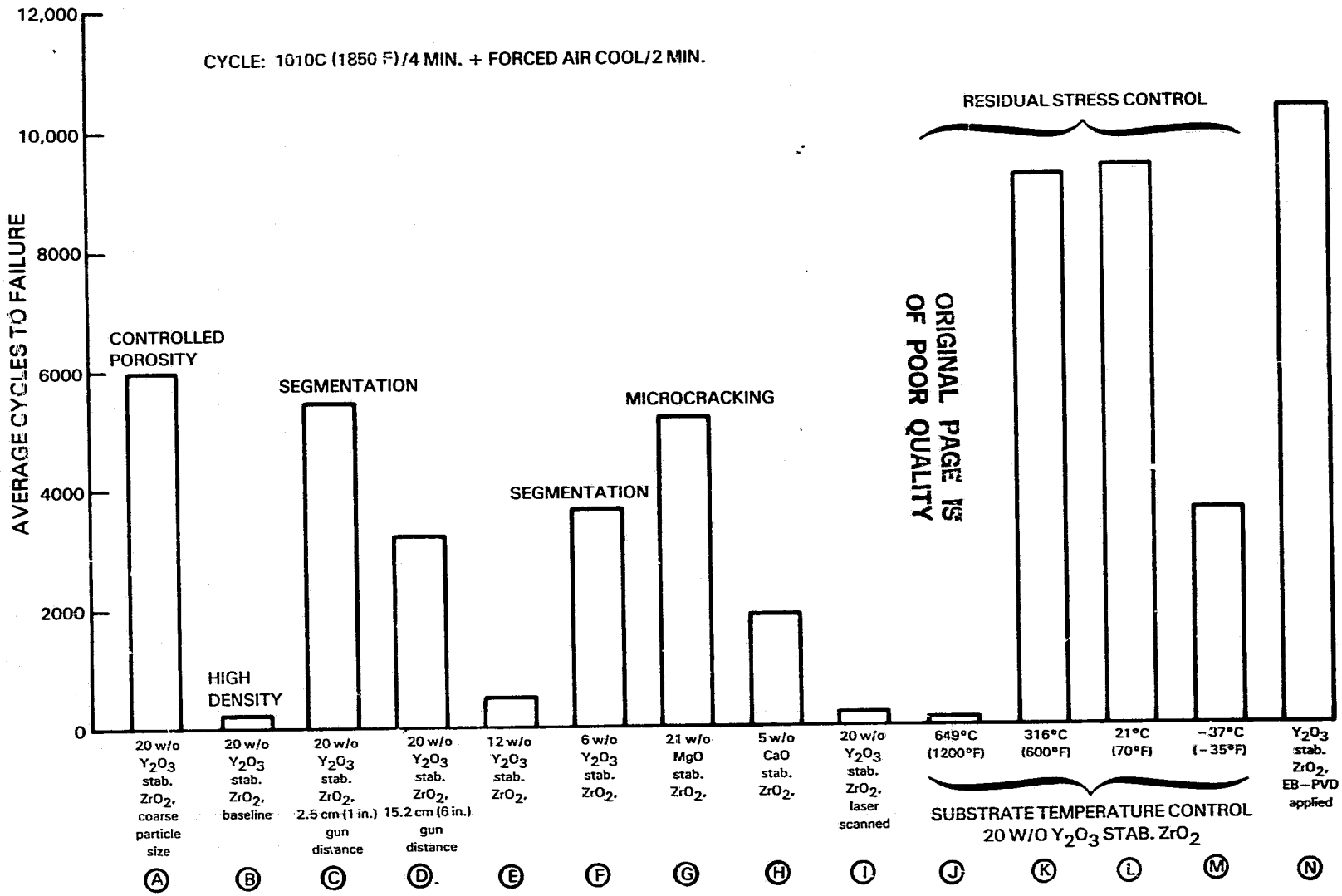

Figure 27 Average Number of Cycles to Failure for Each Ceramic Coating System Tested in the Burner Rig.

Differences observed in coating performance were believed to be related to the different strain relief mechanisms induced by the various coating application methods. Significant differences in performance were seen to be related in particular to the initial particle size of the ceramic plasma spray powder. The bars which were coated with the coarse powder (System A) exhibited the highest average life to ceramic failure of all systems sprayed with uncontrolled substrate temperature, while all three of the baseline bars coated with the finer powder (System B) failed during the first day of testing. This difference in performance is attributed to the difference in microstructure. The coarse particle size powder results in a microstructure with a considerable amount of porosity and a slight degree of microcracking, while the finer powder produces an extremely dense structure, as shown previously in Figure 19. As explained in Section 5.1.2, both porosity and microcracking are means of relieving thermal stresses in the ceramic, by reduction of elastic modulus and consequent coating stress reduction in strain controlled conditions. The very dense structure produced using the finer powder results in higher ceramic stresses and early ceramic failure.

The bars coated with 20% YSZ sprayed from a 2.5 cm (1 inch) distance (System C) exhibited only a slightly lower average life than those sprayed from the standard 7.6 cm (3 inch) distance. Although this coating was extremely dense due to the high heat during coating deposition, vertical cracks were present which formed a segmented microstructure, similar to Figure 18. As indicated in Section 5.1.2, segmentation provides an excellent means for relieving thermal stresses. However, this system also contained flaws parallel to the plane of the coating, which could lead to coating failure. Extremely good processing control would be required to fully optimize this system by eliminating the flaws in the plane of the coating while still maintaining perpendicular cracks which penetrate through, but not beyond, the thickness of the ceramic.

The 20% YSZ system sprayed from the 15.2 cm (6 inch) gun distance (System D) exhibited an average life to failure which was approximately half that of the systems sprayed from the standard 7.6 cm (3 inch) distance. A relatively poor bond between ceramic particles resulting from the large standoff distance was believed to be responsible for the loss of spallation resistance. This condition is illustrated in Figure 28 and Figure 29 as very prominent boundaries or cracks between particles of the sprayed ceramic, many oriented predominately in the plane of the coating.

The 12% Y_2O_3 stabilized ZrO_2 (System E) resulted in an extremely low average life to ceramic spalling (approximately 500 cycles). X-ray diffraction analyses indicated no phase transformation which would be expected to cause failure due to volume changes. Metallographic evaluation indicated a very dense microstructure with limited microcracking (Figure 30). This correlates with the fact that a fine particle size powder was used as the initial material. Although coarser particle size powders of this composition have not been investigated, it was assumed that the resulting high porosity coating would provide coating life equivalent to that which resulted from the high porosity 20% YSZ composition, since both systems theoretically contain a fully stabilized cubic crystal structure.

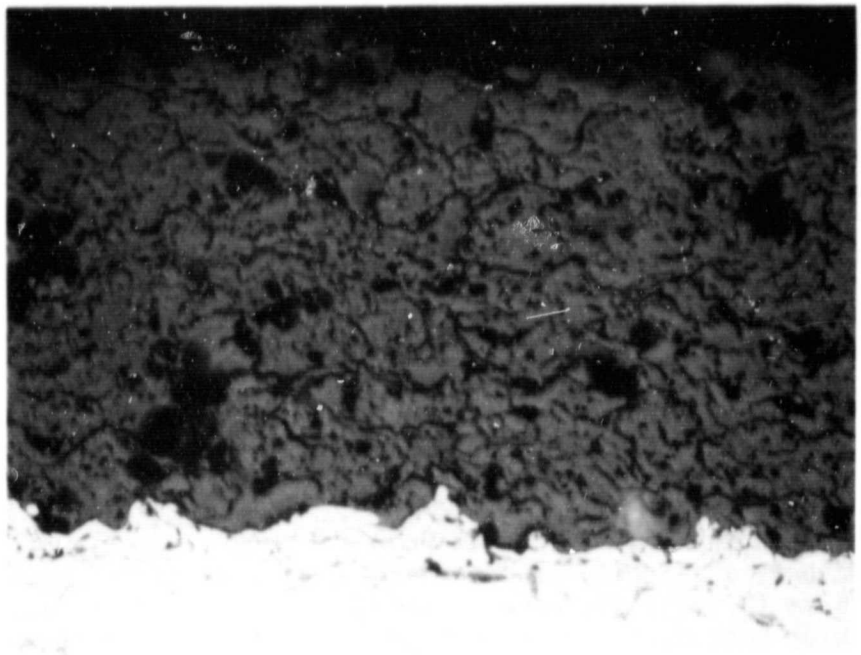

250X

250X

Figure 28 Light Microscope Photographs of Pre-Test (top) and Post-Test (bottom) Microstructures of a 20 w/o Y_2O_3 Stabilized ZrO_2 Coating Applied Using a 15.2 cm (6 inch) Gun to Specimen Distance Exhibiting Prominent Boundaries (Cracks) Between Particles Oriented Parallel to the Plane of the Coating.

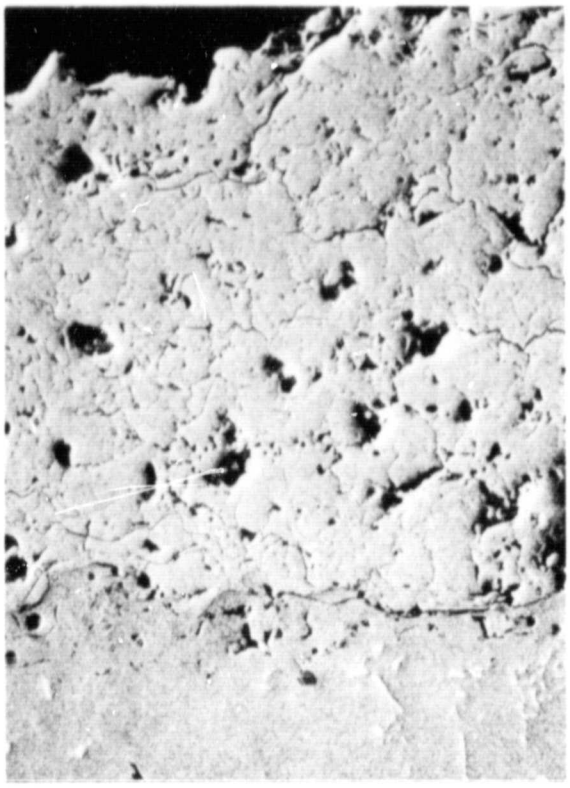

300X

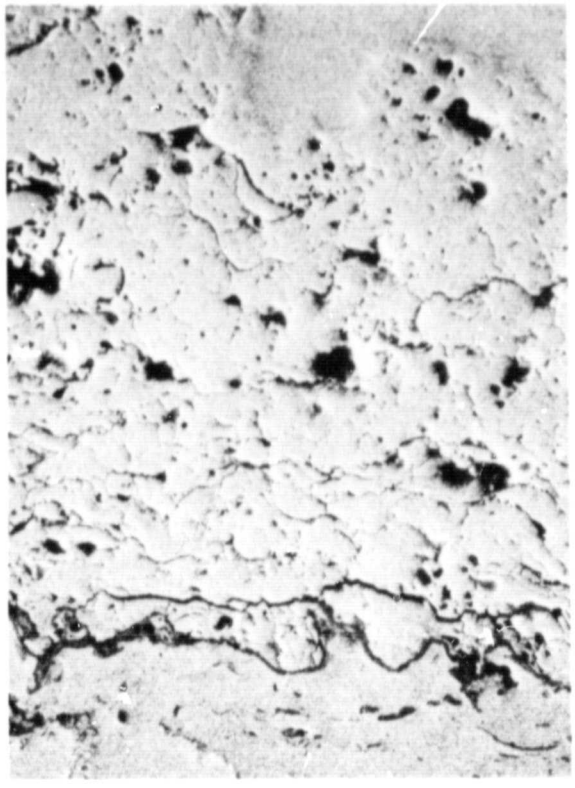

300X

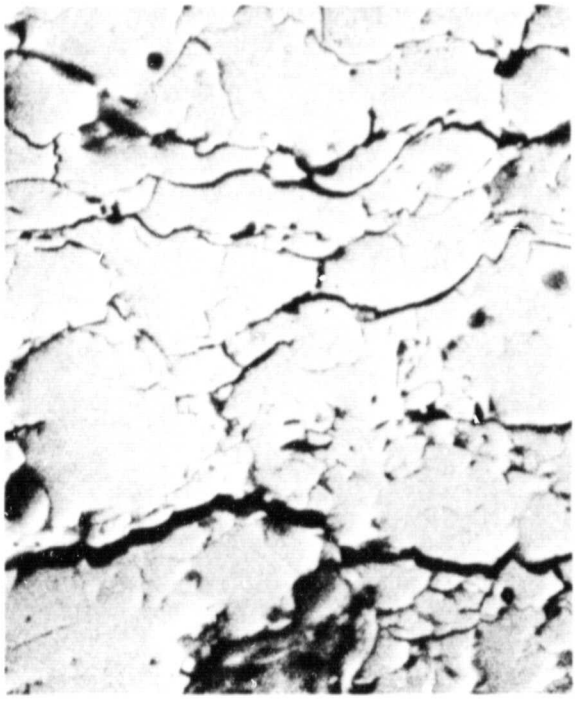

1000X

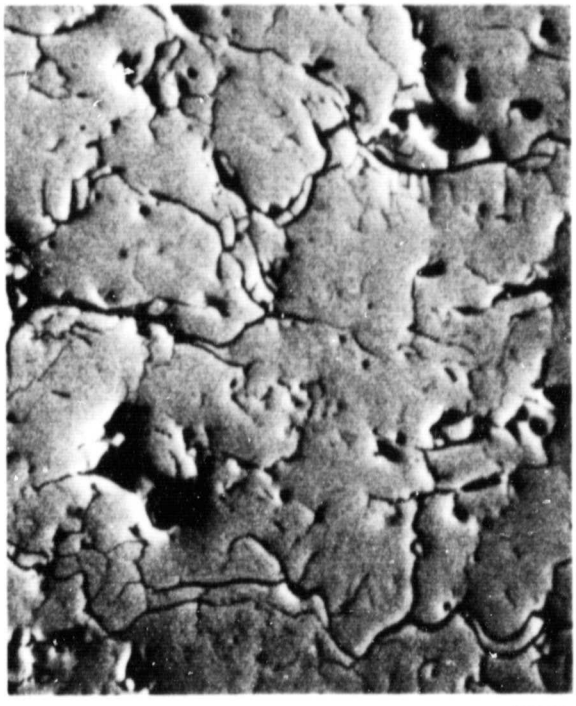

1000X

Figure 29 SEM Photographs of Pre-Test (Left) and Post-Test (Right) Microstructures of a 20 w/o Y_2O_3 Stabilized ZrO_2 Coating Applied Using a 15.2 cm (6 inch) Gun to Specimen Distance Exhibiting Prominent Boundaries (Cracks) Between Particles Oriented Parallel to the Plane of the Coating.

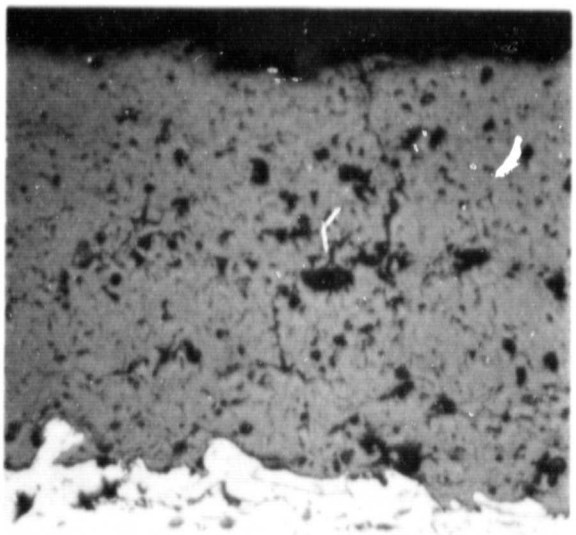

250X

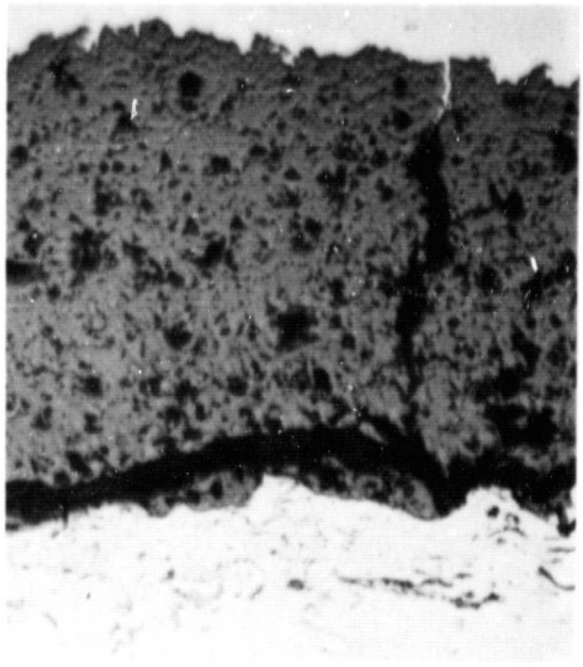

250X

300X

300X

Figure 30 Light Microscope (Top) and SEM (Bottom) Photographs of Pre-Test (Left) and Post-Test (Right) Microstructures of a 12 w/o Y_2O_3 Stabilized ZrO_2 Coating.

While the average life to spallation failure for the three 6% YSZ specimens (System F) was only moderate (3673 cycles), it was felt that this coating system may prove to be beneficial for several reasons. As is shown in Table III, one of the three specimens tested failed after a very short time (1570 cycles) relative to the other two (4410 and 5040 cycles). This was apparently related to the fact that this specimen was in test during a period when the actual temperature during the hot portion of the cycle was higher than the desired 1,010°C (1850°F), due to errors in the temperature measurement methods.

Metallographic examination of the 6% YSZ coating before and after test (Figure 31) indicates a relatively dense structure with numerous vertical segmentation cracks. As discussed previously, these cracks are thought to provide strain tolerance by increasing ceramic compliance in the plane of the coating.

The 21 w/o MgO stabilized ZrO_2 ceramic (System G) exhibited an average of greater than 5000 cycles of life prior to spallation failure. Metallographic examination of the microstructure indicated that a considerable amount of microcracking (Figure 32) was present in the MgO-ZrO_2 structure which is believed to have provided an effective strain tolerance mechanism. This microcracking is discontinuous and in random directions, which appears to enable it to act mainly as a strain relief mechanism without encouraging spallation of the ceramic. Metallographic examination suggests that the presence of free MgO particles contributed to the existence of random microcracks.

The calcia stabilized zirconia coating (System H) exhibited a very low life relative to other systems tested, giving an average life to spallation failure of less than 2000 cycles. Metallographic examination revealed a relatively dense structure with a large amount of coarse branched cracking (Figure 33). These cracks were very open, progressing in directions both perpendicular to the plane of the coating forming the segmented type structure and parallel to the plane of the coating just above the metallic/ceramic interface. The latter condition (cracks parallel to the plane of the coating) was considered to be responsible for the early failure of this coating system, especially since these cracks were present even in the pretest condition. CaO stabilized ZrO_2 has a slightly lower coefficient of expansion than either MgO or Y_2O_3 stabilized ZrO_2, making the thermal expansion mismatch between the metallic substrate and the ceramic layer greater. This condition was apparently responsible for the extensive macro cracking which was evident in this system.

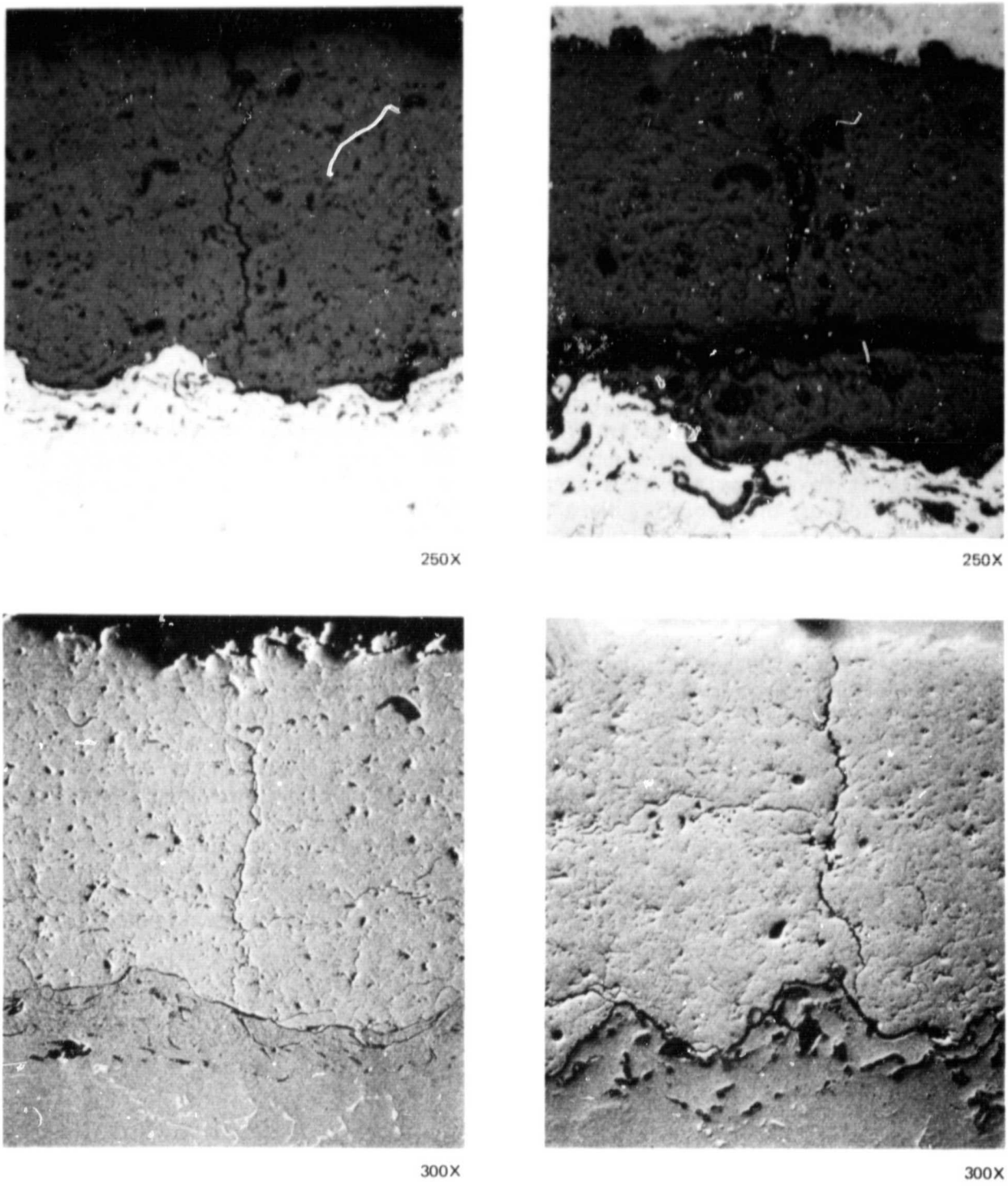

Figure 31 Light Microscope (Top) and SEM (Bottom) Photographs of Pre-Test (Left) and Post-Test (Right) Microstructures of a 6 w/o Y_2O_3 Stabilized ZrO_2 Coating Exhibiting Vertical Cracks which Formed a "Segmented" Structure.

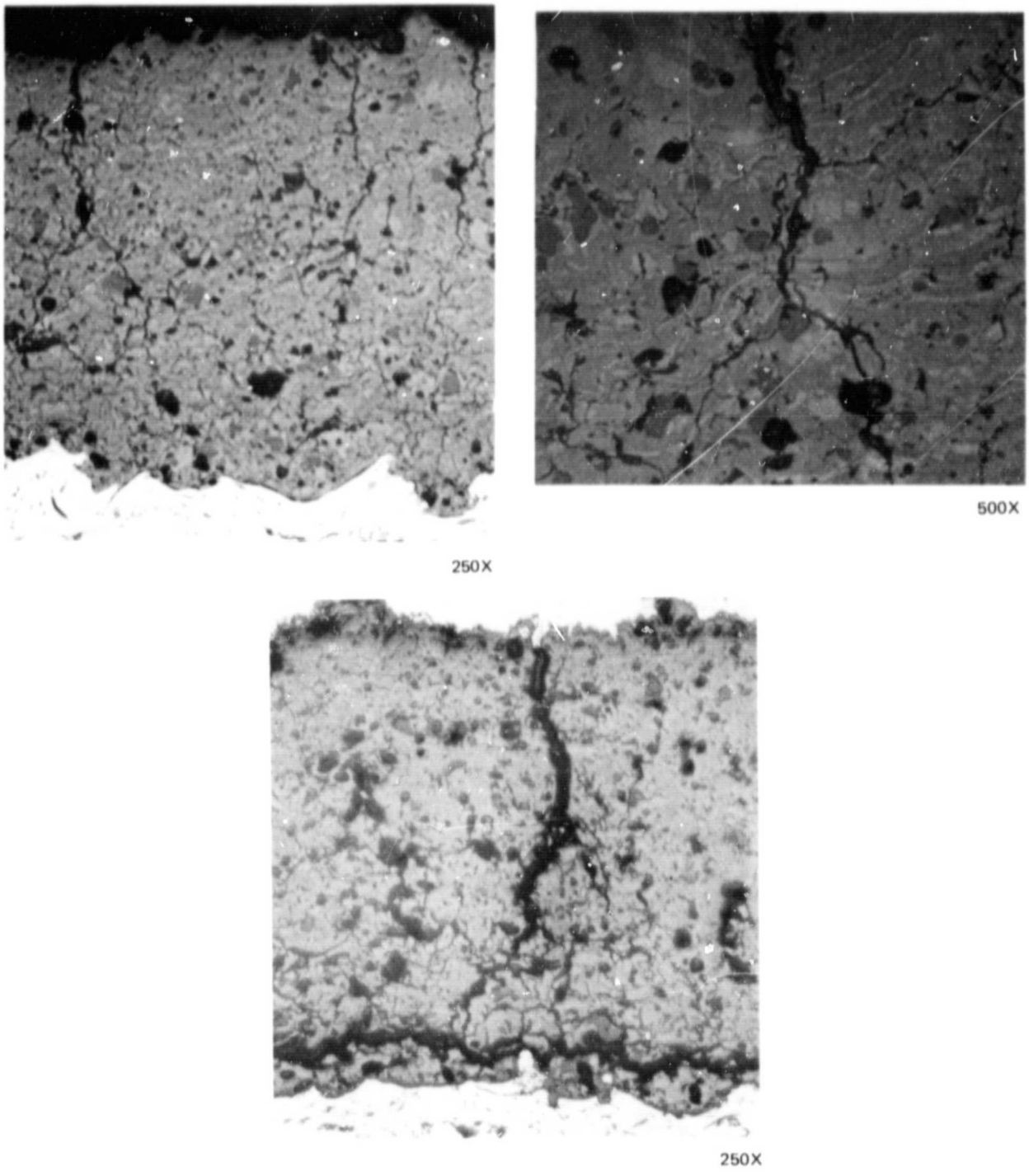

Figure 32 Light Microscope Photographs of Pre-Test (Top) and Post-Test (Bottom) Microstructures of a 21 w/o MgO Stabilized ZrO_2 Coating.

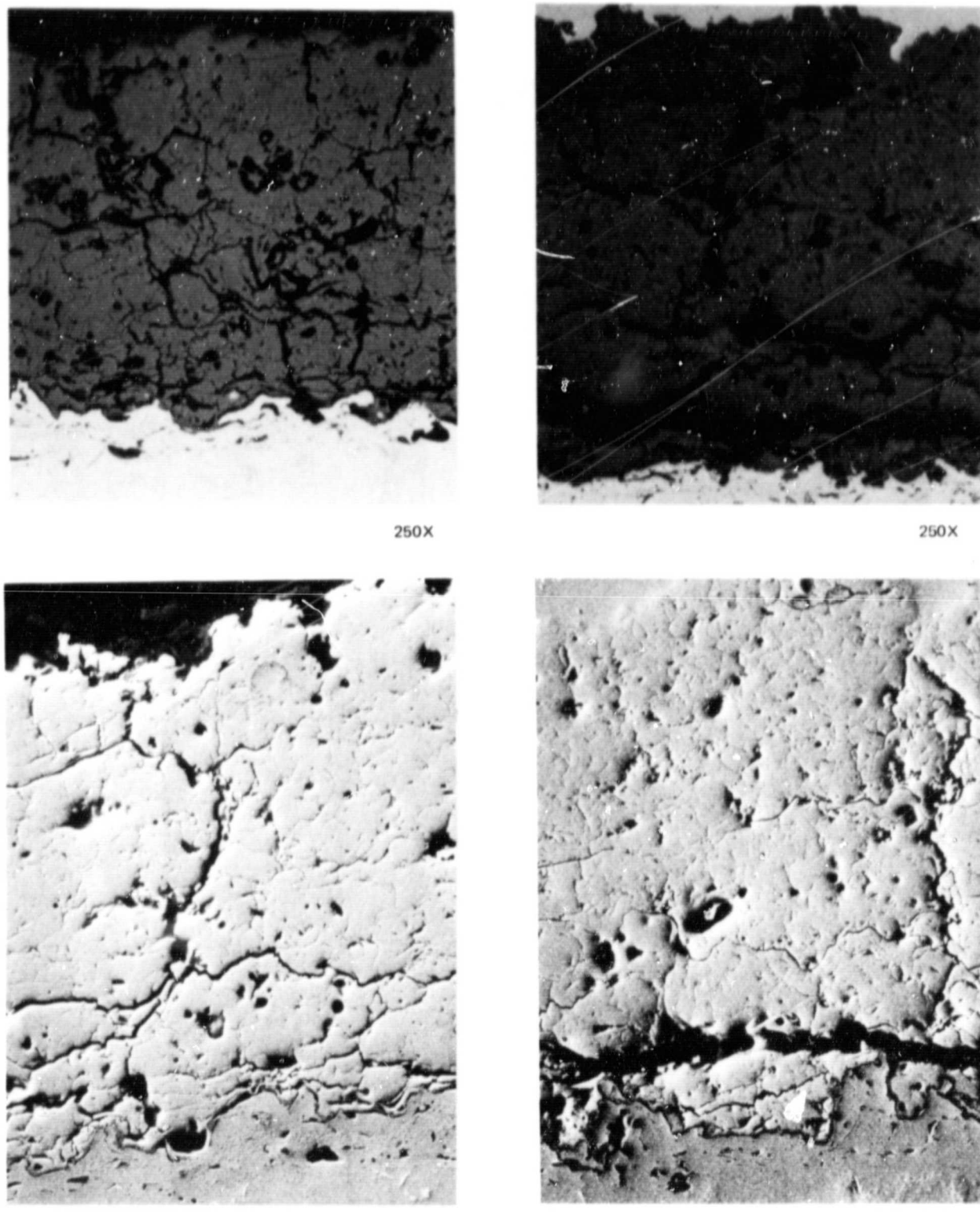

250X 250X

300X 300X

Figure 33 Light Microscope (Top) and SEM (Bottom) Photographs of Pre-Test (Left) and Post-Test (Right) Microstructures of a 5 w/o CaO Stabilized ZrO_2 Coating.

As mentioned in Section 5.1.3.3, three bars were treated using a laser scanning process after plasma spray coating with 20 w/o Y_2O_3 stabilized ZrO_2 (System I). The bars were heated to approximately 843°C (1550°F) during the scanning process in order to prevent spallation of the ceramic layer. Visual examination of these bars suggested that the desired glazing and segmentation characteristics had been achieved (Figure 34); however, when added to the burner rig test, all three specimens failed within the first day (220 cycles average) of testing. Spallation occurred over the entire length of the bar, with a thin layer of ceramic remaining on the surface (Figure 35). Metallographic examination of the pretest structure revealed that the scanning had not produced cracking and melting which extended entirely through the ceramic layer (Figure 36). Therefore, damaging macrocracks appear to have progressed through the more porous inner structure in a direction parallel to the plane of the coating causing spalling. Another factor which may have contributed to the early failure was the degree of preheating used during the scanning process. As a result of the large thermal contraction of the substrate relative to the ceramic layer during cooling, a high residual compressive stress state occurred in the ceramic. Upon further cycling, this residual stress is expected to have contributed to the ultimate failure of the ceramic layer.

Substrate temperature control produced very promising results, with the intermediate substrate temperatures [21 and 316°C (70 and 600°F)] specimens (Systems K and L) exhibiting the longest lives. Even greater thermal cyclic life could have been be achieved except for two factors: the duration of the tests exceeded the oxidation life of the metallic bond coating, and weakening of the substrate during test caused the specimens to bend, causing coating spallation. Figure 37 shows the severe oxidation of the metallic bond coating which caused deterioration of the bond at the metallic/ceramic interface. Oxidation of the NiCoCrAlY layer also resulted in a volume expansion, which effectively forced spallation of the ceramic. The cooling air passage of the MAR-M 509 substrate also oxidized, weakening the specimen and causing it to bend during test due to centrifugal loads (Figure 38). This bending applied additional stresses to the ceramic material. For these reasons, it is expected that controlling substrate temperature may provide an even greater benefit than that exhibited in this series of tests.

All four of the bars coated using the EB-PVD process previously developed by Pratt & Whitney Aircraft (System N) exhibited a relatively high life, averaging greater than 10,000 cycles to failure. Metallographic examination of this coating system revealed that the desired columnar structure had been achieved (Figure 39). This columnar structure forms naturally as a result of shadowing effects during coating deposition in the EB-PVD process. The columnar structure is essentially a "segmented" coating structure, only on a much finer scale than can be achieved with plasma sprayed systems.

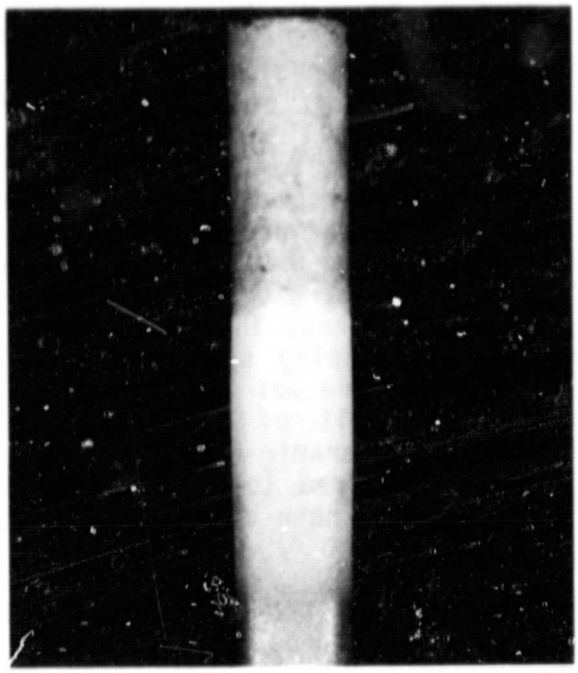

1X

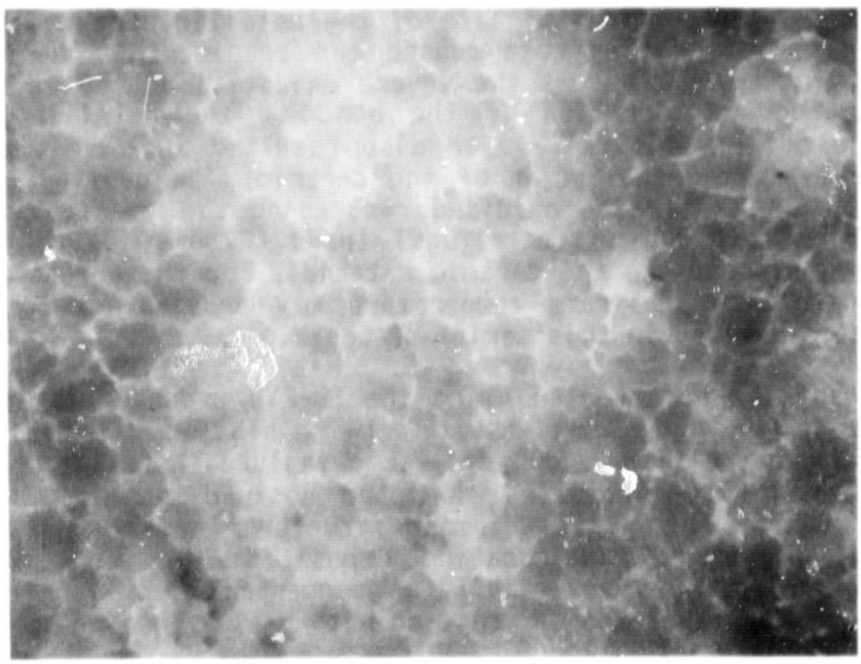

22X

Figure 34 Surface Condition of Laser Scanned Bars for Burner Rig Test. The parameters used were a power input of 5 kw, a scanning speed of 76.2 cm (30 in.)/min, and a 7.62 cm (3 inch) long elliptical beam.

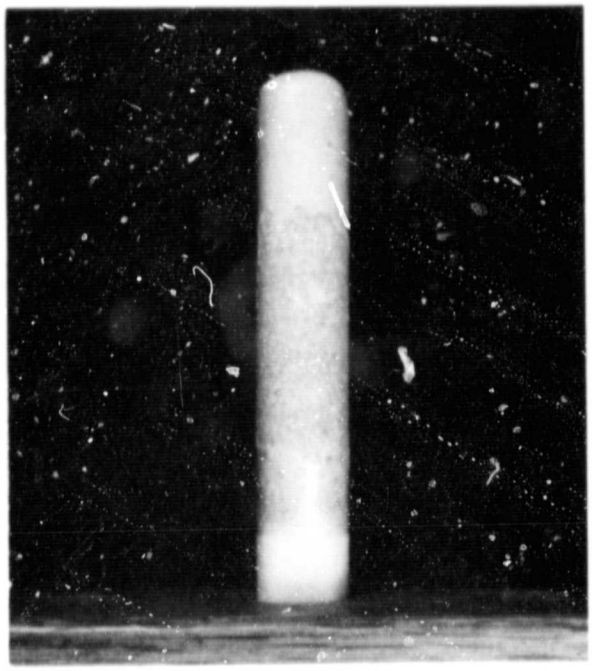

1X

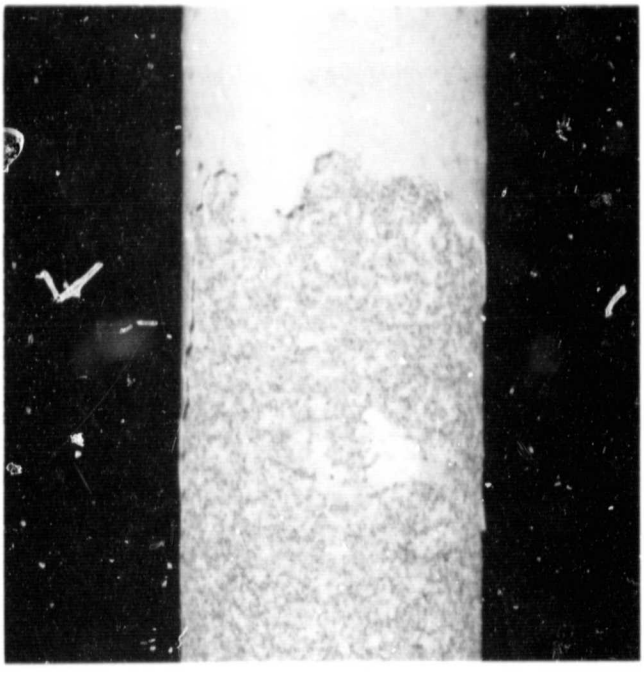

3X

Figure 35 Typical Spallation Failure of a Laser Scanned Specimen After only 200 Cycles of Burner Rig Testing.

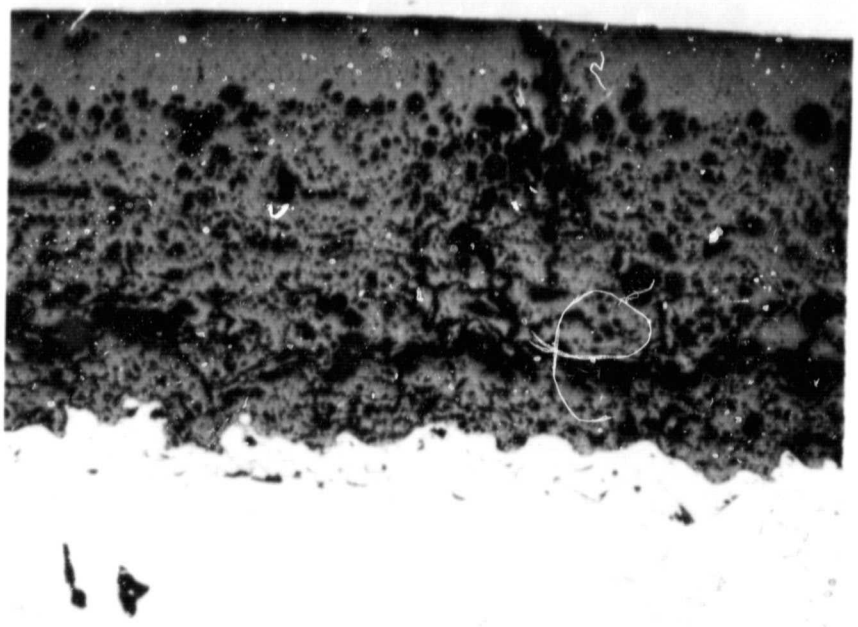

100X

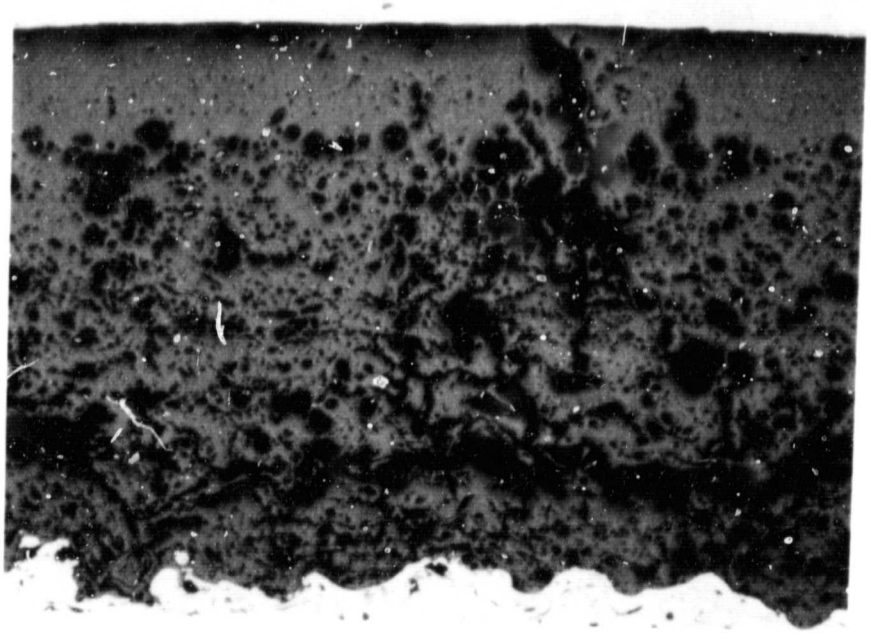

200X

Figure 36 Pre-Test Microstructures of a 20 w/o Y_2O_3 Stabilized ZrO_2 Coating After Laser Scanning.

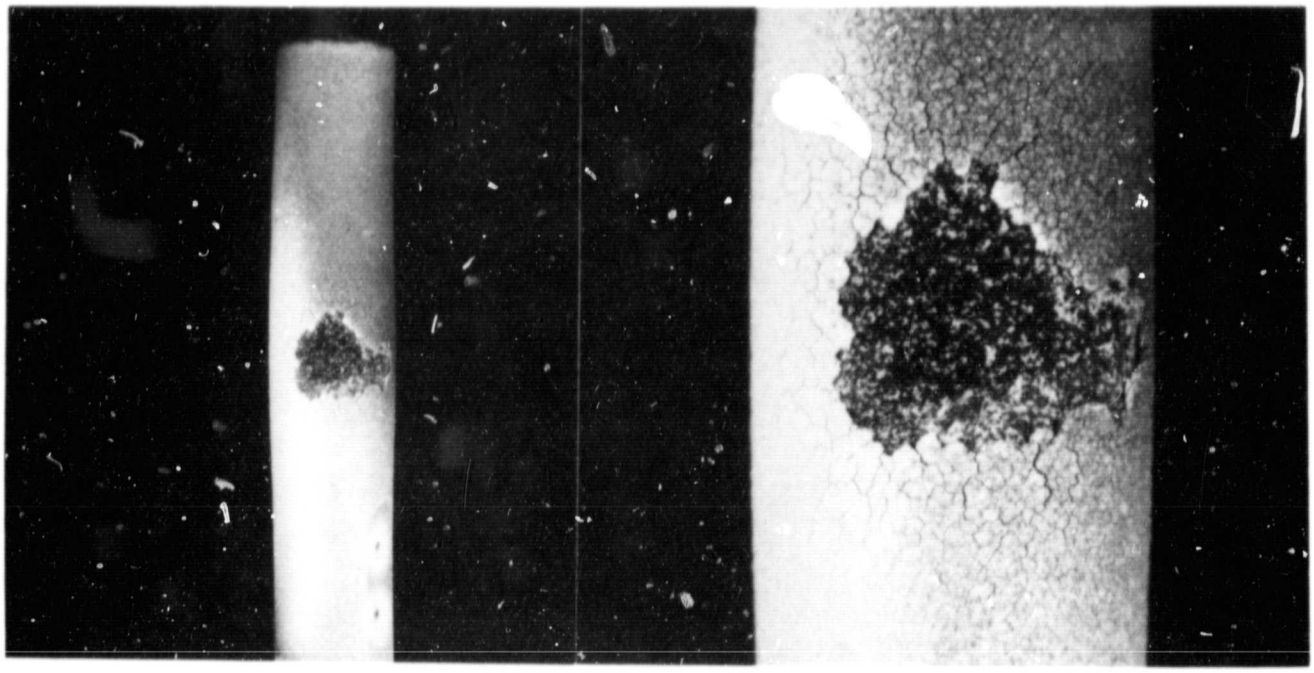

1X 4X

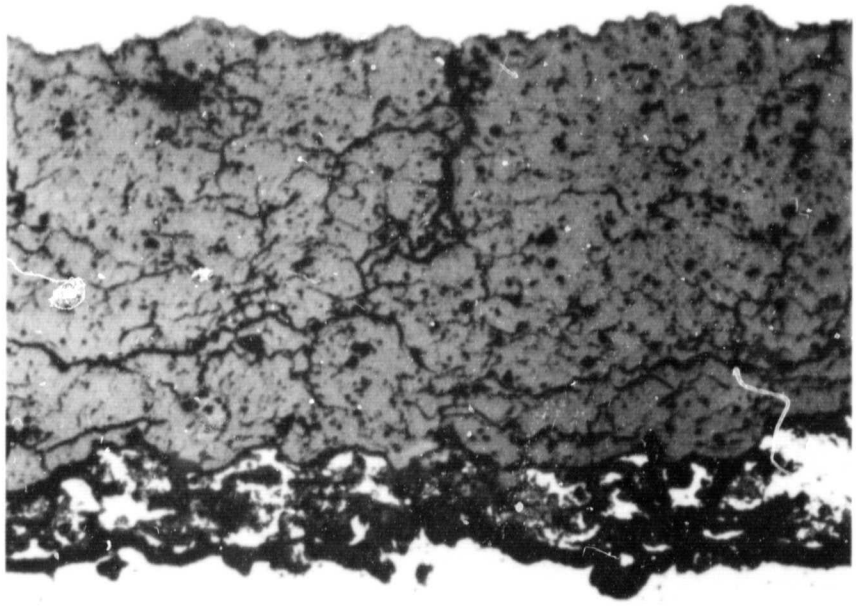

200X

Figure 37 Specimen Coated With a 20 w/o Y_2O_3 Stabilized ZrO_2 While Maintaining a 21°C (70°F) Substrate Temperature Showing Oxidation of the NiCoCrAlY Bond Coating Which Contributed to Ceramic Spallation.

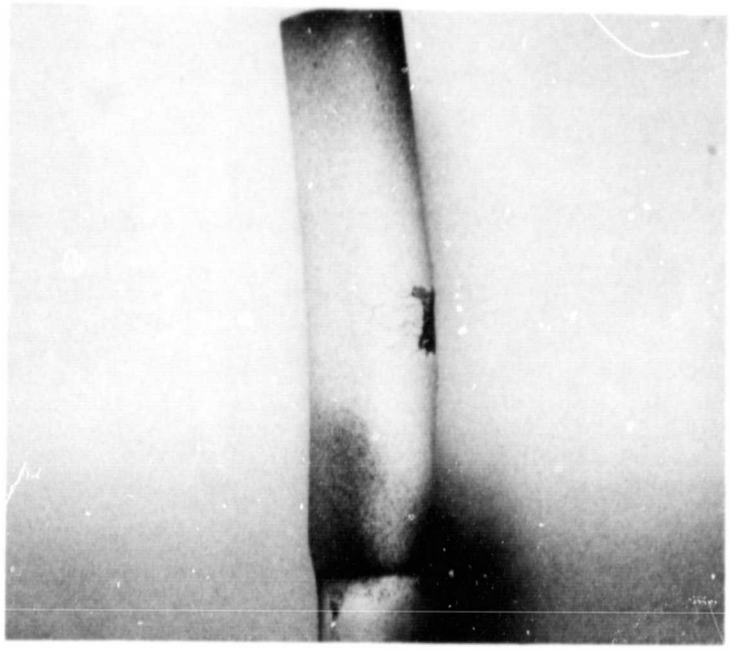

1X

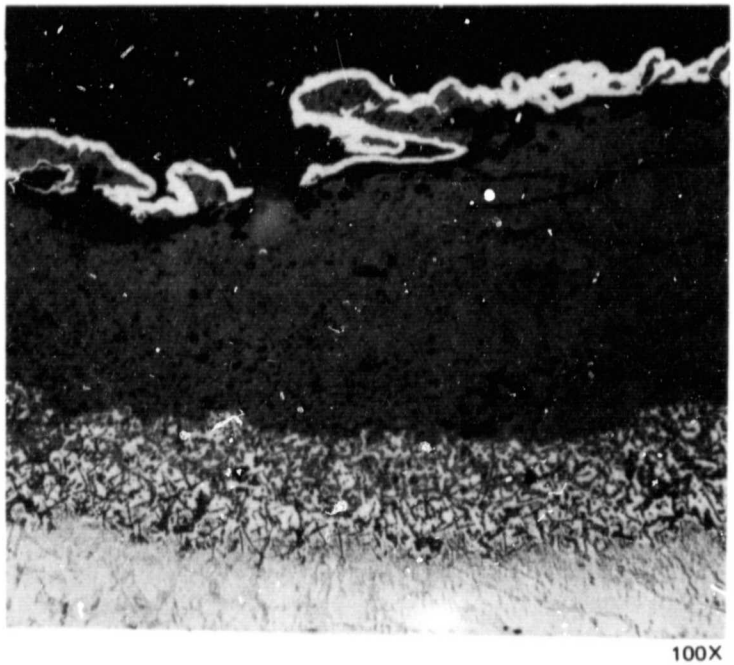

100X

Figure 38 Specimen Coated With a 20 w/o Y_2O_3 Stabilized ZrO_2 While Maintaining a 21°C (70°F) Substrate Temperature Showing Bending of the Bar (Top) which Resulted from Oxidation of the PWA 647 Substrate in the Uncoated Internal Cavity (Bottom).

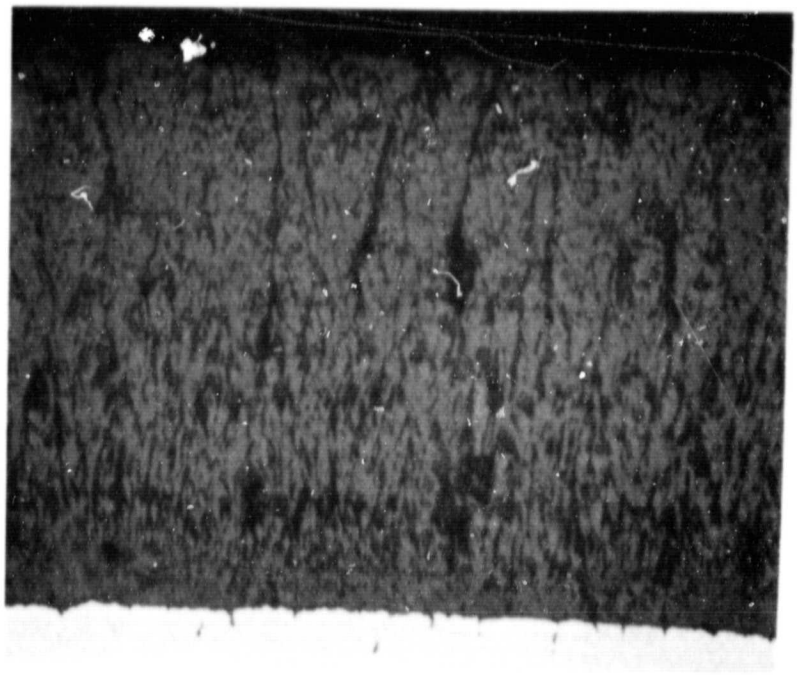

250X

300X

Figure 39 Pre-Test Microstructure of the EB-PVB Applied Y_2O_3 Stabilized ZrO_2 Coating System Showing "Columnar" Effect which Results from Shadowing During the Coating Process.

5.1.4.1.4 Selection of Coatings for First Engine Test

Based on the results of burner rig testing, the following plasma sprayed coating systems were selected for the first engine test.

20% YSZ (coarse particle size)
21% MSZ
6% YSZ

Each coating was applied manually (head held spray gun) to a nominal thickness of 0.25 mm (10 mils) over a 0.008 - 0.013 cm (0.003 - 0.005 inch) thick NiCoCrAlY metallic bond coat.

Ceramic coatings were applied with a plasmadyne SG100 plasma spray torch with the following process parameters:

40 kw power level
7.6 cm (3 inch) gun distance

Powder feed rates were:

20 YSZ	36 g/min.
21 MSZ	40 g/min.
6 YSZ	53 g/min.

The selection of these systems was based primarily on average life to failure in burner rig testing. However, there were a few systems which exhibited relatively high performance but were not selected due to processing difficulties. The first of these systems was the EB-PVD applied 20% YSZ. As explained in a previous section, considerable difficulty is encountered in achieving the desirable Figure 16a microstructure on complex geometry turbine hardware, so that engine evaluation of the EB-PVD coating was not considered feasible. While the 20% YSZ ceramic sprayed from a 2.5 cm (1 inch) gun distance exhibited an average number of cycles to failure which was nearly equivalent to that of the same ceramic sprayed from the 7.6 cm (3 inch) gun distance, this system was not selected based on previously discussed concerns about the production suitability of a process requiring such precise control of process parameters.

The other specimens which exhibited good performance were those coated while maintaining substrate temperatures of 21 and 316°C (70 and 600°F). These systems were not selected for the initial engine test because equipment required to maintain this low substrate temperature while spraying engine components was not available at the time the first engine set of vanes was sprayed. As described in a subsequent section, this technique was used on components tested in the final engine test.

5.1.4.2 Analysis of Residual Stress Effects

To provide additional understanding of the residual stress effects observed on bars coated with controlled substrate temperatures, thermal and stress analyses were conducted to model thermal barrier coating response to substrate temperature control. These analyses are described in the following paragraphs.

5.1.4.2.1 One-Dimensional Thermal Model

The thermal calculation was generated by considering the one-dimensional thermal conduction through the thickness of a flat slab. During application of the ceramic and the bond layer, the outer surface is growing, and the effects of the moving boundary must be taken into account. The analytical method adopted is analogous to the finite element method. The slab was divided into a number of layers, or elements through the thickness, with each of the elements having an assumed linear temperature distribution between the end points or nodes. The degrees of freedom were taken to be the temperatures at each of the nodes, and the appropriate function was minimized. The growing surface element outside nodal position was assumed to be a linear function of time. This motion enters directly into the minimization. The transient integration was done by employing a backward difference in time, which is an implicit integration scheme and therefore stable for all time steps. The resulting matrix is tridiagonal, but not symmetric, and was solved by factoring into upper and lower triangular matrices.

The analysis employing the one dimensional calculation was applied to sample cases. Each sample case gave results that were within a few percent of known solutions. Appendix C summarizes the analytical derivation for the thermal response of a slab with a growing thickness.

5.1.4.2.2 One-Dimensional Thermal Analysis and Results

The thermal analysis consisted of the following steps:

1. Identification of the outer surface heat transfer coefficients and environmental temperature best approximating the recorded thermal response of the outer surface of the substrate during application of the ceramic (or bond) coating without substrate temperature control.

2. Prediction of the specimen thermal history during coating application with various substrate control temperatures.

3. Identification of outer surface heat transfer coefficients and environmental temperature best approximating the recorded thermal response of the outer surface of the substrate during a typical burner rig cycle.

4. Prediction of the specimen thermal history during a typical burner rig cycle simulating engine operation.

The material properties used were obtained from Ref. 10 and were assumed to vary linearly with temperature. Figure 40 summarizes the boundary conditions assumed for the analysis.

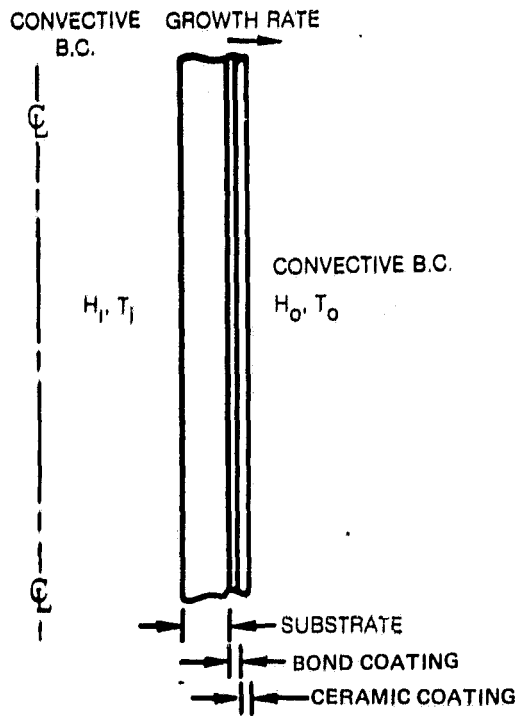

CASE	CONDITIONS
NO CONTROL APPLICATION (SOLID ROD)	$H_i = 0$, H_o AND T_o ADJUSTED TO MATCH EXPERIMENTAL CURVE AT SUBSTRATE-BOND INTERFACE (INSIDE RADIUS = 0). CERAMIC GROWS AT CONSTANT GROWTH RATE
CONTROL APPLICATION (HOLLOW ROD)	$H_i = \infty$, T_i = CONTROL TEMP., H_o AND T_o SAME AS NO CONTROL CASE. CERAMIC GROWS AT CONSTANT GROWTH RATE (INSIDE RADIUS 0.085 in)
OPERATION	$H_i = 0$, H_o AND T_o GIVEN AND MATCHED TO EXPERIMENTAL RESULTS. NO CERAMIC GROWTH.

Figure 40 Boundary Conditions for Thermal Analysis.

Calibration of the thermal analysis was achieved by utilizing thermal data recorded during application. In Figures 41 and 42 the numerical fit to the recorded data during bond and ceramic coating application is shown. Once the heat transfer coefficient and environmental temperature were determined from a fit to the data, the thermal history for the substrate temperature control cases was evaluated and the outer surface temperature history for the bond and ceramic layers was calculated. These predicted temperature distributions were then used to obtain an approximation for the thermal strain free temperature of each layer which was taken to be equal to the temperature of the layer when it was deposited.

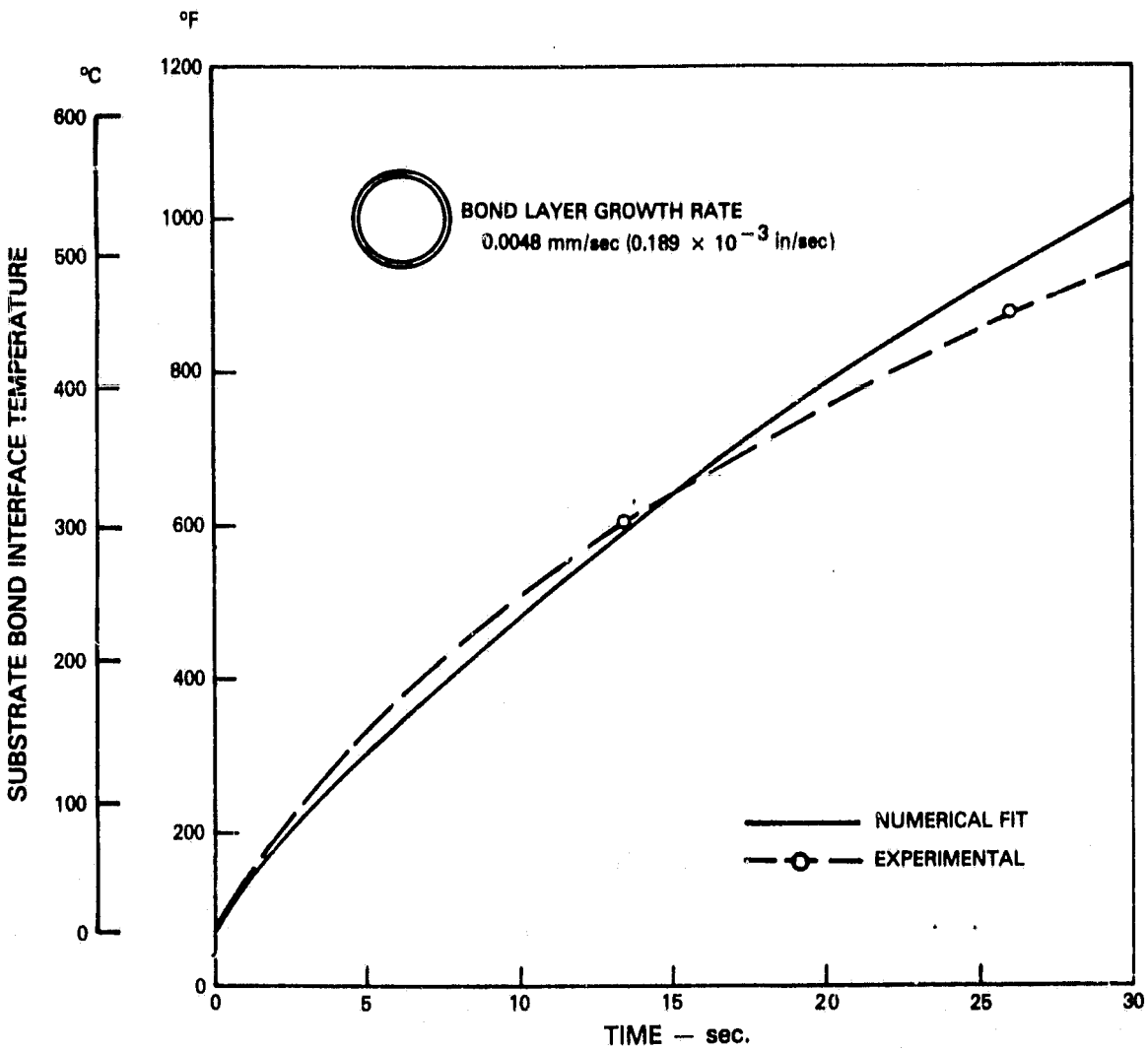

Figure 41 Bond Application Calibration.

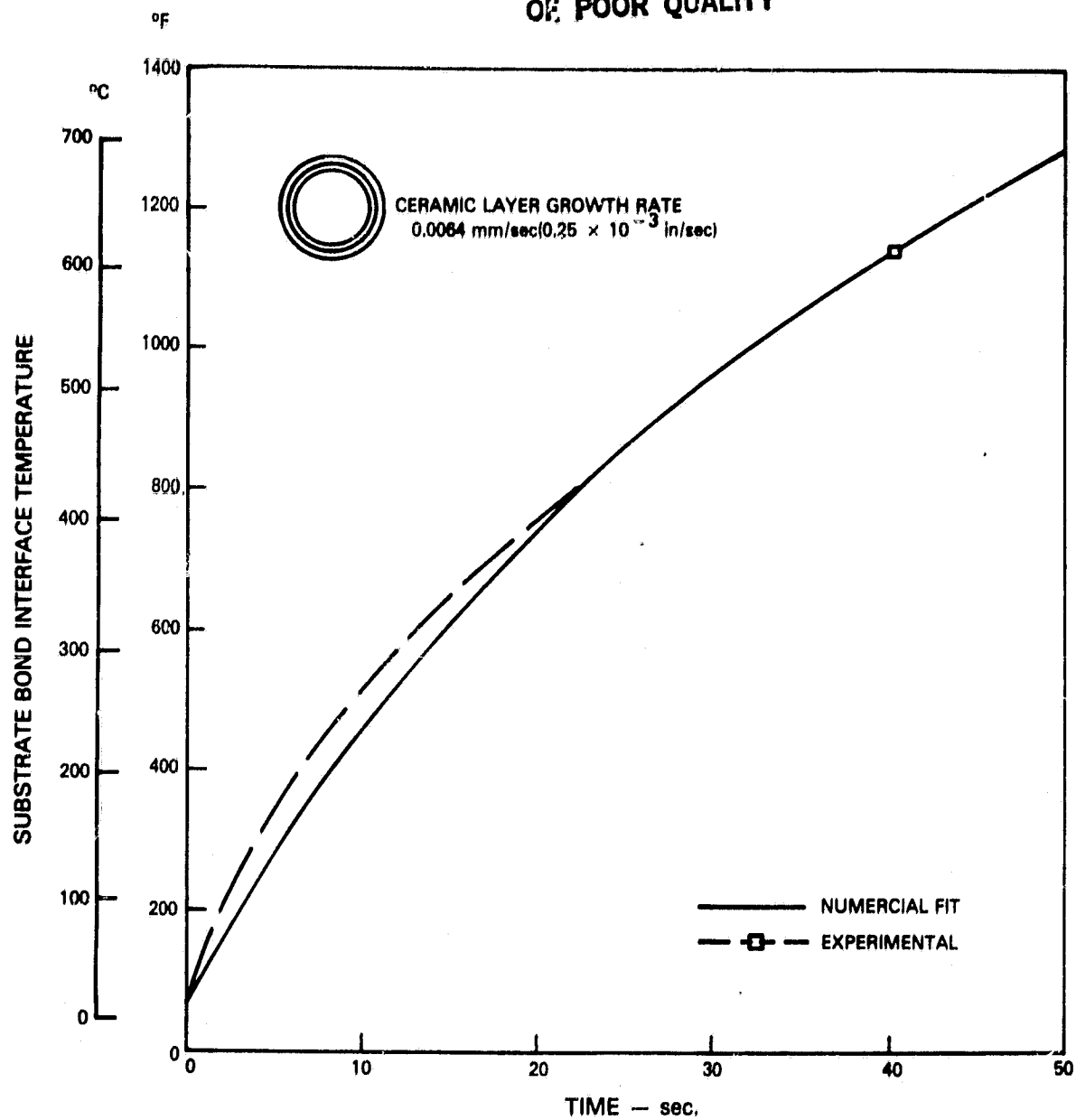

Figure 42 Ceramic Application Calibration.

The thermal history during burner rig testing was evaluated in a manner similar to the analysis for the application process. The boundary conditions were assumed to be convective on the outside surface and insulated on the inside surface. This is a reasonable assumption because of the low convective heat transfer coefficients on the inside surface. The two outside surface convection constants, the heat transfer coefficient and environmental temperature were then determined by numerically simulating the steady cyclic response during burner rig testing. Figure 43 illustrates the predicted cyclic temperature variation at the outside surface while Figure 44 compares a typical numerically predicted cycle with experimental measurements.

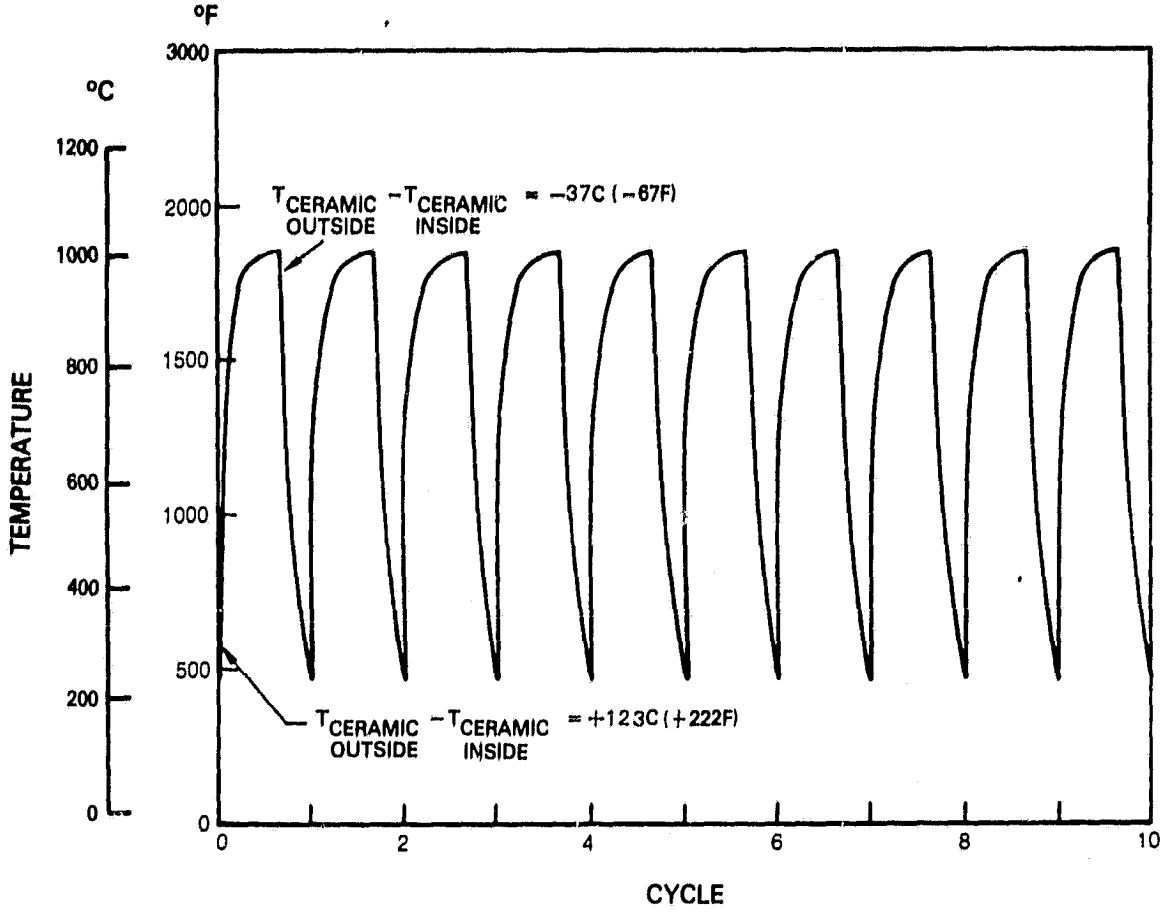

Figure 43 Cyclic Thermal History at Ceramic Outside Surface.

The maximum temperature difference through the ceramic during heating and cooling was determined to be 123°C (222°F) and 37°C (67°F), respectively. This difference will contribute to the thermal loading. The difference is sensitive to the heat transfer coefficient assumed, but it never exceeded 167°C (300°F) for any of the analyzed conditions. The 167°C (300°F) difference was used for a conservative estimate of the stresses in the two dimensional analyses.

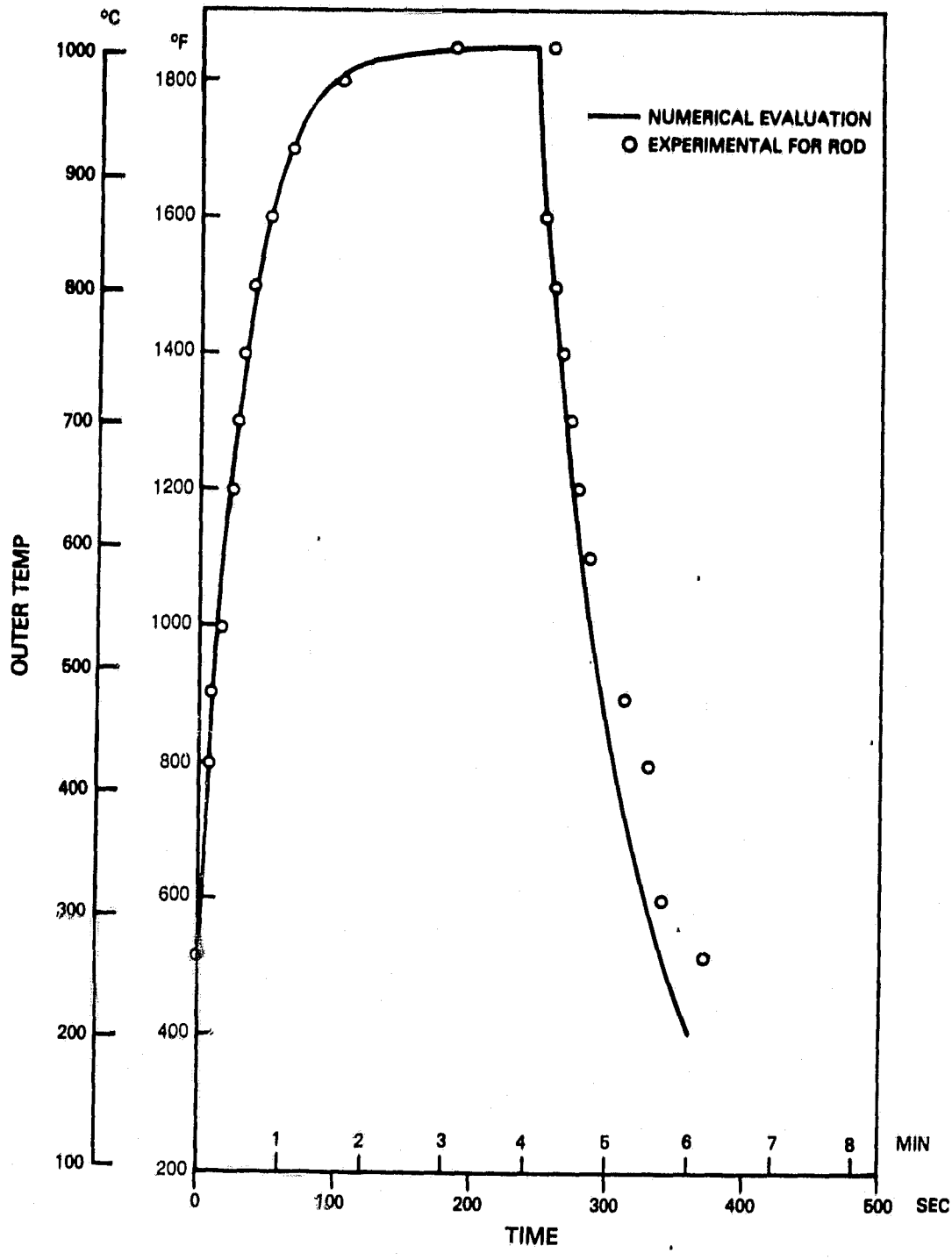

Figure 44 Typical Thermal Cycle at Ceramic Outside Surface.

5.1.4.2.3 One-Dimensional Stress Model

The stress calculation was performed by considering the one-dimensional, radial, through thickness stresses in a solid and hollow cylinder. The cylinder was assumed to be free at the axial ends and was divided into a number of concentric layers. The elasticity equations were applied in each layer, with the normal axial strain assumed constant and equal in each layer. The boundary conditions were taken to be: (1) the outside and inside surface free of normal radial stress, and (2) at the contacting surfaces both the normal radial stress and the normal circumferential strain are continuous. The application of the boundary conditions resulted in two equations with two unknown constants for each layer in the cylinder. The equations were solved simultaneously in each layer for the constants, and the stresses and strains were calculated. Each of the layers was assumed to have a constant thermal strain-free temperature with a varying thermal loading. The coordinate system used for the above rod analysis is shown in Figure 45a. For comparison purposes, analytical expressions for the through thickness response of circular disks also were derived. The coordinate system used in the disk analysis is shown in Figure 45b. Although not shown here, the analytical results indicated the simpler disk model should adequately describe the thermomechanical response of thermal barrier coatings on cylindrical specimens. The complete derivation for the stress analysis is presented in Appendix D.

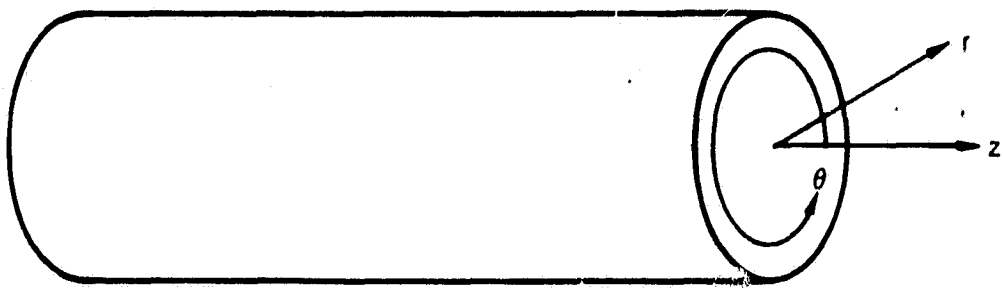

A CYLINDRICAL ROD COORDINATE SYSTEM WITH LAYERS ALONG CONSTANT r

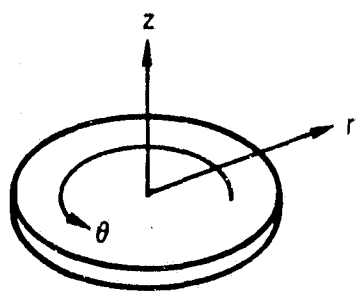

B CYLINDRICAL DISK COORDINATE SYSTEM WITH LAYERS ALONG CONSTANT Z

Figure 45 Coordinate Systems Employed in Stress Analysis.

5.1.4.2.4 One-Dimensional Stress Analysis and Results

The thermal loadings and thermal strain-free temperatures were obtained from the thermal analysis previously described. Six thermal loads were considered:

(1) Uniform 21°C (70°F) in ceramic, bond and substrate,

(2) Uniform 21°C (70°F) in bond and substrate with a rising 122°C (220°F) linear variation in the ceramic,

(3) 58°C (137°F) in bond and substrate with a decreasing 37°C (67°F) linear variation in the ceramic,

(4) Uniform 1010°C (1850°F) in ceramic, bond and substrate

(5) Uniform 888°C (1630°F) in bond and substrate with rising 122°C (220°F) linear variation in the ceramic, and

(6) Uniform 1010°C (1850°F) in bond and substrate with a decreasing 37°C (67°F) linear variation in the ceramic.

Cylinders were investigated which typically had a 0.30 mm (0.012 inch) ceramic coating thickness and 0.13 mm (0.005 inch) bond layer thickness on a substrate with an outside radius of 0.64 cm (0.250 inch).

Cylinders with temperature control where the substrate temperature was held at one of four values, -40°C (-40°F), 21°C (70°F), 316°C (600°F) and 649°C (1200°F) had an inside radius of 2.16 mm (0.085 inch) Rods without temperature control were solid. Any changes from the typical geometry are noted.

The measure of the ceramic strength was taken to be the maximum normal mechanical strain or fracture strain of a similar ceramic (Ref. 10). The fracture strain was taken to be 0.0017 mm/mm (in./in.) at 21°C (70°F) and 0.0025 mm/mm (in./in.) at 1010°C (1850°F) with the variation in this range approximately linear. The mechanical strain is defined as the total strain minus the thermal strain.

Tables VI and VII summarize the predicted ceramic mechanical strains for the typical geometry, for cases when the thermal strain-free temperature of the bond is equal to the thermal strain-free temperature of the substrate. Table VI is for the ceramic/bond coating interface while Table VII is at the outside surface of the ceramic coating. Comparison of the radial strain values with the fracture strain values shows that the -40°C (-40°F), 21°C (70°F) and 316°C (600°F) control temperature cases should not fail by spalling. Spalling is characterized by positive radial mechanical strains (ϵ_r) greater than the fracture strain. However, the 649°C (1200°F) case will form cracks at room

temperature that propagate along a surface of constant radius, and will appear as spalling. This result is in agreement with previously discussed experimental observations. The case without temperature control should form cracks propagating along planes of constant angle (θ) or planes of constant axial position (z), characterized by positive circumferential and axial mechanical strains greater than the fracture strain, and would appear as radial columns (segmentation cracks). Experimental observations have indicated that segmentation cracks generally appear at room temperature for the non-control, -40°C (-40°F control), 21°C (70°F control), and the 316°C (600°F) control conditions. Tables VI and VII also indicate that under operating conditions, the 316°C (600°F) control temperature case should have the best response (lowest mechanical strains). The outer surface mechanical strains were calculated to increase with substrate radius but the increase was relatively small over the values of interest. An increase in ceramic thickness by a factor of two will cause an increase in strain by a factor of 1.34. The inner surface mechanical strains, however, show no significant change when either the ceramic thickness or rod diameter is varied. Figures 46, 47 and 48 present the predicted normal circumferential and radial mechanical strains as a function of radius for three temperature control cases. The normal axial mechanical strain is not shown because it is approximately equal to the normal circumferential mechanical strain. It is interesting to note that the variation through the thickness is approximately linear for each of the cases considered.

It should be noted that the results presented in Tables VI and VII and Figures 46 through 48 are limited by the assumption that no segmentation cracking is present, and all interpretations should include this limitation.

In general, the results predicted from the one-dimensional stress analysis are in good agreement with observed behavior of experimental specimens. Specifically, the analysis predicted the observed failure of the ceramic coating at sufficiently severe thermal loadings and at room temperature when the substrate was allowed to reach high temperature during application of the coating.

TABLE VI

CERAMIC/BOND COATING INTERFACE MECHANICAL STRAINS X 10^3

1D Results
Figure 45a Coordinate System

Control Temp	Strain	Thermal Loading: No Gradient, Room Temp	No Gradient, Oper Temp	Up Gradient, Room Temp	Up Gradient, Oper Temp	Down Gradient, Room Temp	Down Gradient, Oper Temp
None	ϵ_r	-0.59	-4.76	-0.57	-4.14	-0.78	-4.80
	ϵ_θ	0.50	5.15	0.50	4.49	0.71	5.16
	ϵ_z	0.42	5.00	0.44	4.37	0.62	5.00
-40°C (-40°F)	ϵ_r	-0.27	-4.44	-0.25	-3.81	-0.46	-4.46
	ϵ_θ	0.28	4.93	0.28	4.27	0.49	4.94
	ϵ_z	0.27	4.83	0.28	4.21	0.47	4.83
21°C (70°F)	ϵ_r	-0.08	-4.25	-0.07	-3.63	-0.28	-4.27
	ϵ_θ	0.08	4.72	0.08	4.07	0.29	4.73
	ϵ_z	0.07	4.64	0.08	4.01	0.27	4.63
316°C (600°F)	ϵ_r	1.08	-3.09	1.08	-2.48	0.89	-3.11
	ϵ_θ	-1.22	3.42	-1.21	2.78	-1.01	3.43
	ϵ_z	-1.20	3.63	-1.19	2.74	-1.00	3.36
649°C (1200°F)	ϵ_r	2.49	-1.68	2.49	-1.08	2.31	-1.69
	ϵ_θ	-2.79	1.86	-2.78	1.22	-2.58	1.86
	ϵ_z	-2.74	1.82	-2.72	1.21	-2.55	1.82

Room Temp	21°C (70°F)	Up Gradient	122°C (220°F)	Substrate Radius	6.4 mm (0.250 inch)
Oper Temp	1010°C (1850°F)	Down Gradient	37°C (67°F)	Ceramic Thickness	0.30 mm (0.012 inch)

TABLE VII

CERAMIC OUTSIDE SURFACE MECHANICAL STRAINS X 10^3

1D Results
Figure 45a Coordinate System

Control Temp	Strain	Thermal Loading: No Gradient, Room Temp	No Gradient, Oper Temp	Up Gradient, Room Temp	Up Gradient, Oper Temp	Down Gradient, Room Temp	Down Gradient, Oper Temp
None	ϵ_r	-5.90	-9.69	-5.25	-7.86	-6.32	-10.23
	ϵ_θ	6.75	11.02	6.23	9.24	7.14	11.51
	ϵ_z	7.02	11.59	6.02	9.10	7.61	12.36
-40°C (-40°F)	ϵ_r	-0.80	-4.58	-0.13	-2.73	-1.23	- 5.14
	ϵ_θ	0.92	5.17	0.33	3.33	1.34	5.70
	ϵ_z	0.96	5.52	-0.03	3.04	1.55	6.29
21°C (70°F)	ϵ_r	-0.61	-4.39	0.07	-2.54	-1.04	- 4.94
	ϵ_θ	0.69	4.95	0.11	3.12	1.11	5.47
	ϵ_z	0.72	5.28	-0.27	2.80	1.31	6.05
316°C (600°F)	ϵ_r	0.46	-3.33	1.11	-1.49	0.03	- 3.87
	ϵ_θ	-0.50	3.76	-1.04	1.97	-0.11	4.26
	ϵ_z	-0.56	4.01	-1.55	1.52	0.03	4.78
649°C (1200°F)	ϵ_r	1.88	-1.90	2.52	-0.09	1.47	- 2.44
	ϵ_θ	-2.11	2.15	-2.59	0.41	-1.74	2.62
	ϵ_z	-2.28	2.29	-3.28	-0.21	-1.68	3.06

Room Temp	21°C (70°F)	Up Gradient	122°C (220°F)	Substrate Radius	6.4 mm (0.250 inch)
Oper Temp	1010°C (1850°F)	Down Gradient	37°C (67°F)	Ceramic Thickness	0.30 mm (0.012 inch)

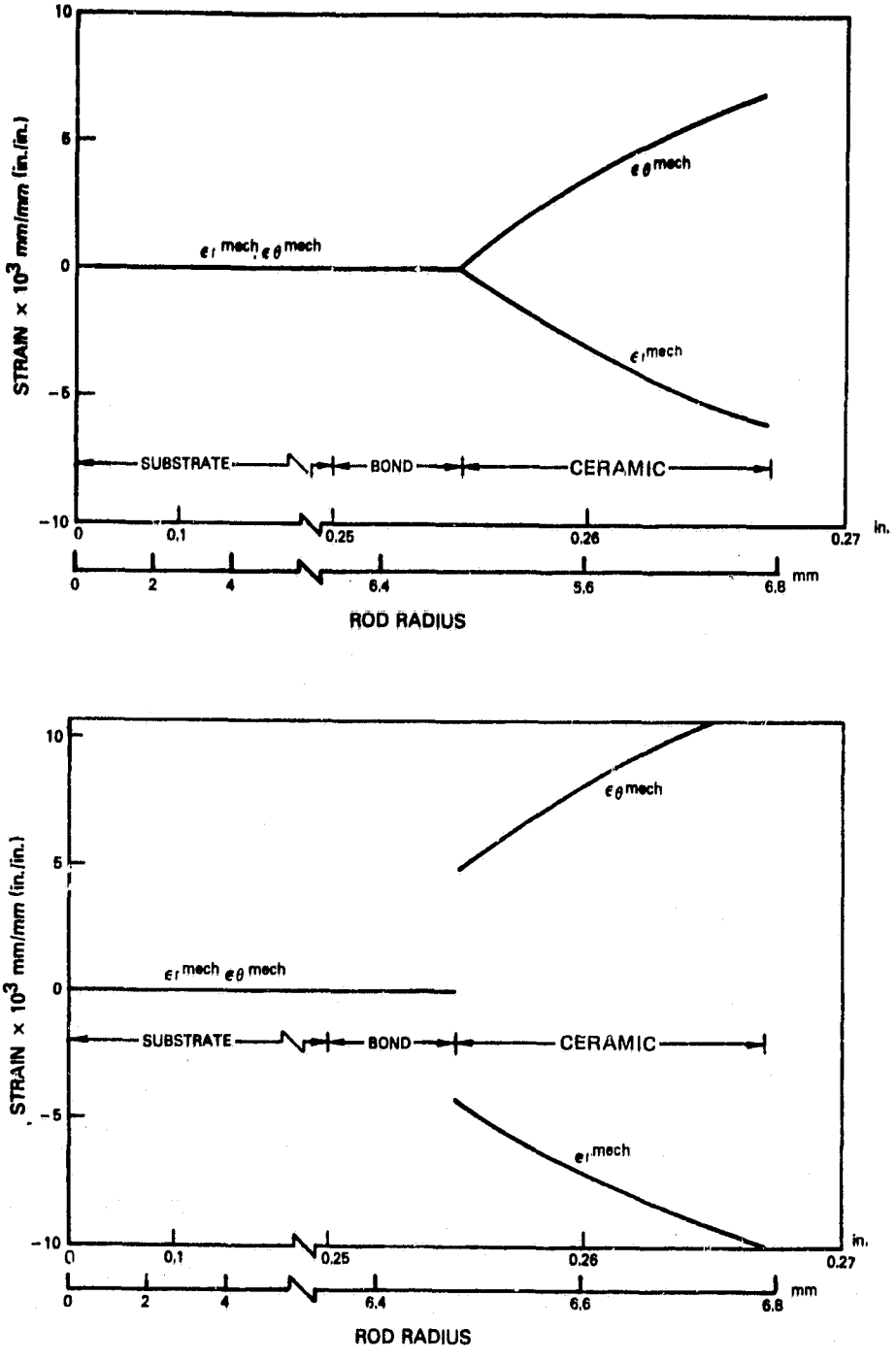

Figure 46 Mechanical Strains at 21°C (70°F) (Top) and 1010°C (1850°F) (Bottom) for No Temperature Control.

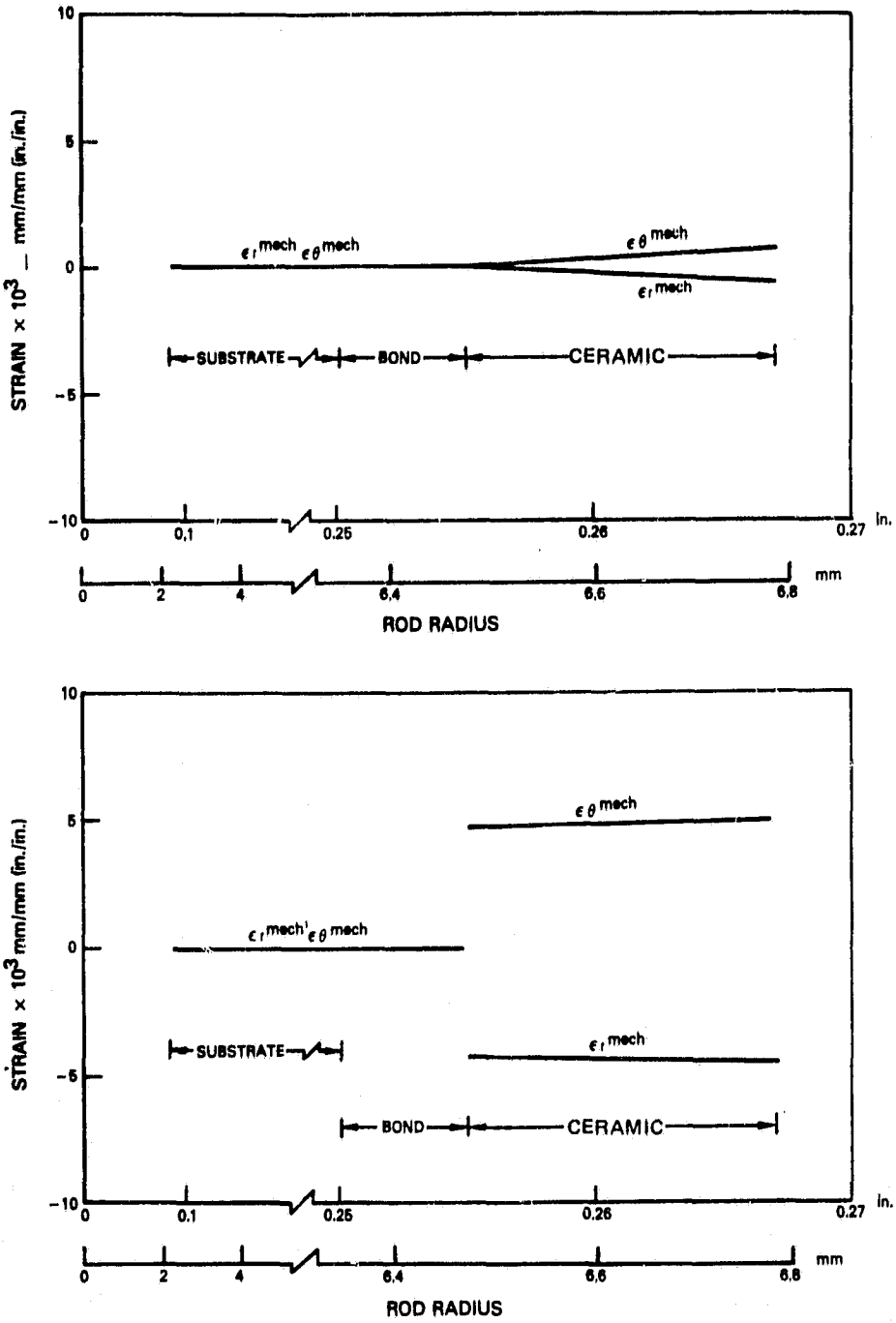

Figure 47 Mechanical Strains at 21°C (70°F) (Top) and 1010°C (1850°F) (Bottom) for 21°C (70°F) Control Temperature.

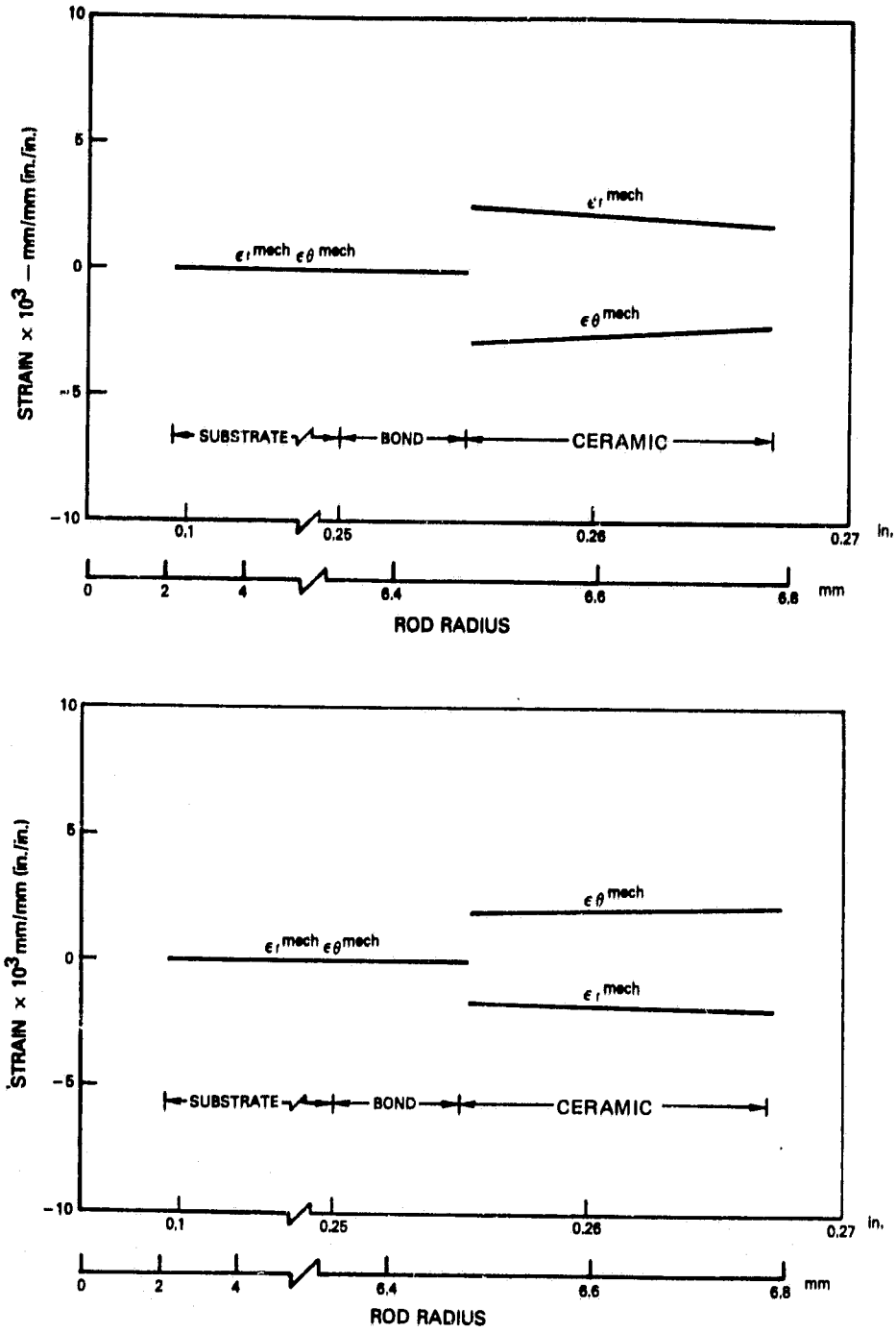

Figure 48 Mechanical Strains at 21°C (70°F) (Top) and 1010°C (1850°F) (Bottom) for 649°C (1200°F) Control Temperature.

5.1.4.3 Monotonic Strain Tolerance Tests

Monotonic strain tolerance testing was performed on plasma and EB-PVD deposited 20% YSZ using standard uniaxial tension and compression testing methods to observe the performance of the strain relief mechanisms for each coating. Results of these tests are listed in Table VIII. The results indicate that the ceramic coatings can tolerate some plastic deformation of the underlying metal and that this strain tolerance increased with increasing temperature. Another trend in the test results was the fact that the thinner (nominal 0.012 cm (0.005 inch) ceramic) coating exhibited higher strain tolerance than the thicker (nominal 0.025 cm (0.010 inch) ceramic) coatings. This was true in both the tensile and compressive modes.

TABLE VIII

STRAIN TOLERANCE TEST RESULTS

Method of Coating Application	Strain Mode	Ceramic Layer Thickness mm (mils)	Test Temperature °C (°F)	Strain to Spall Initiation, %
Plasma Spray	Tensile	0.13 (5)	RT[1]	1.1[2]
			316 (600)	1.0
			649 (1200)	7.2
			982 (1800)	4.5
		0.25 (10)	RT	1.6[2]
			982 (1800)	3.0
	Compressive	0.13 (5)	RT	1.4
			316 (600)	5.2
			649 (1200)	2.0
			982 (1800)	3.3
		0.25 (10)	RT	1.0
			982 (1800)	2.5
EB-PVD	Tensile	0.13 (5)	RT	1.5[2]
			316 (600)	-
			649 (1200)	6.1[2]
			982 (1800)	17.6[2]
		0.25 (10)	RT	1.3[2]
			982 (1800)	12.2
	Compressive	0.13 (5)	RT	1.8
			316 (600)	2.0
			649 (1200)	4.8
			982 (1800)	15.0
		0.25 (10)	RT	1.8
			982 (1800)	11.2

1; RT = room temperature
2; MAR-M 509 substrate failure occurred prior to any spall initiation

5.1.4.4 Initial Engine Testing

Vanes coated with the three selected coating systems (Section 5.1.4.1.4) were tested in a JT9D-7Q engine to determine their durability under actual operating conditions. A Post- Certification Accelerated Cyclic Endurance Running (PACER) test cycle was used. The PACER cycle simulates long term airline operation in a reduced period of time by operating at thrusts and temperatures above maximum airline experience. The test procedure is described in greater detail in Section 1.0 of Appendix A.

All coating systems tested showed promise for satisfying JT9D vane platform coating requirements in service, even though results show that some coating systems were more prone to spalling. Spalling was minimal on the inside diameter platform for all coating systems. Thermal barrier coated vane platforms reduced the severity and frequency of platform cracking compared to B/M vanes. Cracks on thermal barrier coated platforms tended to be more severe in regions where spalling occurred, suggesting that the thermal barrier coating inhibited thermal fatigue cracks. Photographs comparing the appearance of an uncracked thermal barrier coated platform with a cracked platform which had only metallic coating are shown in Figure 49.

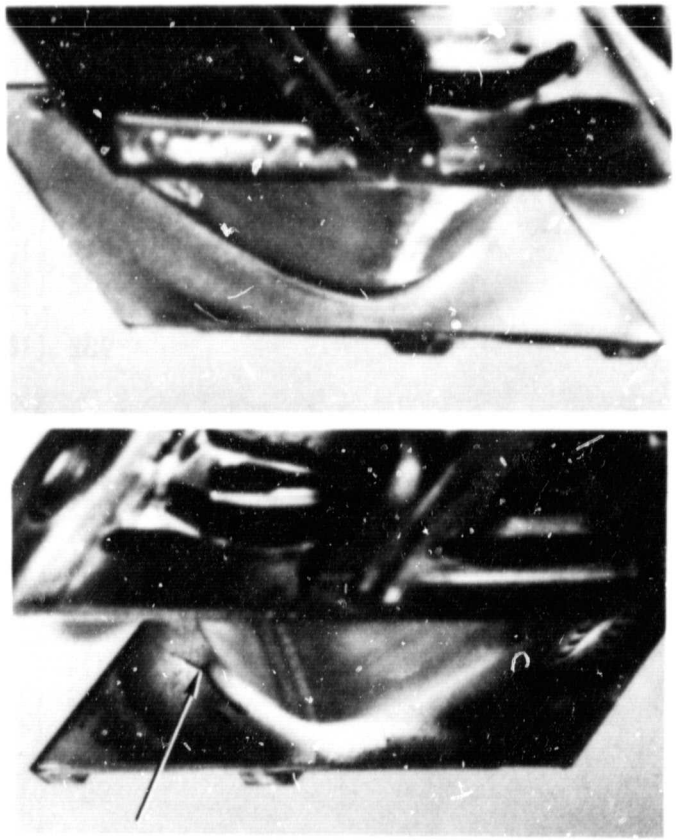

Figure 49 Photographs of Vanes From First Engine Test Comparing Uncracked Thermal Barrier Coated Platform (Top) With Cracked (Arrow) Uncoated Bill-of- Material Platform (Bottom).

The distribution of spalling for each coating system is shown in Table IX. No spalling was observed for the 6% YSZ coating system on either platform. The high spalling incidence observed for the 21% MSZ ceramic coating was at first believed to have occurred because most of the vanes with this coating system were located within a hot spot. The locations of the hot spots were determined using post engine test temperature estimates made from vane leading edge conditions. However, subsequent laboratory results showed that chemical and phase instabilities occur in this coating system at higher temperatures, as discussed in the following section. This is now felt to be responsible for the increased incidence of spalling in the 21% MSZ system.

TABLE IX

INITIAL ENGINE TEST RESULTS

System	Number of Vanes	Number of Vanes Exhibiting Significant Spalling	
		O.D.	I.D.
6% YSZ	5	0	0
20% YSZ	6	2	1
21% MSZ	7	5	1

Ceramic coating thickness profiles indicated considerable variation compared to the nominal 0.025 to 0.038 cm (0.010 to 0.015 inch) thickness specified prior to coating application. Typical variations of coating thickness are shown in Figure 50. This variation is believed related to the imprecision of the manually controlled plasma spray process used for application of the ceramic coatings.

Metallographic evaluation of the thermal barrier coated platform areas of several of the vanes was conducted after 1033 cycles of endurance engine exposure.

Typical microstructures of the NiCoCrAlY/6% YSZ coating showed 10 to 15% porosity in the ceramic layer (Figure 51) with limited evidence of through thickness segmentation cracking as shown in Figure 52. Vane platform ceramic segmentation cracking was clearly less extensive than observed for 6% YSZ ceramic coated laboratory specimens in the Process Refinement evaluation conducted prior to engine test. While this was apparently caused by effects related to the different geometries between the laboratory test bars and the turbine vanes, the exact reasons are not clear.

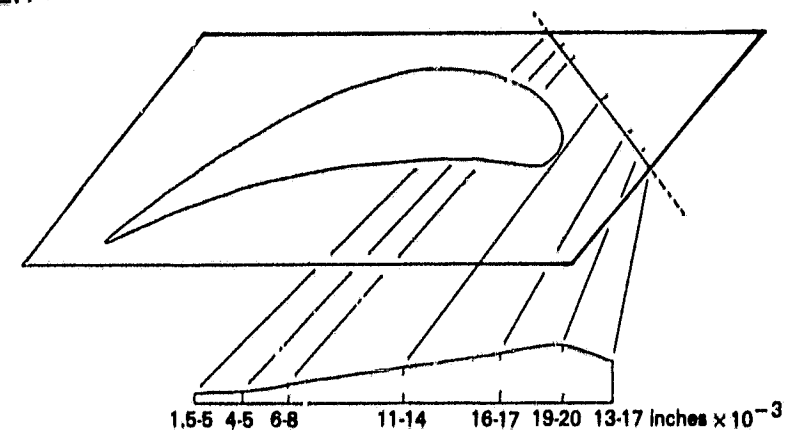

VANE POSITION NO. 16

6 w/o Y_2O_3-ZrO_2

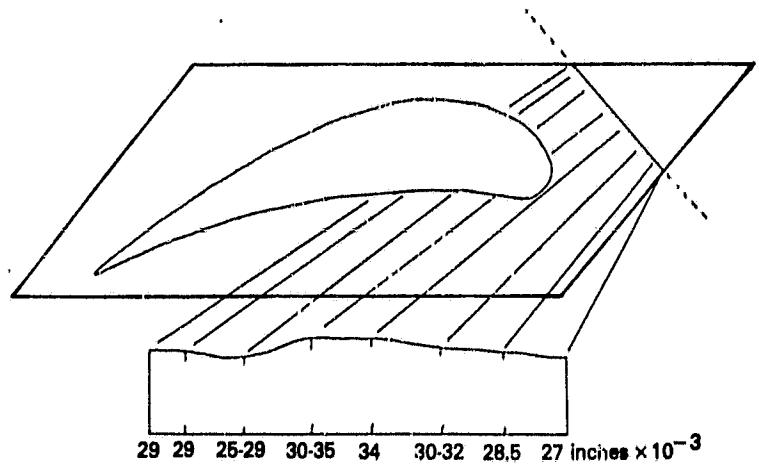

VANE POSITION NO.9

20 w/o Y_2O_3-ZrO_2

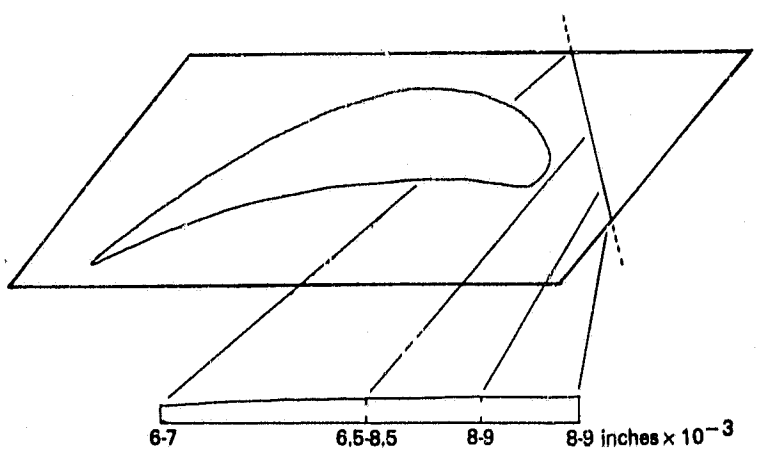

VANE POSITION NO. 19

21 w/o MgO-ZrO_2

Figure 50 Typical Coating Thickness Variations Observed on ID Leading Edge of Vanes Coated With Three Candidate Ceramic Compositions.

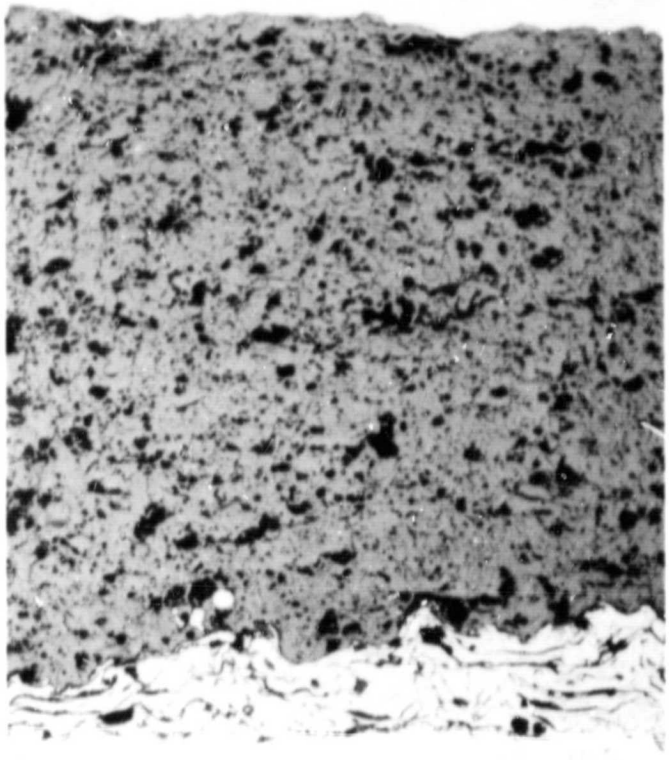

150X

Figure 51 Typical 6 w/o Y_2O_3 Stabilized ZrO_2 As Observed on the OD Platform.

Scanning electron microscopy of the NiCoCrAlY/6% YSZ coating showed no evidence of the formation of in-plane cracks (cracks oriented in the plane of the coating) which would lead to spalling. Extensive randomly oriented microcracking was observed in scanning electron micrographs of this ceramic (Figure 53 bottom). NiCoCrAlY metallic layer oxidation was observed to be minimal after engine exposure.

Examination of the 20% YSZ coating showed in-plane cracking within the ceramic layer. This increased amount of in-plane cracking in the 20% YSZ as compared to the 6% YSZ is consistent with the higher level of spalling observed on vanes coated with 20% YSZ. The most severe cracking occurred near the metal-ceramic interface, Figure 54, where spalling typically has been observed to originate in laboratory cyclic thermal tests. The porosity in the 20% YSZ coatings was typically 15-20% although the distribution of the porosity tended to be non-uniform as shown in Figure 54.

The 21% MSZ ceramic coating was observed to contain excessive internal ceramic microcracking as a result of progressive formulation of the monoclinic phase during engine test (Figure 55). This phenomenon may be seen more clearly during examination by scanning electron microscopy as shown in Figure 56. Reversion of cubic zirconia to the monoclinic phase is related to the metastable character of MgO-ZrO_2 ceramics under severe thermal exposure conditions.

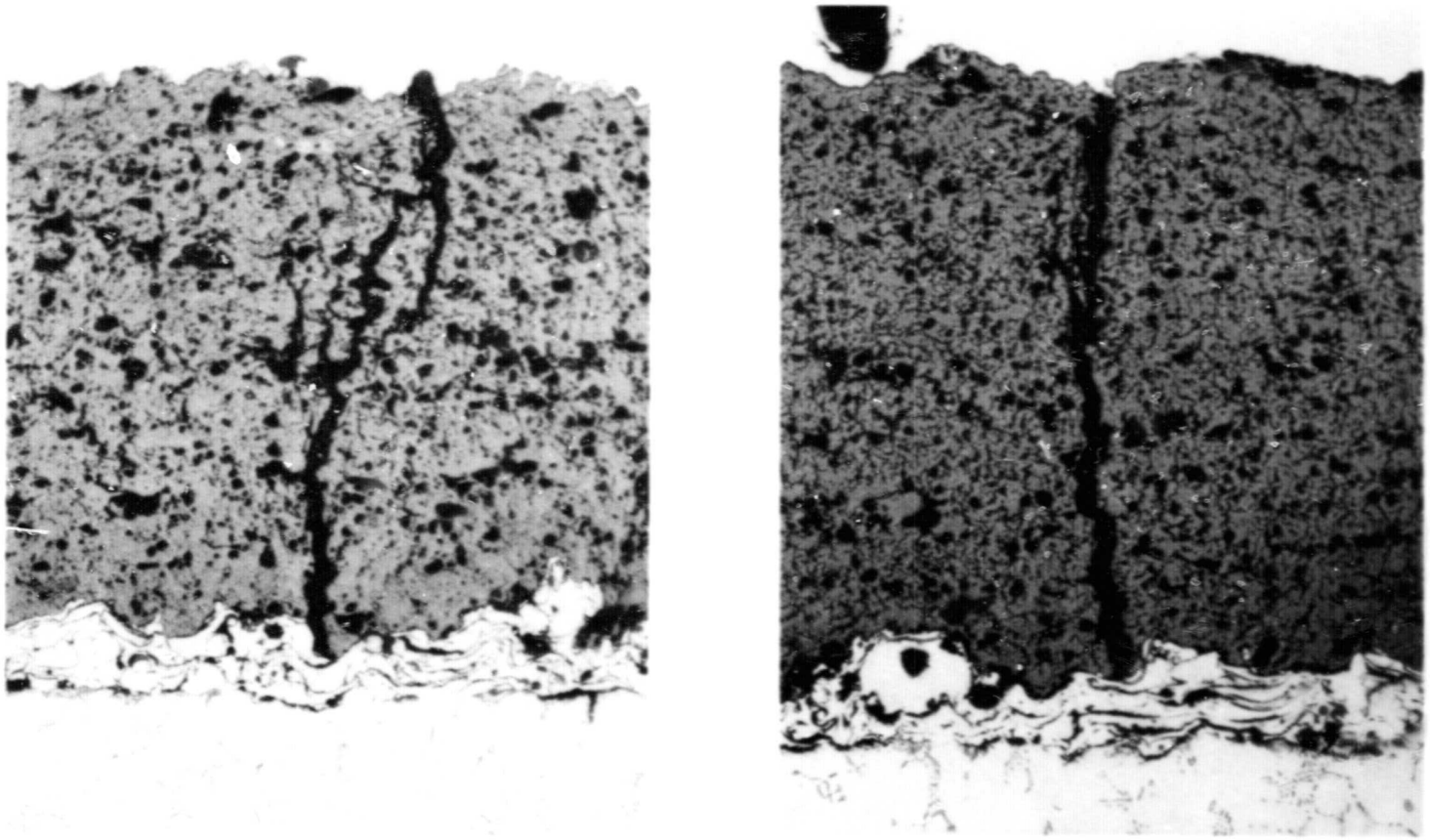

Figure 52 Segmentation Cracks through Ceramic Coating which Existed to a Limited Extent on 6 w/o YSZ Coated Vane Platforms.

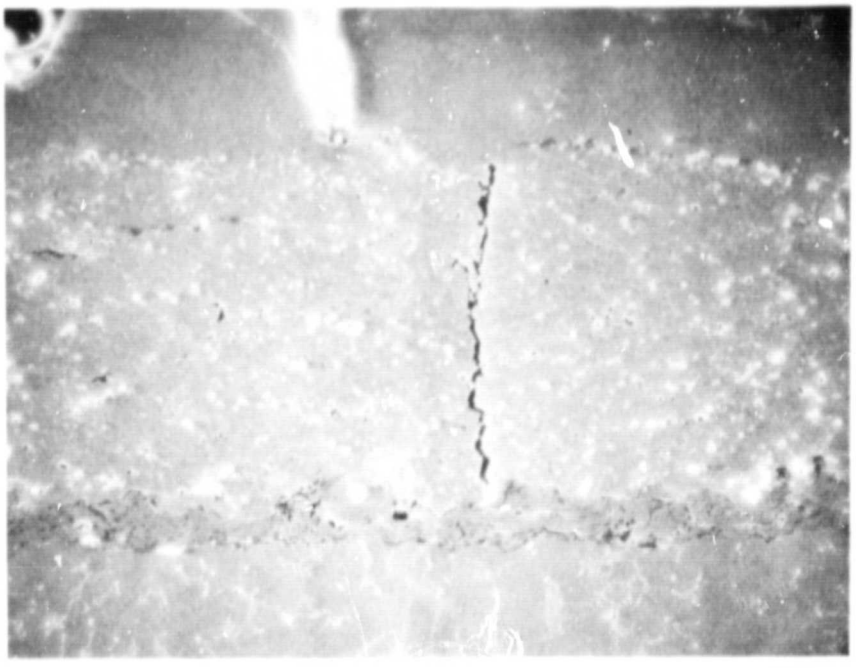

200X

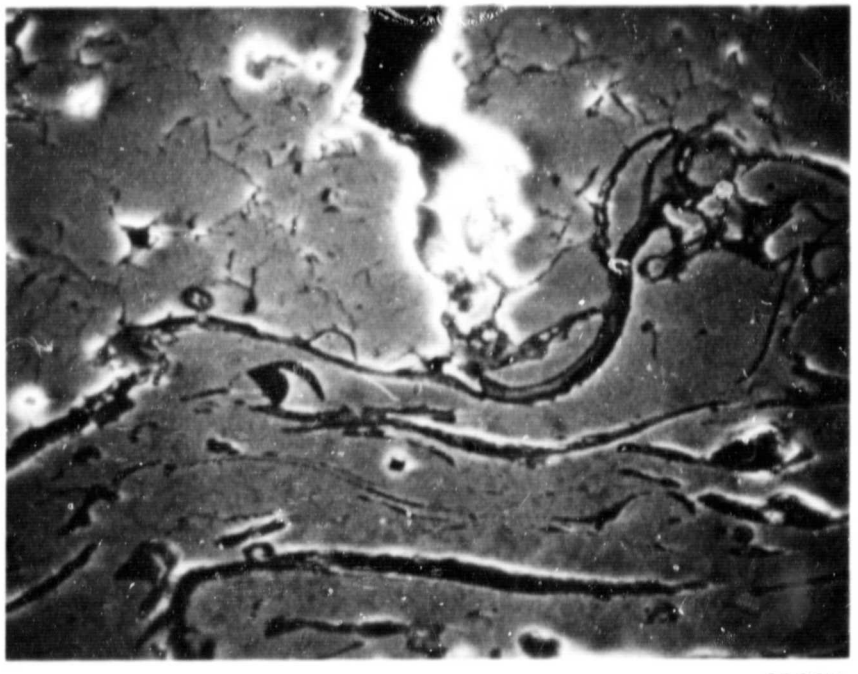

1000X

Figure 53 Scanning Electron Micrographs of Typical Vertical Crack Showing Absence of Lateral Cracks at Interface between 5% YSZ Ceramic Coating and Metallic Bond Coat. Lower photomicrograph is a higher magnification view of the root of the crack shown in the low-magnification (upper) photomicrograph.

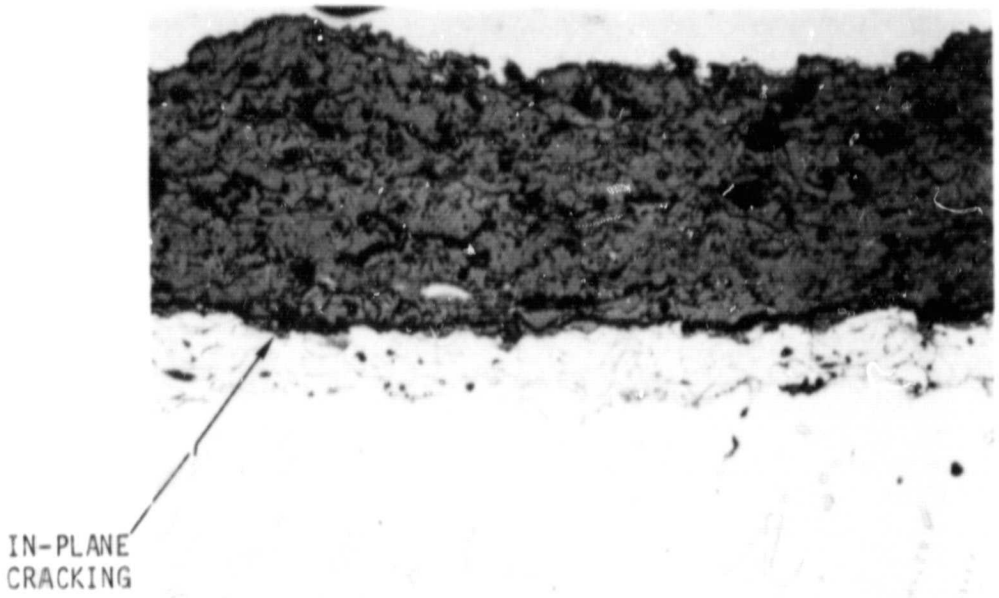

150X

Figure 54 Typical 20 w/o Y_2O_3 Stabilized ZrO_2 Microstructure Observed on First Engine Test Vane. Arrow indicates in-plane cracking.

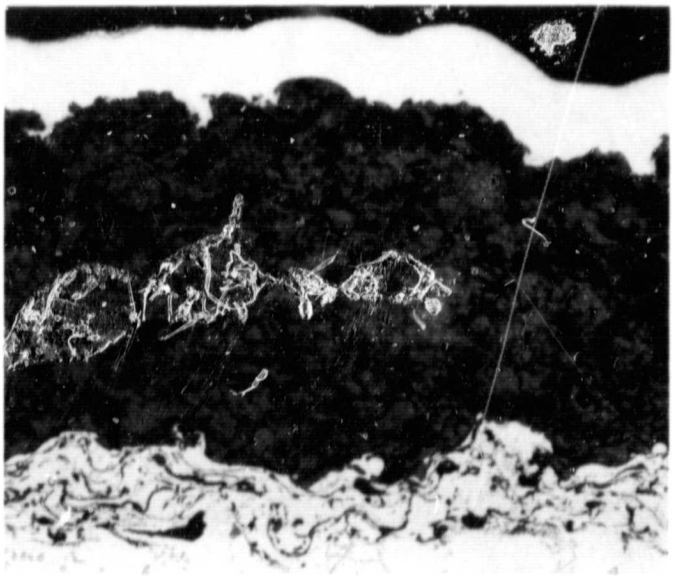

150X

Figure 55 Loosely Bonded 21 w/o MgO Stabilized ZrO_2 Ceramic Structure Resulting from Progressive Monoclinic Phase Transformation During Cyclic Engine Exposure.

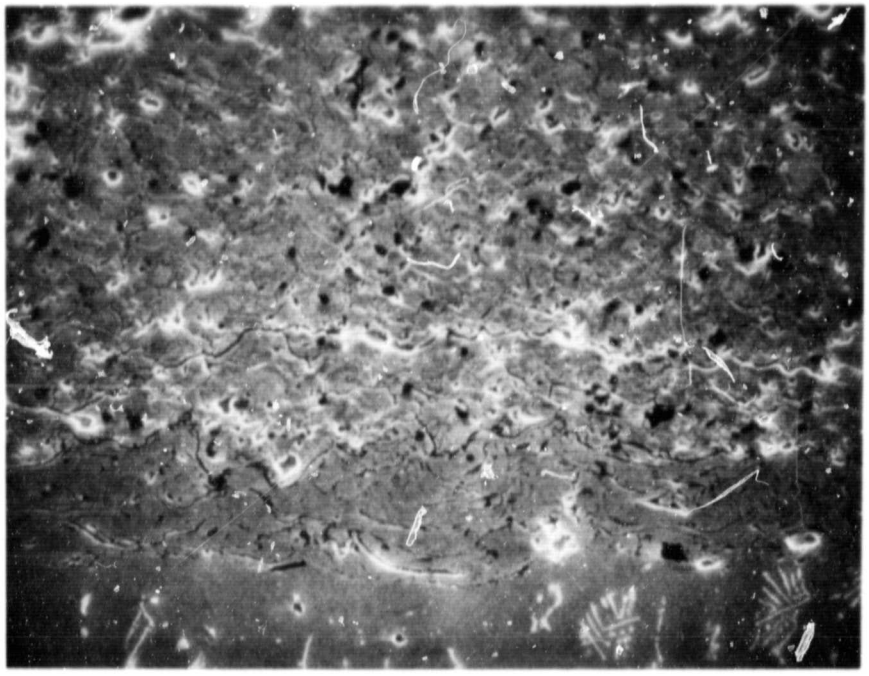

200X

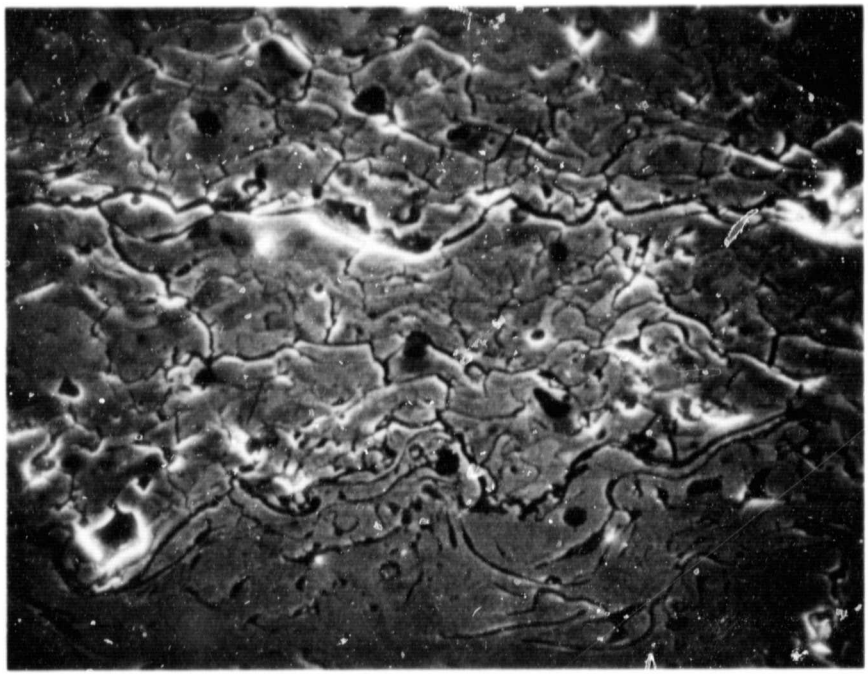

500X

Figure 56 Scanning Electron Micrographs of 21 w/o MgO Stabilized ZrO_2 Coating Showing Extensive Internal Ceramic Microcracking.

C-2

5.1.4.5 Summary of Initial Laboratory and Engine Evaluation

To summarize the laboratory coating performance observations, several ceramic coating chemistry and process variations were evaluated, with three candidates being identified for initial engine evaluation. Five zirconia based compositions were evaluated, three with various levels of Y_2O_3, one with MgO and one with CaO as additions to stabilize the cubic ZrO_2 structure. The three most promising compositions identified in burner rig testing contained 21% MgO, 20% Y_2O_3, and 6% Y_2O_3.

Plasma parameters studied included powder particle size distribution, powder feed rate, and plasma gun-to-work piece distance. In addition, techniques were developed to control the level of residual stress in plasma sprayed ceramic coatings, and post-coat laser processing was investigated as a method to control ceramic structure. Preliminary process-structure studies established base-line plasma spray conditions and indicated some significant process effects. Powder particle size was shown to have a significant effect on structure, with coarser powders producing higher levels of porosity. Powder feed rate was shown to have little effect on structure in the range of 10 to 40 gm/minute. Ceramic structure was relatively insensitive to gun-to-workpiece distance in the range of 5.1 to 19.1 cm (2 to 7.5 inches). However, at a distance of 2.5 cm (1 inch), denser ceramic structures with substantial amounts of desirable segmentation cracking were produced. These segmentation cracking geometries were accompanied by less desirable in-plane cracking, indicating the need for very precise process control to generate reproducible structures at close distances.

Burner rig testing of various structures produced by process parameter variations indicated that the porous structure produced by coarse powder was much more desirable than the dense structure produced by fine powder. The segmentation cracking produced by spraying at a close [2.5 cm (1 inch)] gun distance also provided relatively good durability, however, as noted previously, concern exists regarding the precise process control needed to reproducibly generate a durable structure at close distances. Durability of ceramics sprayed from 15.2 cm (6 inches) was relatively low; this result was attributed to a subtle change in the structure, resulting in poor bonding between ceramic particles, as compared to the structure produced at the 7.6 cm (3 inch) baseline distance. The largest effect of processing on the durability of plasma sprayed ceramic coatings was found to result from variations of the state of residual stress in the coating, which was controlled by varying the temperature of the substrate during ceramic deposition. Life differences as large as 70X were found between ceramics sprayed on substrates maintained between room temperature and 316°C (600°F) and on substrates maintained at 648°C (1200°F), with one of the higher temperature specimens failing spontaneously prior to the initiation of testing.

In addition to the plasma spray coatings noted above, a YSZ ceramic applied by electron beam vapor deposition was evaluated in the burner testing, with very promising results. This coating was not selected for engine evaluation because process technology for application to engine components is not developed.

Coatings selected for engine evaluation included a 6% YSZ, a 20% YSZ, and a 21% MSZ composition, all of which had relatively similar durability in the laboratory burner rig tests. The 20% YSZ composition was sprayed with a porous structure, comparable to that produced with coarse powder on burner rig specimens. The 21% MSZ ceramic had a heavily microcracked structure on the components, also as on laboratory specimens. In contrast to the relatively dense 6% YSZ ceramic with extensive segmentation cracking which was evaluated on burner rig specimens, the 6% YSZ coating applied to components had a porous structure with relatively little segmentation cracking. Evaluation of these three coatings after engine testing indicated significant differences of performance in contrast to the similar performance of all three coatings in laboratory tests. The 6% YSZ coating performed best and the 21% MSZ coating performed relatively poorly. It was thought that the difference of relative laboratory and engine response might be due to higher temperature exposure in the engine. Tests reported in the following discussion of process optimization were directed toward assessment of this hypothesis.

5.1.5 Process Optimization

As discussed in the last section, results of the initial engine test raised several questions concerning the relative durability of the three ceramic compositions tested. Foremost among these was the clear differentiation among the three compositions tested in the engine as compared to their relatively similar performance in the 1010°C (1850°F) burner rig tests. Temperature was thought to be the primary difference between burner rig and engine testing which might have caused the different results, with the engine running hotter than the rigs. One objective of the process optimization effort thus was to evaluate the relative burner rig performance of the three candidate compositions at a higher temperature. Also of concern was the large variation of ceramic thickness measured on engine hardware and the potential influence of thickness on ceramic durability. Therefore, a second objective of this phase was to systematically evaluate ceramic thickness effects in a laboratory program. A third objective not directly related to the results of the first engine evaluation but of concern for long-term coating performance was the influence of metallic layer oxidation on coating durability and failure mode. Results of experimental work directed toward addressing some of these concerns are described in the following paragraphs.

5.1.5.1 Oxidation Testing

Since the primary objective of the oxidation tests was to evaluate behavior of the MCrAlY bond coat, only one ceramic composition was studied. Plasma sprayed and electron beam physical vapor deposited (EB-PVD) 20% YSZ/NiCoCrAlY coatings were applied to 1.3 cm (0.5 inch) diameter by 2.5 cm (1 inch) long specimens for oxidation test exposure. NiCoCrAlY metallic layer thicknesses were 0.013 cm (0.005 inch) for all specimens. Specimens with 0.013 cm (0.005 inch) and 0.025 cm (0.010 inch) thick ceramic layers were prepared by both coating processes.

Test specimens were placed in ambient pressure, electric furnaces and exposed in air to controlled temperatures of 982, 1093, or 1149°C (1800, 2000, or 2100°F) for test times up to 3000 hours on a continuous basis, as shown in Table X. Individual specimens of each coating were removed from test for metallographic evaluation at approximately the expected life of the NiCoCrAlY layer and at about half the expected life of the NiCoCrAlY layer in order to determine whether the structure or thickness of the surface ceramic coating layer affected oxidation of the metallic interlayer.

TABLE X

FURNACE OXIDATION EXPOSURE TIMES
FOR THERMAL BARRIER COATINGS

Coating	Ceramic Thickness cm (inch)	Exposure Temperature °C (°F)	Maximum Exposure Time (hr)
Plasma Sprayed NiCoCrAlY 20% YSZ	0.013 (0.005)	982 (1800)	3000
Plasma Sprayed NiCoCrAlY 20% YSZ	0.025 (0.010)	982 (1800)	3000
Plasma Sprayed NiCoCrAlY 20% YSZ	0.013 (0.005)	1093 (2000)	1248
Plasma Sprayed NiCoCrAlY 20% YSZ	0.025 (0.010)	1093 (2000)	1248
Plasma Sprayed NiCoCrAlY 20% YSZ	0.013 (0.005)	1149 (2100)	790
Plasma Sprayed NiCoCrAlY 20% YSZ	0.025 (0.010)	1149 (2100)	790
Electron Beam Vapor Deposited NiCoCrAlY 20% YSZ	0.013 (0.005)	982 (1800)	3000
Electron Beam Vapor Deposited NiCoCrAlY 20% YSZ	0.025 (0.010)	982 (1800)	3000
Electron Beam Vapor Deposited NiCoCrAlY 20% YSZ	0.013 (0.005)	1093 (2000)	1248
Electron Beam Vapor Deposited NiCoCrAlY 20% YSZ	0.025 (0.010)	1093 (2000)	1248
Electron Beam Vapor Deposited NiCoCrAlY 20% YSZ	0.013 (0.005)	1149 (2100)	790
Electron Beam Vapor Deposited NiCoCrAlY 20% YSZ	0.025 (0.010)	1149 (2100)	790

Metallographic evaluation of exposed specimens indicated that oxide scale thickness was generally equivalent [0.0008 - 0.0010 cm (0.0003 - 0.0004 inch)] at the ceramic-metal interface for specimens with both 0.013 and 0.025 cm (0.005 and 0.010 inch) ceramic surface layers, as shown in Figure 57 for EB-PVD coatings exposed for 3000 hours at 982°C (1800°F). Plasma sprayed systems exposed for equivalent times also exhibited 0.0008 to 0.0010 cm (0.0003 to 0.0004 inch) of oxide scale build up at the metallic interface, although internal oxidation was clearly evident in the plasma sprayed metallic layer, as shown in Figure 58. Specimens exposed at 1093 and 1149°C (2000 and 2100°F) also showed no effect of ceramic layer thickness or deposition procedure on oxide scale thickness, although oxide scale thicknesses were significantly greater for the higher temperature exposures, as shown in Figure 59. Internal oxidation for the plasma sprayed metallic layers was very severe for these high temperature exposures, causing frequent pit defects extending to the substrate interface, as shown in Figure 60.

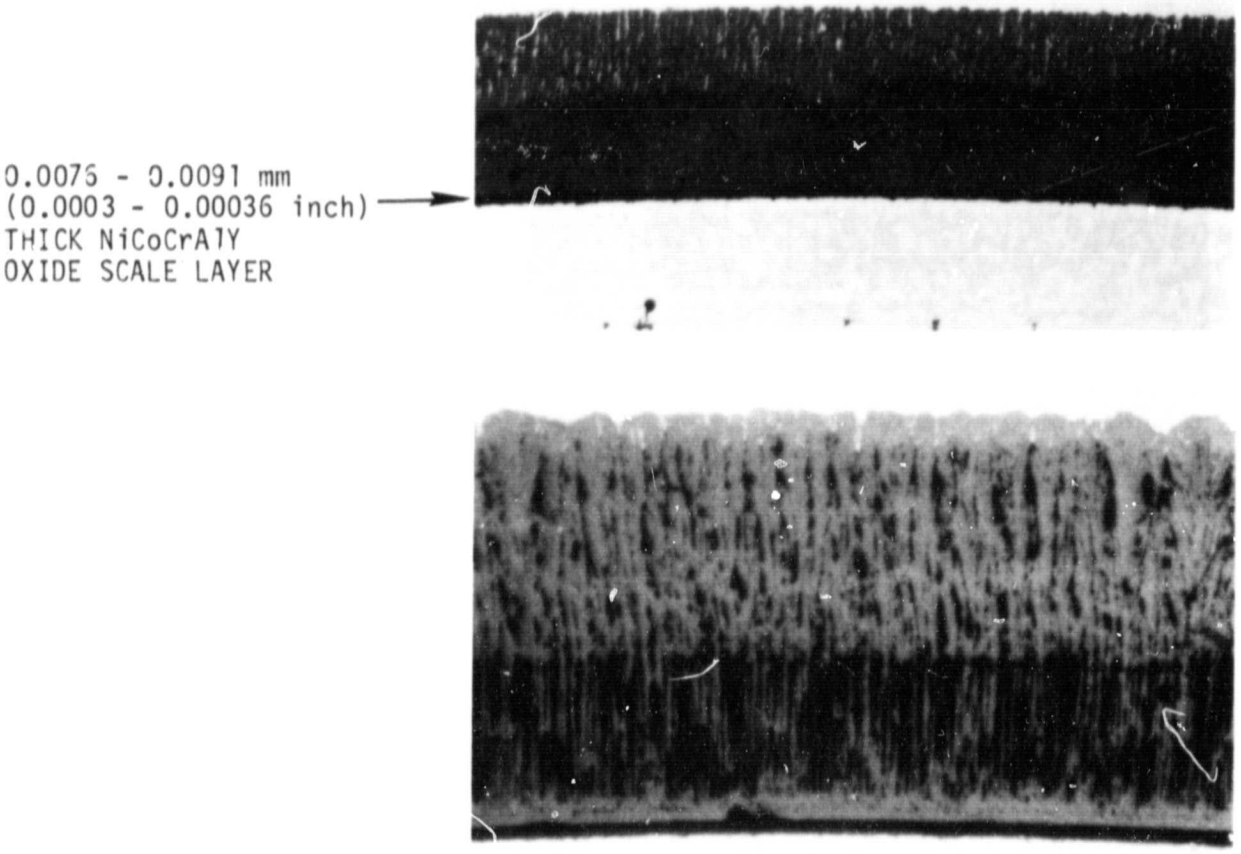

Figure 57 Microstructures of Electron Beam Vapor Deposited NiCoCrAlY, 20 w/o Y_2O_3 Stabilized ZrO_2 Ceramic Coatings Exposed for 3000 hours in a 982°C (1800°F) Furnace Oxidation Test:
Top Coating With 0.127 mm (0.005 inch) Ceramic Surface Layer - Magnification: 200X
Bottom Coating With 0.254 mm (0.010 inch) Ceramic Surface Layer - Magnification: 200X.

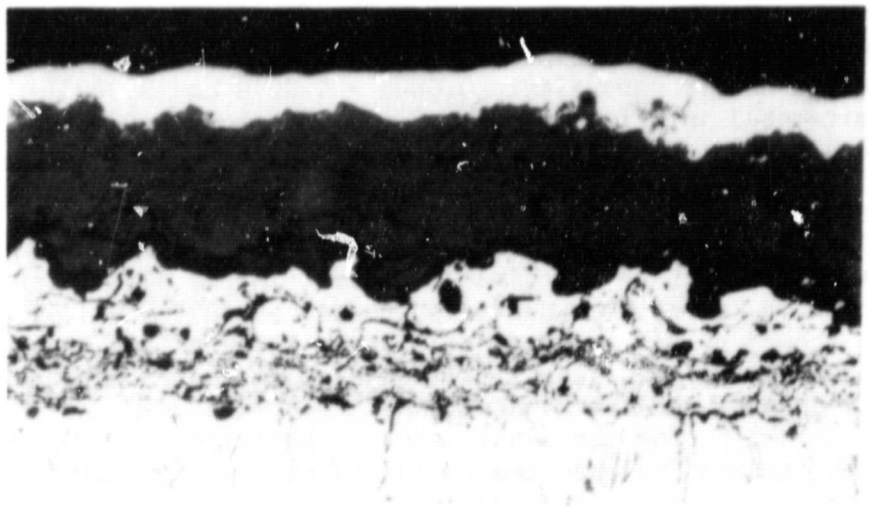

Figure 58 Microstructure of Plasma Sprayed NiCoCrAlY, 20 w/o Y_2O_3 Stabilized ZrO_2 Coating Exposed for 3000 hours at 982°C (1800°F) - Ceramic Layer Thickness 0.127 mm (0.005 inch) - Magnification: 200X.

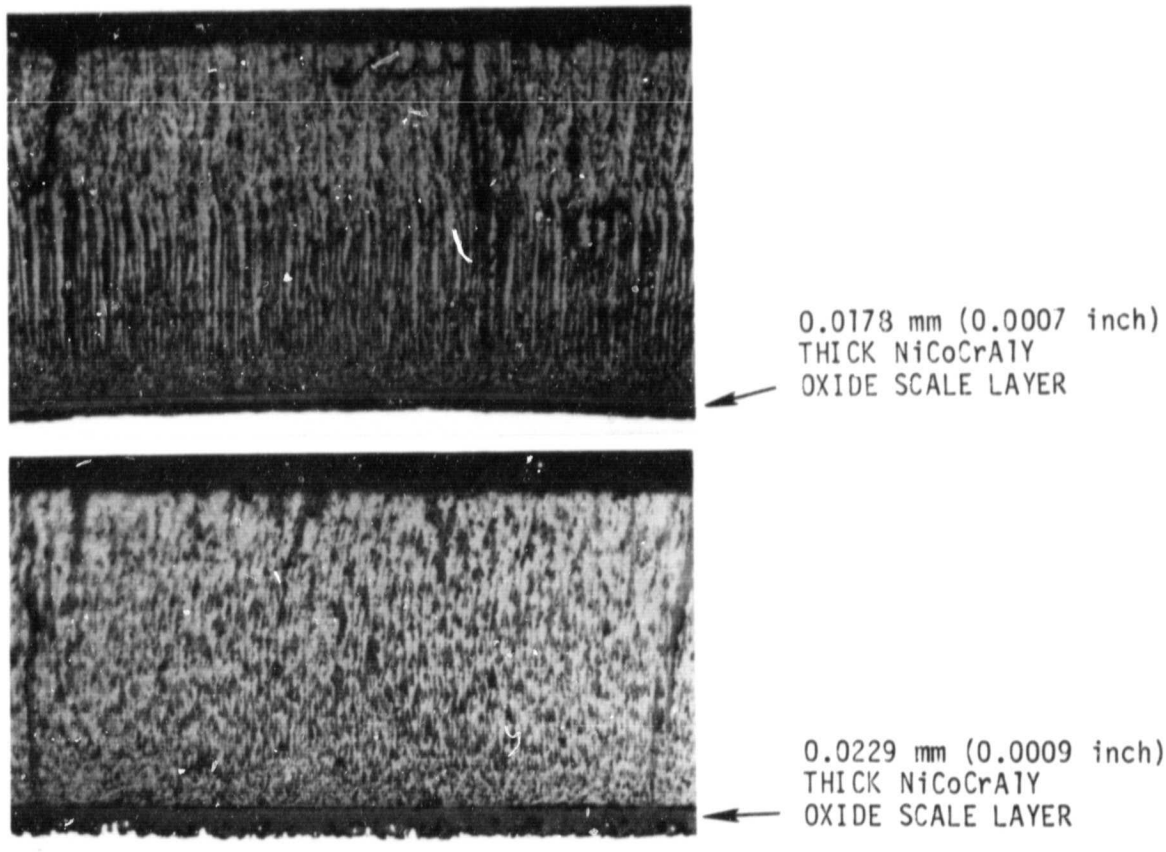

Figure 59 Microstructures of Electron Beam Vapor Deposited NiCoCrAlY, 20 w/o Y_2O_3 Stabilized ZrO_2 Coatings After Furnace Oxidation Test Exposure - Surface Ceramic Layer Thickness 0.0254 mm (0.010 inch)
Top Oxidation Exposure 1248 hours at 1093°C (2000°F)
Bottom Oxidation Exposure 789.5 hours at 1149°C (2100°F)

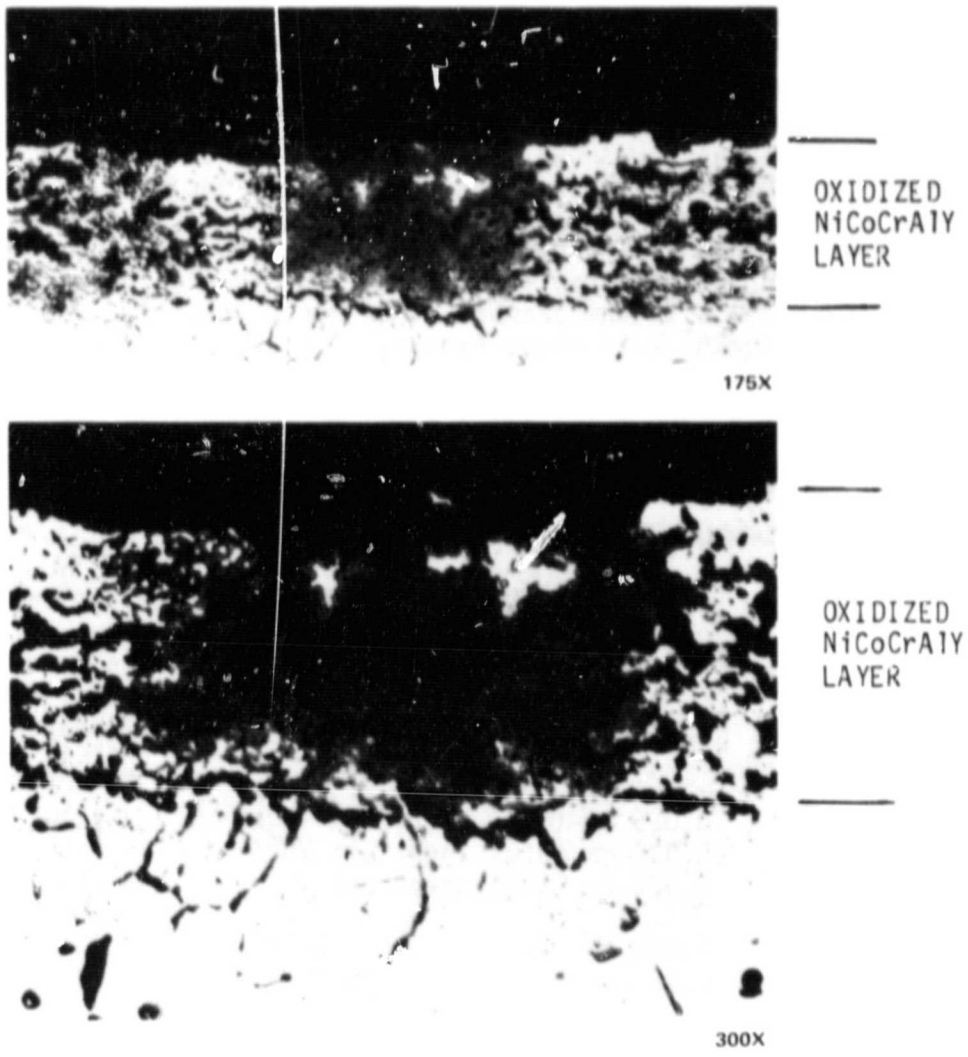

Figure 60 Microstructures of Plasma Sprayed NiCoCrAlY, 20 w/o Y_2O_3 Stabilized ZrO_2 Coating After 790 hours of Oxidation Exposure at 1149°C (2100°F). The 0.127 mm (0.005 inch) surface layer spalled as a result of extensive oxidation of the NiCoCrAlY interlayer.

For all coatings and exposures the rate of oxide scale build up was similar to that expected for bare NiCoCrAlY surfaces, indicating that the surface zirconia ceramic caused little or no reduction in the rate of oxygen transport from the atmosphere to the metallic bond coating/ceramic interface.

Oxide scale thickness was unaffected by ceramic thickness or ceramic structure although internal oxidation was much more severe for the plasma sprayed bond coat. Internal oxidation damage was entirely absent from the EB-PVD bond coat. Internal oxidation in the plasma sprayed bond coats would be expected to be substantially reduced or eliminated if high-quality low-pressure chamber sprayed bond coats were used rather than those produced by conventional spraying in air (Ref. 11). Evaluation of chamber sprayed MCrAlY thus was undertaken as part of the burner rig evaluation described in the next section.

5.1.5.2 Burner Rig Evaluation

Based on questions raised by the first engine test results and by the oxidation test results described above, the fourteen ceramic composition/processing variations shown in Table 5-XI were selected for higher temperature (1066°C (1950°F)) burner rig evaluation. Also included in this test program were three Y_2O_3-ZrO_2 compositions applied over airsprayed NiCoCrAlY by NASA with no substrate temperature control. Low-pressure chamber spray NiCoCrAlY bond coating (systems 13 and 14, Table 5-XI) were applied by the HOWMET Corp. in a vacuum chamber at 50 mm Hg pressure, using an Electro Plasma Inc. 100 KW torch. With these exceptions, all other bars in this test program had air plasma sprayed metallic and ceramic layers applied by the P&WA Manufacturing Research and Development group.

TABLE 5-XI

CANDIDATE COATING SYSTEMS SELECTED FOR FINAL LABORATORY EVALUATION IN THE PROCESS REFINEMENT TASK
[0.013 cm (0.005 Inch) NiCoCrAlY Metallic Layer]

System Identification	Ceramic Layer	Substrate Process Temperature for Ceramic Spraying °C (°F)	Plasma Gun-to-Specimen Distance cm (inch)
1	0.025 cm (0.01 inch) 20% YSZ	21 (70)	7.6 (3)
2	0.025 cm (0.01 inch) 20% YSZ	149 (300)	7.6 (3)
3	0.025 cm (0.01 inch) 20% YSZ	316 (600)	7.6 (3)
4	0.038 cm (0.015 inch) 20% YSZ	149 (300)	7.6 (3)
5	0.05 cm (0.02 inch) 20% YSZ	149 (300)	7.6 (3)
6	0.025 cm (0.010 inch) 6% YSZ	149 (300)	7.6 (3)
7	0.038 cm (0.015 inch) 6% YSZ	149 (300)	7.6 (3)
8	0.05 cm (0.02 inch) 6% YSZ	149 (300)	7.6 (3)
9	0.025 cm (0.010 inch) 21% MSZ	149 (300)	7.6 (3)
10	0.038 cm (0.015 inch) 21% MSZ	149 (300)	7.6 (3)
11	0.05 cm (0.02 inch) 21% MSZ	149 (300)	7.6 (3)
12	0.025 cm (0.010 inch) 20% YSZ	149 (300)	2.5 (1)
13[a]	0.025 cm (0.010 inch) 20% YSZ	Uncontrolled	7.6 (3)
14[a]	0.025 cm (0.010 inch) 20% YSZ	149 (300)	7.6 (3)

NOTE: a = Low-Pressure Chamber Sprayed NiCoCrAlY Metallic Bond Coating

Results of 1066°C (1950°F) burner rig tests, conducted as described in Section 5.1.4.1, are listed in Table 5-XII and shown in bar chart form in Figure 61. The following sections describe the significance of these results as they relate to each of the areas of concern noted above.

TABLE 5-XII

BURNER RIG TEST RESULTS FROM FINAL PROCESS REFINEMENT TASK

Systems Identification	System Number (from Figure 61)	Thickness cm (inch)	Substrate Temperature °C (°F)	Cycles to Failure
20% YSZ	1	0.025 (0.010)	21 (70)	6690
		0.025 (0.010)	21 (70)	6840
		0.025 (0.010)	21 (70)	9270
	2	0.025 (0.010)	149 (300)	7550
		0.025 (0.010)	149 (300)	10000
		0.025 (0.010)	149 (300)	10580
	3	0.025 (0.010)	316 (600)	5710
		0.025 (0.010)	316 (600)	8300
		0.025 (0.010)	316 (600)	10580
	2	0.025 (0.010)	149 (300)	6840
		0.025 (0.010)	149 (300)	6860
		0.025 (0.010)	149 (300)	10580
	4	0.038 (0.015)	149 (300)	6840
		0.038 (0.015)	149 (300)	6210
		0.038 (0.015)	149 (300)	10580
	5	0.051 (0.020)	149 (300)	6010
		0.051 (0.020)	149 (300)	6840
		0.051 (0.020)	149 (300)	10580
6% YSZ	6	0.025 (0.010)	149 (300)	5620
		0.025 (0.010)	149 (300)	9200
		0.025 (0.010)	149 (300)	10580
	7	0.038 (0.015)	149 (300)	1570
		0.038 (0.015)	149 (300)	3860
		0.038 (0.015)	149 (300)	4350
	8	0.051 (0.020)	149 (300)	320
		0.051 (0.020)	149 (300)	1050
		0.051 (0.020)	149 (300)	1280

TABLE 5-XII (Cont'd)

Systems Identification	System Number (from Figure 61)	Thickness cm (inch)	Substrate Temperature °C (°F)	Cycles to Failure
21% MgO ZrO_2	9	0.025 (0.010)	149 (300)	3600
		0.025 (0.010)	149 (300)	4550
		0.025 (0.010)	149 (300)	5770
	10	0.038 (0.015)	149 (300)	3600
		0.038 (0.015)	149 (300)	5400
		0.038 (0.015)	149 (300)	5590
	11	0.051 (0.020)	149 (300)	3600
		0.051 (0.020)	149 (300)	5370
		0.051 (0.020)	149 (300)	10210
20% Y_2O_3 ZrO_2	12	0.025 (0.010)	Uncontrolled	550[a]
		0.025 (0.010)	149 (300)	3600[a]
		0.025 (0.010)	149 (300)	9070[a]
	13	0.025 (0.010)	149 (300)	720[b]
		0.025 (0.010)	149 (300)	820[b]
		0.025 (0.010)	149 (300)	3970[b]
	14	0.025 (0.010)	Uncontrolled	160[b]
		0.025 (0.010)	Uncontrolled	360[b]
		0.025 (0.010)	Uncontrolled	390[b]
6% Y_2O_3 ZrO_2	Supplied by NASA	0.038 (0.015)	Uncontrolled	1560
		0.038 (0.015)	Uncontrolled	3760
8% Y_2O_3 ZrO_2	Supplied by NASA	0.038 (0.015)	Uncontrolled	3990
		0.038 (0.015)	Uncontrolled	3350
		0.038 (0.015)	Uncontrolled	2230
12% Y_2O_3 ZrO_2	Supplied by NASA	0.038 (0.015)	Uncontrolled	3870

NOTE: a = 2.5 cm (1 inch) Gun Distance
b = Low Pressure Chamber NiCoCrAlY Plasma Spray Gun

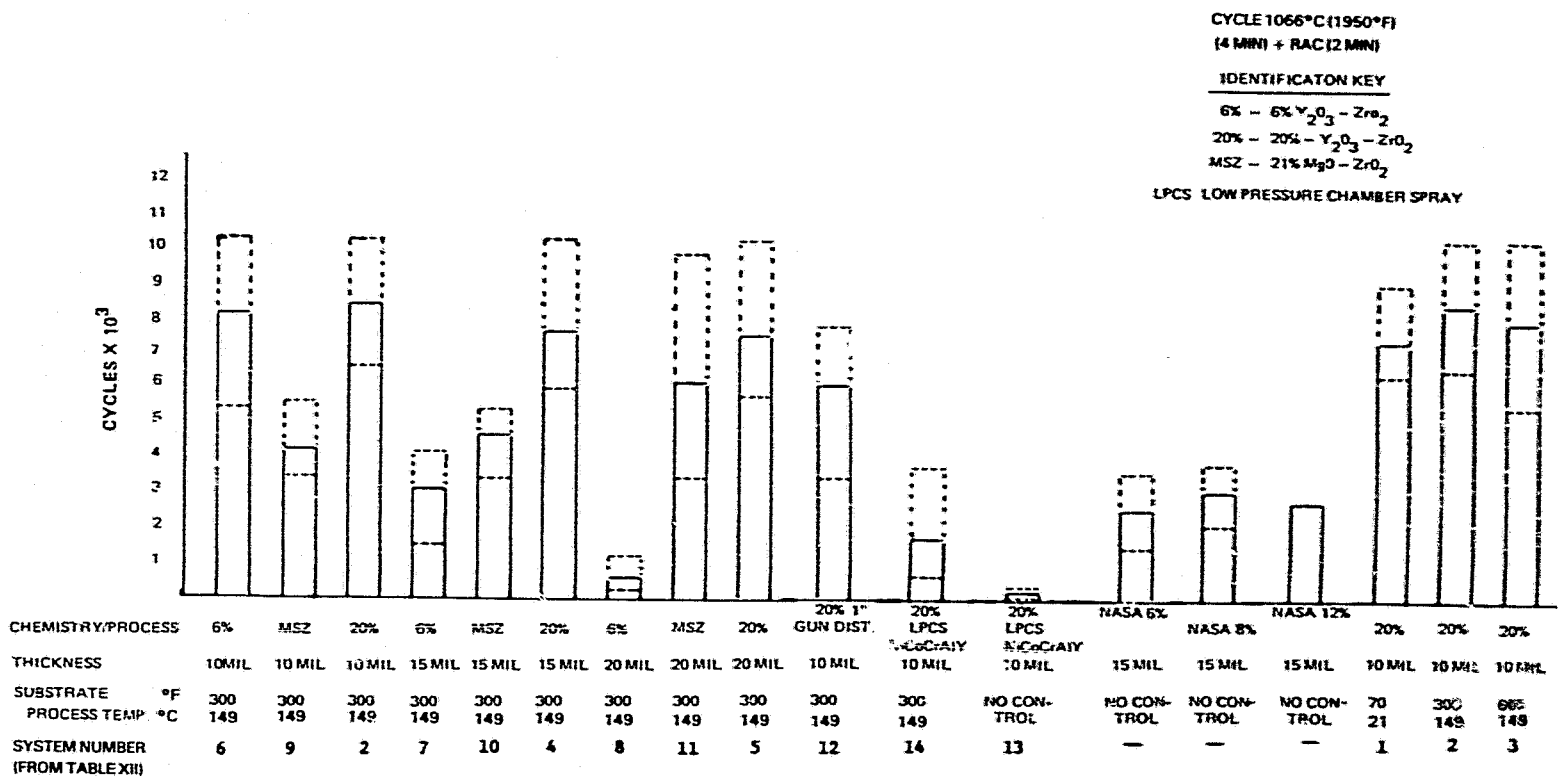

Figure 61 Spalling Life of Thermal Barrier Coatings Exposed During Final Process Refinement Burner Rig Test

5.1.5.2.1 Effect of Increased Cyclic Temperature

The spalling resistance of 0.025 cm (0.010 inch) thick ceramic coating layers, produced using a 149±28°C (300±50°F) substrate temperature during plasma spraying, is equivalent for 6 percent Y_2O_3 (segmented) and 20 percent Y_2O_3 (high porosity) ZrO_2. The cyclic life of these controlled-temperature process ceramics at 1066°C (1950°F) is even greater than that observed in the previous 1010°C (1850°F) tests of ceramic coatings produced with uncontrolled substrate temperatures.

Comparison of pretest and post-test microstructures for 6% YSZ and 20% YSZ ceramics (Figures 62 and 63) indicates that for both materials residual porosity was reduced as a result of high temperature exposure. This reduction is believed to result from sintering densification during the 1066°C (1950°F) maximum temperature portion of the test cycle. Significant densification at this temperature suggests that self diffusion in plasma sprayed ceramics is much more rapid than would be expected for hot pressed or fused ceramics of similar composition.

Since reduction in porosity is associated with reduction in cyclic thermal life, sintering densification may be considered a primary degradation mode for these high porosity coatings. Although sintering of residual porosity was observed in the 6% YSZ ceramic, sintering of through-thickness segmentation cracks was not observed. Since the 6% YSZ ceramic depends primarily on segmentation cracking to achieve its strain tolerance, the segmented material might be expected to show relatively less degradation than the high porosity 20% YSZ coating at test temperatures higher than 1066°C (1950°F).

The cyclic life of 0.025 cm (0.010 inch), 21% MSZ ceramic layers in the 1066°C (1950°F) test was reduced by approximately fifty percent compared with the 6% and 20% YSZ (Figure 61). In the 1010°C (1850°F) previous tests, the three ceramic materials were observed to have similar lives. A comparison of pretest and post test microstructures of 21% MSZ ceramics (Figure 64) indicates that the degree of internal microcracking increased significantly during test exposure. This is believed to be related to the high degree of reversion from the cubic phase to the monoclinic phase observed in previous burner rig tests and in the first engine test. Since this reversion significantly changes volume, progressive formation of the monoclinic phase would be expected to result in progressive microcrack formation. Linking of excessive quantities of these internal microcracks is believed to contribute to ceramic spalling. Since increased test temperature contributes to increased instability and microcrack density, increased temperature is believed to have reduced the life of the 21% MSZ ceramic at 1066°C (1950°F) relative to the Y_2O_3 stabilized zirconias.

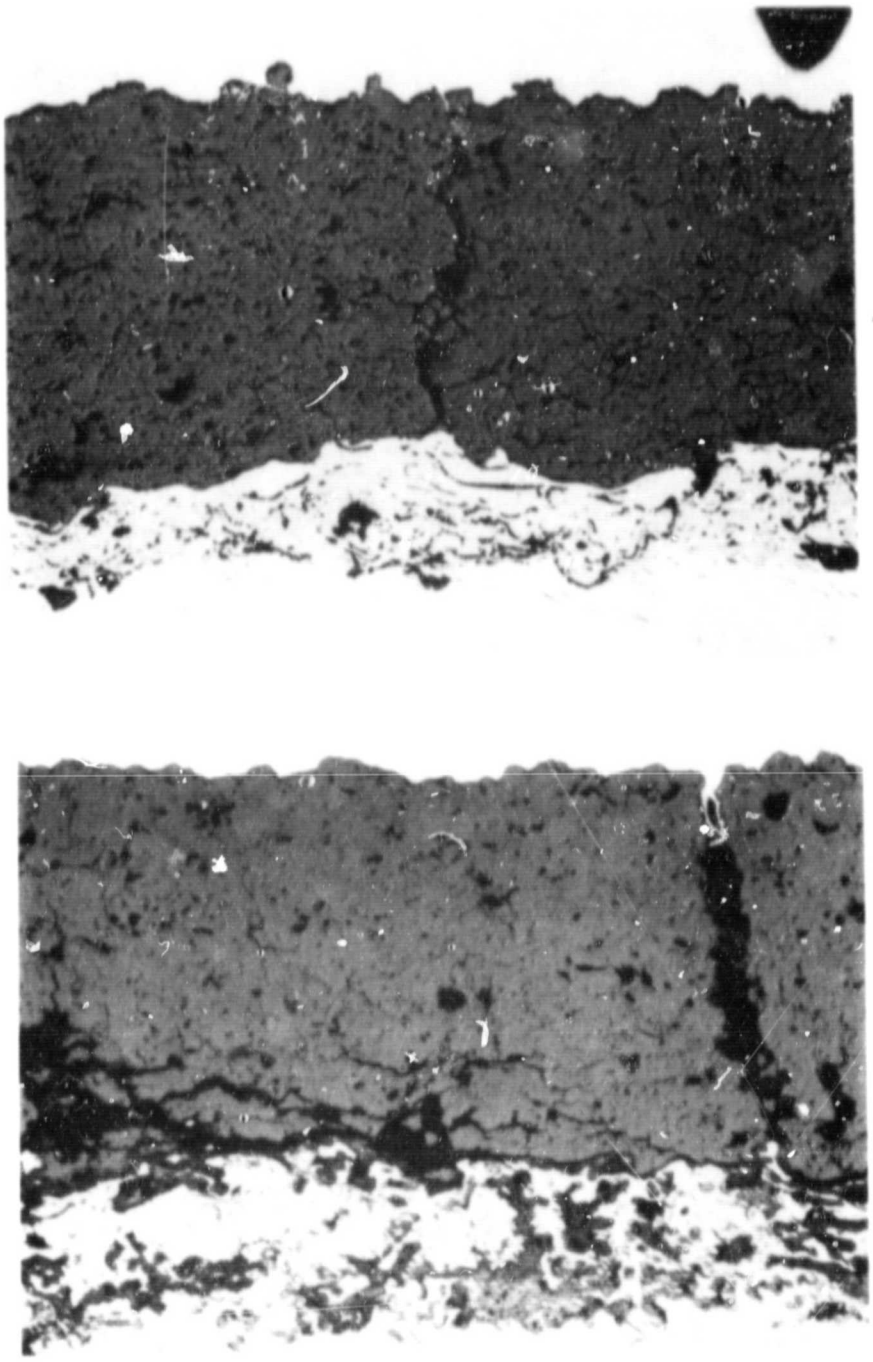

Figure 62 Microstructure of NiCoCrAlY, 6 w/o Y_2O_3 Stabilized ZrO_2 Coating With 0.254 mm (0.010 inch) Ceramic Layer. Ceramic layer plasma sprayed with substrate temperature controlled at 149°C (300°F) during deposition.

Top — As Coated Structure - Magnification: 200X
Bottom — Structure After 5620 Cycles of Burner Rig Exposure - Magnification: 200X

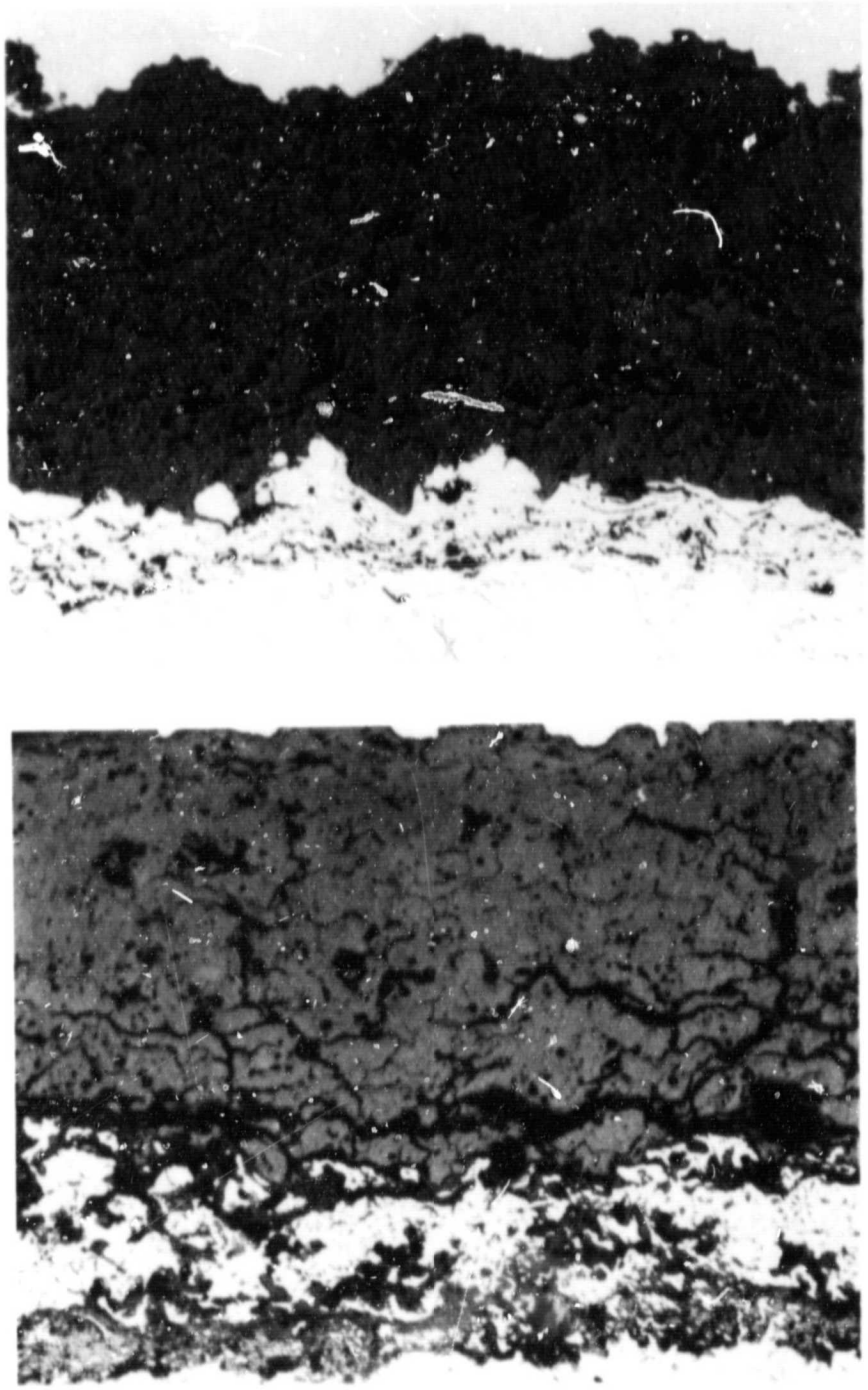

Figure 63 Microstructure of NiCoCrAlY, 20 w/o Y_2O_3 ZrO_2 Coating with 0.254 mm (0.010 inch) Ceramic Layer. Ceramic layer plasma sprayed with substrate temperature controlled at 149°C (300°F) during deposition.

Top As Coated Structure - Magnification: 200X
Bottom Structure After 7550 Cycles of Burner Rig Exposure - Magnification: 200X

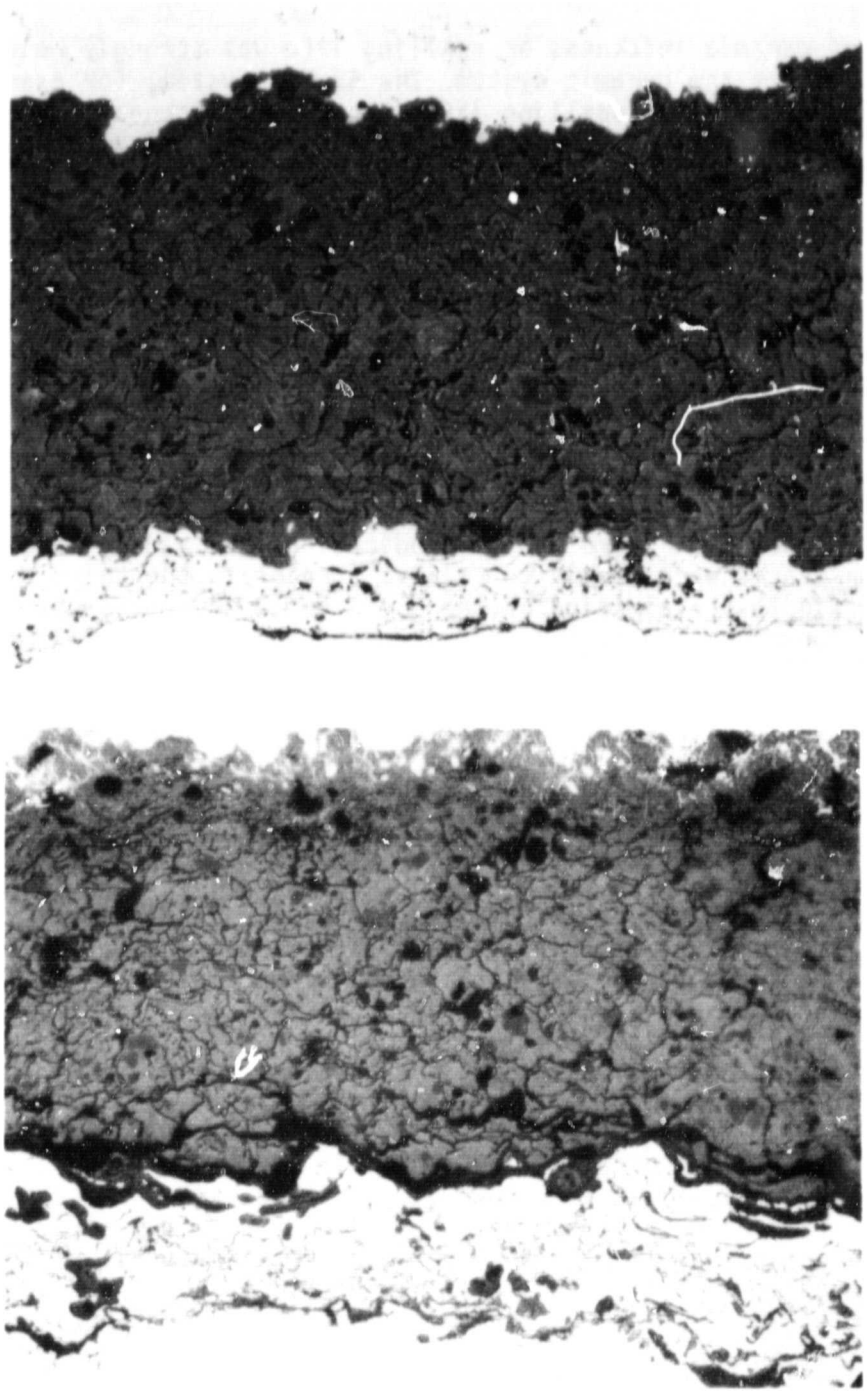

Figure 64 Microstructure of NiCoCrAlY, 21 w/o MgO Stabilized ZrO_2 Coating With 0.254 mm (0.010 inch) Ceramic Layer. Ceramic layer plasma sprayed with substrate temperature controlled at 149°C (300°F) during deposition.

Top As Coated Structure - Magnification: 200X
Bottom Structure After 7550 Cycles of Burner Rig Exposure - Magnification: 200X.

5.1.5.2.2 Effect of Ceramic Thickness

The effect of ceramic thickness on spalling life was strongly related to the characteristics of the ceramic system. The 6% YSZ system, for example, showed a significant decrease in spalling life as ceramic thickness increased in the range from 0.025 cm (0.010 inch) (8000 cycles average life) to 0.05 cm (0.020 inch) (less than 1000 cycles), as shown in Figure 61. This strong dependence of spalling life is believed related to a decrease in the ability of segmentation cracking to relieve thermal expansion mismatch strains as ceramic thickness increases. For a fixed segment size, in-plane stress at the base of a segment increases with segment thickness. Thus, for a fixed segment size, coating durability may be expected to decrease with increasing thickness.

While segmentation cracks penetrate to the bond coat for all coating thicknesses, as shown in Figure 65, the average diameter of segments formed in 0.025, 0.038 and 0.051 cm (0.010, 0.015 and 0.020 inch), 6% YSZ ceramic coatings was approximately constant at 0.088 cm (0.035 inch). For the 0.051 cm (0.020 inch) ceramic, lateral cracking was observed even in the pretest condition, as shown in Figure 65 top, indicating that widely spaced segmentation cracks were unable to relieve strains in the thick ceramic layer. Post burner rig test evaluation of the 0.051 cm (0.020 inch) coating showed spalling failure occurred as a result of propagation of lateral cracks near the ceramic-metal interface, similar to that occurring for thin coatings (Figure 65 bottom). Pre-existing lateral cracks (or unrelieved strains) caused the spalling failure to occur earlier for the thicker coating, however.

The above result is in marked contrast to the first engine test result, where 6% YSZ coatings as thick as 0.051 cm (0.020 inch) exhibited excellent performance. As noted in Section 5.1.5, a higher level of porosity and microcracking and a lower level of segmentation cracking were observed on the initial engine test hardware as compared to the typical laboratory burner rig bars for this ceramic composition. These observations indicate that, whereas the benefits of segmentation as a strain relief mechanism may be limited at coating thickness beyond 0.025 cm (0.010 inch), the compliance enhancement provided by relatively high levels of porosity and microcracking continue to produce a durable ceramic coating at thicknesses up to 0.051 cm (0.020 inch) in the 6% YSZ composition.

The 20% YSZ and 21% MSZ ceramics showed little sensitivity of spalling life to ceramic thickness, as shown in Figure 61. In these cases the ceramics achieved their strain tolerance by virtue of a relatively uniform distribution of defects throughout the ceramic layer to lower their effective elastic modulus. Although the defects were different in character (porosity in 20% YSZ and microcracks in 21% MSZ), the uniform distribution of the defects throughout the ceramic appears to have acted to reduce strains that lead to the formation of lateral spalling cracks even in 0.051 cm (0.020 inch) coatings. Again, these observations are consistent with the excellent engine performance of thick 6% YSZ coatings containing relatively high but stable levels of porosity and microcracking.

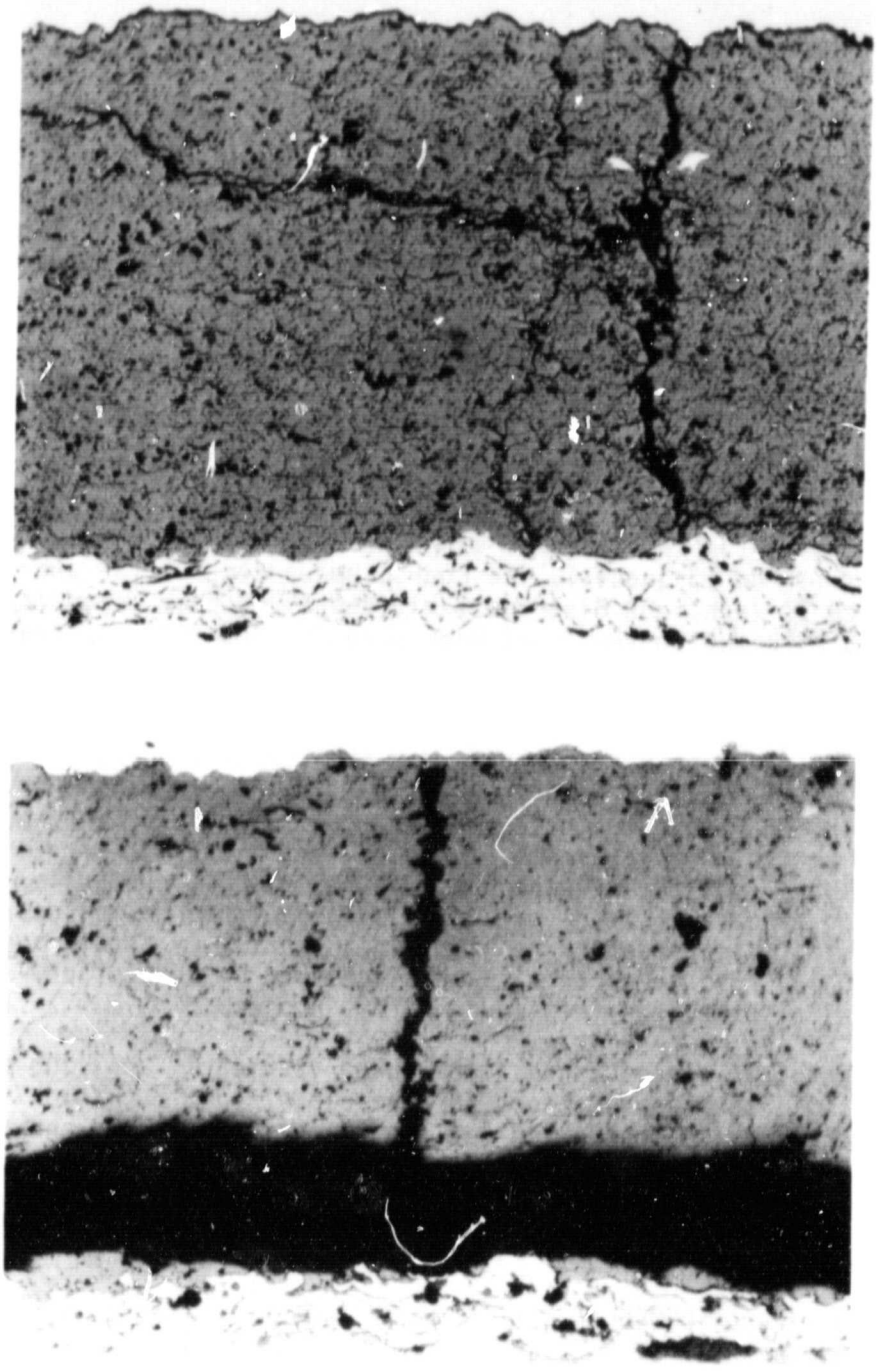

Figure 65 Microstructure of NiCoCrAlY, 6 w/o Y_2O_3 Stabilized ZrO_2 Coating With 0.51 mm (0.020 inch) Ceramic Layer. Ceramic Layer Plasma Sprayed With Substrate Temperature Controlled at 149°C (300°F) During Deposition.

Top As Coated Structure - Magnification: 200X
Bottom Structure After 1280 Cycles of Burner Rig Exposure - Magnification: 200X.

5.1.5.2.3 Coatings With Process Modifications

A series of coatings were evaluated to determine the effect of process modification on ceramic life. Among these modifications were variations in plasma gun to specimen distance, NiCoCrAlY interlayer characteristics, and substrate temperature within the range identified to be favorable during the initial process refinement evaluation. Specimens of 6, 8, and 12 percent Y_2O_3 ZrO_2 ceramic coatings were also provided by NASA for comparative evaluation.

The 0.025 cm (0.010 inch), 20% YSZ ceramic layers produced by plasma spraying with a gun-to-specimen distance of 2.5 cm (1 inch) and the substrate temperature controlled at 149°C (300°F) yielded a structure with coarse (0.114 to 0.127 cm (0.045 to 0.050 inch) diameter) segments formed by through-thickness cracks. Porosity was less than 5% in these high energy input coatings compared with the 15 to 20% porosity produced for other 20% YSZ coatings evaluated in this program which were sprayed at gun-to-specimen distances of 7.6 cm (3 inches). The coarse segmented 20% YSZ specimens coated with a 2.5 cm (1 inch) gun distance exhibited lives that were reduced by about 25% compared with the conventional high porosity 20% YSZ coatings, as shown in Figure 61. The life of the coarse segmented, 20% YSZ coatings was similarly reduced relative to the somewhat finer segmented 6% YSZ coatings.

Two groups of specimens were sprayed with the standard porosity, 20% YSZ over a NiCoCrAlY layer that had been sprayed in a low pressure chamber; one group used a 149°C (300°F) substrate temperature control, the other used no temperature control during ceramic spraying. The NiCoCrAlY metallic interlayers were sprayed in a low pressure (50 mm Hg), controlled-atmosphere chamber using fine (-325 mesh) powder to minimize internal defects and improve oxidation life. This procedure resulted in a relatively smooth metallic layer surface (140-180 rms) compared with that achieved by conventional air spraying (300-400 rms) of other specimens during this program.

The smooth metallic-ceramic interface caused very early spalling of the ceramic at the interface location, as a result of poor mechanical bonding. Specimens sprayed with controlled low substrate temperatures showed significantly greater spalling life than those sprayed with uncontrolled substrate temperatures. However, lives of all specimens with smooth chamber sprayed MCrAlY interfaces were low relative to others with rough air sprayed MCrAlY interlayers, as shown in Figure 61.

The spalling life of 0.025 cm (0.010 inch), 20% YSZ ceramics sprayed with substrate temperatures of 21, 149 and 315°C (70, 300 and 600°F) over air-sprayed MCrAlY layers was generally equivalent, as shown in Figure 61, indicating that temperature control need not be stringent to achieve acceptable life in production coatings. This range of temperature was previously identified as providing satisfactory results in the initial process refinement evaluation.

Specimens provided by Pratt & Whitney Aircraft were coated by NASA with a nominal 0.013 cm (0.005 inches) of air sprayed NiCoCrAlY and 0.038 cm (0.015 inches) of 6, 8, or 12 percent Y_2O_3 ZrO_2. The structures of these ceramic coatings were similar to each other, each exhibiting 15 to 20% porosity as shown in Figure 66. Spalling life of the NASA supplied coatings was generally equivalent for all three ceramic chemistries, as shown in Figure 61, indicating that the lives were probably a function of their similar structures and not a strong function of their varying chemistries.

5.1.5.3 Selection of Final Engine Test Candidates

Based on the burner rig test results described above, it was decided to re-evaluate the three compositions used in the first engine test, but to use substrate temperature control in the range of 21 to 316°C (70 to 600°F) for application of these coatings to engine hardware. To implement this decision, an apparatus was constructed which provided cooling air to the vane platforms during ceramic deposition to control the platform temperature. These plasma sprayed, stabilized zirconia coatings provided about the same, or better, level of durability in the burner rig tests as other 0.038 cm (0.015 inch) thick partially stabilized coatings tested in this program.

5.2 COOLING SYSTEM EVOLUTION

A ceramic coating on the turbine vane platforms provides increased resistance to the transfer of heat from the hot gas environment to the vane metal platform, relative to conventional cooling. This can produce two potential benefits: either cooling air can be reduced, resulting in improved thrust specific fuel consumption; or vane substrate metal temperatures can be reduced, resulting in improved durability. A combination of these two approaches was used in the subject program.

Three major constraints were placed on the cooling system design for this test program: the maintainability and durability of the bill-of-material vane had to be preserved, the design had to mate with existing engine hardware, and the airfoil cooling design could not be changed. In addition, JT9D-70/59 bill-of-material vane castings had to be used for the test hardware, to keep the cost of testing down.

Feasibility studies had shown that acceptable platform metal temperatures could be maintained with a thin [0.025 - 0.038 cm (0.010 - 0.015 inch)] layer of low thermal conductivity ceramic coating in combination with an internal impingement cooling scheme specifically designed to accommodate the platform external heat loads. The resulting thermal barrier coated/impingement cooled vane platform requires less cooling air flow than the bill-of-material film cooled vane platforms which increases the efficiency of the engine.

The development of the cooling system was carried out in two major steps. An initial design was made, using analytical models coupled with experimental data. This design was then evaluated in an engine which underwent a test program that simulated long term airline operation in a reduced period of time by operating at thrust and temperature cycles beyond normal airline operation. The results of the initial engine test were used to refine the design, which was demonstrated in the final engine test.

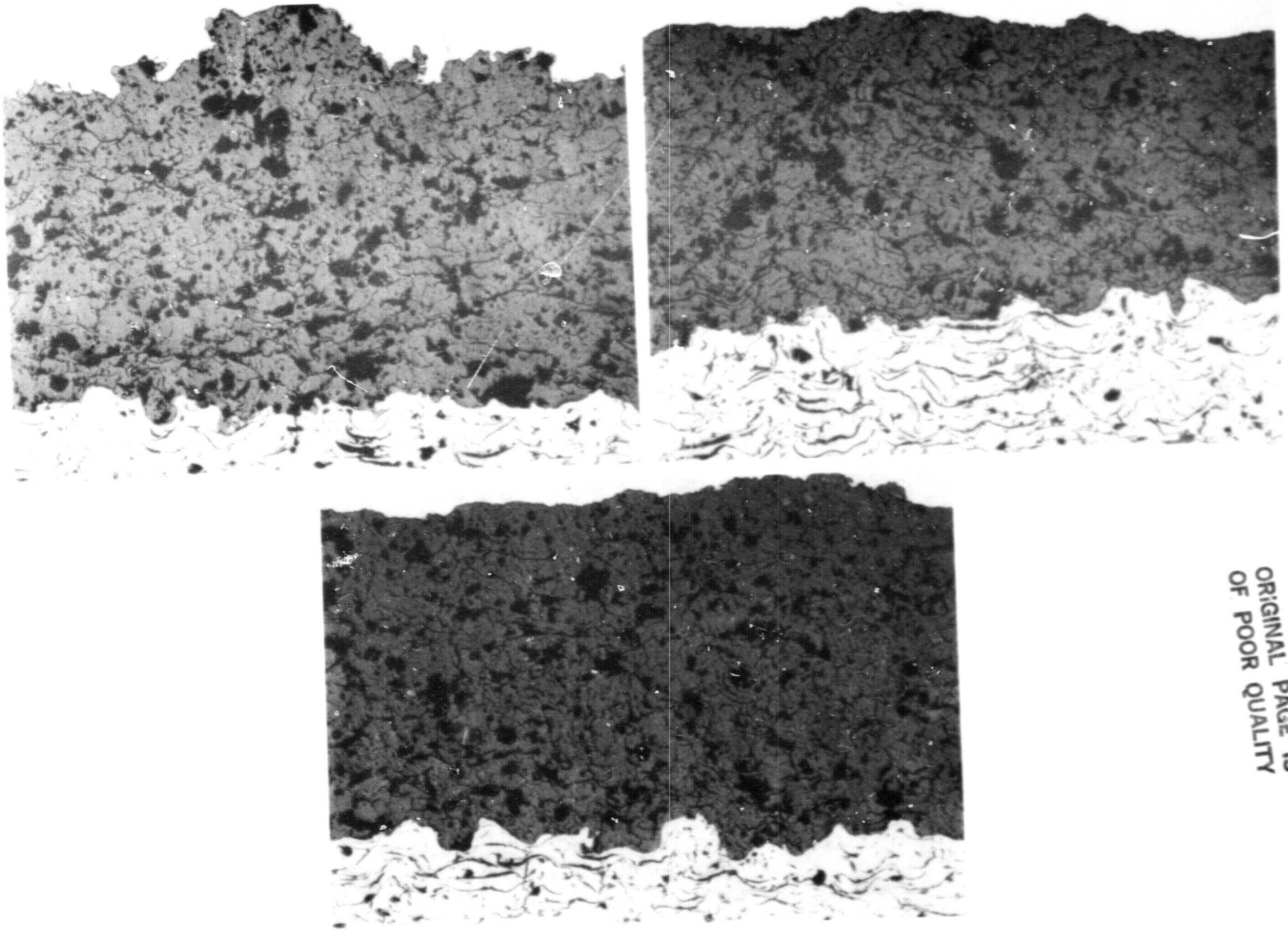

Figure 66 Pretest Microstructures of NASA Coatings with 0.381 mm (0.015 inch) Ceramic Layers.
Top Left - 6 w/o Y_2O_3 Stabilized ZrO_2 Ceramic - Mag.: 150X
Top Right - 8 w/o Y_2O_3 Stabilized ZrO_2 Ceramic - Mag.: 150X
Bottom - 12 w/o Y_2O_3 Stabilized ZrO_2 Ceramic - Mag.: 150X

A finite element analysis was used to determine the ceramic/impingement cooling scheme required to accommodate the platform heat loads and meet the imposed design constraints. The aerodynamics as well as the radiative and convective heat transfer coefficients of the coated vane platform surface were assumed to be the same as the bill-of-material vane. Internal heat transfer coefficients were obtained with the standard correlation used in impingement designs. External heat transfer coefficients were obtained from the latest data acquired in large scale rig testing of blade and vane platform geometries. Coating thickness was chosen from rig results of cyclic temperature testing on the spallation characteristics of laboratory specimens and also from the constraint of utilizing reduced cooling air while maintaining acceptable platform metal temperatures. (See Section 5.1 for a discussion on how coating thickness was determined.) External hot gas driving temperatures were acquired through standard treatment of the inlet temperature profile and the effect of cooling air flowing over the platform leading edge. A reduction in the external gas temperature profile near the platform due to the cooling air was calibrated from published film effectiveness data obtained in large scale rig tests (Ref. 12). These boundary condition data and assumptions were input to the finite element analysis to define the three-dimensional temperature, stress, and strain distributions throughout the platform. Particular attention was paid to the ceramic coating/substrate interface. Iteration on the impingement geometry and cooling flow rate in the analysis were required until the desired metal temperature distribution in the substrate was obtained.

Impingement plates designed to produce the necessary cooling flow distribution to the ID and OD platforms in the first engine test are shown in Figure 67. The impingement plates direct the flow of air to the proper areas of the platform in discrete jets of high velocity air, producing large internal heat transfer coefficients for heat removal.

The impingement plates were designed to be easily weldable to the vane platform. INCO 625 was chosen as the impingement plate material because of its strength and weldability. The impingement plate was stamped from 0.076 cm (0.030 inch) sheet stock, and the impingement holes made using a numerically controlled laser drill. The laser drill produces a conical hole, larger at the laser entrance. For this reason, the holes were drilled from the upstream side of the impingement plate to produce a nozzle-shaped hole, further improving the aerodynamic and heat transfer characteristics of the impingement system. Airflow calculations indicated that the proper distribution of cooling air between the front and rear platform impingement plates required enlarging the area of the cooling air supply tunnel through the vane attachment hardware at both the ID and OD. Figure 68 is a photograph of the vane showing the enlarged tunnel in the ID attachment before installation of the impingment plates and application of the ceramic coating to the platforms.

Eighteen vanes were fabricated using the configuration described above, for engine testing. Photographs of the completed vane platform ID and OD assembly including instrumentation are shown in Figures 69 and 70. Cold flow calibration tests were then conducted on selected vanes to determine if the design flow distribution to the airfoil had been affected by the installation of the platform impingement system. Following satisfactory flow testing the vanes were installed in an engine and tested according to the procedures outlined in Appendix A for the initial engine test.

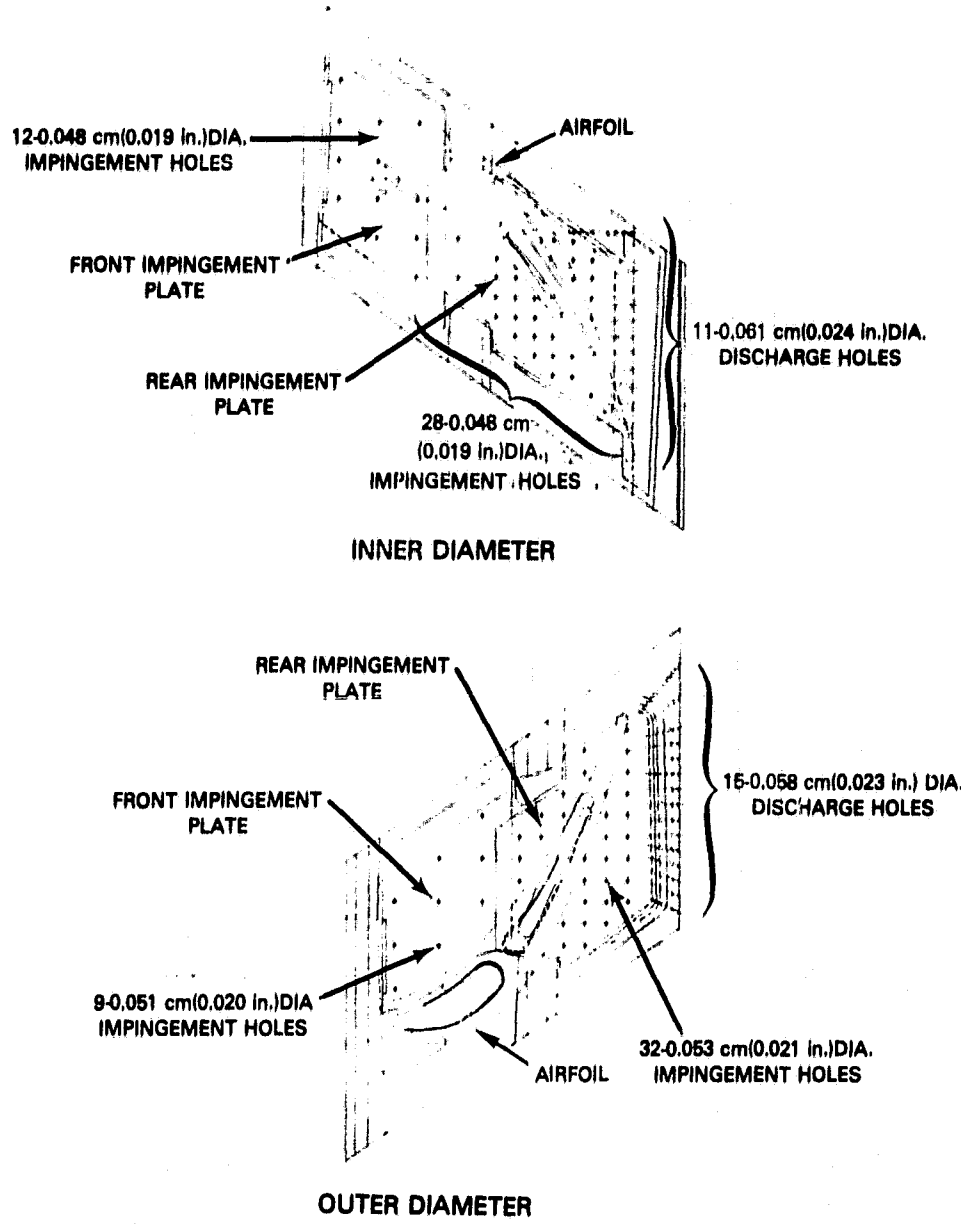

Figure 67 Vane Platform Cooling Hole Patterns for the Initial Engine Test.

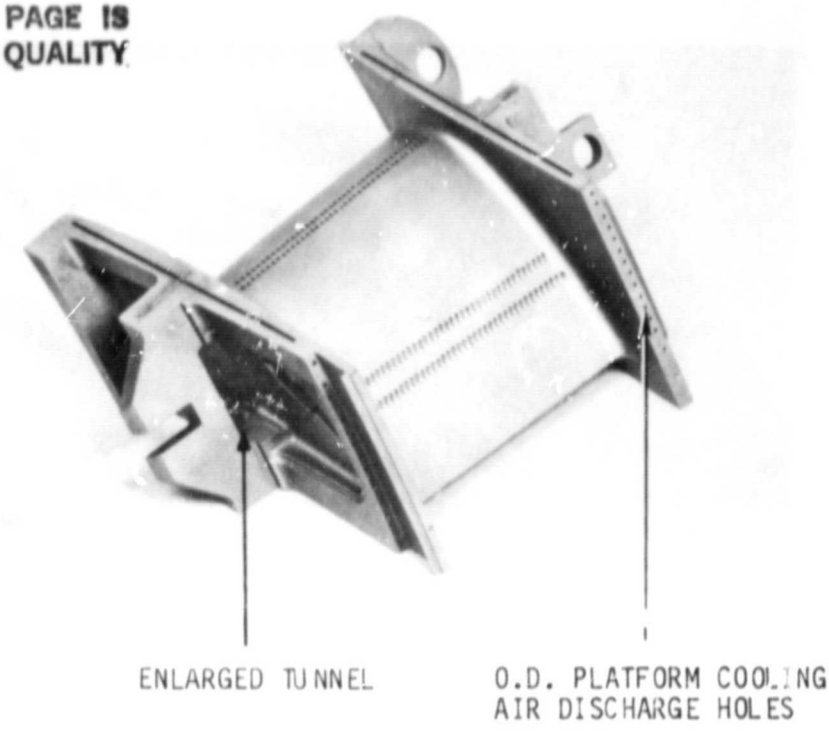

Figure 68 Enlarged Tunnel in Vane Inner Diameter Platform Attachment for Initial Engine Test.

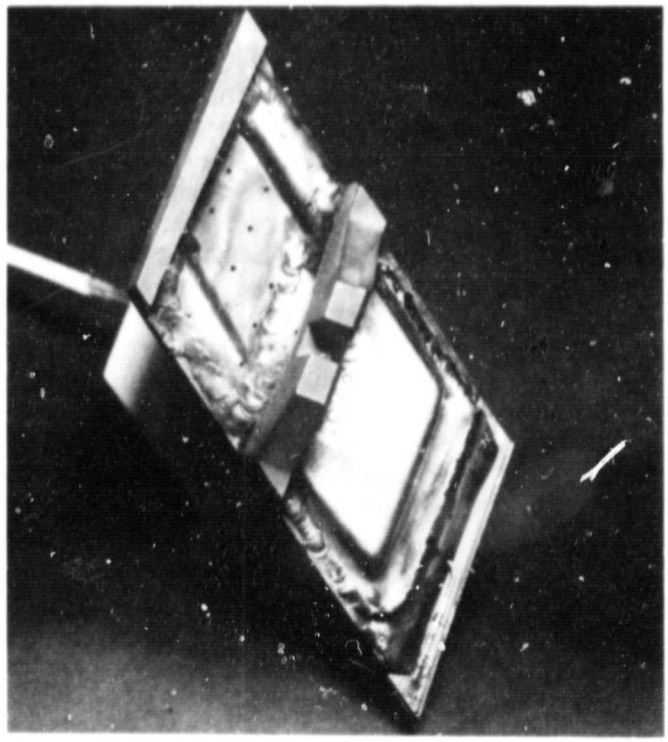

Figure 69 Completed Vane Inner Diameter Platform Assembly for Initial Engine Test - Interface temperature sensor installation is shown.

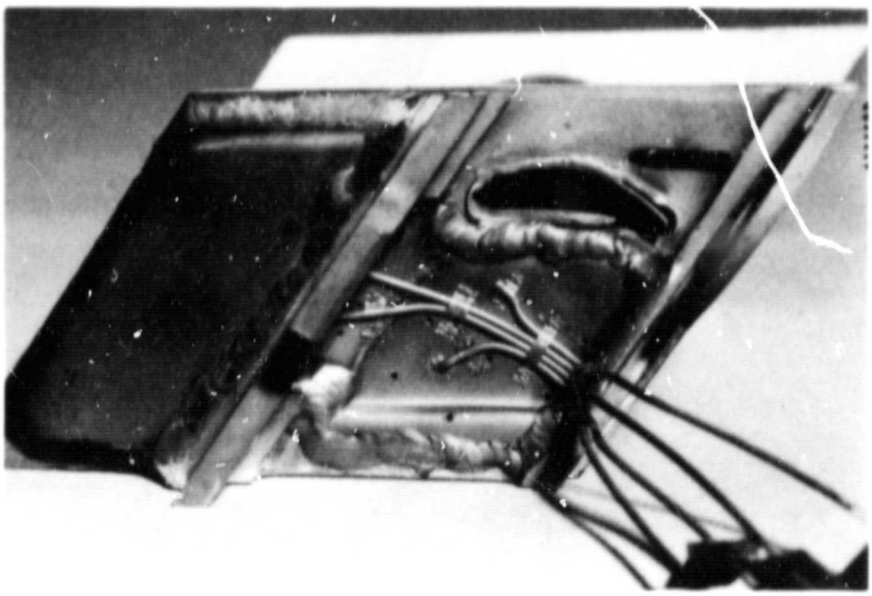

Figure 70 Completed Vane Outer Diameter Platform Assembly for Initial Engine Test - Static pressure sensor installation is shown.

The initial engine test revealed several areas where the cooling system design could be improved. Refinements were made to the design based on these discoveries, resulting in the final design described in Section 3.0. These cooling system design refinements are described as follows:

A major problem with the initial cooling system design was that all inner diameter platforms had an incomplete weld along the trailing edge of the impingement plate. The rear impingement plate and vane casting did not seal along the plate rear edge. During welding, the impingement plate lifted off the vane casting allowing a large discharge path for the impingement air. This defect was not apparent during the inspection that followed vane assembly, because the flow guide at the rear of the impingement plate obscured it. Cold flow testing of the selected vane assemblies did not reveal the leakage because the overall flow capacity was dominated by the airfoil. As a result, the inner diameter platform was overcooled. The problem was solved in the second design by including a slot in the impingement plate weld area, over which the weld bead is made. The slot guarantees positive plate to vane bonding. The source of the leak and results of the corrective measures taken are shown schematically in Figure 71. A photograph showing a cutaway of view of the second design that eliminated the leak is shown in Figure 72.

Some outer diameter impingement holes were plugged by weld material, because they were located too close to the weld area in the first design. This contributed to undercooling in the outer diameter platform and was partially responsible for the greater occurrence of spalls and cracks on the outer diameter platforms relative to the inner diameter, as shown in Figure 73. In the second design the holes were shifted away from the weld area and welding procedures were improved, eliminating the problem.

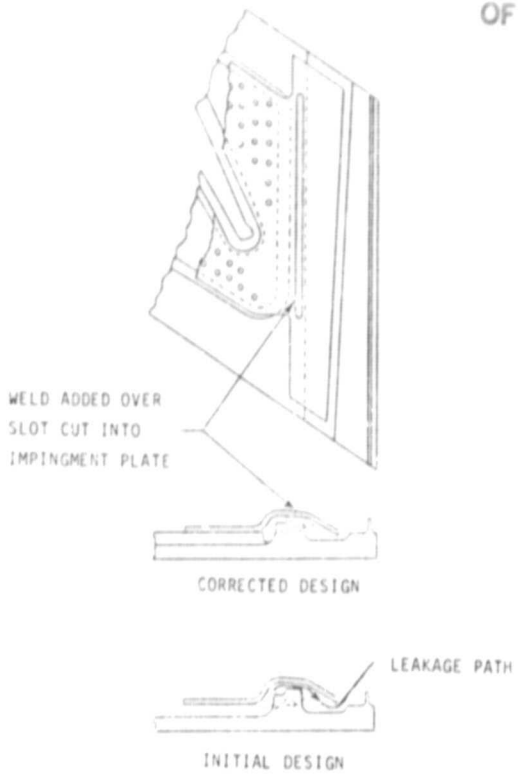

Figure 71 Inner Diameter Impingement Air Leakage Path was corrected for the Final Engine Test.

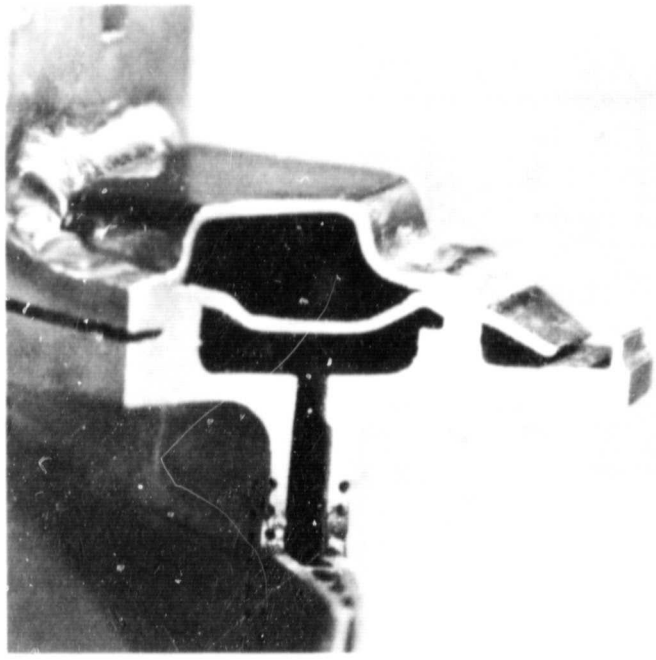

Figure 72 Cutaway View of the Design that Corrected the Impingement Air Leakage.

ORIGINAL PAGE IS
OF POOR QUALITY

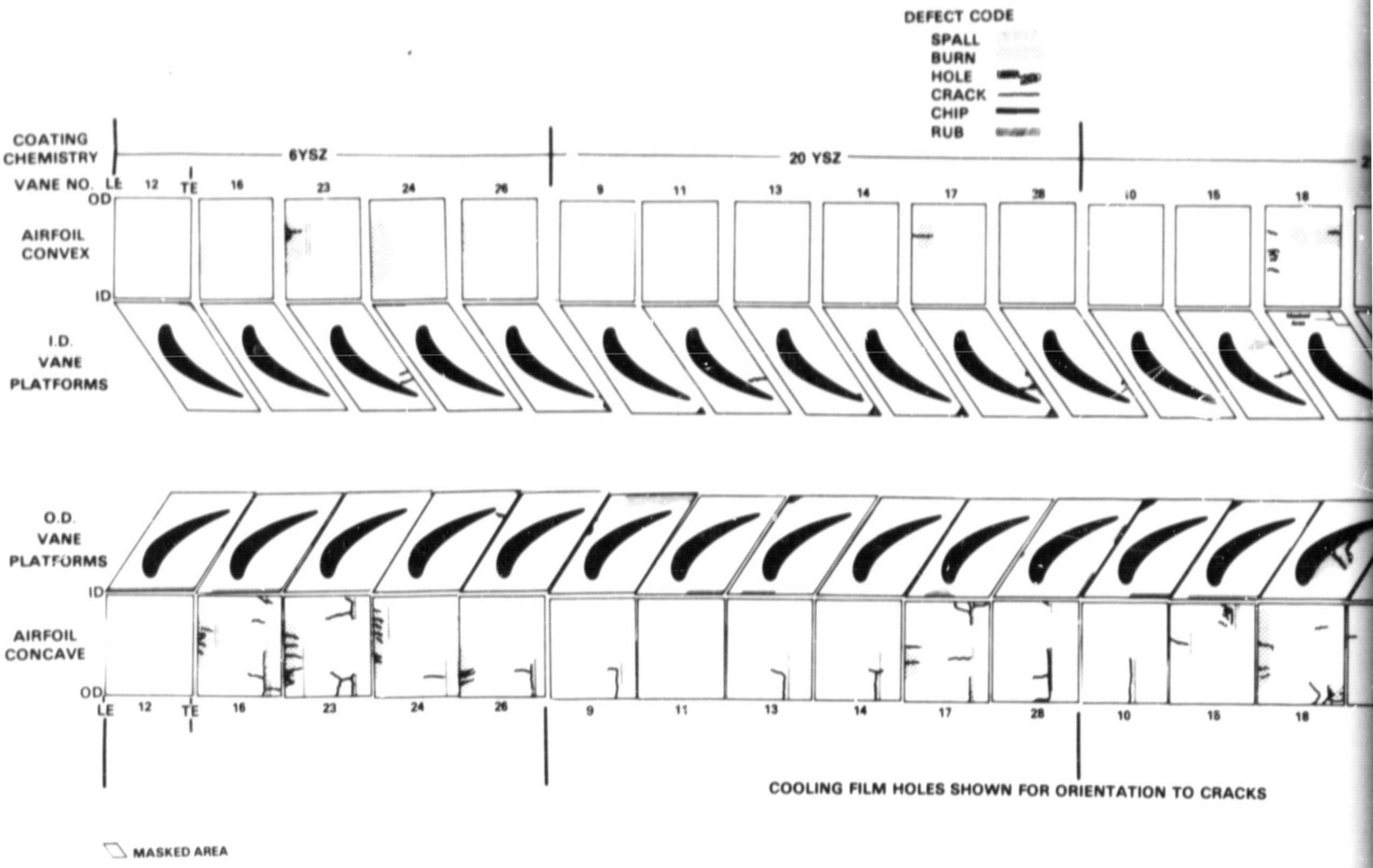

FOLDOUT FRAME

Figure 73 Schema
Initia

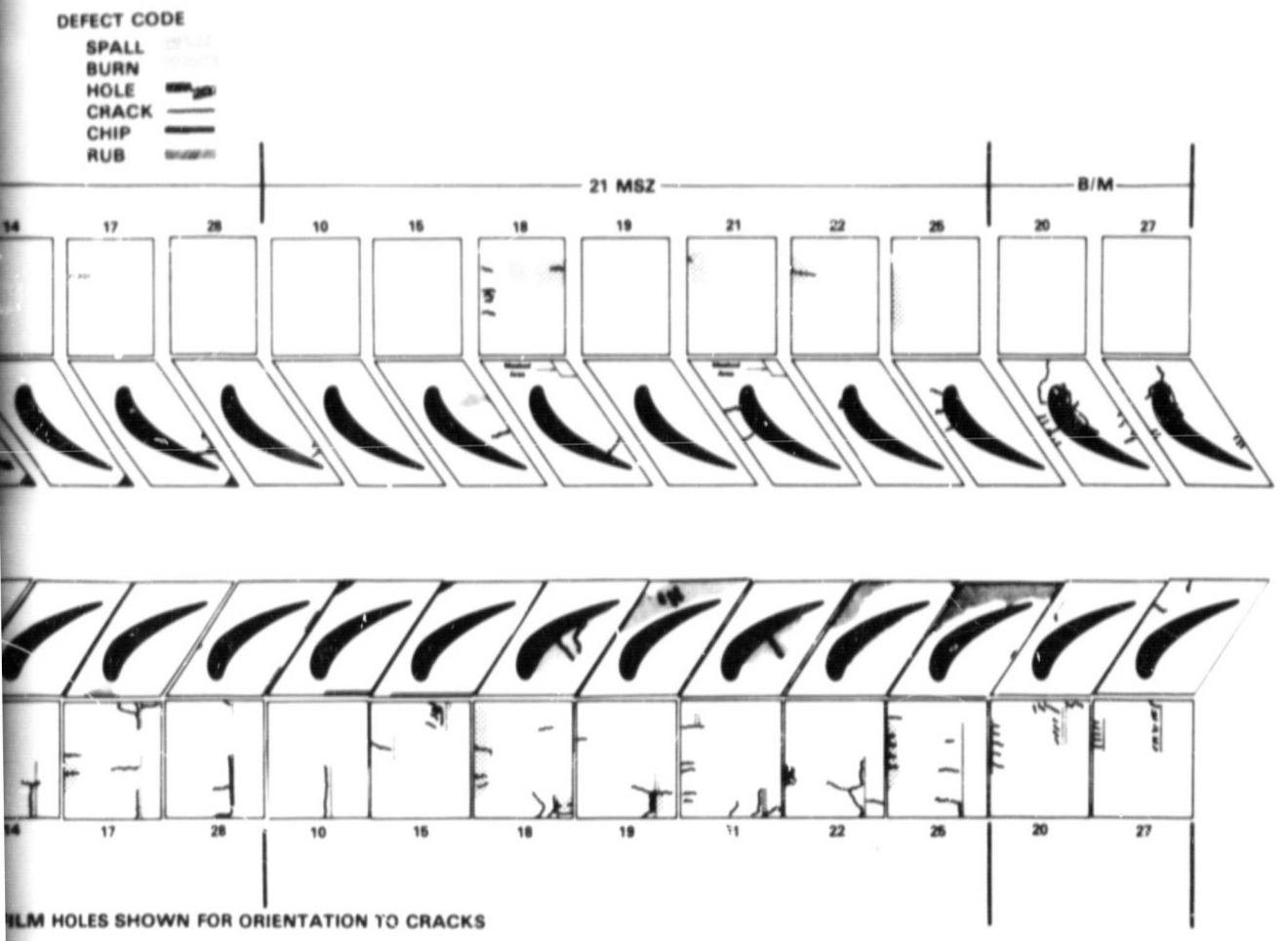

Figure 73 Schematic Representation of Vane Platform Condition Following Initial Engine Test.

The airfoil was also undercooled in the first design, evidenced by a greater degree of airfoil cracking than normal. Due to incomplete segregation of the airfoil and platform cooling air, more cooling airflow was going to the inner diameter platform (especially with the defective weld) and less to the airfoil than was planned. Segregation of airfoil and platform cooling air was included in the second design, eliminating this problem. This was accomplished using a parapet between the impingement plate and platform which acted as a flow dam that totally isolated airfoil and platform cooling air as shown in Figure 74.

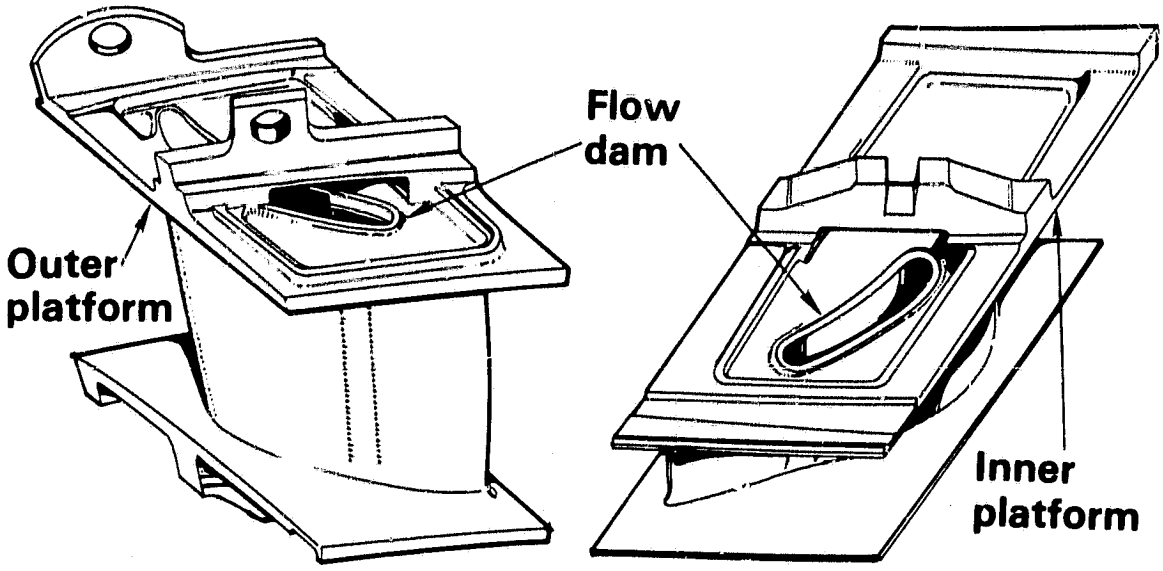

Figure 74 Vane and Platform Cooling Air Isolated by Flow Dams.

Some "hot spots" in the vane platform were identified by vane platform temperature measurements during initial engine testing. In general, the data indicated cool leading edges relative to hotter trailing edges. In the second design these hot areas were eliminated by redistributing the impingement plate hole pattern to cool these areas further. In addition, the trailing edge discharge flow area was increased and the exit holes skewed toward the hot gas path to provide increased cooling to the aft section of the platforms.

6.0 ENERGY IMPACT

The fuel saving potential of thermal barrier coatings applied to turbine vane platforms was estimated in the ECI-PI Feasibility Analysis (Ref. 1) based on performance, airline acceptability, and engine market projections available in 1977. This estimate has been updated to reflect a revision of the initial availability date. The original and updated estimates are both based on the 1977 market projections and are shown side-by-side in Table XIII for convenient comparison.

TABLE XIII

POTENTIAL FUEL SAVINGS EVALUATION
(World Fleet of JT9D Powered Aircraft)

	1977 Estimate	Current Estimate*
Start of service date	January 1982	June 1983
Fuel saving, percent	0.2	0.2
Number of engines affected:		
New buy	1620	*1200
Retrofit	2535	*3000
Total	4155	4200
Cumulative fuel saved through year 2005 10^6 liters (10^6 gal)		
New buy	560(1[illegible])	421(114)
Retrofit	420(111)	443(117)
Total	980(259)	874(231)

* Assumes airline acceptability in all JT9D engines as defined by the 1977 market projections.

The final engine test demomstrated that acceptable durability can be achieved with 44% reduction in cooling airflow with the combination of 6% YSZ coating and the final impingement cooling system configuration. This success implies that the TSFC improvements estimated in the 1977 study (Table XIV) can be achieved, and provides strong encouragement for airline acceptability. The initial application is in the JT9D-7R4G and H models, which entered airline service in March 1983. These are the most advanced and highest rated engines in the JT9D family.

TABLE XIV

1977 ESTIMATE OF ENGINE EFFECTS
(Per JT9D Engine)

TSFC improvement, %	
Takeoff	0.17
Climb	0.17
Average Cruise	0.17
Hold	0.17
EGT improvement, °C	
Takeoff	2
Climb	2
Weight change	0

	Engine Model	
	-7	-70/59/7Q
Price change, $	-5500	-35,000
Kit price (Attrition), $	-6300	-32,200 (Attrition)
Maintenance cost change, $/hr		
Materials	0	-1.35
Labor @ $30 per manhour	-1.10	-1.10

The 1977 analysis showed excellent airline acceptability, with negligible payback periods, as shown on Table XV, compared to an acceptability limit of 5 years (see Ref. 1). It is inappropriate to update the acceptablility evaluation at this time because the development of automatic plasma spray equipment is continuing in an effort to improve coating thickness control and reduce the cost of the thermal barrier coating system. However, because of the large acceptability margin in the 1977 evaluation and the expected benefits of the production development effort, it is reasonable to assume that the system will be acceptable to the airlines. For the updated fuel saving estimate shown on Table XIII, it was assumed that the system would be acceptable to the airlines in all JT9D models, including retrofit to all existing JT9D engines, starting in mid-1983.

TABLE XV

1977 ESTIMATE OF AIRLINE COSTS
(Per Aircraft)

Airplane Model	747-200		DC10-40
Operating Costs Changes, $/Year	Engine Model		
	-7	-70/7Q	-59
Fuel	-16,135	-17,330	-6,990
Maintenance	-20,100	-44,840	-25,220
Block Speed Effect	0	0	0
Total	-36,235	-62,170	-32,210

Type of Investment	New Buy		Retrofit		New Buy	Retrofit
Required Airline Investment Changes, $:	Engine Model					
	7	-70/7Q	7	-70/7Q	-59	-59
Installed Engines	-22,000	-140,000	-25,300	-128,800	-105,000	-96,600
Spare Engines	+5,000	-38,000	-6,900	-35,150	-24,150	-22,220
Spare Parts	-4,400	-28,000	-5,000	-25,760	-21,000	-19,320
Total	-32,400	-206,220	-37,200	-189,720	-150,150	-138,140
Payback Period, Years	0	0	0	0	0	0
DOC Change, %	-0.3	-0.3			-0.3	

APPENDIX A

TEST FACILITIES AND PROCEDURES

1.0 INITIAL ENGINE TEST

1.1 Test Configuration

Twenty test vanes were mounted in the high pressure turbine section area of the test engine (X-619) which was built to be equivalent to a bill-of-material JT9D-7Q production engine but was instrumented to a much greater degree than a production engine. The various coating systems, instrumentation, and cooling configurations that were used for each vane are given in Table A-I. There were two instrumented bill-of-material vanes among the 20 test vanes, for comparison purposes. The location of the test vanes in the engine are shown in Figure A-1.

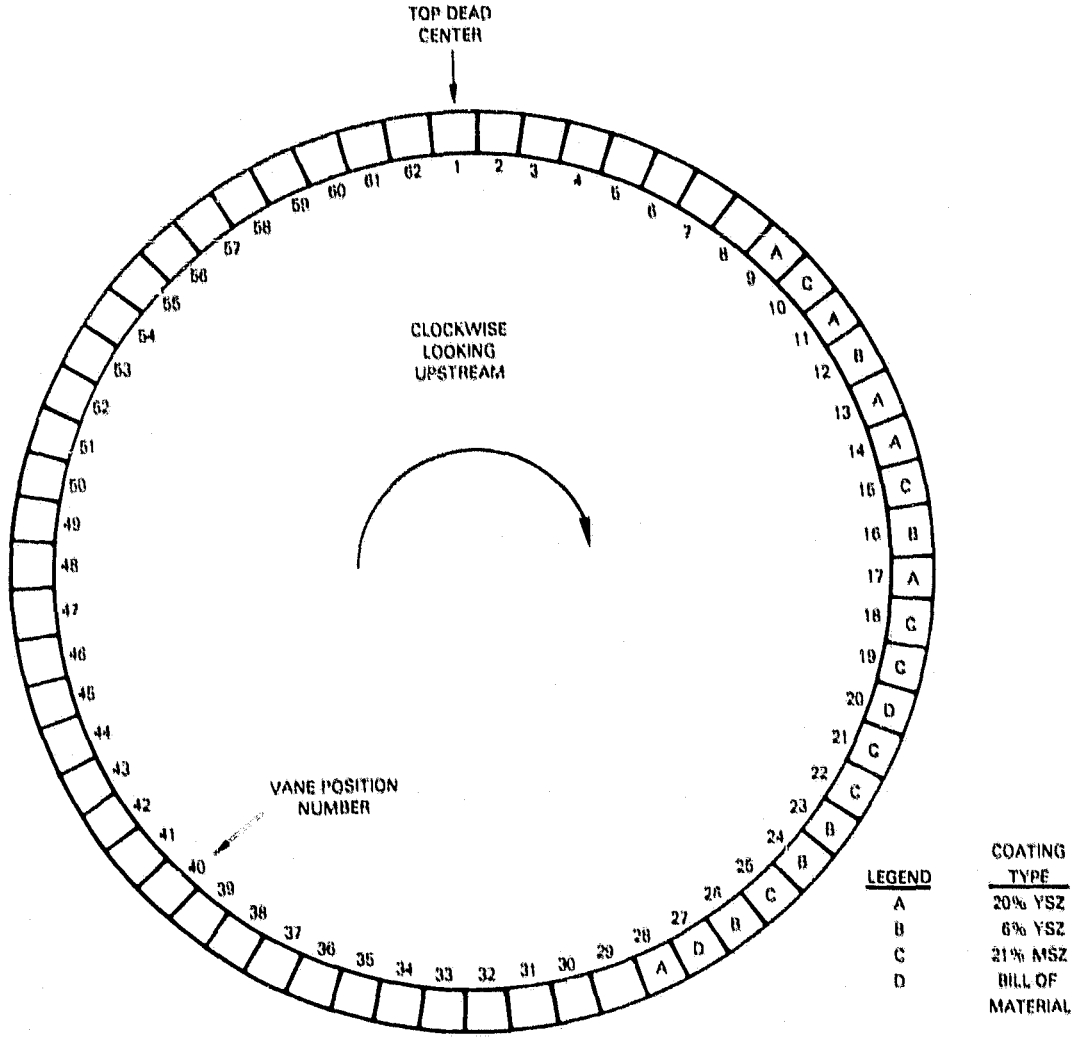

Figure A-1 Circumferential Locations of the Twenty Test Vanes. The vanes were mounted in the high pressure turbine section area of the test engine.

TABLE A-I

TEST CONFIGURATION

Vane Engine Position	Platform Coating System	Instrumentation Type	Platform Cooling Scheme
9	20% YSZ	Metal Thermocouple	Impingement
10	21% MSZ	Metal Thermocouple	Impingement
11	20% YSZ	Pressure Sensor	Impingement
12	6% YSZ	Metal Thermocouple	Impingement
13	20% YSZ	Air Thermocouple	Impingement
14	20% YSZ	Pressure Sensor	Impingement
15	21% MSZ	Non-instrumented	Impingement
16	6% YSZ	Non-instrumented	Impingement
17	20% YSZ	Air Thermocouple	Impingement
18	21% MSZ	Pressure Sensor	Impingement
19	21% MSZ	Metal Thermocouple	Impingement
20	B/M	Metal Thermocouple	Film
21	21% MSZ	Pressure Sensor	Impingement
22	21% MSZ	Air Thermocouple	Impingement
23	6% YSZ	Pressure Sensor	Impingement
24	6% YSZ	Air Thermocouple	Impingement
25	21% MSZ	Pressure Sensor	Impingement
26	6% YSZ	Air Thermocouple	Impingement
27	B/M	Metal Thermocouple	Film
28	20% YSZ	Metal Thermocouple	Impingement

YSZ - Yttria Stabilized Zirconia.
MSZ - Magnesium Stabilized Zirconia. Percentages of stabilizers are by weight.
B/M - Bill-of-Material Metallic.

All of the test vanes, except the bill-of-material, had a ceramic coating and an impingement cooling system.

1.2 Test Procedure

The basic test program was a Post-Certification Accelerated Cyclic Endurance Running (PACER) durability test. The specific power versus time endurance schedule is shown in Figure A-2. The cycle consists of operation at flight idle, simulated reverse, ground idle, takeoff, and a series of intermediate points. This endurance test accumulated 208 hours of engine time and 1000 thermal cycles. Total time at takeoff and simulated full reverse power levels was 83.3 hours. The test was run in B-150 stand, described in Section 1.4.

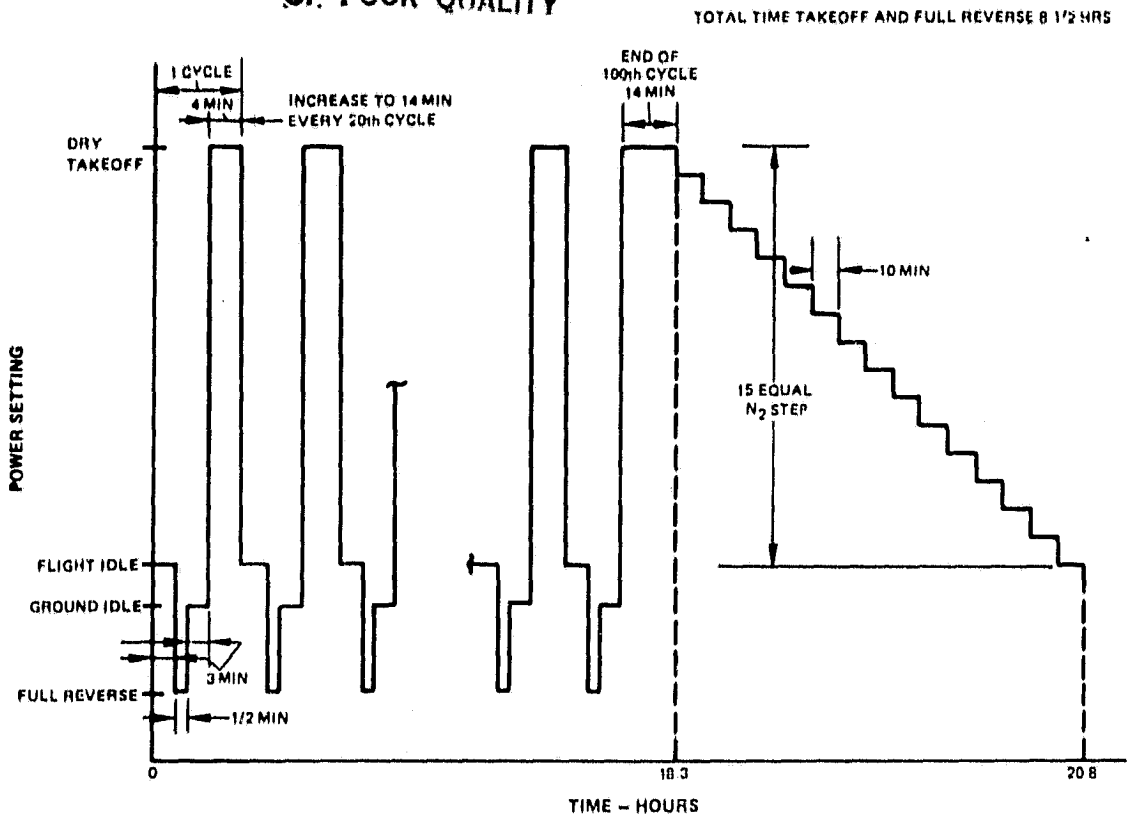

Figure A-2 Post-Certification Accelerated Cyclic Endurance Running (PACER) Procedure. This procedure accumulated 1000 thermal cycles for this durability test.

1.2.1 Pre-Cyclic Endurance Calibration Tests

A baseline calibration was run at the six points listed in Table A-II.

TABLE A-II

BASELINE CALIBRATION

Point No.	Observed Thrust N (lbf)	Stabilization Time Required Before Data Acquisition
1	minimum	10 min.
2	177,928 (40,000)	7 min.
3	200,169 (45,000)	7 min.
4	213,513 (48,000)	7 min.
5	226,858 (51,000)	7 min.
6	242,871 (54,600)	7 min.

1.2.2 Post Cyclic Endurance Calibration Tests

After completion of the basic cyclic engine endurance test, a post-endurance calibration was performed consisting of points 1 through 6 from the Pre-Cyclic Endurance Calibration Tests, given in Table A-II.

1.3 Instrumentation

1.3.1 Test Engine Instrumentation

The engine and stand instrumentation used in B-150 sea level test facility is shown in Table A-III.

TABLE A-III

INSTRUMENTATION FOR DURABILITY TEST OF
THERMAL BARRIER COATED VANES IN INITIAL ENGINE TEST

Parameter Name	Quantity and Description of Instrumentation
Atmospheric Pressure	1 Digital Barometer
Engine Inlet Total/Static Pressure	8 Pitot static probes - in place during calibrations only
Diffuser Case Static Pressure	1 Pressure transducer
Low Pressure Turbine Exit Total Pressure	6 Production rakes (manifolded)
Ambient Temperature	1 Air Thermocouple
Low Pressure Compressor Exit Total Temperature	2 Probes in Borescope ports
Turbine Exit Total Temperature	6 Production (rakes plus harness average
Low Pressure Compressor Rotor Speed	1 Hamilton Standard Tachometer
High Pressure Compressor Rotor Speed	1 Hamilton Standard Tachometer
Fuel Flow	2 Turbine meters
Flowmeter Temperature	2 Thermocouples
HPC Stator Vane and Bellcrank Angles (SVA)	2 Position potentiometers
Thrust	2 Load cells
Relative Humidity or Wet Bulb Temperature	1 Lithium bromide type sensor

1.3.2 Special Instrumentation and Accuracy

Three basic types of instrumentation were used to assess the effectiveness of the various thermal barrier coated turbine vane platforms: pressure sensors to measure cooling airflow pressure drops, thermocouples to measure the temperatures at the interface of the vane platform and thermal barrier coating, and air thermocouples to measure cooling airflow temperatures.

Sixteen of the test vanes with thermal barrier coated platforms and two of the test vanes with bill-of-material platforms had various combinations of pressure sensors, metal/ceramic interface thermocouples, and air thermocouples. The following sections describe the location and intent of the instrumentation packages. Specific reference to the installation of each instrumentation item is available on P&WA layout drawing L-110541 sheet 2.

1.3.2.1 Thermal Barrier Coated Platform Pressures

Inner diameter pressure instrumentation measured both the absolute cooling supply pressure and the pressure across the front and rear inner diameter impingment plates. Outer diameter pressure taps were installed to measure the absolute cooling air supply level, the pressure drop across the front and rear impingment plates, and the pressure drop resulting from the cooling air tunnel passage in the vane support assembly.

A schematic showing the locations of the pressure sensors is shown in Figure A-3. A typical pressure sensor installation is shown in Figure A-4. This type of installation was chosen because of the low velocity cooling air flow in the vane. The accuracy of the pressure sensor is within the accuracy of the data system, described in Section 1.4.2 of this appendix.

1.3.2.2 Thermal Barrier Coated Platform Air Temperatures

Air thermocouples located in inner and outer diameter platform cooling air cavities measure the cooling air supply temperatures before and after crossing the impingment plates. A bare wire sensor configuration was chosen for the air thermocouples to provide better temperature recovery and reduced conduction losses. Figure A-5 shows the air thermocouple configuration. The thermocouple locations are noted in Figure A-3. Conduction errors are considered negligible for this application due to the construction of the thermocouple cables. The thermocouples are made from ISA type "S" thermocouple wire, which has an accuracy of +1.4°C (+2.5°F) from 0 to 537°C (32 to 1000°F), and $\pm$0.25 percent from 537 to 1482°C (1000 to 2700°F).

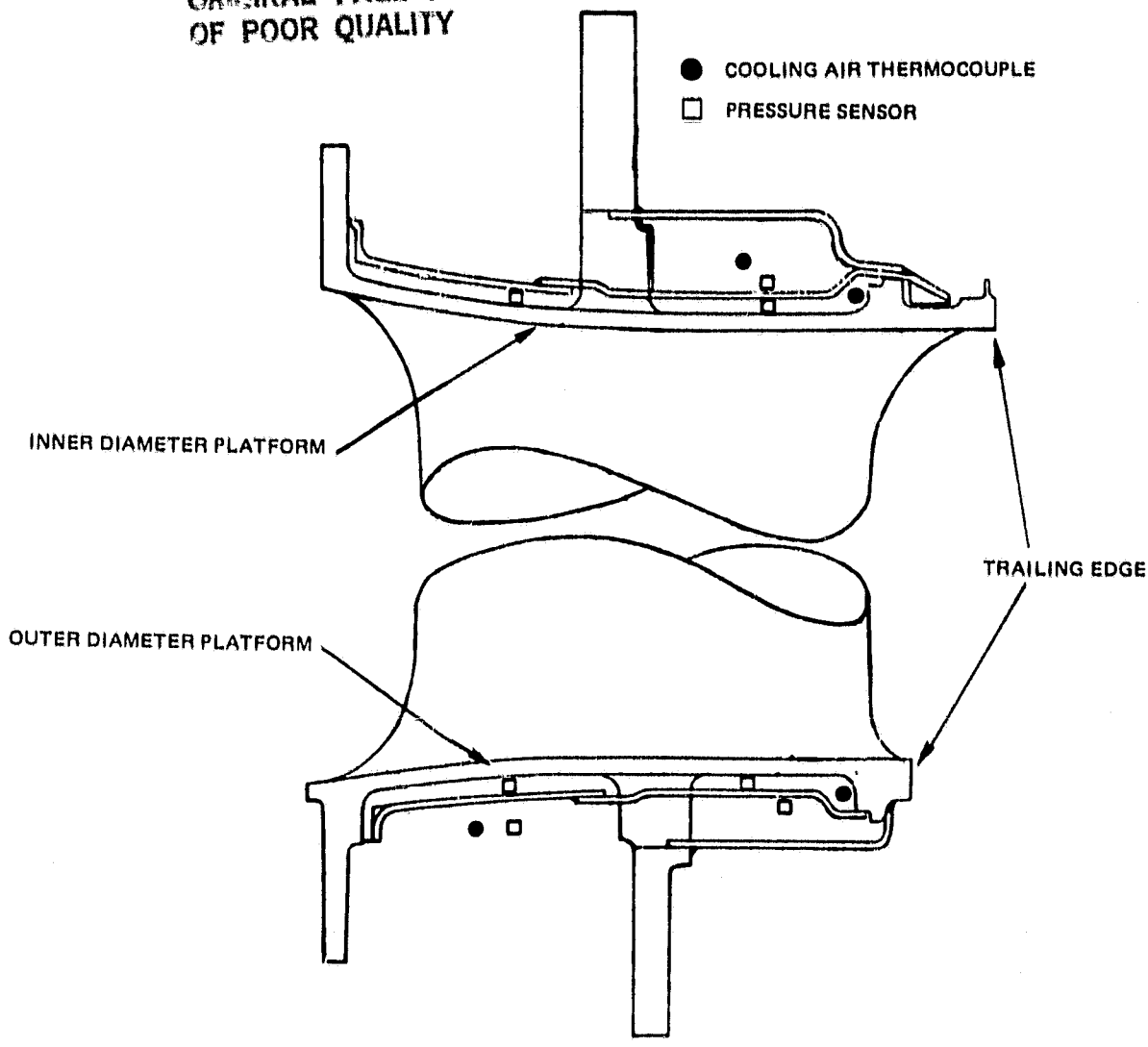

Figure A-3 Location of Pressure Sensors and Cooling Air Thermocouples.

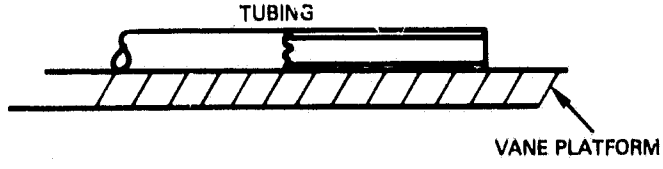

Figure A-4 Typical Pressure Sensor Installation. The tube has a 0.813 mm (0.032 inch) outer diameter, and a 0.508 mm (0.020 inch) inner diameter.

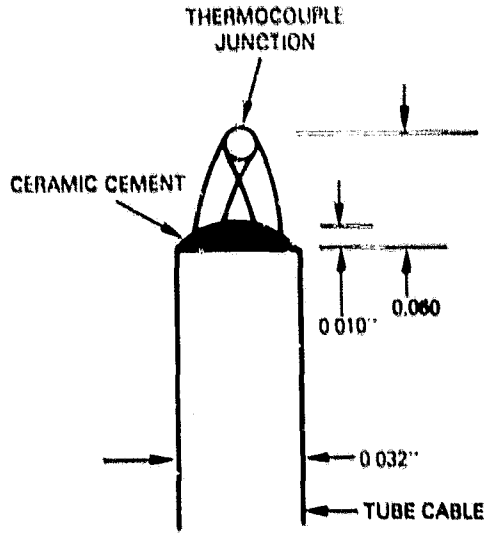

Figure A-5 Air Thermocouple Configuration. ISA Type "S" thermocouple wire; conduction effects from the cables are minimized. Dimensions noted are in inches.

1.3.2.3 Thermal Barrier Coated Platform Metal/Ceramic Interface Temperatures

The locations of the metal/ceramic interface thermocouples were selected at regions of the inner diameter and outer diameter platforms which experience the most severe thermal loads. Inner platform thermocouples were positioned at the trailing edge corners. Four thermocouple locations were selected to monitor the outer platform metal temperatures. Two of these were at the trailing edge corners where the highest platform temperatures were expected. A third sensor was located in the rear impingement plate region to determine the effectiveness of the impingement plates on cooling the platform. The remaining thermocouple was positioned at the forward acute corner of the platform to measure the platform metal temperature where active cooling is impractical to install. The locations of these four thermocouples provided a good representation of the outer platform temperatures. The locations shown schematically in Figure A-6 were based on both production engine experience and a finite element heat transfer analysis of the thermal barrier coated vane platforms with coolant impingement plates. Based on the analysis, a maximum temperature of about 1177°C (2150°F) was expected at the obtuse trailing edge corner of the platforms that experience the peak circumferential combustor temperatures. Metal temperatures in the other selected regions of the platforms was expected to be as high as 1093°C (2000°F).

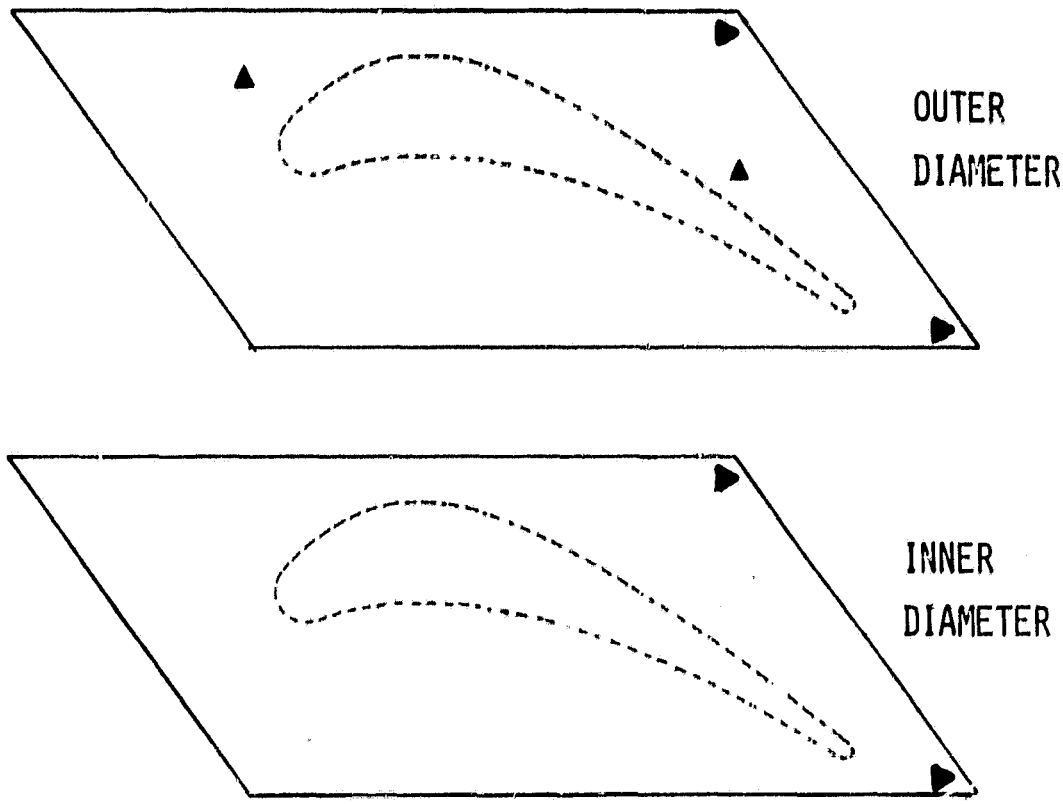

Figure A-5 Ceramic Coating/Vane Interface Thermocouple Locations. The locations of these thermocouples provided a good representation of the platform temperatures.

The metal thermocouples are also made of type "S" thermocouple wire, and are encapsulated within 0.050 cm (0.020 inches) of the ceramic/metal interface of the vane platform, as shown in Figure A-7. This configuration was chosen as the best for this type of application on the basis of durability, accuracy, and degree of difficulty in fabrication. An analysis which assumed a linear temperature gradient across the vane platform predicted that in the maximum temperature range expected during the test (1065 to 1176°C (1950 to 2150°F)) the thermocouple measurement was within 3.0 percent of the actual interface temperature.

1.3.2.4 Bill-of-Material Vane Platform Metal Temperatures

Two bill-of-material vanes were instrumented with four outer platform thermocouples and two inner platform thermocouples to compare cooling effectiveness of the bill-of-material film cooling scheme to that of the thermal barrier coated vane platforms with cooling air impingement plates. The thermocouple locations were approximately the same as those for the thermal barrier coated platform.

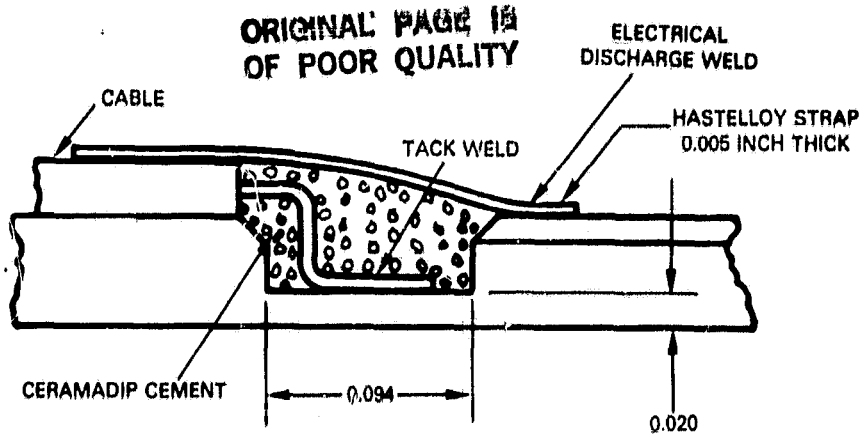

Figure A-7 Metal Thermocouple Configuration. The thermocouple junction was mounted in vane platform 0.508 mm (0.020 inch) from the ceramic coating/vane interface. Dimensions noted are in inches.

1.4 Test Facility

1.4.1 Test Facility Description

The engine was tested in B-150 at the Brown Field Test Facility of Rohr Industries, San Diego, California. B-150 stand is an open air, cantilever design, as shown in Figure A-8. It is sized to handle all engines currently in use. The stand is situated so that the inlet of an engine mounted on the stand faces west into the prevailing winds, reducing inlet distortion. Stand services include fuel analysis from the Rohr chemistry lab, and a large workshop for engine dressing, instrumentation calibration and repair.

1.4.2 Test Facility Data Acquisition Capabilities

Primary Data System

The Brown Field data acquisition system uses a Systems Engineering Laboratories' 810A computer. This data system uses a multiplexer in conjunction with a high speed digital computer and digital magnetic tape transport. The multiplexer samples each of 136 analog inputs at a rate of 100 samples per second. A sampling of all data channels can be taken at 1.36 second intervals for each test condition. The number of samples can be varied at the discretion of the test operator. A minimum of 30 samples is normal. Raw data is fed to the high speed digital computer which records the data on a Kennedy 3110 digital magnetic tape recorder. The tape can be used for off-line data reduction. The results of the on-line calculations are recorded on a Systems 733A high speed shuttle line printer and a Calcomp Model 525 X-Y Plotter.

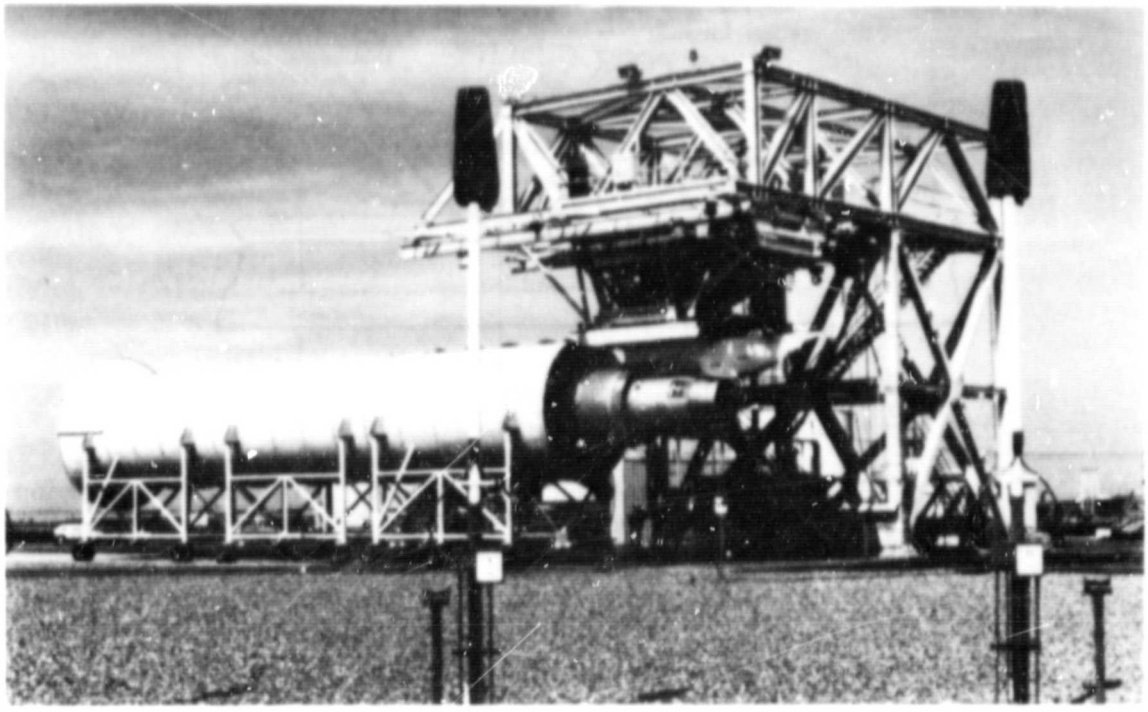

Figure A-8 JT9D Engine Mounted on B-150 Stand. The engine inlet faces west, to reduce inlet distortion from adverse winds.

With appropriate programming the above data system can be used for transient data recording directly onto magnetic tape in an output format for direct data reduction at P&WA. In this mode, almost any combination of pressures, temperatures and strain gages up to a total of 136 channels can be recorded. Another capability of the system is to display any output parameter in "real time". This means that performance parameters such as corrected thrust or corrected low pressure rotor speed can be displayed to the operator for power setting. The parameters that can be measured by the data system are shown in Table A-IV.

TABLE A-IV

MEASURABLE PARAMETERS

Parameter Description	Range Min.	Range Max.	Estimated Accuracy
Low Pressure Compressor Rotor Speed	0	4000 RPM	±5 RPM
High Pressure Compressor Rotor Speed	0	9000 RPM	±5 RPM
Gross Thrust (2)	0	257,997 N (58000 lbf)	±0.25% Full Scale
Ambient Pressure	97 (14.0)	105 kPa (15.3 PSIA)	±0.07% Full Scale
Fan Discharge Total Pressure	0	103 kPa (15 PSIG)	±0.25% Full Scale
High Pressure Compressor Discharge Static Pressure	0	2,758 kPa (400 PSIG)	±0.25% Full Scale
Low Pressure Turbine Discharge Total Pressure	0	103 kPa (15 PSIG)	±0.25% Full Scale
8 Separate Engine Inlet Static Pressure	0	±34 kPa (±5 PSID)	±0.25% Full Scale
Fan Face Total Static to Differential Pressure (8)	0	-305 cm (-120 in) H_2O	±0.5% Full Scale
Fan Face Total Pressure (8)	-1 (-0.15)	1.0 kPa (+0.15 PSID)	±5% Full Scale
Ambient Temperature	0	38°C (100°F)	±0.5°F
Inlet Temp	C (32)	38°C (100°F)	±0.5°F
High Pressure Turbine Discharge Total Temperature	0	1093°C (2000°F)	±0.5% of Reading
Low Pressure Turbine Exit Total Temperature	0	760°C (1400°F)	±0.5% of Reading
Fuel Sample Temperature	0	38°C (100°F)	±1°F

TABLE A-IV(Continued)

MEASURABLE PARAMETERS

Parameter Description	Range Min.	Range Max.	Estimated Accuracy
Fuel Sample Specific Gravity	0.73	.87	±0.15% of Reading
Fuel Inlet Temperature (2)	0	38°C (100°F)	±0.7°C (±1°F)
Fuel Flow (2)	20	65 GPM	±0.25% of Reading
Stator Vane Angle	-40°	+15°	±1°
Power Lever Angle	60°	130°	±1°
Wind Speed	0	48 km/hr (30 MPH)	±0.8 km/hr (±0.5 MPH)
Wind Direction	0	360°	±5°
Relative Humidity	0	100%	±5% Full Scale
Low Pressure Compressor Total Temperature	0	152°C (305°F)	±0.5% of Reading
High Pressure Compressor Total Temperature	0	649°C (1200°F)	±0.5% of Reading
Low Pressure Compressor Total Pressure	0	172 kPa (25 PSIG)	±0.25% Full Scale
Low Pressure Compressor Static Pressure	0	172 kPa (25 PSIG)	±0.25% Full Scale

Secondary Data System

The High Accuracy Pressure and Temperature Data Acquisition System was used in addition to the B-150 stand data system. The High Accuracy Pressure and Temperature Data Acquisition System is portable and has the capacity to record up to 400 inputs (bipolar millivolt) and 336 pressure inputs on eight 48-port scanivalve transducers. The channel capacity at B-150 stand is limited to the number of 61-pin cables and portable pressure lines installed at the stand. Each 61-pin cable provides 20 inputs. Thirty five temperatures and 16 pressures were recorded on the High Accuracy Pressure and Temperature Data Acquisition System in B-150 stand in support of the Thermal Barrier Coating Endurance Test. Data is recorded at a rate of 20 channels per second for temperature and 11 channels per second for pressures. Data is scanned, digitized by an integrating digital volt-meter, and recorded on magnetic tape.

Special features of the data recording system include:

1. Channel delete capability
2. Three wire guarded system
3. Variable start and end point scan selection
4. Manual channel monitoring
5. Secondary pressure calibrations

Temperatures

All International Standards Association type "K" and type "S" thermocouples were routed through Uniform Temperature Reference units. Each unit has 30 input channels, which include an ice point reference (0°C (32°F)) supplied by a Joseph Kaye Ice Point Cell.

Pressures

All pressure measurements were recorded on 48-port scanivalved transducer using 400 psig transducers.

Data Reduction for High Accuracy Pressure and Temperature Data Acquisition System

Data recorded on the High Accuracy Pressure and Temperature Data Acquisition System were transmitted to the Sigma 8 computer system located in the Pratt & Whitney Aircraft Engineering Building in East Hartford, via telephone trasmission lines. Data were processed on-line with hardcopy and computer cards generated in East Hartford. In addition, data were recorded on the High Accuracy Pressure and Temperature Data Acquisition System magnetic tape unit and were processed off-line (after the engine test) on the Sigma 8 computer if necessary.

The accuracy of the High Accuracy Pressure and Temperature Data Acquisition System, exclusive of probe and thermocouple wire accuracy, is listed in the following tabulation:

Pressure

$\pm$0.1% Full Scale of Transducer Range

Temperature

Chromel/Alumel - Type "K"; $\pm$0.25°C ($\pm$0.45°F)

Platinum/Platinum 10 percent Rhodium - Type "S"; $\pm$0.6°C ($\pm$1.00°F)

2.0 FINAL ENGINE TEST

2.1 Test Configuration

The same JT9D-7Q experimental engine (X-619) that was used in the initial test was also used in the final engine test. Twenty-six test vanes were positioned around the entire annulus of the test engine's high pressure turbine. The vane positions, coating systems, instrumentation, and cooling configurations that were used for each vane are given in Table A-V. There were two instrumented bill-of-material vanes among the 26 test vanes, for comparison purposes. Also included in the 26 vanes were two vanes with thermal barrier coated platforms that had been tested in the initial engine test and had accumulated a total of 2033 PACER cycles and 454 hours hot time during subsequent testing. The locations of the test vanes in the engine are shown in Figure A-9. These locations were selected to provide similar heat loads to vanes coated with different coating systems.

2.2 Test Procedure

Prior to the endurance test, a company-funded nacelle performance test was run in Rohr Industries' B-150 stand. Although the test did not affect the results of the final endurance test, airfoil leading edge distress which occurred during the performance test required removal of two vanes with ceramic coated platforms prior to running the endurance test (vane positions 5 and 24 were replaced with P&WA test vanes). A description of this testing is given in Table A-VI.

The basic endurance test program was a Post-Certification Accelerated Cyclic Endurance Running (PACER) durability test, modified to conserve fuel. The cycle consisted of operation at ground idle, takeoff and a series of intermediate points repeated every hundredth cycle. The specific power versus time endurance schedule is shown in Figure A-10. This endurance test accumulated 159 hours of engine time and 1500 thermal cycles. Total time at takeoff was 54 hours. The test was run in C-10 stand, described in Section 2.4 of this appendix.

2.2.1 Pre-Cyclic Endurance Calibration Tests

A baseline calibration was run at the six points listed in Table A-VII.

2.2.2 Post-Cyclic Endurance Calibration Tests

Post calibration tests were combined with the basic cyclic engine endurance test to conserve fuel. After completion of the 1500th PACER cycle, the twelve equal 7 minute steps of N2 (see Figure A-10) were substituted with steps similar to points 1 through 11, as shown in Table A-VI.

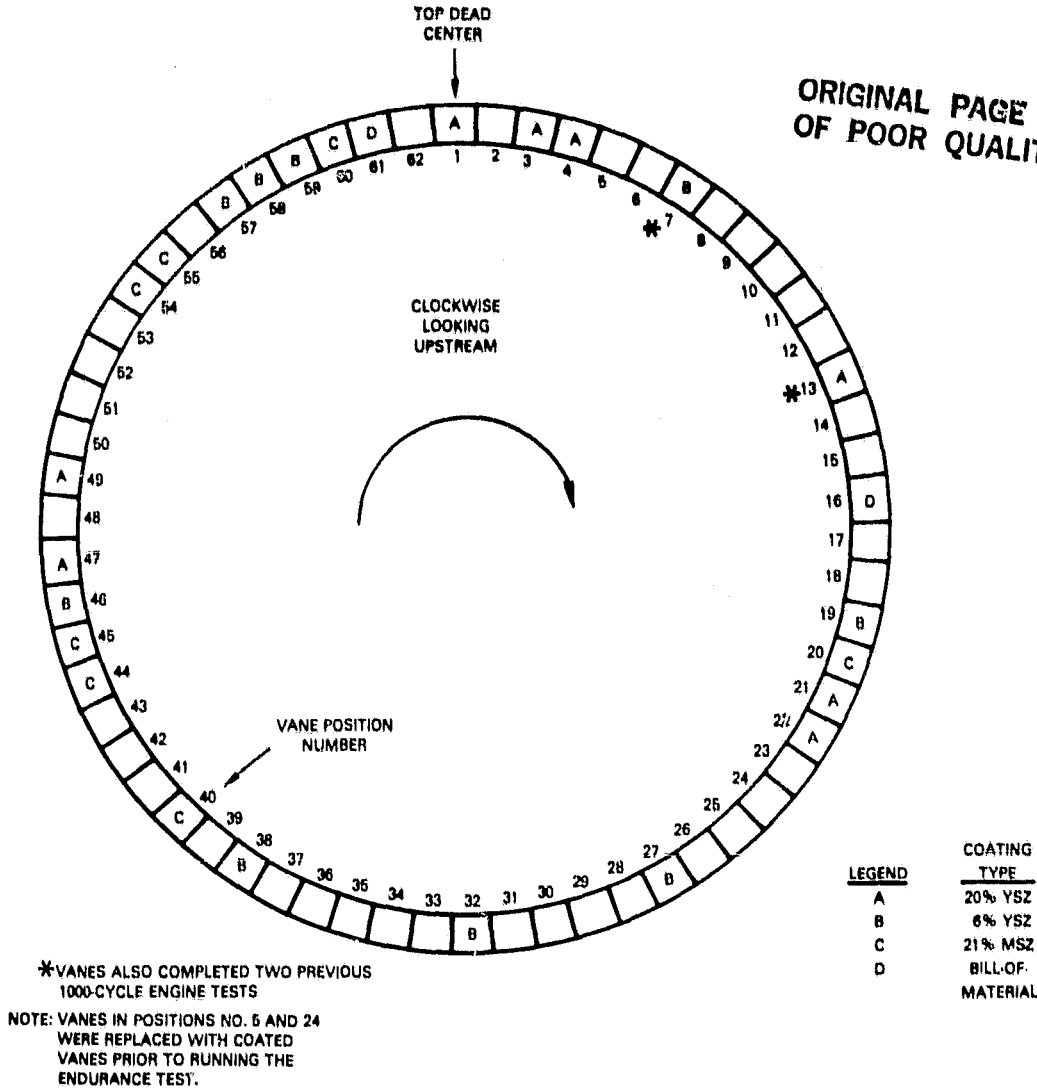

Figure A-9 Circumferential Location of the Twenty-Six Test Vanes. The vanes were mounted in the high pressure turbine section area of the test engine.

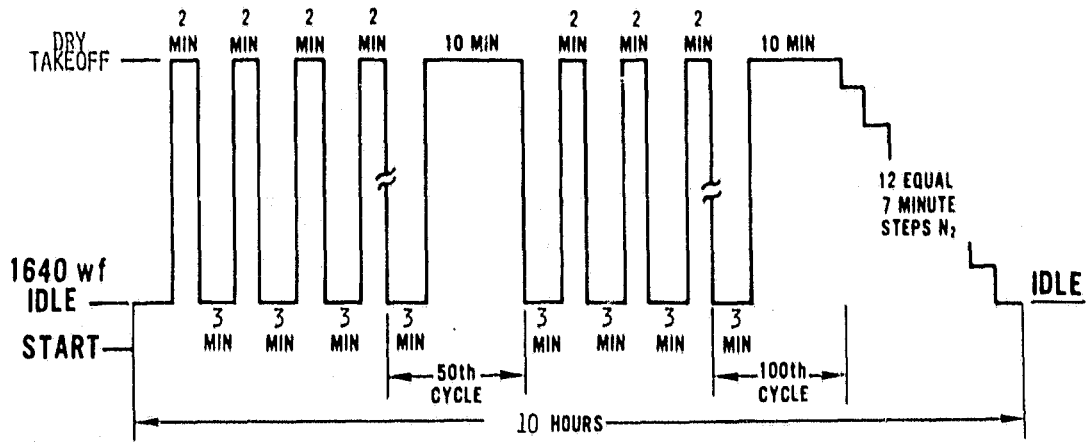

Figure A-10 Post-Certification Accelerated Cyclic Endurance Running (PACER) Procedure. The cycle was modified from the original PACER cycle to conserve fuel. The test engine accumulated 1500 thermal cycles using this procedure.

2.3 Instrumentation

2.3.1 Test Engine Instrumentation

The engine and stand instrumentation used in the C10 sea level test facility is given in Table A-VIII.

TABLE A-V

TEST CONFIGURATION

Vane Engine Position	Coating System	Instrumentation	Platform Cooling Scheme
1	20% YSZ	OD Metal Thermocouples	Impingement
3	20% YSZ	OD Air Thermocouple	Impingement
4	20% YSZ	OD Metal Thermocouple	Impingement
5*	21% MSZ	Non-instrumented	Impingement
7	6% YSZ	Non-instrumented	Impingement
13	20% YSZ	Non-instrumented	Impingement
16	Bill-of-Material	OD Metal Thermocouples	Film
19	6% YSZ	Non-instrumented	Impingement
20	21% MSZ	Non-instrumented	Impingement
21	20% YSZ	Non-instrumented	Impingement
22	20% YSZ	ID Metal Thermocouples	Impingement
24*	20% YSZ	Non-instrumented	Impingement
27	6% YSZ	Non-instrumented	Impingement
32	6% YSZ	OD Metal Thermocouples	Impingement
38	6% YSZ	Non-instrumented	Impingement
40	21% MSZ	Non-instrumented	Impingement
44	21% MSZ	OD Pressure Sensor	Impingement
45	21% MSZ	OD Metal Thermocouples	Impingement
46	6% YSZ	OD Pressure Sensor	Impingement
47	20% YSZ	Non-instrumented	Impingement
49	20% YSZ	Non-instrumented	Impingement
54	21% MSZ	Non-instrumented	Impingement
55	21% MSZ	Non-instrumented	Impingement
57	6% YSZ	OD Metal Thermocouple	Impingement
58	6% YSZ	Non-instrumented	Impingement
59	6% YSZ	OD Air Thermocouple	Impingement
60	21% MSZ	Non-instrumented	Impingement
61	Bill-of-Material	OD Metal Thermocouples	Film

YSZ - Yttria Stabilized Zirconia
MSZ - Magnesium Stabilized Zirconia

Percentages of stabilizers are by weight

*Replaced with P&WA test vanes at end of performance tests.

Note: Vanes 7 and 13 completed two previous 1,000 cycle engine tests.

TABLE A-VI

PRATT & WHITNEY AIRCRAFT FUNDED
ENGINE PERFORMANCE TEST PROGRAM

Point Number	Corrected Net Thrust - N (lbf)	Stabilization Time (minutes)
1	244,652 (55,000)	7
2	235,756 (53,000)	5
3	226,859 (51,000)	5
4	213,515 (48,000)	5
5	200,170 (45,000)	5
6	186,825 (42,000)	5
7	173,481 (39,000)	5
8	155,688 (35,000)	5
9	88,964 (20,000)	5
10	66,723 (15,000)	5
11	Ground Idle	5

(This test sequence was repeated four times)

TABLE A-VII

BASELINE CALIBRATION

Observed Point No.	Stabilization Time Thrust - N (lbf)	Required Before Data Acquisition
1	minimum	10 min.
2	177,929 (40,000)	7 min.
3	200,170 (45,000)	7 min.
4	213,515 (48,000)	7 min.
5	226,859 (51,000)	7 min.
6	242,873 (54,600)	7 min.

TABLE A-VIII

ENGINE INSTRUMENTATION FOR DURABILITY TEST OF
THERMAL BARRIER COATED VANES IN FINAL ENGINE TEST

Parameter Name	Quantity and Description of Instrumentation
Engine Inlet Total/Static Pressure	8 Pitot static probes - in place during calibrations only
Diffuser Case Static Pressure	1 Pressure transducer
Low Pressure Turbine Exit Total Pressure	6 Production rakes (manifolded)
Ambient Temperature	1 Air Thermocouple
High Pressure Compressor Exit Total Temperature	2 Probes in Borescope ports
Turbine Exit Total Temperature	6 Production Rakes (manifolded)
Low Pressure Compressor Rotor Speed	1 Tachometer
High Pressure Compressor Rotor Speed	1 Tachometer
Fuel Flow	2 Turbine meters
Fuel Temperature	2 Thermocouples in turbine meters
High Pressure Compressor Stator Vane and Bellcrank angles	2 Potentiometers

2.3.2 Special Instrumentation and Accuracy

As in the first engine test, three types of instrumentation was used to assess the effectiveness of the various thermal barrier coated first stage turbine vane platforms: pressure sensors to measure cooling airflow pressure drop, metal thermocouples to measure the temperatures at the interface of the vane platform and thermal barrier coating, and air thermocouples to measure cooling airflow temperatures. Cable routing was carefully chosen to minimize the possibility of obstructing the cooling airflow path of the instrumented vanes.

Ten of the test vanes with thermal barrier coated platforms and two test vanes with bill-of-material platforms had various combinations of pressure sensors, metal/ceramic interface thermocouples, and air thermocouples. The following sections describe the location and intent of the instrumentation packages. (Specific reference to the installation of each instrumentation item is available on Pratt & Whitney Aircraft layout drawing L-112307, sheet 2.)

The locations of the special instrumentation were selected to allow evaluation of the ceramic coating performance over a wide range of metal/ceramic layer interface temperatures in the engine environment.

Metal/ceramic interface thermocouple locations were selected at regions of the inner diameter and outer diameter platforms which include the most severe thermal loads. The locations of the metal/ceramic interface thermocouples shown schematically in Figure A-11 were based on the previous engine test experience and a finite element heat transfer analysis of the thermal barrier coated vane platforms with improved coolant impingement plate hole patterns. Pressure sensor locations for measuring cooling air supply level and pressure drop through the impingment plates and cooling air thermocouple locations are shown in Figure A-12.

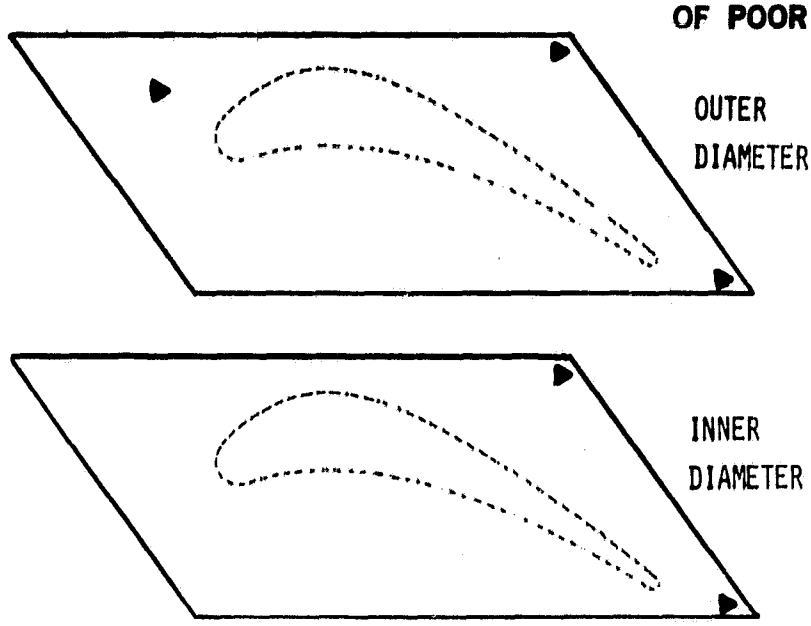

Figure A-11 Ceramic Coating/Vane Interface Thermocouple Locations. The locations of these thermocouples provided a good representation of the platform temperatures.

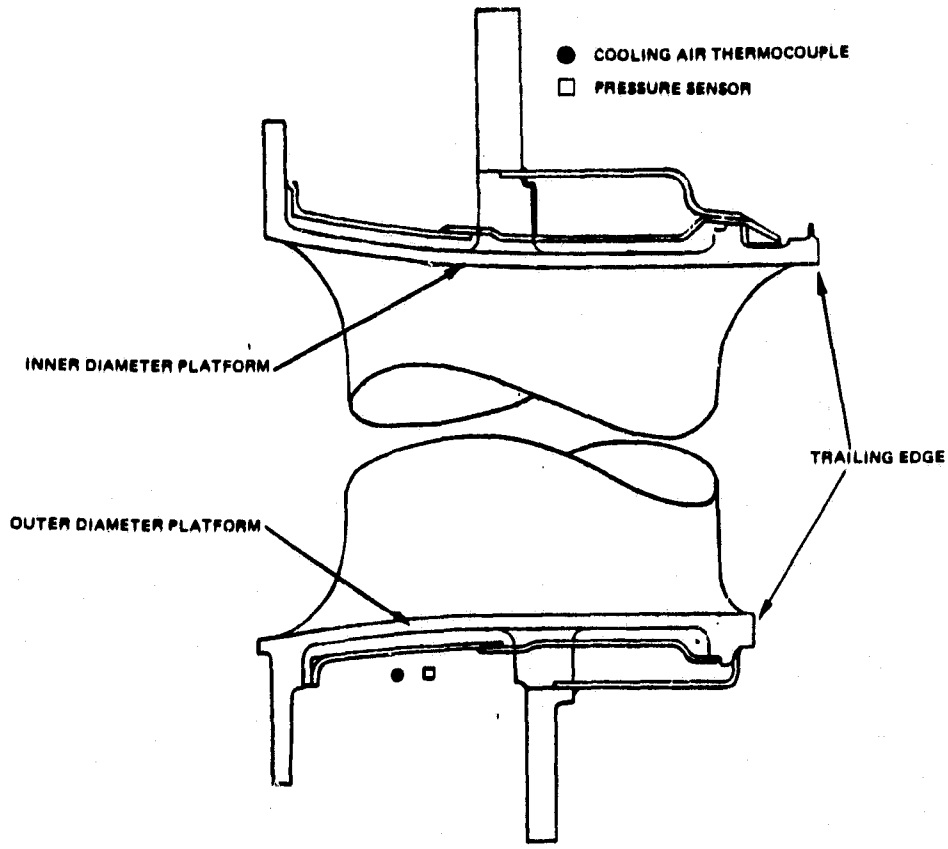

Figure A-12 Typical Locations of Pressure Sensors and Cooling air Thermocouples.

A typical pressure sensor installation is shown in Figure A-13. This type of installation was chosen for reliability, and is especially suited for regions of low velocity cooling air flow. The accuracy of the pressure sensors are within the accuracy of the data system, described in Section 2.4.4 of this appendix.

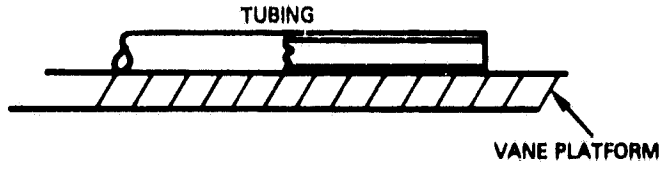

Figure A-13 Typical Pressure Sensor Installation. The tube has a 0.813 mm (0.032 inch) outer diameter, and a 0.508 mm (0.020 inch) inner diameter.

A bare wire sensor configuration was chosen for the air thermocouples to provide better response and reduced conduction losses. Figure A-14 shows the air thermocouple configuration. The air thermocouples were constructed of 0.081 cm (0.032 inch) diameter chromel alumel wire for improved durability with respect to the final engine test without loss of accuracy. Conduction errors are considered negligible for this application due to the construction of the thermocouple cables. The thermocouples are made from "K" thermocouple wire, which has an accuracy of +1.1°C (+2.0°F) from 0 to 277°C (32 to 530°F) and ±0.375% from 277 to 1260°C (530°F to 2300°F).

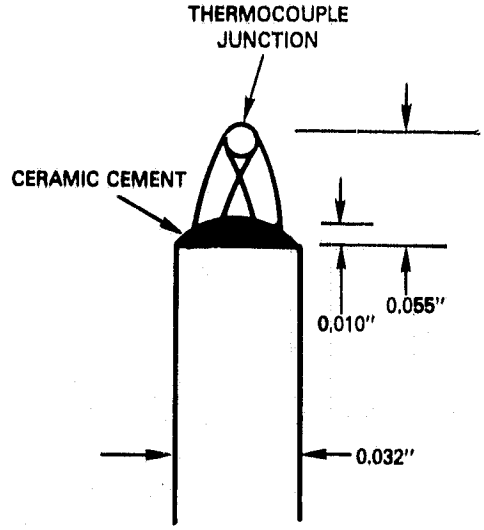

Figure A-14 Air Thermocouple Configuration. ISA type "K" thermocouple wire. The thermocouple is designed to minimize response time and conduction errors, while maintaining the durability necessary for the test. Dimensions are in inches.

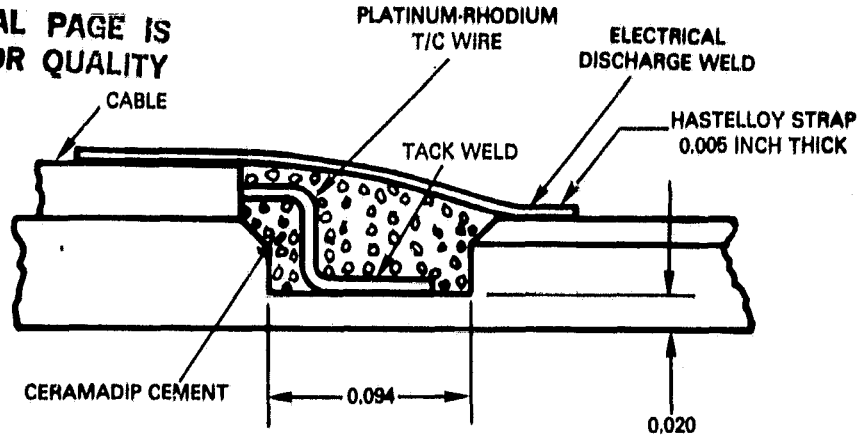

Figure A-15 Metal Thermocouple Configuration. The thermocouple is mounted 0.050 cm (0.020 inches) from the ceramic coating/vane interface, and is estimated to have a bias of only 3.0% from the true interface temperature. Dimensions are in inches.

The metal/ceramic interface thermocouples are made of type "S" thermocouple wire, and are encapsulated within 0.051 cm (0.020 inches) of the ceramic/metal interface of the vane platform, as shown in Figure A-15. This configuration, which is an improvement over the configuration used in the first engine endurance test, was chosen as the best for this type of application on the basis of durability, accuracy, and ease of fabrication. Durability of the metal/ceramic interface thermocouples was improved by using shorter wire lengths between the sheathing and weld bead. An analysis which assumed a linear temperature gradient across the vane platform predicts that in the temperature range expected during the test the thermocouple measurement was within 3.0 percent of the actual interface temperature.

2.3.2.1 Outer Diameter Platform Metal Temperatures

Thermocouple locations selected to monitor the outer platform metal temperatures are shown in Figure A-11. Two of these are at the trailing edge corners where the highest platform temperature gradients are expected. One thermocouple was positioned at the forward acute corner of the platform to measure the platform metal temperature where substantive cooling is impractical to install. The locations of these thermocouples provided a good representation of the outer platform temperatures.

2.3.2.2 Outer Diameter Platform Cooling Air Temperatures and Pressure

Air thermocouples were located on the outer platform to measure the cooling air temperature before crossing the impingement plate. Pressure taps were installed to measure the absolute cooling air supply level and allow determination of the cooling airflow traveling through the impingement plates.

2.3.2.3 Inner Diameter Platform Metal Temperatures

Thermocouple locations on the inner platform are shown in Figure A-11. Two thermocouples located at the trailing edge corner are expected to measure the highest metal temperatures. The corner locations were selected based on the design analysis, which predicted these regions to operate at the highest temperature.

2.3.2.4 Bill-of-Material Vane Platform Metal Temperatures

Two bill-of-material vanes were instrumented with three outer platform thermocouples to compare cooling effectiveness of the bill-of-material film cooling scheme to that of the thermal barrier coated vane platforms with cooling air impingement plates. The thermocouple locations covered approximately the same trailing edge corner areas as those for the thermal barrier coated platforms, and are shown in Figure A-16.

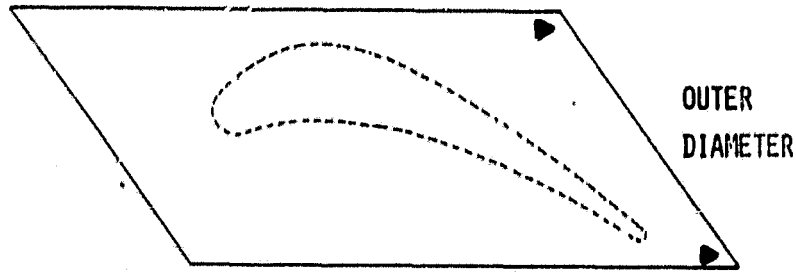

Figure A-16 Bill-of-Material Vane Thermocouple Locations. The locations of these thermocouples provided a good representation of the platform temperatures.

2.3.3 Pre-Endurance Test Airflow Calibration

Sixteen vanes were diagnostically flow checked to determine inner and outer diameter platform flows prior to engine testing. The remaining test vanes contained platform metal thermocouples and could not be airflow checked due to the routing path of the instrumentation leads. The results of the airflow calibration are shown in Table A-IX. The lower limit of the tolerance flow band in terms of airflow parameter was 2.68×10^{-3} and 3.10×10^{-3} for the inner and outer diameter platforms, respectively. Three outer platform flows which did not meet this minimum requirement were subsequently passed for engine testing based on previous engine experience of thermal barrier coated platforms. The airflow parameter is $W\sqrt{T}/Pa$, where:

W	Airflow, lbm/sec
T	Temperature, °R
P_a	Absolute Pressure, lb/in^2 absolute

TABLE A-IX
PRE-TEST AIRFLOW CALIBRATION RESULTS

Vane Engine Position	Airflow Parameter, $W\sqrt{T/Pa} \times 10^3$ Inner Diameter Platform	Outer Diameter Platform
03	3.643	3.215
19	3.688	3.910
20	3.950	4.218
21	3.134	3.107
27	4.455	3.443
38	4.819	3.429
40	3.312	3.728
44	4.248	3.792
46	3.526	4.131
47	4.200	3.697
49	3.090	2.890
54	2.876	3.635
55	2.778	2.789
58	2.881	4.249
59	3.865	4.003
60	3.533	2.700

2.3.4 Post-Endurance Test Airflow Calibration

Four vanes were selected for airflow checks of the inner and outer diameter platforms following engine testing. The results which are given in Table A-X indicate minimum flow requirements were maintained during the engine test.

TABLE A-X
POST-TEST AIRFLOW CALIBRATION RESULTS

Vane Engine Position	Airflow Parameter, $W\sqrt{T/Pa} \times 10^3$ Inner Diameter Platform	Outer Diameter Platform
19	4.03	3.727
38	3.95	3.712
49	2.80	3.269
60	3.11	3.360

2.4 Test Facility

2.4.1 Test Facility Description

The C-10 stand is a full scale, sea level engine test facility located in Pratt & Whitney Aircraft's Government Products Division test complex near West Palm Beach, Florida. The facility is designed to handle up to 333,617 N (75,000 lbf) of forward thrust, and 111,206 N (25,000 lbf) reverse thrust. Endurance testing of engine/ nacelle configurations and performance compliance testing can be performed on the stand. The stand is capable of testing JT9D, F100, JT8D, and TF30 engines.

The test stand is designed to simulate an airplane wing mounting by locating the engine ahead and away from interfering structures. The test stand structure is built on a 30 x 37 x 5 ft thick concrete foundation, located in a 200 x 150 ft asphalt-paved test area. A test facility layout is shown in Figure A-17. The stand consists of three vertical columns 2 feet in diameter, with a horizontal arm extending out from the columns. When installed in the stand, the engine centerline is 9 ft from the centerline of the vertical columns, and 14 to 16 ft above the paved surface, depending upon the type of engine being tested.

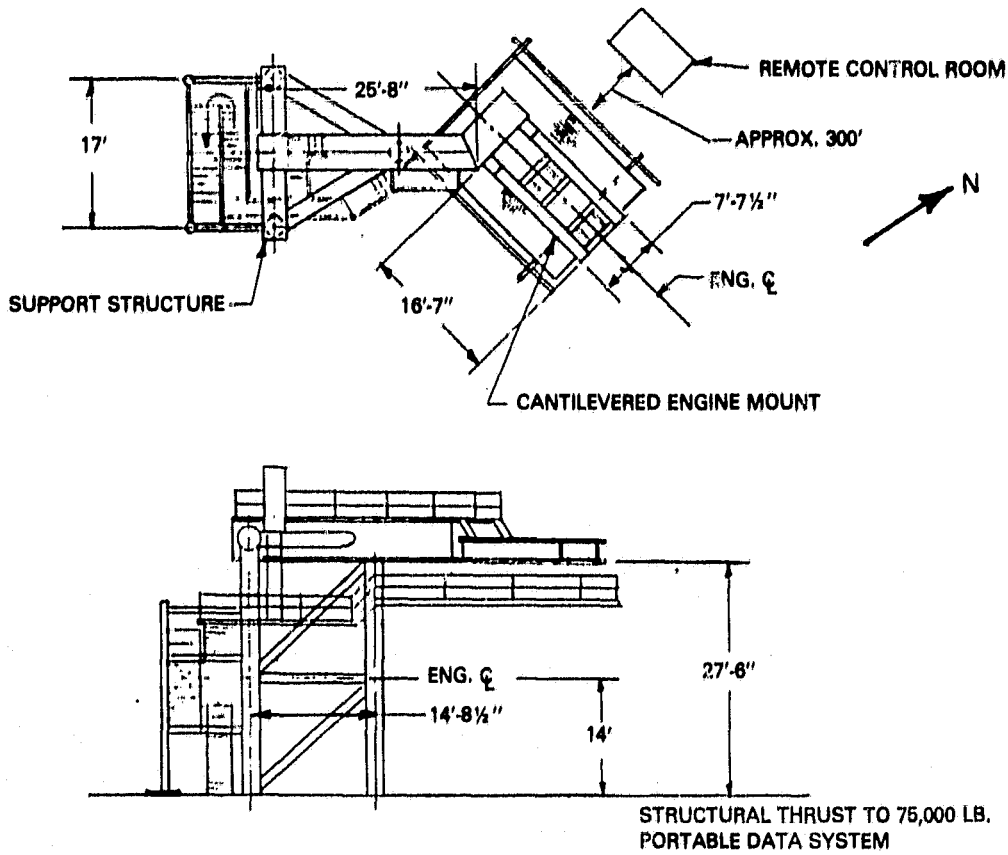

Figure A-17 C-10 Test Stand Layout. The test stand is designed to simulate an airplane wing mounting by locating the engine ahead and away from interfering structures.

The test stand is oriented so that the engine inlet faces 78° from north, the direction of the prevailing winds at this location, which increases the total time that conditions are favorable for testing.

2.4.2 Test Facility Instrumentation

The basic stand instrumentation consists of manually read engine instrumentation, and meteorological instruments for determining if conditions are favorable for testing.

Engine instrumentation leads run to a patch panel on the engine, allowing quick hookup to the stand data system. When the engine is mounted in the stand, a mating patch panel on the stand is connected to the engine's panel. This technique allows maximum use of the stand for testing, reducing test costs. It is estimated that an engine can be mounted on the stand in less than a day, in most cases. In addition, engine instrumentation transducers are mounted close to the engine on the stand patch panel to reduce data transmission inaccuracies and pneumatic transmission line effects.

The stand data acquisition system, called the Continuous Monitor System (CM), consists of a 14 channel tape recorder for recording data, an oscillograph for data display, and signal conditioning equipment. The signal conditioning equipment is capable of conditioning thirteen data channels: eight data channels for temperature, pressure, and position measurements; and five channels for speed or flow measurements. A list of the parameters that can be measured on C-10 stand is given in Table A-XI, including the ranges and estimated accuracies of the measurements.

TABLE A-XI

INSTRUMENTATION RANGES AND ACCURACIES

Parameter	Range Minimum	Range Maximum	No. of Channels	System Accuracy
Ambient Pressure	71(28)	79 cm (31 in.) Hg	1	± 0.03 cm Hg (±0.01 in. Hg)
Bell Crank Stator Vane Angle	-40	+10°	1	± 0.5°
Bellmouth Lip Temperature	0	38°C (100°F)	8	± 0.6°C (± 1°F)
Fuel Flow	0	9,071 kg/hr (20,000 lbm/hr)	2	± 1.0%
Fuel Inlet Pressure	0	689 kPa (100 psig)	1	± 34 kPa (±5 psig)
Fuel Inlet Temperature	0	38°C (100°F)	1	±0.6°C (± 1°F)
Fuel Sample Specific Gravity	measurement made at fuel supply tank and provided to test stand			± 0.001
Fuel Sample Temperature	measurement made at fuel supply tank and provided to test stand			±0.6°C (± 1°F)
Gearbox Breather Pressure (U Tube)	3	40 cm (16 in.) Hg	1	± 0.25 cm (±0.1 in. Hg)
High Pressure Compressor Rotor Speed	0	9000 rpm	2	± 10 rpm
High Pressure Compressor Total Temperature (Borescope Location)	-1 (30)	1316°C (2400°F)	2	±0.6°C (± 1°F)
High Pressure Compressor Discharge Static Pressure	0	3,447 kPa (500 psig)	1	± 0.05% full scale
High Pressure Turbine Discharge Individual Temperatures	0	1316°C (2400°F)	6	±0.6°C (± 1°F)
High Pressure Turbine Discharge Average Temperature (If Applicable)	0	1316°C (2400°F)	1	±0.6°C (± 1°F)

TABLE A-XI (Continued)

INSTRUMENTATION RANGES AND ACCURACIES

Parameter	Range Minimum	Range Maximum	No. of Channels	System Accuracy
Low Pressure Compressor Rotor Speed	0	4000 rpm	2	± 10 rpm
Low Pressure Compressor Total Temperature	0	1316°C (2400°F)	1	±0.6°C (± 1°F)
Low Pressure Compressor Total Pressure	0	3,447 kPa (500 psig)	1	± 0.05% full scale
Low Pressure Compressor Static Pressure	0	3,447 kPa (500 psig)	1	± 0.05% full scale
Low Pressure Turbine Discharge Average Temperature	0	1316°C (2400°F)	1	±0.6°C (± 1°F)
Low Pressure Turbine Discharge Individual Temperatures	0	1316°C (2400°F)	6	±0.6°C (± 1°F)
Low Pressure Turbine Discharge Total Pressure	0	177 cm (70 in.) Hg	1	± 0.07% full scale
Main Oil Pressure	0	689 kPa (100 psig)	1	± 0.07% full scale
Main Oil Temperature	66 (150)	177°C (350°F)	1	±0.6°C (± 1°F)
Oil Quantity Status	2	45 l (12 gallons)	1	± 0.9 l (±0.25 gallons)
Power Lever Angle	0	130°	1	± 1°
Relative Humidity	measurement obtained from Instrumentation Lab			± 5%
Thrust (Bridge A & B)	0	334 kN (75,000 lbf)	1	± 0.7% full scale

TABLE A-XI (Continued)

INSTRUMENTATION RANGES AND ACCURACIES

Parameter	Range Minimum	Range Maximum	No. of Channels	System Accuracy
Turbine Cooling Supply Pressure	0	689 kPa (100 psig)	1	± 0.07% full scale
Vibration Amplitude	0	0.025 cm S.A. (0.010 inches S.A.)	6	± 5%
Wind Direction	0	360°	1	± 5°
Wind Speed	0	144 km/hr (90 mph)	1	± 3 km/hr (± 2 mph)

2.4.3 Stand Services

Two fixed 7.5 ton hoists are available for mounting, handling, and dismounting engines. The stand is also equipped with a hydraulic restraint system in case of hoist failure. A stationary, hydraulic work platform is provided for working on the engine, hooking up instrumentation, or working on test stand itself.

A portable 75 ft long, 14 feet diameter duct is available to control recirculation during large, high bypass ratio engine testing.

A washdown area is located under the engine mount. A list of other stand services is given in Table A-XII.

TABLE A-XII

STAND SERVICES

Service	Description
Shop air	0.2 kg/sec, 689 kPa (0.6 lbm/sec, 100 psig)
Starter air	1.1 kg/sec, 414 kPa (lbm/sec, 60 psig)
Instrument air	22.6 kg/min, 586 kPa (50 lbm/min, 85 psig), at ambient temperature
Nitrogen	9.3 cmm, 3,447 kPa (100 cfm, 500 psig)
Jet A fuel	340 lpm, 586 kPa (90 gpm, 85 psig)
Nacelle fire suppression system	2, 34 kg (75 lbm) bottles of CO_2
Fire-fighting water	757 lpm (200 gpm) at 827 kPa (120 psig)
Electrical	120 - 208 VAC, 3 phase, 60 Hz 480 VAC, 3 phase, 60 Hz 120 VAC, 3 phase, 400 Hz 24 VDC

2.4.4 Portable Add-On Data System

The High Accuracy Pressure and Temperature Data Acquisition System was used in addition to the C-11 stand data system. The High Accuracy Pressure and Temperature Data Acquisition System is portable and has the capacity to record up to 400 inputs (bipolar millivolt) and 336 pressure inputs on eight 48-port scanivalve transducers. It is anticipated that 35 temperatures and 16 pressures were recorded on the High Accuracy Pressure and Temperature Data Acquisition System in support of the Thermal Barrier Coating Second Engine Endurance Test. Data is recorded at a rate of 20 channels per second for temperature and 11 channels per second for pressures. Data is scanned, digitized by an integrating digital volt-meter, and recorded on magnetic tape. Special features of the data recording system include:

1. Channel delete capability
2. Three wire guarded system
3. Variable start and end point scan selection
4. Manual channel monitoring
5. Secondary pressure calibrations

Temperatures

All International Standards Association type "K" and type "S" thermocouples were routed through Uniform Temperature Reference units. Each unit has 30 input channels, which include an ice point reference (0°C (32°F)) supplied by a Joseph Kaye Ice Point Cell.

Pressures

All pressure measurements were recorded on 48-port scanivalved transducer using 400 psig transducers.

Accuracy

The accuracy of the High Accuracy Pressure and Temperature Data Acquisition System, exclusive of probe and thermocouple wire accuracy, is:

Pressure	±0.1% Full Scale of Transducer Range
Temperature	Chromel/Alumel thermocouples - Type "K": ± 0.25°C (±0.45°F) platimum/platinum-10% rhodium thermocouples - Type "S": ±0.5°C (±1°F)

APPENDIX B

PRODUCT ASSURANCE

1.0 INTRODUCTION

The Product Assurance system provided for the establishment of quality requirements and determination of compliance with these requirements, from procurement of raw material until the completion of the experimental test. The system ensures the detection of nonconformances, their proper disposition, and effective corrective action.

Materials, parts, and assemblies were controlled and inspected to the requirements of the JT9D Thermal Barrier Coated Vanes Program. A full production-type program requires inspection to the requirements indicated on the drawings and pertinent specifications. On experimental programs Engineering may delete or waive noncritical inspection requirements that are normally performed by Experimental Quality Assurance.

Parts, assemblies, components and end-item articles were inspected and tested prior to delivery to ensure compliance to all established requirements and specifications.

The results of the required inspections and tests were documented as evidence of quality. Such documents, when requested, were made available to designated Government Representatives for on-site review.

Standard Pratt & Whitney Aircraft Commercial Products Division Quality Assurance Standards currently in effect and consistent with Contractual Quality Assurance Requirements were followed during execution of this task. Specific standards were applied under the contract in the following areas:

1. Purchased Parts and Experimental Machine Shop
2. Experimental Assembly
3. Experimental Test
4. Instrumentation and Equipment
5. Data
6. Records
7. Reliability, Maintainability and Safety

2.0 PURCHASED PARTS AND EXPERIMENTAL MACHINE SHOP

Pratt & Whitney Aircraft has the responsibility for the quality of supplier and supplier-subcontractor articles, and effected its responsibility by requiring either control at source by Pratt & Whitney Aircraft Vendor Quality Control or inspection after receipt at Pratt & Whitney Aircraft. Records of inspections and tests performed at source were maintained by the supplier as specified in Pratt & Whitney Aircraft Purchase Order requirements.

Quality Assurance made certain that required inspections and tests of purchased materials and parts were completed either at the supplier's plant or upon receipt at Pratt & Whitney Aircraft.

Receiving inspection included a check for damage in transit, identification of parts against shipping and receiving documents, drawing and specification requirements, and a check for Materials Control Laboratory release. Positive identification and control of parts was maintained pending final inspection and test results.

The parts manufactured in Pratt & Whitney Aircraft Experimental Machine Shop were subject to Experimental Construction procedures to ensure that proper methods and responsibilities for the control of various quality standards were followed.

Drawing control was maintained through an engineering drawing control system. Parts were identified with the foregoing system. Quality Assurance personnel are responsible for reviewing drawings to ensure that the proper inspection requirements are indicated.

Non-conforming experimental articles involved in this program were detected and identified by Experimental Construction, by vendors, or by Experimental Quality Assurance. Non-conforming articles were reviewed by Engineering and Experimental Quality Assurance personnel in deciding disposition. Records of these decisions, including descriptions of the non-conformances were maintained by Experimental Quality Assurance and reviewed by the cognizant Government Quality Assurance Representative.

3.0 INSTRUMENTATION AND EQUIPMENT

Instrumentation and equipment were controlled under the Pratt & Whitney Aircraft Quality Assurance Plan which includes controls on the measuring and test equipment in Experimental Test to specific procedures. All testing and measuring equipment carries a label indicating its status (controlled, monitor or calibrated) and, when applicable, the date of calibration and next due date.

The accuracy of gages and equipment used for quality inspection functions was maintained by means of a control and calibration system. The system provided for the maintenance of reference standards, procedures, records, and environmental control when necessary. Gages and tools used for measurements were calibrated utilizing the aforementioned system.

Reference standards were maintained by periodic reviews for accuracy, stability, and range. Certificates of Traceability establish the relationship of the reference standard to standards in the National Bureau of Standards (NBS). Calibration of work standards against reference standards was accomplished in environmental-controlled areas.

Initial calibration intervals for gaging and measuring equipment were established on the basis of expected usage and operating conditions. The computerized gage control system provided a weekly listing of all gages and equipment requiring calibration, highlighting overdue items.

4.0 RECORDS

Quality Assurance personnel ensured that records pertaining to quality requirements were adequate and maintained as directed in Experimental Quality Assurance procedures and in accordance with contractual requirements.

Rig build and operating record books were maintained in accordance with Engineering Department requirements. In addition, a consolidated record of operating times for each component test article used in the experimental program was maintained.

5.0 RELIABILITY, MAINTAINABILITY AND SAFETY

Standard production engine design techniques and criteria, which consider product reliability and maintainability in context with all other requirements (such as performance, weight and cost), were used in defining the parts for the JT9D Thermal Barrier Coated Vanes Program. The significant stress areas of the modified parts were analyzed to ensure that their structural margins were equal to or better than those of the bill-of-material parts.

The safety activities at Pratt & Whitney Aircraft are designed to fully comply with the applicable sections of the Federal Aviation Regulations, Part 33 Air Worthiness Standards: Aircraft Engines, as established by the Federal Aviation Administration.

APPENDIX C

GOVERNING EQUATIONS FOR HEAT CONDUCTION ANALYSIS

Consider a plate uniform total thickness, h, and infinite in the plane of the plate, if the temperatures vary through the thickness only, then heat conduction will be governed by minimizing the following integral

$$\pi = \int_o^h \left[\frac{1}{2} K \left(\frac{\partial T}{\partial X} \right)^2 + \rho c T \frac{\partial T}{\partial t} \right] dx \qquad \text{(C-1)}$$

where K is the thermal conductivity
T is the temperature
ρ is the density
c is the specific heat
x is the position, and
t is the time

Divide the plate into a number of layers, or elements, and assume for each element that the temperature varies linearily. The temperature in element j, contributes π_j to the total integral π or

$$\pi_j = \int_{x_{i-1}}^{x_i} \left[\frac{1}{2} K \left(\frac{\partial T_j}{\partial x} \right)^2 + \rho c T_j \frac{\partial T_j}{\partial t} \right] dx \qquad \text{(C-2)}$$

where element j extends from the node at x_{i-1} to the node at x_i and

$$T^j(x,t) = \left(\frac{x - x_{i-1}}{x_i - x_{i-1}} \right) T_i(t) + \left(\frac{x_i - x}{x_i - x_{i-1}} \right) T_{i-1}(t) \qquad \text{(C-3)}$$

where T_i is the temperature of node.

Note that every element has end point locations that do not vary with time except the outside element N, extending from x_{N-1} to x_N. The position of x_N will be assumed to grow at a constant rate

$$v = \frac{dx_N}{dt} \qquad \text{(C-4)}$$

For the outside element N

$$\frac{\partial T^N}{\partial t} = \left(\frac{x-x_{N-1}}{x_N-x_{N-1}}\right)\dot{T}_N + \left(\frac{x_N-x}{x_N-x_{N-1}}\right)\dot{T}_{N-1} - \left[\frac{x-x_{N-1}}{(x_N-x_{N-1})^2}\right] vT_N + \frac{v\,T_{N-1}}{(x_N-x_{N-1})} - \left[\frac{x_N-x}{(x_N-x_{N-1})^2}\right] vT_{N-1} \tag{C-5}$$

For the remaining elements

$$\frac{\partial T^j}{\partial t} = \left(\frac{x-x_{j-1}}{x_j-x_{j-1}}\right)\dot{T} + \left(\frac{x_j-x}{x_j-x_{j-1}}\right)T_{j-1},\quad j \neq N \tag{C-6}$$

and for all the elements

$$\frac{\partial T^j}{\partial x} = \frac{T_j-T_{j-1}}{x_j-x_{j-1}} \tag{C-7}$$

The unknown quantities are the temperatures at the nodal points T_j. The governing equations for T_j can be found by substituting Eqs. (C-5) through (C-7) into (C-2) and then summing each of the π_j to find the total integral, π. Taking the derivative of π with respect to each of the variables T_j results in the following

$$\frac{1}{6}\rho_{j+1}C_{j+1}h_{j+1}\dot{T}_{j+1} + \frac{1}{3}\left(\rho_{j+1}C_{j+1}h_{j+1} + \rho_j C_j h_j\right)\dot{T}_j + \frac{1}{6}\rho_j C_j h_j \dot{T}_{j-1} = \frac{K_{j+1}}{h_{j+1}}T_{j+1} - \left(\frac{K_{j+1}}{h_{j+1}} + \frac{K_{j+1}}{h_j}\right)T_j + \frac{K_j}{h_j}T_{j-1} + L_j \tag{C-8}$$

where $h_j = x_j - x_{j-1}$, and L_j is the contribution due to the motion of point x_N, or

$$L_j = \begin{cases} 0 & j = 0,1,2,\ldots,N-2 \\ \rho_N C_N v\left(-\frac{1}{3}T_{N-1} - \frac{1}{6}T_N\right) & j = N-1 \\ \rho_N C_N v\left(-\frac{1}{6}T_{N-1} + \frac{2}{3}T_N\right) & j = N \end{cases} \tag{C-9}$$

The quantities $T_{-1}(t)$ and $T_{N+1}(t)$ are founded from the boundary conditions at the surfaces, which will be taken to be convective, or

$$K_N \frac{\partial T_N}{\partial x} = H_N \left(T_{a_N} - T_N\right) \text{ at } x = x_N = h \tag{C-10}$$

and

$$K_1 \frac{\partial T_o}{\partial x} = Ho \left(T_o - T_{a_o}\right) \text{ at } x = x_o = 0 \tag{C-11}$$

where H_k is the convective heat transfer coefficient at node x_k, and
T_{a_k} is the outside environmental temperature at node x_k.

Using differences for the derivative gives the temperature T_{-1} and T_{N+1} as

$$T_{N+1} = \frac{h_N H_N}{k_N} \left(T_{a_N} - T_N\right) + T_N \tag{C-12}$$

$$T_{-1} = \frac{h_1 H_o}{k_1} \left(T_1 - T_{a_o}\right) + T_1 \tag{C-13}$$

The transient problem will be solved by using backward differences in time for the derivatives in Eq. (C-8) or

$$\dot{T}_j = \frac{T_{j,k} - T_{j,k-1}}{\Delta t} \tag{C-14}$$

Substituting Eq. (C-14) into Eq. (C-8) and including Eqs. (C-12) and (C-13), results in the following matrix equation.

$$\begin{bmatrix} B_1 & C_1 & 0 & \cdots & & & \\ A_2 & B_2 & C_2 & \cdots & & & \\ 0 & A_3 & B_3 & \cdots & & & \\ 0 & 0 & A_4 & \cdots & & & \\ 0 & \cdots & A_{N-1} & B_{N-1} & C_{N-1} & 0 & \\ 0 & \cdots & 0 & A_N & B_N & C_N & \\ 0 & & 0 & 0 & A_{N+1} & B_{N+1} & \end{bmatrix} \begin{Bmatrix} T_{o,k} \\ T_{1,k} \\ T_{2,k} \\ \cdots \\ T_{N-2,k} \\ T_{N-1,k} \\ T_{N,k} \end{Bmatrix} = \begin{Bmatrix} D_1 \\ D_2 \\ D_3 \\ \cdots \\ D_{N-1} \\ D_N \\ D_{N+1} \end{Bmatrix} \tag{C-15}$$

where

$$B_1 = \frac{\rho_1 C_1 h_1}{3\Delta t} + \frac{k_1}{h_1} + H_o$$

$$C_1 = \frac{\rho_1 C_1 h_1}{6\Delta t} - \frac{k_1}{h_1}$$

$$A_j = \frac{\rho_{j-1} C_{j-1} h_{j-1}}{6\Delta t} - \frac{k_{j-1}}{h_{j-1}} \qquad j = 2,3,\ldots, N-1$$

$$B_j = \frac{\rho_{j-1} C_{j-1} h_{j-1} + \rho_j C_j h_j}{3\Delta t} + \frac{k_j}{h_j} + \frac{k_{j-1}}{h_{j-1}} \qquad j = 2,3,\ldots, N-1$$

$$C_j = \frac{\rho_j C_j h_j}{6\Delta t} - \frac{k_j}{h_j} \qquad j = 2,3,\ldots, N-1$$

$$A_N = \frac{\rho_{N-1} C_{N-1} h_{N-1}}{6\Delta t} - \frac{k_{N-1}}{h_{N-1}}$$

$$B_N = \frac{\rho_{N-1} C_{N-1} h_{N-1} + \rho_N C_N h_N}{3\Delta t} + \frac{k_N}{h_N} + \frac{k_{N-1}}{h_N} + \frac{\rho_N C_N v}{3}$$

$$C_N = \frac{\rho_N C_N h_N}{6\Delta t} - \frac{k_N}{h_N} + \frac{\rho_N C_N v}{6}$$

$$A_{N+1} = \frac{\rho_N C_N h_N}{6\Delta t} - \frac{k_N}{h_N} + \frac{\rho_N C_N v}{3}$$

$$B_{N+1} = \frac{\rho_N C_N h_N}{3\Delta t} + \frac{k_N}{h_N} + H_N - \frac{2\rho_N C_N v}{3}$$

$$D_1 = \frac{\rho_1 C_1 h_1}{6\Delta t} T_{1,k-1} + \frac{\rho_1 C_1 h_1}{3\Delta t} T_{o,k-1} + H_o T_{a_o}$$

$$D_{N+1} = \frac{\rho_N C_N h_N}{3\Delta t} T_{N,k-1} + \frac{\rho_N C_N h_N}{6\Delta t} T_{N-1,k-1} + H_N T_{a_N}$$

$$D_j = \frac{\rho_j C_j h_j}{6\Delta t} T_{j,k-1} + \frac{\rho_{j-1} C_{j-1} h_{j-1}}{6\Delta t} T_{j-2,k-1} + \frac{\rho_j C_j h_j - \rho_{j-1} C_{j-1} h_{j-1}}{3\Delta t} T_{j-2,k-1},$$

$$j = 2,3,\ldots, N$$

The tridiagonal system, Eq. C-15), can be solved for the temperatures by dividing into lower and upper triangular matrices. The algorighm can be found in many standard numerical analysis texts.

APPENDIX D

GOVERNING EQUATIONS FOR THERMAL STRESS ANALYSIS

Consider a uniform multilayer plate of total thickness h in the x-y plane. Assume that plate edges given by

$$f(x,y) = 0 \tag{D-1}$$

are far from the region of interest, then: (1) the stresses will not vary in the x or y direction, and (2) the stress state is isotropic in the x-y plane. Assume there are no loads on the surfaces

$$z = \pm \frac{h}{2} \tag{D-2}$$

The equilibrium equations and the boundary conditions then imply the stress state, in each layer i, is given by

$$\sigma_x^{\,i} = \sigma_y^{\,i} = \sigma^i(z) \tag{D-3}$$

where $\sigma^i(z)$ is a function to be determined.

Hooke's Law requires

$$\varepsilon_r^{\,i} = \varepsilon_\theta^{\,i} = \frac{1}{E_i}\left(1-\nu_i\right)\sigma^i(z) + \alpha_i[T(z) - T_{o_i}] \tag{D-4}$$

$$\varepsilon_z^{\,i} = -\frac{2\nu_i}{E_i}\sigma^i(z) + \alpha_i[T(z) - T_{o_i}] \tag{D-5}$$

$$\gamma_{r\theta}^{\,i} = \gamma_{\theta z}^{\,i} = \gamma_{rz}^{\,i} = 0 \tag{D-6}$$

where E_i is Young's Modulus for Layer i

ν_i is Poisson's Ratio for Layer i

T_{o_i} is the "Stress Free Temperature" for Layer i, and

α_i is the coefficient of expansion for Layer i

where the coordinates have been transformed from rectangular (x, y, z) to polar (r, θ, z). The strain displacement relations are the

$$\varepsilon_r^{\,i} = \frac{\partial u^i}{\partial r} \qquad \gamma_{rz}^{\,i} = \frac{\partial u^i}{\partial z} + \frac{\partial w^i}{\partial r}$$

$$\varepsilon_\theta^{\,i} = \frac{u^i}{r} \qquad \gamma_{\theta z}^{\,i} = 0 \qquad \text{(D-7)}$$

$$\varepsilon_z^{\,i} = \frac{\partial w^i}{\partial z} \qquad \gamma_{r\theta}^{\,i} = 0$$

where u is the radial displacement

w is the axial displacement, and

v is the circumferential displacement vanishes by symmetry.

The displacements can be found from Eqs. (D-4) through (D-7) to be

$$u^i(r,z) = C_2^{\,i} rz + C_1^{\,i} r \qquad \text{(D-8)}$$

$$w^i(r,z) = F_z^{\,i}(z) - \frac{1}{2} C_2^{\,i} r^2 \qquad \text{(D-9)}$$

where

$$F_z^{\,i}(z) = \int_{z_{i-1}}^{z} \varepsilon_z^{\,i}(z)\, dz + F_z^{\,i-1}(z_{i-1}) \qquad \text{(D-10)}$$

and

$$F_z^{\,o}(z) = 0$$

The displacements are continuous at the interfaces of the layers and, therefore, all of the $C_1^{\,i}$ are identical as well as the $C_2^{\,i}$ or

$$C_1^{\,i} = C_1 \qquad \text{(D-11)}$$

$$C_2^{\,i} = C_2 \qquad \text{(D-12)}$$

The remaining two constants C_1 and C_2 are found by requiring that the total in plane force and moment are zero or

$$\int_{-\frac{h}{2}}^{\frac{h}{2}} \sigma_r(z)\, dz = 0 \tag{D-13}$$

$$\int_{-\frac{h}{2}}^{\frac{h}{2}} z\sigma_r(z)\, dz = 0 \tag{D-14}$$

Equations (D-13) and (D-14) result in

$$\begin{aligned} A_{22}C_2 + A_{21}C_1 &= b_2 \\ A_{12}C_2 + A_{11}C_1 &= b_1 \end{aligned} \tag{D-15}$$

where

$$A_{11} = \sum_{i=1}^{N} \frac{E_i(z_1 - z_{i-1})}{(1-\nu_i)}$$

$$A_{12} = A_{21} = \sum_{i=1}^{N} \frac{E_i(z_i^2 - z_{i-1}^2)}{2(1-\nu_i)}$$

$$A_{22} = \sum_{i=1}^{N} \frac{E_i(z_i^3 - z_{i-1}^3)}{3(1-\nu_i)}$$

$$b_1 = \sum_{i=1}^{N} \frac{\alpha_i E_i}{1-\nu_i} \left\{ \int_{z_{i-1}}^{z_i} T(z)dz - T_{o_i}(z_i - z_{i-1}) \right\}$$

$$b_2 = \sum_{i=1}^{N} \frac{\alpha_i E_i}{1-\nu_i} \left\{ \int_{z_{i-1}}^{z_i} T(z)zdz - \frac{1}{2} T_{o_i}(z_1^2 - z_{i-1}^2) \right\}$$

and h_i is the thickness of layer i.

For a layered cylinder such that layer i is between r_{i-1} and r_i, first assume a plane strain solution in the r-θ plane. Then for an axisymmetric stress state the circumferential displacement vanishes, and there are no variations in the circumferential direction. The remaining equilibrium equation for each layer i is

$$\frac{\partial \sigma_r^i}{\partial r} + \frac{\sigma_r^i - \sigma_\theta^i}{r} = 0 \tag{D-16}$$

For the nonvanishing strains, the strain displacement equations are:

$$\varepsilon_r^i = \frac{du^i}{dr} \tag{D-17}$$

and

$$\varepsilon_\theta^i = \frac{u^i}{r} \tag{D-18}$$

Hooke's Law can be written as

$$\varepsilon_r^i = \left(\frac{1+\nu_i}{E_i}\right)\left[(1-\nu_i)\sigma_r^i - \nu_i \sigma_\theta^i\right] + \alpha_i(1+\nu_i)(T-T_{o_i}) \tag{D-19}$$

$$\varepsilon_\theta^i = \left(\frac{1+\nu_i}{E_i}\right)\left[(1-\nu_i)\sigma_\theta^i - \nu_i \sigma_r^i\right] + \alpha_i(1+\nu_i)(T-T_{o_i}) \tag{D-20}$$

The stresses can be found in terms of the radial displacement u by solving Eqs. (D-19) and (D-20) for the stresses and then substituting for the strains by using Eqs. (D-17) and (D-18) resulting in one equation in the unknown radial displacement. Solving this equation and back substituting gives the stresses as

$$\sigma_r^i = C_1^i + \frac{C_2^i}{r^2} - \frac{\alpha_i E_i}{r^2}\int_{r_{i-1}}^{r} rT(r)dr \tag{D-21}$$

$$\sigma_\theta^i = C_1^i - \frac{C_2^i}{r^2} + \frac{\alpha_i E_i}{r^2}\int_{r_{i-1}}^{r} rT(r)dr - \alpha_i E_i T(r) \tag{D-22}$$

while the displacement is

$$u^i = r\,\varepsilon_\theta^i \tag{D-23}$$

where

$$\varepsilon_\theta^{\,i} = \left(\frac{1+\nu_i}{E_i}\right)\left\{(1-2\nu_i)\,C_1^{\,i} - \frac{C_2^{\,i}}{r^2} + \frac{\alpha_i E_i}{r^2}\int_{r_{i-1}}^{r} T(r)rdr + \nu_i\alpha_i E_i T(r) - \alpha_i E_i T_{o_i}\right\} \qquad \text{(D-24)}$$

The boundary conditions between layers require that the radial displacement, or equivalently the hoop strain ε_θ, is continuous and the radial stress is continuous. At the outer surface, r_N, the radial stress is zero and at the inner surface, the radial stress is zero, but if

$$r_o = 0$$

the cylinder is solid and

$$C_2^{\,1} = 0$$

for the stresses to be finite at the center of the cylinder.

The boundary conditions then require the solution of the following simultaneous equations. At the inside surface

$$C_2^{\,1} = 0 \text{ if } r_o = 0$$

or

$$\frac{C_2^{\,1}}{r_o^{\,2}} + C_1^{\,1} = 0 \qquad \text{if } r_o \neq 0$$

At the interface between layers

$$\frac{C_2^{\,i}}{r_1^{\,2}} + C_1^{\,i} - \frac{C_2^{\,i+1}}{r_i^{\,2}} - C_1^{\,i+1} = \frac{\alpha_i E_i}{r_i^{\,2}}\int_{r_{i-1}}^{r} T(r)\,rdr \qquad i = 1,2,\ldots, N-1$$

and

$$-\frac{C_2^{\,i}}{E_i r_i^{\,2}} + \left(\frac{1-2\nu_i}{E_i}\right)C_1^{\,i} + \frac{C_2^{\,i+1}}{E_{i+1} r_i^{\,2}} - \left(\frac{1-2\nu_{i+1}}{E_{i+1}}\right)C_1^{\,i+1} =$$

$$(\nu_{i+1}\alpha_{i+1} - \nu_i\alpha_i)T(r_i) - \alpha_{i+1}T_{o_{i+1}} + \alpha_i T_{o_i} - \frac{\alpha_i}{r_i^{\,2}}\int_{r_{i-1}}^{r_i} rT(r)dr \qquad i = 1,2,\ldots, N-1$$

At the outside surface

$$\frac{C_2^N}{r_N^2} + C_1^N = \frac{\alpha_N E_N}{r_N^2} \int_{r_{N-1}}^{r_N} rT(r)dr$$

There will be a total axial force at the ends of the bar due to the axial stresses σ_z^i, given by

$$\sigma_z^i = \nu_i(\sigma_r^i + \sigma_\theta^i) - \alpha_i E_i [T(r) - T_{o_i}] \quad \text{(D-25)}$$

substituting for the stresses

$$\sigma_z^i = 2\nu C_1^i + \alpha_i E_i T_{o_i} - \alpha_i E_i (1+\nu_i) T(r) \quad \text{(D-26)}$$

The force at the ends of the bars, F, is simply

$$F = 2\pi \sum_{i=1}^{N} \int_{r_{i-1}}^{r_i} \sigma_z^i(r) r dr \quad \text{(D-27)}$$

In order to remove the force assume the Poisson ratio of each layer is the same and represent this value by ν. Also assume a uniform axial strain $\overset{\Delta}{\epsilon}_z$ has been added to the bar. The additional axial stress in each layer is

$$\sigma_z^i = E_i \overset{\Delta}{\epsilon}_z \quad \text{(D-28)}$$

and since Poisson's ratio is the same in every layer, the other stress components do not vanish.

Using Eqs. (D-25) and (D-28), the total force is zero, or

$$F + 2\pi \sum_{i=1}^{N} \int_{r_{i-1}}^{r_i} E_i \overset{\Delta}{\epsilon}_z r dr = 0 \quad \text{(D-29)}$$

and therefore

$$\overset{\Delta}{\epsilon}_z = \frac{-F}{2\pi \sum_{i=1}^{N} \frac{1}{2} E_i (r_i^2 - r_{i-1}^2)} \quad \text{(D-30)}$$

The total axial stress in each layer becomes

$$\sigma_z^{\,i} = 2\nu\, C_1^{\,i} + \alpha_i E_i T_{o_i} - \alpha_i E_i (1+\nu) T(r) + E_i \overset{\Delta}{\epsilon}_z \qquad \text{(D-31)}$$

while the radial and circumferential stresses do not change and are given by Eqs. (D-19) and (D-20), respectively. The resulting mechanical strains can be found from Hooke's Law as

$$\epsilon_r^{i,\text{mech}} = \frac{1}{E_i}\left[\sigma_r^{\,i} - \nu(\sigma_\theta^{\,i} + \sigma_z^{\,i})\right] \qquad \text{(D-32)}$$

$$\epsilon_z^{i,\text{mech}} = \frac{1}{E}\left[\sigma_z - \nu(\sigma_r + \sigma_\theta)\right]$$

$$\epsilon_\theta^{i,\text{mech}} = \frac{1}{E}\left[\sigma_\theta - \nu(\sigma_r + \sigma_z)\right]$$

The thermal strain is simply

$$\epsilon_r^{i,\text{thermal}} = \epsilon_\theta^{\,i,\text{thermal}} = \epsilon_z^{\,i,\text{thermal}} = \alpha_i[T(r) - T_{o_i}] \qquad \text{(D-33)}$$

The total strain is found by summing the mechanical and thermal parts.

REFERENCES

1. Gaffin, W. O. and Webb, D. E., "JT8D and JT9D Jet Engine Component Improvement Program - Task I Feasibility Analysis - Final Report," NASA CR-159449, April 1979.

2. Liebert, C. et. al., "Durability of Zirconia Thermal Barrier Ceramic Coatings on Air-Cooled Turbine Blades in Cyclic Jet Engine Operation," NASA TM X-3410, 1976.

3. Grisaffe, S. J. and Levine, S. R., Proceedings of First DOE/EPRI Conference on Advanced Materials for Alternative Fuel Capable Directly Fired Heat Engines, Castine, ME, 1979, p. 680.

4. Ruckle, D. L., "Evaluation of Plasma-Sprayed Ceramic Coatings for Turbine Engine Components," Thin Solid Films, 64 (1979), p. 327.

5. Bratton, R. J., et. al., "Evaluation of Present-Day Thermal Barrier Coatings for Industrial/Utility Applications," Thin Solid Films, 73 (1980) p. 429.

6. McKee, D. W. et. al., "Resistance of Plasma-Sprayed Ceramic Thermal-Barrier Coatings for Gas Turbine Applications," Proceedings of First DOE/EPRI Conference on Advanced Materials for Alternative Fuel Capable Directly Fired Heat Engines, Castine, ME, 1979, p. 258.

7. Hodge, P. E., et. al., "Evaluation of the Hot Corrosion Behavior of THermal Barrier Coatings," Thin Solid Films, 73 (1980), p. 447.

8. Stecura, S., "Two-Layer Thermal Barrier Coating for High Temperature Components," American Ceramic Society Bulletin, 56(12), Dec. 1977.

9. Grot, A. S., and Martyn, J. K., "Behavior of Plasma-Sprayed Ceramic Thermal-Barrier Coating for Gas Turbine Applications," American Ceramic Society Bulletin, 60(8), Aug. 1981, p. 807.

10. Sevcik, W. R. and Stoner, B. L., "An Analytical Study of Thermal Barrier Coated First Stage Blades in a JT9D Engine," Pratt & Whitney Aircraft Group, PWA-5590, Jan. 1978 (NASA CR-135360).

11. Pennisi, F. J. and Gupta, D. K., "Tailored Plasma Sprayed MCrAlY Coatings for Aircraft Gas Turbine Applications," NASA CR-165234, January, 1981.

12. Blair, M. F., "An Experimental Study of the Heat Transfer and Film Cooling on Large Scale Turbine Endwalls," ASME Journal of Heat Transfer, Nov. 1974, pp 524-529.

13. Sumner, I. E. and Ruckle, D., "Development of Improved-Durability Plasma Sprayed Ceramic Coatings for Gas Turbine Engines", AIAA Paper No. 80-1193, June 1980.

14. Cassenti, B. N., Brinkley, A. M., and Sinko, G. C., "Thermal and Stress Analysis of Thermal Barrier Coatings", AIAA Paper No. 81-1482, July 1981.